EXPLOITING VERTICALLY POINTING DOPPLER RADAR FOR ADVANCING SNOW AND ICE CLOUD OBSERVATIONS

INAUGURAL–DISSERTATION

ZUR

ERLANGUNG DES DOKTORGRADES

DER MATHEMATISCH-NATURWISSENSCHAFTLICHEN FAKULTÄT

DER UNIVERSITÄT ZU KÖLN

VORGELEGT VON

MAXIMILIAN MAAHN

AUS BERGISCH GLADBACH

KÖLN, 2015

BERICHTERSTATTER:
PD Dr. Ulrich Löhnert
Prof. Dr. Roel Neggers
Prof. Dr. Herman Russchenberg

TAG DER MÜNDLICHEN PRÜFUNG:
14.01.2015

CONTENTS

ABSTRACT

Ice and snow particles play a key role in the atmosphere of the Earth and affect—among others—cloud physics and radiative properties, precipitation, and surface albedo. As a consequence, ice and snow have major impact on weather and climate. However, in situ observations of ice clouds and snowfall are difficult and sparse. This leads to a great potential of remote sensing, which can provide observations at high temporal and spatial resolutions. Among the various types of remote sensing instruments, ground-based vertically pointing Doppler radars are one of the most promising concepts: Doppler radars are the only instruments which can penetrate also optically thick clouds and, at the same time, are capable of measuring the fall velocity of hydrometeors. However, the observables of Doppler radars are only indirectly linked to cloud and precipitation properties. The required transfer functions are not uniquely defined resulting in substantial uncertainties of radar-based ice cloud and snowfall retrievals.

In the context of studying ice and snow with radars, this study investigates two key issues: (I) the need for additional snowfall measurements with radar and (II) the potential of higher moments of the radar Doppler spectrum for observing ice cloud properties.

To address Key Issue I, an improved spectral processing scheme for the MRR, a compact precipitation Doppler radar, is introduced. The scheme significantly enhances the radar sensitivity and allows observations of snowfall profiles (Publication I). One year of MRR observations from three polar sites in East Antarctica and Svalbard are investigated with respect to changes of snowfall within the vertical column (Publication II). The transformation found is used for assessing the snowfall measurement uncertainties of the radar onboard the CloudSat satellite which is the only source of global snowfall estimates. However, the lowest 1200 m above the surface are contaminated by ground clutter so that the measurements cannot be exploited (blind zone). The analysis shows that snowfall amount is underestimated when using CloudSat. Also, a blind zone reduced by 50% does not improve the snowfall estimation in all aspects.

For Key Issue II, the potential of higher moments for observations of ice cloud properties, an advanced radar simulator capable of simulating the full Doppler radar spectrum is developed (Additional Study I). The radar simulator is used to forward model in situ aircraft observations of stratocumulus ice clouds obtained during the ISDAC campaign in Alaska (Publication III). The combination of in situ data and ground-based radar observations with the 35 GHz MMCR radar in Barrow, Alaska, is used to develop a novel method for deriving

temperature-dependent particle mass-size relations. Subsequently, the impact of replacing measurements by various parameterizations is investigated for projected particle area and particle size distribution. For this, moments of the radar Doppler spectrum of the MMCR are statistically compared to forward modeled ISDAC data. It is found that the use of higher moments of the Doppler spectrum such as skewness and kurtosis as well as the slopes of the Doppler peak gives additional information when identifying the parameterization methods which lead to most consistent results. Radar-based ice cloud retrievals are often underdetermined and additional observables are desirable. The potential of increasing the number of observables using higher moments and slopes is evaluated based on the developed forward model, parameterizations, and coefficients (Additional Study II). An idealized retrieval based on simulated measurements is successfully developed for moderate turbulence levels. Retrieved are parameters describing particle mass, area, and size distribution. It is shown that a retrieval including higher moments and the slopes provides a higher number of degrees of freedom for signal than a dual-frequency retrieval based on the conventional moments such as radar reflectivity factor and mean Doppler velocity. This highlights the great potential for enhancing observations of ice clouds with higher radar moments.

ZUSAMMENFASSUNG

Eis- und Schneepartikel spielen in der Erdatmosphäre eine Schlüsselrolle. Sie beeinflussen Prozesse und Strahlungseigenschaften von Wolken, Niederschlag und die Oberflächenalbedo, wodurch sie wesentlichen Einfluss auf Wetter und Klima haben. Allerdings sind in situ Messungen von Eiswolken und Schneefall schwierig und selten. Hieraus ergibt sich ein großes Potential von Fernerkundungsverfahren, die kontinuierliche Beobachtungen bei hohen zeitlichen und räumlichen Auflösungen liefern können. Unter den verschiedenen Fernerkundungsverfahren, sind vertikal ausgerichtete, bodengebundene Dopplerradare besonders hervorzuheben: Sie sind das einzige Instrument das sowohl durch optisch dicke Wolken hindurch schauen kann als auch die Fallgeschwindigkeit von Hydrometeoren messen kann. Die Beobachtungsgrößen von Dopplerradaren sind jedoch nur indirekt mit Eigenschaften von Eiswolken und Niederschlag verbunden, was zu erheblichen Unsicherheiten bei der Anwendung von radarbasierten Retrievals führt.

In diesem Zusammenhang werden in dieser Arbeit zwei Schwerpunkte untersucht: (I) die Notwendigkeit von zusätzlichen Beobachtungen von Schneefall mittels Radars und (II) das Potential höherer Momente des Radardopplerspektrums für die Beobachtung mikrophysikalischer Eigenschaften von Eiswolken.

Zur Behandlung von Schwerpunkt I wird ein verbessertes, spektrales Prozessierungsverfahren für MRR, ein kompaktes Dopplerradar, vorgestellt. Das neue Verfahren verbessert die Sensitivität des Radars deutlich und erlaubt die Aufzeichnung von vertikalen Schneefallprofilen (Publikation I). Es werden jeweils zwölfmonatige MRR Beobachtungen von drei polaren Stationen in der Ostantarktis und auf Spitzbergen auf vertikale Veränderungen des Schneefallprofils untersucht. Die Ergebnisse werden verwendet, um auf die Unsicherheit von Schneefallmessungen mit dem Radar des CloudSat Satelliten zurückzuschließen (Publikation II). CloudSat kann zwar als einziges Instrument globale Beobachtungen von Schneefall aufzeichnen, jedoch sind die untersten 1200 m der Atmosphäre durch Festechos der Erdoberfläche kontaminiert und können nicht verwendet werden. Es wird gezeigt, dass dies die mittels CloudSat beobachtete Schneefallmenge verringert und dass selbst eine Reduzierung des von Festechos betroffenen Höhenbereichs um 50% solche Fehler nicht vollständig beheben würde.

Für Schwerpunkt II, das Potential höherer Momente zur Beobachtung von Eiswolkeneigenschaften, wird ein fortschrittlicher Radarsimulator entwickelt, der auch vollständige Dopplerspektren simu-

lieren kann (Weiterführende Studie I). Der Radarsimulator wird benutzt, um in situ Flugzeugbeobachtungen von Stratocumulus-Eiswolken zu simulieren, die während der ISDAC Kampagne in Alaska aufgezeichnet wurden (Publikation III). Die Kombination von Flugzeugdaten und Beobachtungen des 35 GHz MMCR Radars in Barrow, Alaska, wird verwendet, um eine neuartige Methode zur Bestimmung temperaturabhängiger Massen-Größen Verhältnisse für Eispartikel zu entwickeln. Im nächsten Schritt werden Messungen von projizierter Partikelfläche und Partikelgrößenverteilung durch geeignete Parametrisierungen ersetzt und die Veränderung untersucht. Dazu werden die vorwärts modellierten Flugzeugmessungen mit MMCR Beobachtungen statistisch verglichen. Es wird gezeigt, dass höhere Momente der Dopplerspektren, wie Schiefe und Wölbung sowie die linke und rechte Steigung des Dopplerpeaks, zusätzliche Informationen für die Bestimmung der geeignetsten Parametrisierungen liefern können. Radarbasierende Retrievals sind häufig durch den Mangel an Messgrößen unterbestimmt. Um zu untersuchen ob höhere Momente und Steigungen als zusätzliche Messgrößen für Retrievals geeignet sind, werden die hier entwickelten Parametrisierungen, Koeffizienten und das Vorwärtsmodel verwendet (Weiterführende Studie II). Für moderate Turbulenzbedingungen kann ein idealisiertes Retrieval für Parameter zur Beschreibung von Partikelmasse, -fläche und -größenverteilung erfolgreich entwickelt werden. Die Ergebnisse zeigen, dass Retrievals, welche höhere Momente und Steigungen verwenden, mehr Freiheitsgrade erfassen können als Retrievals, welche zwei verschiedene Frequenzen, jedoch nur die herkömmlichen Momente, Radar-Reflektivitätsfaktor und mittlere Dopplergeschwindigkeit, verwenden. Dies unterstreicht das große Potential von höheren Momenten für verbesserte Beobachtungen von Eiswolken.

Part A

INTRODUCTION

1 MOTIVATION

Ice plays a key role in the Earth's atmosphere. While ice crystals are, as the name implies, single crystals, aggregates of thousands of ice crystals are called snow crystals or snowflakes (*AMS*, 2014). In practice, it is usually assumed that ice clouds consist mainly of suspended ice crystals while snowflakes precipitate out of clouds (*Waliser et al.*, 2009). However, this categorization of frozen hydrometeors into two species is to a certain extent artificial (*Schmitt and Heymsfield*, 2014), because there is no clear separation between ice and snow with respect to fall velocity and even the smallest ice crystals sediment, albeit very slow. At the same time, it is also possible to find aggregated crystals within ice clouds (e. g., *Brown and Francis*, 1995; *Korolev et al.*, 1999) and single, unaggregated ice crystals can be observed as precipitation falling to the surface in very cold conditions (e. g., *Magono and Lee*, 1966; *Hogan*, 1975).

In this thesis, frozen water within ice or mixed phase clouds is termed ice and precipitating particles are termed snow. See Schmitt and Heymsfield (2014) for an alternative definition.

Independent of the precise discrimination, both hydrometeor species play a key role in the climate system. With a global mean snowfall rate of 0.28 mm h^{-1} (*Kulie and Bennartz*, 2009), snowfall is a crucial component of the atmospheric water cycle contributing to the majority of precipitation in high latitudes (Figure 1) and acting as a source for glaciers and ice shields. Also rainfall is mostly initiated via the ice phase in mid- and high latitudes: *Löhnert et al.* (2014) found that the ice phase was involved for 97% of the total precipitation amount for a mid-latitude site in Germany. In addition, snowfall and precipitation in general are an important freshwater input into the oceans influencing ocean surface buoyancy and deep water formation (*Liu and Curry*, 1997). At the land surface, snow can have major impact on society by influencing e. g., traffic (*Call*, 2011) and winter recreation (*Rutty and Andrey*, 2014). From a meteorological perspective, snow has a major impact on the albedo of the Earth (*Vavrus*, 2007; *Waliser et al.*, 2011) which is one of the most important feedback mechanism for global climate (*Hall*, 2004). Similarly, ice clouds influence the albedo by shortwave reflective cooling, but at the same time, they also emit longwave radiation back to the Earth's surface and contribute to the greenhouse warming. Recent studies indicate that for high ice clouds, the latter effect outweighs the other (*IPCC*, 2014, FAQ 7.1).

Despite their importance, many processes related to ice clouds and snowfall are not yet fully researched. Apart from the exact determination of the influence of ice clouds on the radiation budget (*Shupe and Intrieri*, 2004), the development of the various crystal shapes as a function of temperature and supersaturation is not yet fully understood

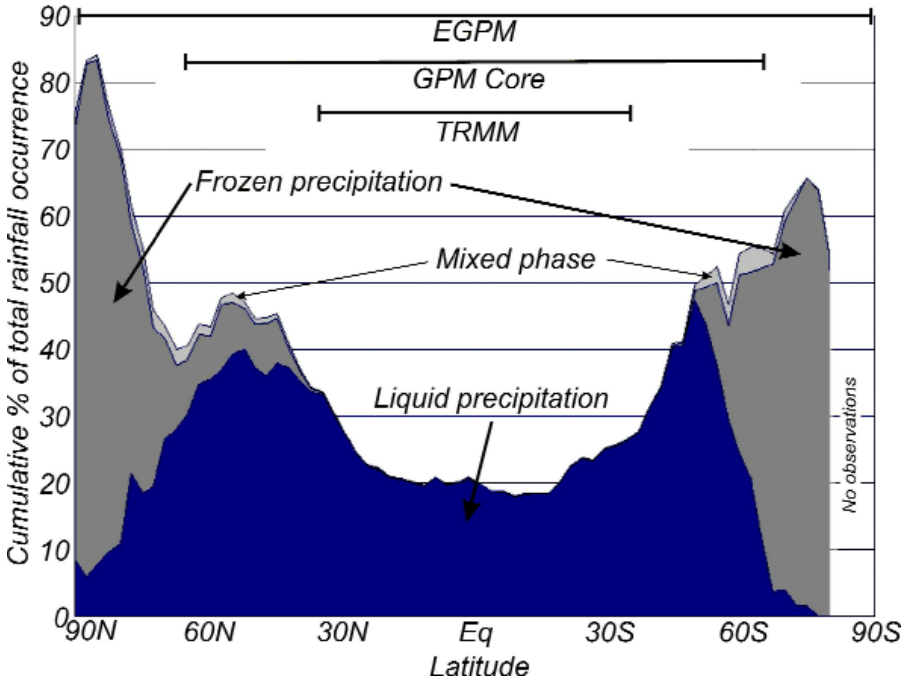

Figure 1: Mean zonal occurrence of oceanic light precipitation (as a percentage of total rainfall occurrence) derived from the Comprehensive Ocean-Atmosphere Data Set using ship-borne meteorological observations (1958-1991). Source: *ESA* (2004) cited in *Levizzani et al.* (2011).

(*Libbrecht*, 2005). Furthermore, the processes relating snowfall to surface deposition are difficult to quantify, especially at high latitudes (*Lenaerts et al.*, 2012).

Due to the complexity even at very small scales, the representation of ice (*Eliasson et al.*, 2011) and snowfall (*Adams*, 2004; *Thompson et al.*, 2004) in *Numerical Weather Prediction* (NWP) models and *Global Climate Models* (GPM) leaves room for improvement (*Li et al.*, 2005, 2007) which causes large uncertainties also with respect to future climate change (*IPCC*, 2014, p. 743). One of the main reasons is that most cloud related processes require parameterizations, because they cannot be resolved by the model and are sub-scale (*Arakawa*, 2004). In addition, the complex interactions between aerosols and hydrometeors are not yet fully understood and most NWP models contain no more than three idealized species of frozen hydrometeors (cloud ice, snow, and graupel). For these, bulk microphysical models are used with empirical parameterizations. These cannot resolve processes depending on particle habit or size because only one moment of the particle size distribution is taken into account. Two moment schemes (e. g., *Seifert and Beheng*, 2006) or even full bin microphysics (e. g., *Lynn et al.*, 2005) have only recently been developed due to the larger computational costs.

The moment treated by one-moment schemes is usually hydrometeor content as mixing ratio.

More and improved observations are essential for increasing the understanding of ice and snow, but their observation is particularly difficult. Traditionally, precipitation gauges are used for measuring snowfall, but they are especially affected by biases induced by wind undercatch and blowing snow (*Yang et al.*, 2005; *Knuth et al.*, 2010; *Thériault et al.*, 2012). In addition, there are only few surface observations of precipitation available at high latitudes and measurements are almost completely missing over sea or over the ice shields (*Schneider et al.*, 2014). For ice clouds, in situ observations are even more sparse, because they are only possible on exposed locations such as high mountains (*Matrosov et al.*, 2001; *Krüger et al.*, 2014) and during aircraft campaigns (e. g., *Verlinde et al.*, 2007; *McFarquhar et al.*, 2011; *Schmid et al.*, 2014). However, in situ aircraft measurements require a lot of resources and hence cannot provide long term observations. At the same time, there are still major problems with the quality of ice clouds measurements (*Baumgardner et al.*, 2012), e. g., due to shattering of the ice crystals at the inlets of the in situ probes (*Field et al.*, 2006).

This gap in observations can be partly closed using remote sensing. Especially satellite-based observations can provide homogeneous, globally available products of precipitation and cloud properties over long time spans (*Levizzani et al.*, 2007, 2011), but also airborne and ground-based remote sensing instruments are frequently used. Remote sensing techniques can be classified either by active and passive measurement principles or by the used frequency range. Numerous techniques exist for observing snow and ice using passive sensors in the visible/infrared frequency range from space (e. g., *Yang et al.*, 2007; *Stengel et al.*, 2014) as well as from the ground (*Knuteson et al.*, 2004). Also instruments operating in the microwave-range are used from space (e. g., *Weng and Grody*, 2000; *Sun and Weng*, 2012) and from from the ground (e. g., *Kneifel et al.*, 2010; *Kneifel*, 2011; *Xie et al.*, 2012). Even though passive sensors cannot provide vertically resolved observations, they are available on multiple spacecrafts for several decades. This allows for investigation of long-term data sets (*Knapp et al.*, 2011) and for operational assimilation into NWP models (*Hou et al.*, 2001).

Profile information of ice clouds can only be obtained from active sensors such as radar (radio detection and ranging) and lidar (light detection and ranging) instruments. While the former is able to completely penetrate ice and mixed phase clouds as well as snowfall, lidars are heavily attenuated by liquid layers and cannot penetrate optically thick clouds. Such layers are frequently found in clouds even below the melting points (*Hu et al.*, 2010). Nevertheless, lidars are successfully used for investigating pure ice clouds from space (*Winker et al.*, 2009) and from the ground (*Sassen*, 1991), partly also in combination with radars (*Delanoë and Hogan*, 2008; *Battaglia and Delanoë*, 2013).

The ability to penetrate also optically thick ice and snow clouds makes radar observations unique. Quantitative and qualitative snowfall measurements using operational, ground-based weather radar networks have recently been enhanced with the advent of polarized radars, which can estimate the particle shape by the difference between horizontally and vertically polarized reflectivity (*Kennedy and Rutledge*, 2011). Unfortunately, weather radar observations are only available in the densely populated parts of the developed world, because their operation is costly. In addition, the sensitivity of weather radars operating at centimeter wavelengths is not sufficient for studying ice clouds, hence millimeter wavelengths need to be used for studying clouds. As a drawback, attenuation is stronger at millimeter wavelengths which limits the range of cloud radars (*Lhermitte*, 1987). The most important millimeter cloud radar is probably the one onboard the CloudSat satellite (*Stephens et al.*, 2002, 2008) which was launched in 2006 and allowed for the first time near-global estimates of snowfall (*Liu*, 2008a) filling the gaps of traditional snowfall observations. CloudSat, however, cannot measure lower than 1200 m above the surface due to contamination with ground clutter (blind zone).

CloudSat cannot observe precipitation at latitudes higher than 82° due to the inclination of its orbit.

Remote sensing observations are per se indirect, i. e., the observation quantities (e. g., brightness temperature, reflectivity) are not directly connected to the desired meteorological quantities (e. g., ice water content, number of particles). Thus, retrieval techniques are required using forward operators and prior knowledge. These retrievals are usually underdetermined, which means that not sufficient information is measured by the radar in order to determine the atmospheric state unambiguously. One reason is that radar observations depend heavily on particle type, projected area, effective density and size distribution. Especially the effective particle density (which depends on particle mass) has a great impact on radar observations and many retrieval products require either prior knowledge of particle mass (*Posselt and Mace*, 2014) or use it as a tuning parameter (*Matrosov*, 1998).

To increase the number of observables, multiple frequencies can be combined (*Sekelsky et al.*, 1999; *Hogan et al.*, 2000; *Kulie et al.*, 2014) exploiting the strong dependence of differential radar reflectivity on particle shape (*Kneifel et al.*, 2011a). Other studies propose to use combinations of several remote sensing instruments exploiting different measurement principles, such as radar-microwave radiometer (*Grecu and Olson*, 2008; *Löhnert et al.*, 2008; *Posselt and Mace*, 2014) or lidar-radar combinations (*Intrieri et al.*, 1993; *Delanoë and Hogan*, 2008). However, when combining different frequencies and/or measurement principles, their different measurement volumes and temporal resolutions have to be taken into account. Otherwise, the different instruments might observe different parts of the cloud with different properties which can lead to large retrieval errors.

Another option to exploit additional information, but without using additional instruments, is to use not only reflectivity, but also other moments of the Doppler spectrum of vertically pointing radars. The mean Doppler velocity corresponds—in the absence of vertical air motion—to the reflectivity weighted mean fall velocity. This can be exploited for constraining ice cloud microphysical properties (*Matrosov et al.*, 2002; *Szyrmer et al.*, 2012). Other studies propose to use the second moment, i. e., Doppler spectrum width (*Mace et al.*, 2002; *Deng and Mace*, 2006), which describes the standard deviation of the Doppler spectrum. While even higher radar moments such as skewness and kurtosis have been used to separate cloud drops from drizzle (*Kollias et al.*, 2011) and for locating supercooled liquid water (*Shupe et al.*, 2004; *Luke et al.*, 2010), no studies so far investigated the use of higher moments for studying ice clouds. An alternative to the use of radar moments is to exploit the full Doppler spectrum, but for ice clouds this was so far only applied to case studies (*Dufournet and Russchenberg*, 2011; *Verlinde et al.*, 2013).

2 OVERVIEW OF THE STUDIES

In the context of studying ice and snow with cloud radars, this study investigates two key issues in greater detail (Figure 2): (I) the need for *Enhanced snowfall observations* with radar and (II) the development, assessment, and retrieval of ice cloud parameterizations *Exploiting higher moments* of the radar spectrum.

To address Key Issue I, an enhanced spectral processing routine for snow observations with a small precipitation radar is introduced in Publication I. This method is used to investigate the vertical variability of snowfall at polar sites in order to asses the impact of the blind zone of the Cloudsat satellite (Publication II).

For Key Issue II, an advanced radar simulator capable of simulating the full radar spectrum and higher moments is developed and presented in Additional Study I. The radar simulator is used to forward model in situ aircraft observations in order to asses ice cloud parameterizations in Publication III. For particle mass, a novel method is developed to derive the mass-size relation from the functional relation between reflectivity and mean Doppler velocity. To evaluate parameterizations of projected area and particle size distribution, additional, higher moments of the radar Doppler spectrum are exploited which have not been used before for observations of ice clouds. Then, in Additional Study II, the potential of these higher radar moments for enhancing ice cloud retrievals is investigated based on the data set obtained in Publication III.

Figure 2 depicts how the five studies of this thesis are linked together. In the following, they are briefly introduced.

2.1 PUBLICATION I: IMPROVED DOPPLER SPECTRA PROCESSING

In Publication I (*Maahn and Kollias*, 2012), an enhanced Doppler spectra processing scheme for *Micro Rain radars* (MRR) is developed in order to allow observations of snowfall. The MRR is a light-weight, low-cost, 24 GHz *Frequency Modulated Continuous Wave* (FCMW) radar (*Klugmann et al.*, 1996). Even though the hardware specifications and the low power consumption make MRR well-suited for observations in remote areas, its observations are restricted to rain due to software limitations: designed as a zenith-pointing profiler, MRR estimates rain rates by converting the radar Doppler spectrum into the drop size distribution $N(D)$ (*Atlas et al.*, 1973; *Peters et al.*, 2005) using a raindrop size-fall velocity ($D - v$) relation (*Gunn and Kinzer*, 1949). While this works well in the absence of vertical air motions (*Peters et al.*, 2002,

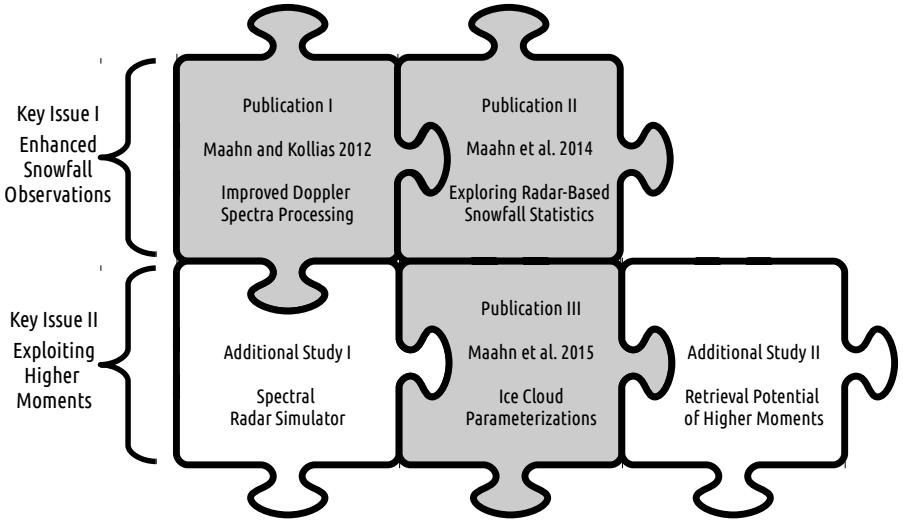

Figure 2: Structure of the thesis with publications (gray) and additional studies (white).

2005), precipitation rates are biased for snow for two reasons which are not taken into account: (a) the $D - v$ relation is different and (b) the dielectric constant is smaller for ice than for liquid water in the microwave region. Even though (b) is partly compensated by the larger size of snowflakes in comparison to equally heavy rain drops, (a) leads to a strong overestimation of precipitation rates in the case of snow. Unfortunately, the MRR standard software does not record the measured equivalent radar reflectivity factor Z_e so that Z_e cannot be used as an alternative to study snowfall. Instead, the radar reflectivity factor Z is estimated from $N(D)$ assuming rain and Mie scattering. *Kneifel et al.* (2011b) presented an alternative method to estimate Z_e directly from MRR's processed Doppler spectrum, but also stated that an increase of the found MRR sensitivity of 3 dBz is required to capture a greater number of snow events. This requires the development of a novel radar processing scheme (*Improved Mrr PROcessing TOOl* – IMProToo) based on MRR raw data which is presented in Publication I and which enhances the MRR sensitivity. To validate the processing scheme and to show the potential of MRR for snow observations, four months of MRR observations obtained at the *Umweltforschungsstation Schneefernerhaus* (UFS) in the Bavarian Alps are compared to co-located observations of a pulsed 35 GHz cloud radar.

IMProToo is available under an open source license at http://gop.meteo.uni-koeln.de/software.

2.2 PUBLICATION II: EXPLORING RADAR-BASED SNOWFALL STATISTICS

An application of the scheme developed in Publication I is presented in Publication II (*Maahn et al.*, 2014): in this study, MRRs are used to investigate vertical changes of snowfall in polar regions within

the so-called blind zone of the radar onboard the CloudSat satellite. CloudSat is part of a constellation of six Earth observation satellites flying in matched orbits (A-train, *L'Ecuyer and Jiang*, 2010). It carries a cloud radar operating at 94 GHz ($\lambda = 3.2$ mm) which is designed for global cloud studies (*Stephens et al.*, 2008; *Tanelli et al.*, 2008). To gain a sufficiently high sensitivity for observation of clouds despite CloudSat's distance to the surface of 705 km to 730 km without exceeding available power or demanding a large antenna, CloudSat uses a long pulse length of 480 m. Oversampling is used to achieve the final vertical resolution of 240 m. The long pulse leads to a complete loss of information within the first 750 m of the atmosphere. The first range gate free of ground clutter is found to be at 1200 m above ground level (agl) (*Marchand et al.*, 2008). In the case of complex orography, the blind zone might even be larger.

Even though designed to study clouds, CloudSat is increasingly used to study snowfall as well; it is the first and only instrument allowing to derive near-global snowfall climatologies (*Liu*, 2008a; *Kulie and Bennartz*, 2009; *Levizzani et al.*, 2011; *Palerme et al.*, 2014). In contrast to rain, attenuation and multi-scattering do not severely affect the observations of snow and even partly cancel each other out (*Matrosov and Battaglia*, 2009). Recently, an official CloudSat snow product was released (*2C-SNOW-PROFILE Wood*, 2011; *Wood et al.*, 2013). These climatologies and products are, however, based on observations above the blind zone assuming that statistics of snowfall do not change while falling toward the surface. The question whether this assumption generally holds true is still open. Some studies find a general increase of radar reflectivity due to aggregation and depositional growth (*Fabry and Zawadzki*, 1995; *Liu*, 2008a; *Matrosov and Battaglia*, 2009; *Wolfe and Snider*, 2012) while other studies find radar reflectivity to be nearly constant in the lowest 2 km (*Stewart et al.*, 2004; *Henson et al.*, 2011).

In Publication II, one year of MRR observations from the Belgian *Princess Elisabeth* station in East-Antarctica (*Gorodetskaya et al.*, 2015) and from two sites in Svalbard, Norway (Ny-Ålesund and Longyearbyen *Maahn*, 2010) are analyzed with respect to changes of the vertical profile of snowfall observations within the blind zone of CloudSat.

2.3 ADDITIONAL STUDY I: SPECTRAL RADAR SIMULATOR

Instrument simulators for remote sensing are essential for sensitivity studies and retrieval developments. To be able to simulate active sensors as well, the *PAssive Microwave radiative TRAnsfer model* (PAMTRA) developed at *University of Cologne* is extended by an advanced active component (now called: *Passive and Active Microwave radiative TRAnsfer model*) and presented in Additional Study I. The radar simulator extends PAMTRA by using the scattering properties of frozen or liquid hydrometeors to simulate the full, polarized radar Doppler

spectrum. To estimate the moments of the radar Doppler spectrum, the methodology presented in Publication I is used. Due to the new active part, passive and active instruments can be simulated at the same time allowing the development of joint radar-microwave radiometer products. In contrast to other combined instrument simulators, PAMTRA is not tailored to a specific mission and can be adapted to diverse instrument specifications. Due to the flexible implementation of hydrometeors, PAMTRA can handle an arbitrary number of liquid and frozen hydrometeors described by discretized distributions of hydrometeor properties or moments of the distribution. This makes coupling with various NWP models, GCMs or in situ measurements simple.

2.4 PUBLICATION III: ICE CLOUD PARAMETERIZATIONS

In Publication III (*Maahn et al.*, 2015), the PAMTRA model introduced in Additional Study I is used to forward model in situ ice cloud observations obtained from aircrafts during the *Indirect and Semi-Direct Aerosol Campaign* (ISDAC). ISDAC took place in the vicinity of the *MilliMeter wavelength Cloud Radar* (MMCR, *Moran et al.*, 1998) at the *Atmospheric Radiation Measurement* (ARM) climate research facility *North Slope of Alaska* (NSA) in Barrow. The MMCR data is processed following the methodology proposed in Publication I. Currently, ISDAC is the only available data set obtained in the vicinity of a vertically pointing Doppler cloud radar which contains ice cloud observations measured by in situ probes using the new, enhanced design of the probe tips (*Korolev et al.*, 2013).

One of the main challenges of radar observations of ice clouds is that the observables are not directly confined to the cloud properties. As a consequence, retrieval techniques are required which for their part require analytical descriptions of the cloud microphysics. Such parameterizations are also essential for NWP models and GCMs. Taking up on on the importance of parameterizations, two main objectives are studied in Publication III.

(1) a novel method to estimate the mass-size relation $m(D)$ is developed using a combination of radar and in situ aircraft observations. Particle mass cannot be measured directly by aircraft in situ probes and measurements with ground-based instruments are challenging. At the same time, the scattering properties of ice crystals depend heavily on particle mass, so that a wrong parameterization of particle mass can lead to large errors. Because both, particle habit and mass-size relation, depend on ambient temperature, the data set is divided into different temperature intervals and analyzed separately.

(2) the effect of describing projected area $A(D)$ and particle size distribution $N(D)$ by various analytical expressions on forward modeling of radar observations is investigated. For this, also the higher

moments of the radar Doppler spectrum (skewness and kurtosis) as well as the slopes of the Doppler peak are used. The higher moments and the slopes have not been exploited before for ice cloud observations. For projected area, power laws are mostly used, and a large variety of parameterizations has been proposed for the particle size distribution. These parameterizations are evaluated by replacing measured projected area and particle size distribution with parameterized versions.

Both objectives together lead to a consistent, joint data set of ISDAC and MMCR observations containing coefficients to describe particle mass, projected area, and particle size distribution as functions of size as well as the corresponding analytical expressions. For liquid water clouds it was found that such prior information has great impact on retrieval accuracy (*Ebell et al.*, 2010). Together with the PAMTRA forward operator, Publication III sets the stage for developing ice cloud retrievals based on the climatology obtained during ISDAC which exploit not only lower, but also higher radar moments.

2.5 ADDITIONAL STUDY II: RETRIEVAL POTENTIAL

In Additional Study II, the forward model of Additional Study I, which includes the radar processing scheme of Publication I, and the data set developed in Publication III are combined to investigate the potential of higher radar moments for retrieval applications.

Until today, ice cloud retrievals have exploited only radar reflectivity Z_e, mean Doppler velocity W (*Matrosov et al.*, 2002; *Szyrmer et al.*, 2012) and—in some cases—spectrum width σ (*Mace et al.*, 2002; *Deng and Mace*, 2006). The use of skewness Sk, kurtosis Ku and the left and right slopes S_l and S_r has not yet been evaluated and the full Doppler spectrum was only investigated for case studies (*Verlinde et al.*, 2013). However, additional information is an urgent need for ice cloud retrievals, because retrievals are usually underdetermined resulting in large uncertainties or the requirement of additional constrains. Even though additional information can also be obtained by multi-instrument combinations (e. g., *Delanoë and Hogan*, 2008; *Grecu and Olson*, 2008), using multiple instrument increases the complexity of measurements and retrievals. This can add new error sources, e. g., due to different spatio-temporal resolutions. Therefore, it would be a major improvement if more information could be exploited from a single instrument which in addition is already widely used.

In contrast to other studies which focused mainly on bulk parameters such as ice water content, here, the parameters describing particle mass, projected area, and particle size distribution are directly included into the retrieval. A retrieval based only on higher moments and the slopes has the advantage that it depends only weakly on radar calibration and vertical air motion. These effects are restricting

other retrievals using radar reflectivity and mean Doppler velocity (e. g., *Szyrmer and Zawadzki*, 2014b). Higher moments and the slopes are, however, strongly influenced by broadening effects of the radar Doppler spectrum due to turbulence and wind shear. To reduce the impact of turbulence on the Doppler spectrum, the radar integration time has recently been reduced to 1 s to 2 s or even less for the radars of the ARM program (*Kollias et al.*, 2007a). Nevertheless, a low turbulence environment is investigated in this study to minimize the influence of turbulence.

In Additional Study II, the retrieval potential of higher moments is first analyzed qualitatively by evaluating response functions and then quantitatively by developing an idealized retrieval based on higher moments. The retrieval is successfully used to estimate the number of independent information pieces which higher moments can contribute to an ice cloud retrieval.

2.6 OUTLINE

This thesis is composed of four parts: Apart from the introduction, Part A also contains a brief overview of the theory of ice clouds and radar observations. Then, Key Issue I *Enhanced snowfall observations* is addressed in Part B containing Publications I and II. Part C presents Key Issue II *Exploiting higher moments* with Additional Study I, Publication III and Additional Study II. Finally, a summary of the key findings of Parts B and C and concluding remarks are given in Part D.

3

THEORY

In the following, a brief introduction into ice cloud microphysics is given moving from micro-scale processes to macro-scale features. After discussing the single scattering properties of ice and snow, the theory of meteorological radar observations is briefly introduced.

3.1 ICE AND SNOW PARTICLES IN THE ATMOSPHERE

3.1.1 *Formation of ice crystals*

Ice particles can form by both homogeneous and heterogeneous nucleation (*Pruppacher and Klett*, 1997; *Reitter*, 2013). *Rogers and Yau* (1989) classifies heterogeneous processes into four mechanisms: (1) deposition of water vapor onto an ice nucleus. (2) heterogeneous condensation of a droplet on an ice nucleus followed by freezing. (3) freezing of a supercooled droplet after immersion of an ice nucleus and—similarly—(4) freezing of a supercooled droplet after contact with an ice nucleation nucleus. Heterogeneous nucleation is, however, limited by the lack of ice nuclei, which are far rarer than cloud condensation nuclei. In addition, homogeneous freezing of SCLW drops occurs only at temperatures colder than $-37\,°C$, and consequently *Super Cooled Liquid Water* (SCLW) drops are frequent. Homogeneous freezing is the only homogeneous nucleation process, because homogeneous ice nucleation by deposition requires non-naturally high supersaturations rates.

3.1.2 *Growth from water vapor*

Ice crystals' growth from water vapor produces a broad range of different ice particle habits—literally every one is unique (Figure 3). Johannes Kepler was probably among the first who described ice and snow particles from a scientific point of view in 1611 (*Kepler and Hardie*, 2014). With the advent of photography, large catalogs with photos of snow and ice crystals were collected showing the large natural variability of particles habits (e. g., *Bentley*, 1901, 1903). Building up on these collections, categorization schemes were developed to classify ice and snow particles with respect to habit (*Magono and Lee*, 1966; *Kikuchi et al.*, 2013). *Nakaya* (1954) (cited in *Marshall*, 1954) was the first one who tried to answer the question what determines the shape of ice particles by laboratory experiments and found a strong dependency on temperature and water vapor supersaturation relative to ice.

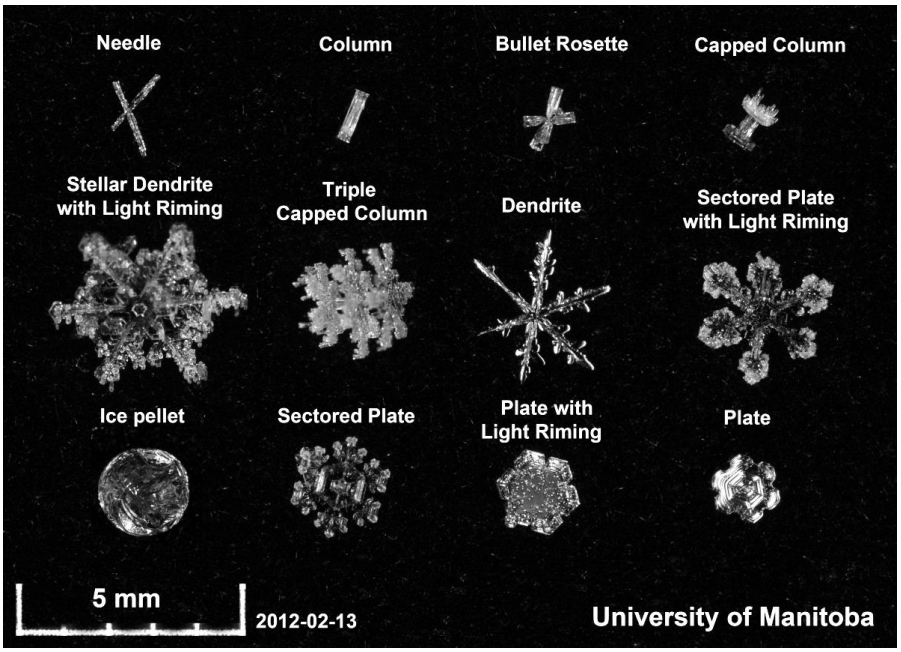

Figure 3: Different kinds of ice crystals, partly with riming, obtained during the Global Precipitation Mission (GPM) Cold-season Precipitation Experiment (GCPEx, *Hudak et al.*, 2012). Figure courtesy of Ronald Stewart.

This concept was extended and refined multiple times (*Magono and Lee*, 1966; *Pruppacher and Klett*, 1997) and recently updated for temperatures below −20 °C (Figure 4) based on cirrus observations (*Bailey and Hallett*, 2009, 2012). In general, ice particles can be mostly described as polycrystals below −22 °C while single-crystal shapes dominate for warmer temperatures. For temperatures below −40 °C, crystal shapes are mostly columnar and for temperatures between −40 °C and −22 °C plate-like shapes prevail. For warmer temperatures, the particle type changes frequently with increasing temperature: From sector plates and dendrites (−22 °C to −8 °C), to hollow columns and needles (−8 °C to −4 °C) and to plates again (−4 °C to 0 °C). At all temperatures, the complexity increases strongly with increasing ice supersaturation and most complex dendrites can be found at temperatures between −15 °C and −10 °C. In this temperature range, the supersaturation over ice with respect to liquid water reaches its maximum so that the Wegener–Bergeron–Findeisen process (i. e., the transport of water vapor from liquid drops to ice crystals, *Korolev*, 2007) works most efficiently. Even though the morphology diagram for ice crystals has been confirmed by several studies, the growth processes are qualitatively and quantitatively not yet fully understood (*Libbrecht*, 2005). For example, there is high variability among ice crystals created in the laboratory under the same environmental conditions, highlighting the sensitivity of growth towards small environmental perturbations (*Libbrecht*, 2005).

See Libbrecht (2005) for an introduction into ice crystal growth from water vapor.

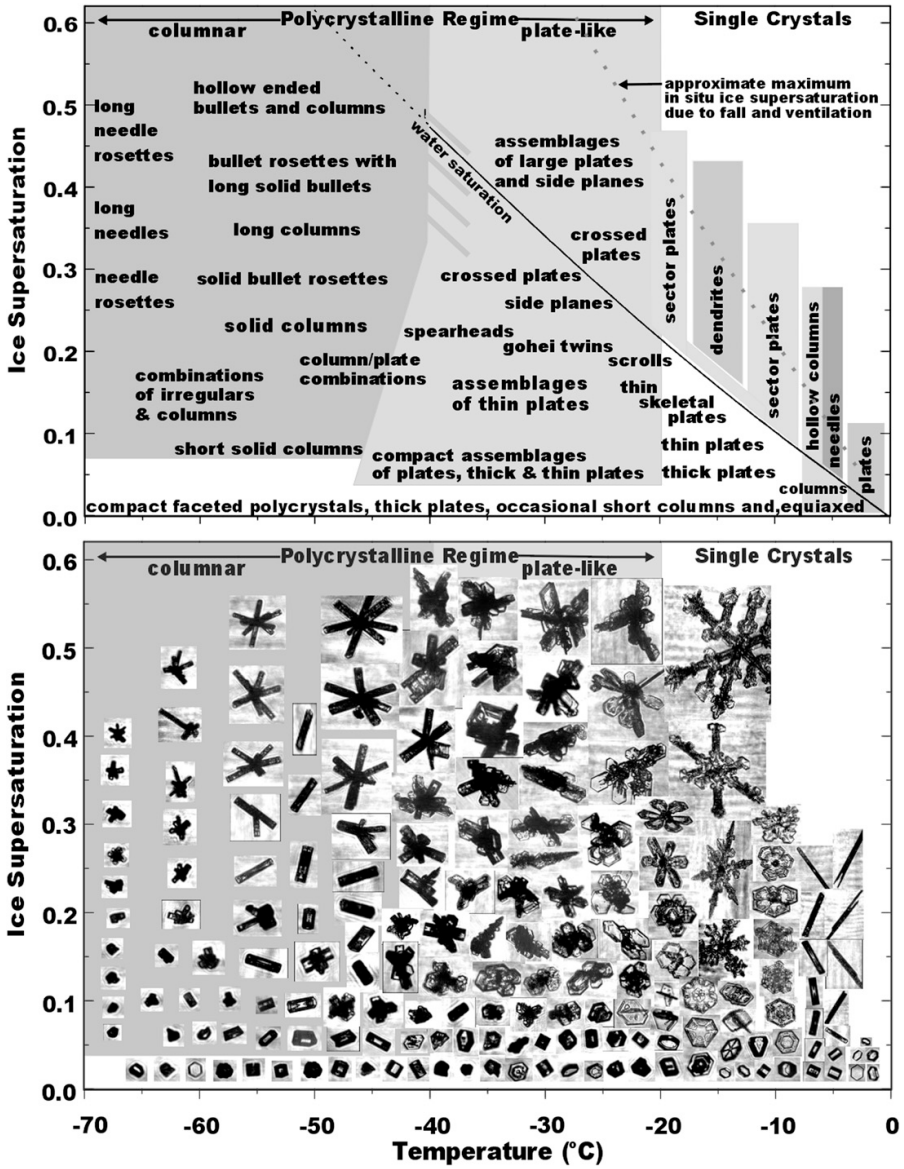

Figure 4: Habit diagram for ice crystals based on laboratory and in situ aircraft observations as a function of temperature and ice supersaturation. Figure taken from *Bailey and Hallett* (2009). © American Meteorological Society. Used with permission.

3.1.3 *Further development*

Under real-world conditions, idealized single-crystal or polycrystal shapes occur only rarely, because a crystal is affected by different environmental conditions during its travel through the cloud. In addition, ice crystals do not only grow from deposition (diffusion), but also from riming and aggregation. The former describes coating with small SCLW drops which freeze to the crystal on contact (see Figure 3 for examples). SCLW occurs frequently (*Boudala et al.*, 2004) at the top of ice clouds (*Rauber and Tokay*, 1991) even at temperatures

Ice clouds containing SCLW are termed mixed phase clouds.

of −30 °C and below (*Wang et al.*, 2004; *Verlinde et al.*, 2007). It has a strong impact on cloud microphysics (*Tremblay et al.*, 1996; *Jiang et al.*, 2000) and radiation (*Shupe and Intrieri*, 2004), but ground-based detection is challenging (*Shupe et al.*, 2008a). Finally, aggregation—merging of several ice crystals—leads to the creation of snow flakes which are composed of up to several thousand ice crystals (*AMS*, 2014). It is distinguished between the "primary" and "secondary aggregation growth region" (*Locatelli and Hobbs*, 1974; *Löhnert et al.*, 2011). The former occurs at temperatures of −5 °C and larger and is related to the higher sticking efficiency caused by a thin quasi-liquid film on the ice surface (*Rosenberg*, 2005). The latter region is caused by the branched structure that is typical for ice crystals in the temperature range −10 °C to −15 °C and which increases the sticking efficiency of ice crystals (*Hobbs et al.*, 1974). If particles fall into sub-saturated air, they may also diminish or even dissolve due to sublimation. Complete sublimation of precipitation below the cloud base is referred to as virga (see Publication II).

3.1.4 *Size descriptor*

In meteorology, bulk characteristics of ice crystals are typically of greater interest than properties of individual ice crystals, because a single crystal has negligible impact on the cloud processes. These bulk properties are often described as a function of size, but the definition of size is not straight forward for aspherical particles. Definition of size as a geometrical property of a particle such as the maximum dimension D might be obvious, but D is not directly related to a physical quantity such as particle (projected) area A or particle mass m. In addition, most instruments can measure only the maximum dimension in two dimensions (2-D). That is, D is the maximum dimension of the projected particle area, but not of the three dimensional (3-D) particle. Assuming a worst case scenario of randomly oriented needles with length L, D has a broad probability distribution with expectation value $\overline{D} = 0.64L$ (*Petty and Huang*, 2011). However, in situ (*Zikmunda and Vali*, 1972), active (*Matrosov et al.*, 2005; *Noel and Sassen*, 2005), and passive remote sensing observations (*Xie et al.*, 2012; *Xie*, 2012) found that the majority of ice particles falls with their major axis horizontally aligned. Even though the alignment is not perfect and particles flutter around the horizontal axis (*Kajikawa*, 1992; *Noel and Sassen*, 2005), this reduces the error of estimating the maximum dimension D from a 2-D image significantly, if the mean particle orientation is considered by the design of the in situ probe.

There is a large variety of other size descriptors: e. g., *Delanoë et al.* (2005, 2014) used mass m or the liquid equivalent diameter D_{melted}. Even though this is the physically most consistent size descriptor, m and D_{melt} are difficult to measure in-situ. Other studies (*Mitchell and*

Heymsfield, 2005; *Baker and Lawson*, 2006) propose to use the area A or an area equivalent diameter D_{area} as size descriptor. *Brown and Francis* (1995), instead, used the mean diameter D_{mean} defined as $(D_x + D_y)/2$ with D_x, D_y defined as the extents in two arbitrary, perpendicular directions defined by the coordinate system of the probe. Because the maximum dimension D can be easily derived from optical measurements, it is widely used as size descriptor for in situ observations (*Jackson et al.*, 2012; *Heymsfield et al.*, 2013) and remote sensing (e. g., *Delanoë and Hogan*, 2008; *Hogan et al.*, 2012; *Szyrmer et al.*, 2012). Hence, the maximum dimension D is used as size descriptor in this study as well.

In the following, D is simply referred to as "particle size".

3.1.5 *Particle mass and area*

Because size D defined as the maximum particle extent is not directly confined to particle mass m and projected area A, empirical relations need to be used. Knowledge of m and A is important for—among others—remote sensing applications (*Matrosov et al.*, 2002; *Szyrmer and Zawadzki*, 2014a; Publication III), and for estimating the particle fall velocity (e. g., *Locatelli and Hobbs*, 1974; *Khvorostyanov and Curry*, 2002; *Heymsfield and Westbrook*, 2010; Publication III) which is required to estimate the mass flux to the surface.

Similar to D, area A is defined as projected area as measured by an optical instrument here. This is not directly connected to the surface of the crystal. Sometimes, one can also find the use of area ratio A_r instead of A which is defined as the ratio between A and a sphere with same D.

For parameterization of m and A, power laws are commonly used

$$m(D) = a \cdot D^b \tag{1}$$

$$A(D) = c \cdot D^d \tag{2}$$

with empirically derived pre-factors a, c and exponents b, d. Most studies define these coefficients only for certain size ranges (*Mitchell et al.*, 1990; *Matrosov*, 2007). While $A(D)$ can be derived relatively easily from ground-based or aircraft in-situ observations using optical instruments (e. g., *Mitchell*, 1996; *Heymsfield and Miloshevich*, 2003), $m(D)$ is particularly difficult to measure in situ. It can be obtained by collecting and melting single particles at the ground, but sample sizes are often very small (*Magono and Lee*, 1966; *Locatelli and Hobbs*, 1974; *Mitchell et al.*, 1990). From aircrafts, only ice water content IWC can be measured directly by evaporation of particles (*Noone et al.*, 1988; *Korolev et al.*, 1998) and $m(D)$ has to be estimated from closure studies (*Brown and Francis*, 1995; *Heymsfield et al.*, 2004). Another, yet rather indirect, possibility is relating mass to area and/or particle shape (*Baker and Lawson*, 2006; *Schmitt and Heymsfield*, 2010; *Jackson et al.*, 2012).

3.1.6 *Particle size distribution*

It is most common to describe the particle size distribution $N(D)$ by the four-parameter modified gamma distribution

$$N(D) = N_0 D^\mu \exp(-\Lambda D^\gamma) \tag{3}$$

and its derivatives gamma, exponential and power-law distribution. N_0 is the intercept parameter, Λ is the slope parameter, and μ and γ are shape parameters. Snowfall is usually described using the two-parameter exponential distribution (*Gunn and Marshall*, 1958; *Houze et al.*, 1979; *Matrosov*, 2007; *Kneifel*, 2011) which is obtained from Equation 3 with $\mu = 0$ and $\gamma = 1$. Early studies described ice clouds using the power law distribution (*Heymsfield and Platt*, 1984, obtained from Equation 3 with $\Lambda = 0$) or the three-parameter gamma distribution (*Schneider and Stephens*, 1995, obtained from Equation 3 with $\gamma = 1$). More recently, the use of the modified gamma distribution has been proposed (*Delanoë et al.*, 2005; *Petty and Huang*, 2011), but other studies suggested log-normal distributions (*Tian et al.*, 2010)

$$N(D) = \frac{N_T}{\sqrt{2\pi} \cdot s \cdot D} \exp(-\frac{\ln^2(D/D_T)}{2s^2}) \tag{4}$$

with N_T intercept parameter, D_T the characteristic diameter and s the width of the distribution. *Kosarev and Mazin* (1991) propose to describe $N(D)$ as a multi modal function by adding several distributions. The diversity of approaches highlights the complexity of the various growth mechanisms (see above), but also the challenges when measuring $N(D)$ in situ with aircrafts (*Baumgardner et al.*, 2012).

In Publication III it is investigated in Sec. 3 how the choice of parameterization for N(D) affects forward modeling of radar observations.

3.1.7 *Quantities used in numerical weather prediction models*

For the description of hydrometeors, *numerical weather prediction* (NWP) models with bulk microphysical schemes use typically parameters such as total number concentration n_{tot}, ice water content IWC or effective radius r_{eff}. While n_{tot} and IWC are directly defined with

$$n_{tot} = \int_0^\infty N(D)\, dD \qquad \text{and} \tag{5}$$

$$IWC = \int_0^\infty N(D)\, m(D)\, dD, \tag{6}$$

the definition of r_{eff} is unique only for liquid drops (*Hansen and Travis*, 1974)

$$r_{eff} = \frac{\int_0^\infty (D/2)^3\, N(D)\, dD}{\int_0^\infty (D/2)^2\, N(D)\, dD}. \tag{7}$$

For ice clouds, D is not directly related to a physical quantity and the third (second) moment is not proportional to mass (area). To overcome this limitation, other definitions have been proposed, but there is no agreement on a convention yet (*McFarquhar and Heymsfield*, 1998).

All moments are defined assuming a size distribution from 0 to ∞, but instruments report only in a certain measurement range from

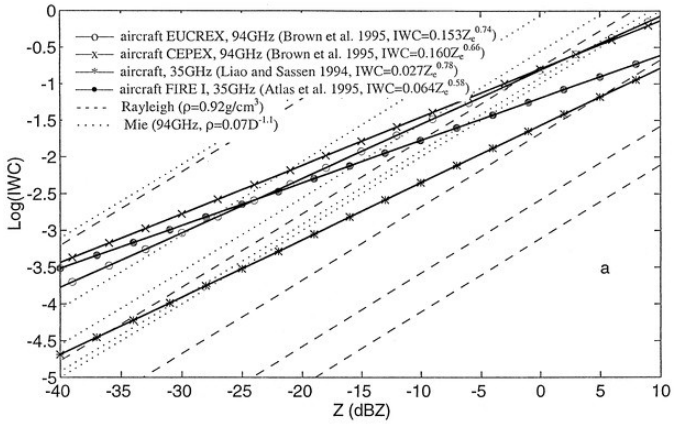

Figure 5: Comparison of various empirical (solid) and theoretical (dashed) $Z_e - IWC$ relations. Figure taken from *Liu and Illingworth* (2000). © American Meteorological Society. Used with permission.

D_{min} to D_{max}. This can introduce biases when estimating moments from measured $N(D)$ which has to be accounted for (see e. g., *Tian et al.* (2010) for mitigation strategies).

3.2 SCATTERING PROPERTIES OF ICE AND SNOW PARTICLES

To relate radar (and microwave radiometer) observations to meteorological quantities (e. g., IWC), knowledge of the single scattering properties is required. This is also mandatory for developing instrument simulators (Additional Study I) that are needed by retrieval techniques (Additional Study II).

Estimation of scattering properties of ice and snow particles is challenging and introduces a large uncertainty in radar observations. Figure 5 shows various, empirical relations to relate IWC to the equivalent radar reflectivity factor Z_e describing the power scattered back by the hydrometeors (e. g., *Liu and Illingworth*, 2000). For this purpose, power laws are used

See Section 3.3 for definition of Z_e.

$$Z_e = \hat{a} \cdot IWC^{\hat{b}} \tag{8}$$

where $\hat{a}$ and $\hat{b}$ are the coefficients that are usually empirically derived. Z_e is the sum of the backscattered power of every individual hydrometeor within the radar volume. This power depends on the backscattering properties of the particle which are described by the backscattering cross section $\sigma_B(D)$, an hypothetical area describing the likelihood that radiation is scattered back at the particle. The backscattering cross section $\sigma_B(D)$ is not only a function of D, but also depends on particle projected area A, density, phase and shape of the particle. All mentioned parameters are highly variable in ice clouds. The easiest approach is to approximate the scattering properties of ice and snow particles by assuming particles with a spherical

shape. This allows the use of Mie theory (*Mie*, 1908; *Bohren and Huffman*, 1983). For particles much smaller than radar wavelength λ, also Rayleigh scattering (*Lord Rayleigh*, 1899; *Young*, 1981) can be assumed, which is a simplified special case of Mie scattering. For these small particles, reflectivity is proportional to the sixth power of particle diameter and defined as

Compare with Equations 12 and 13, the constants are only required to allow the simple definition of reflectivity factor Z (Equation 11).

$$\sigma_B(D) = \frac{\pi^5 \, |K|^2 \, D^6}{\lambda^4} \tag{9}$$

where $|K|^2$ is the dielectric factor derived from the refractive index which describes how radiation propagates through the particle. The refractive index of solid ice for microwave wavelengths is known from empirical studies (e.g. *Warren and Brandt*, 2008), but assuming solid ice is only realistic for particles like hail (*Herman and Battan*, 1961). Already *Marshall and Gunn* (1952) proposed to calculate the refractive index by approximating the particle as a homogeneous mixture of air and ice with effective density ρ. This approach was improved later by *Bohren and Battan* (1980) who proposed to use the approach of *Garnett* (1904) to estimate the mixed refractive index. Much later, this method was called the soft sphere approach (*Liu*, 2004), in contrast to the—less widely used—solid sphere approach where the scattering properties are estimated by a sphere of pure ice, but with a reduced, mass-equivalent radius (*Liu and Curry*, 2000; *Evans et al.*, 2002). For ice approximated using the soft sphere approach, the backsacttering cross section $\sigma_B(D)$ is proportional to D^4 (*Field et al.*, 2005), because the reduction of density with size D compensates partly the D^6 dependence of Rayleigh scattering.

Obviously, the approximation of ice crystal shape with a sphere is far from reality and more realistic results can be obtained by assuming an ellipsoidal instead of a spherical shape. To describe an ellipsoid, the aspect ratio AR is required in addition to size D. Aspect ratio AR is defined as the ratio between maximum dimension D and D_{short} describing the extent of the particle perpendicular to maximum dimension D (*Hogan et al.*, 2012). Several studies found AR to vary typically between 0.5 and 0.7 (*Korolev and Isaac*, 2003; *Tyynelä et al.*, 2011; *Hogan et al.*, 2012). Because Mie theory can only be applied to spheres, the—computationally much more expensive—T-Matrix method (*Waterman*, 1965; *Mishchenko*, 2000) has been frequently used to model the scattering properties of soft spheroids (e. g., *Kummerow and Weinman*, 1988; *Hogan et al.*, 2000). Even though the assumption of an ellipsoidal soft sphere is a severe simplification of the particle shape as well, several studies found that approximating ice and snow crystals as horizontally aligned ellipsoids with an aspect ratio AR of 0.6 is a good compromise between computational effort and accuracy for particles with size D smaller than wavelength λ (*Liu*, 2004; *Kneifel et al.*, 2011a; *Tyynelä et al.*, 2011; *Hogan et al.*, 2012). For larger particles, intra-particle resonance effects occur and $\sigma_B(D)$ oscillates with

AR is sometimes denoted as axial ratio as well.

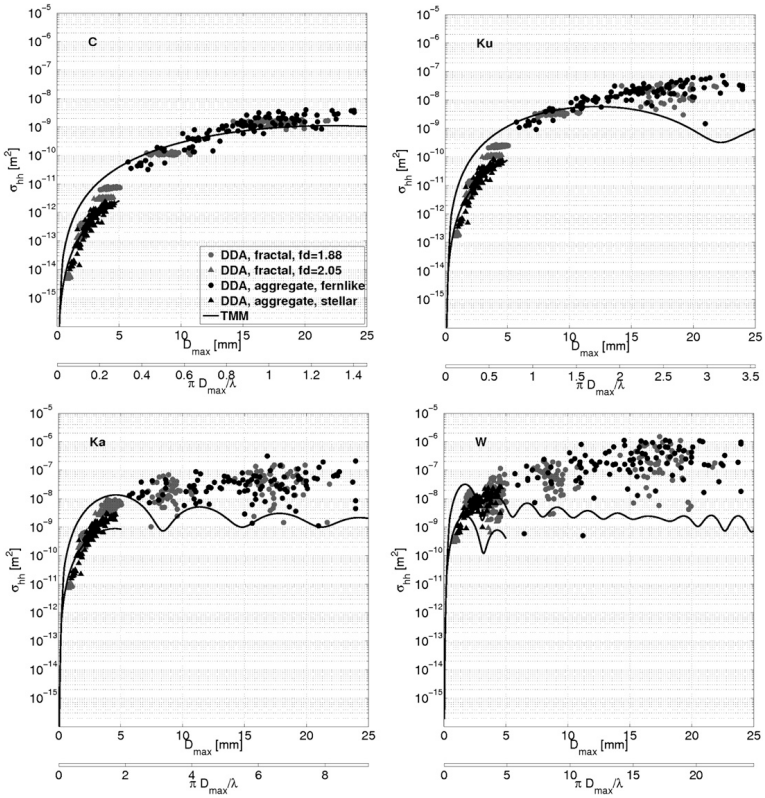

Figure 6: Backscattering cross section σ_B as a function of maximum dimension D for 5.6 GHz (C-band, $\lambda = 54$ mm, top left), 13.6 GHz (K_u-band, $\lambda = 22$ mm, top right), 35.6 GHz (K_a-band, $\lambda = 8.4$ mm, bottom left), and 94.0 GHz (W-band, $\lambda = 3.2$ mm, bottom right). Soft spheroids with an aspect ratio of 0.65 using two different mass-size relations (solid lines) are compared to DDA computations for fern-like aggregates (black circles), stellar aggregates (black triangles), and two kinds of aggregates of fractal crystals (gray circles and triangles). The maximum diameter sphere size parameter is also shown. Figure taken from *Tyynelä et al.* (2011). © American Meteorological Society. Used with permission.

increasing D (Figure 6). Because natural particles do not show these resonance effects due to their much more heterogeneous structure, this can lead to a systematic underestimation of $\sigma_B(D)$ in the order of up to two magnitudes. Consequently, spheroidal particle models can only be used at C and K_u-band independent of snow particle size, and at higher frequencies, more complex models need to be used for particles which are larger than the wavelength λ.

The most common method to estimate scattering properties for large, complex particles is the discrete dipole approximation method (DDA, *DeVoe*, 1964, 1965). The method splits up a single particle into a finite array of polarizable points, for which the dipole moments are estimated in response to the local electric field. This allows modeling of arbitrary particle shapes. In Figure 6, backscattering cross sections σ_B for aggregates estimated with DDA computations are presented

which show—in contrast to soft-spheroids—no resonance effects, although the large scatter highlights the high variability of particle shape and mass. The computing time required for DDA calculations is very high and as a consequence, DDA cannot be included into an instrument simulator online, but the scattering properties of the particles need to be estimated beforehand (*O'Brien and Goedecke*, 1988; *Evans and Stephens*, 1995a). Recently, several groups released data bases of DDA calculations containing not only idealized particles but also more complex particle shapes such as aggregates (*Liu*, 2008b; *Petty and Huang*, 2010; *Tyynelä et al.*, 2011, 2014). As a disadvantage, theses databases are less flexible because they contain only a certain selection of particles which can introduce constrains into the forward model, e. g., with respect to the mass-size relation.

It is disputed who should share honors with Rayleigh for the Rayleigh-Gans theory. Candidates besides Gans are Debye, Rocard, Kichhoff and Born so that Bohren and Huffman (1983, pp. 158) proposes playfully to call the approximation "RGDRKBU—the U is reserved for as yet unknown claimants".

The Gans (*Gans*, 1912) extension of the Rayleigh theory is valid for particles with low density such as soft spheres. Recently it was found that it is not only a computationally efficient alternative to the T-Matrix method for particles smaller than the wavelength λ (*Hogan et al.*, 2012), but gives also consistent results for larger particles (*Hogan and Westbrook*, 2014). As a drawback, the Rayleigh-Gans approximation is not yet available for arbitrarily angles (as required for passive applications) and also polarization effects cannot be modeled (*Hogan and Westbrook*, 2014).

3.3 OBSERVING ICE AND SNOW CRYSTALS WITH RADARS

3.3.1 *Weather radars*

The history of radar meteorology can be found in Atlas (1990) in great detail.

A radar (*Radio Detection and Ranging*) transmits radio pulses and receives the backscattered signal of the target as a function of distance to the instrument. After rapid development in World War II for aerial surveillance, pioneers like *Marshall et al.* (1947) and *Atlas* (1948) were the first who tried to measure precipitation quantitatively with radars. Traditionally, the backscattered signal is called radar reflectivity factor Z and is converted into rainfall rate $\dot{R}$ using a $Z - \dot{R}$ relation similar to Equation 8

$$Z = \dot{a} \cdot \dot{R}^{\dot{b}} \tag{10}$$

where the coefficients $\dot{a}$ and $\dot{b}$ are determined empirically (e.g. *Marshall and Palmer*, 1948). Depending on the phase of precipitation and on the type of event (e. g., convective vs. stratiform), $\dot{a}$ and $\dot{b}$ vary drastically introducing an uncertainty of up to 100% for operational weather radars. In the simple case of Rayleigh scattering, radar reflectivity is proportional to D^6 for liquid particles, which leads to the definition of radar reflectivity factor Z as

$$Z = \int_0^\infty N(D)\, D^6 \, dD \tag{11}$$

Table 1: Overview over microwave bands used in radar meteorology with corresponding frequency and wavelength range (*ITU*, 2000).

BAND	FREQUENCY [GHZ]	WAVELENGTH [MM]
S	2 – 4	150 – 75
C	4 – 8	75 – 37.5
X	8 – 12	37.5 – 25
K_u	12 –18	25 – 16.7
K	18 –27	16.7 – 11.1
K_a	27 – 40	11.1 – 7.5
W	80 – 110	3.8 – 2.7

where $N(D)$ is the particle size distribution. The unit of Z is mm^6m^{-3}, but it is usually expressed in "decibels with respect to a reference level of $1\,mm^6m^{-3}$" or simply "dBz" (*Smith*, 2010). Rayleigh scattering can only be assumed for the full size range of rain drops for C-band or S-band radars (see Table 1 for corresponding frequencies and wavelengths λ), for larger frequencies, the Rayleigh condition $\lambda \ll D$ does not hold true any more and the particle backscattering cross section $\sigma_B(D)$ has to be estimated from e. g., Mie or T-Matrix theory. From $\sigma_B(D)$, radar reflectivity η is estimated with

In this study, the notation dBz is preferred to dBZ following the convention proposed by Smith (2010).

$$\eta = \int_0^\infty N(D)\,\sigma_B(D)\,dD \tag{12}$$

and converted into the equivalent radar reflectivity factor with

$$Z_e = \frac{\lambda^4}{|K_w|^2\pi^5}\,\eta \tag{13}$$

For brevity, the equivalent radar reflectivity factor Z_e is often simply referred to as "reflectivity" in the following.

where $|K_w|^2$ is the dielectric factor for water. Z_e is defined such that $Z_e = Z$ for rain and Rayleigh scattering. Because the phase of the observed hydrometeors is often unknown, for $|K_w|^2$ the value of 0.93 is taken as a convention which is the dielectric factor for liquid water and cm wavelengths (*Smith*, 1984; *Rinehart*, 1991, p. 65). For frozen hydrometeors such as ice particles or snow, $|K|^2$ of Equation 9 has a different value than $|K_w|^2$ and the exponent b of the mass-size relation (Equation 1) is not 3. Consequently, Z_e is not equal to Z for observations of frozen particles, and in the following only Z_e is used .

3.3.2 *Doppler radars*

Doppler radars measure apart from range and reflectivity also the shift of the phase of the electromagnetic wave caused by the Doppler effect found by *Doppler* (1842). Weather radars use the measured Doppler velocity e. g., for estimation of the wind field (*Probert-Jones*,

1960) or for early detection of tornadoes (*Brown et al.*, 1978). If the radar is pointed vertically, the measured Doppler velocity is equal to the fall velocity of the hydrometeors assuming the absence of vertical air motion. For rain, the fall velocity can be translated into particle size (*Gunn and Kinzer*, 1949) so that the drop size distribution $N(D)$ of rain can be gained assuming Rayleigh scattering (*Probert-Jones*, 1960; *Atlas et al.*, 1973). Amongst others, this method is used by the standard processing scheme of the Micro Rain Radar (MRR, *Klugmann et al.*, 1996; *Peters et al.*, 2005), which is described in Publication I. However, this approach does not work for snowfall, because the change of particle fall velocity v with size D and mass m depends heavily on particle shape (*Hobbs et al.*, 1974; *Mitchell*, 1996).

The Doppler velocity is measured by the phase shift between transmitted and received signal. As a consequence, the Doppler velocity measurement is unambiguous only for a phase shift of $\pm\pi$. The corresponding maximal Doppler velocity is called Nyquist velocity and is estimated with

$$v_{nyq} = \mathrm{PRF}\,\lambda/4 \tag{14}$$

where PRF is the radar pulse repetition frequency (*Rinehart*, 1991, p 79). The spectrum is recorded from $-v_{nyq}$ to v_{nyq} discretized into n_{fft} spectral bins corresponding to the number of *Fast Fourier Transformation* (FFT) points. If $|v_{nyq}|$ is overspent, velocity aliasing effects occur, i. e., a wrong Doppler velocity shifted by an even multiple of $|v_{nyq}|$ is assigned to the measurement. See Publication I for a discussion of aliasing effects for vertically pointing radars and a proposed correction scheme.

3.3.3 *Polarimetric radars*

Bringi and Chandrasekar (2001) give an extensive introduction into polarimetric radar measurements.

Polarimetric radars can receive and/or transmit electromagnetic waves in two orthogonal components, mostly horizontal and vertical polarization. Polarimetric observables such as differential reflectivity, linear depolarization ratio or differential phase can give additional information about the non-sphericity of the particles. Recently, operational weather radar networks have been upgraded to polarimetric radars which are used for improved rainfall rate estimation (*Seliga and Bringi*, 1976), target classification (*Bringi et al.*, 1986a,b) and attenuation correction (*Bringi et al.*, 1990). Since polarimetric observables give only little additional information for vertically pointing observations of solid hydrometeors, they are not further discussed in this thesis.

3.3.4 *Cloud radars*

The sensitivity of conventional weather radars is sufficient for observation of rain and snow particles, but usually not for detection of

cloud drops and cloud ice. Increasing the sensitivity would require either larger antennas or more powerful transmitters—both would make the radar more costly and bulky. Because backscattering of small particles is proportional to λ^{-4} (*Lhermitte*, 1987), radars at millimeter wavelengths are better suited for observing clouds and hence frequently called cloud radars. At millimeter wavelengths, attenuation is much stronger, but measurements of vertical profiles of several kilometers range are possible when using the window frequencies at K_a-band (see Table 1 for corresponding frequency and wavelength λ) or W-band. Even though millimeter radars were developed much earlier, technical limitations prevented the use of millimeter radars for meteorological purposes until first studies using K_a-band (*Pasqualucci et al.*, 1983) and W-band (*Lhermitte*, 1987) systems were carried out in the 1980s. Recently, cloud radars have become an established tool for observing ice clouds (e. g., *Kollias et al.*, 2007b).

Zenith pointing cloud radars can also be used for observations of the particle fall spectrum. Even though for ice it is not possible to derive bulk parameters directly from the spectrum as it has been proposed by e. g., *Atlas et al.* (1973) for rain, the spectrum includes additional, exploitable information about ice particles. For this, the peak of the Doppler spectrum caused by the hydrometeors has to be separated from the radar noise level as described in Publication I. So far, the Doppler spectrum was directly exploited only for case studies (e. g., *Shupe et al.*, 2004; *Dufournet and Russchenberg*, 2011; *Verlinde et al.*, 2013), and most studies use moments of the Doppler spectrum instead such as the mean Doppler velocity W (first moment) defined as

Reflectivity Z_e can be considered as the zeroth moment.

$$W = \frac{\sum_i \eta_v(i) v(i)}{Z_e} \tag{15}$$

with η_v the spectral reflectivity, and v the Doppler velocity. The sum is taken over all bins i of the Doppler spectrum which belong to the peak caused by the hydrometeors. In the absence of vertical air motion, W is equal to the reflectivity-weighted mean particle fall velocity. The width of the spectrum is described by the standard deviation of the Doppler spectrum called Doppler spectrum width σ (second, central moment)

There is no common convention for the sign of W, but in this study, positive W refer to particles falling toward the ground.

$$\sigma = \sqrt{\frac{\sum_i \eta_v(i)(v(i) - W)^2}{Z_e}}. \tag{16}$$

σ depends not only on the particle size distribution and the corresponding fall velocities, but also on kinematic broadening by wind shear and turbulence occurring within the volume observed by the radar (See Additional Study I and Publication III for further details). Even though several studies used W (e.g., *Matrosov et al.*, 2002; *Szyrmer et al.*, 2012) and σ (*Mace et al.*, 2002; *Deng and Mace*, 2006) for observa-

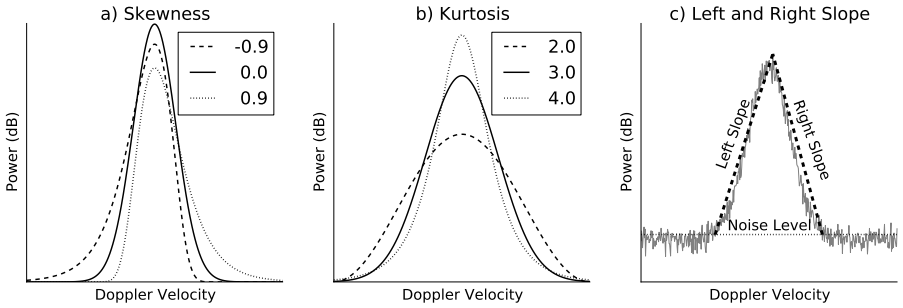

Figure 7: Examples of idealized radar Doppler spectra for different values of (a) skewness Sk, (b) kurtosis Ku, and (c) left S_l and right slope S_r. Figure taken from *Maahn et al.* (2015).

tions of ice clouds, also higher moments of the spectrum can be used. Skewness Sk, the third centralized moment,

$$Sk = \frac{\sum_i \eta_v(i)(v(i) - W)^3}{Z_e \sigma^3}, \tag{17}$$

describes whether the peak is tilted to the left ($Sk < 0$) or right ($Sk > 0$, Figure 7.a). Kurtosis Ku, the fourth centralized moment, defined as

$$Ku = \frac{\sum_i \eta_v(i)(v(i) - W)^4}{Z_e \sigma^4}, \tag{18}$$

is a measure of the shape of the peak. While Ku equal to 3 indicates a Gaussian shape, smaller values relate to a more round tip while spectra with a more pointed tip show Ku values larger than 3 (Figure 7.b). In addition to the moments, the Doppler spectrum can also be described by the left slope S_l and the right slope S_r (*Kollias et al.*, 2007a) of the peak (Figure 7.c)

Note that also the sign of Sk and the definitions of S_l and S_r depend on the used convention for the sign of W

$$S_l = \frac{N_v - \eta_v(i_p)}{v(i_l) - v(i_p)} \tag{19}$$

$$S_r = \frac{N_v - \eta_v(i_p)}{v(i_r) - v(i_p)} \tag{20}$$

where N_v is the mean spectral noise level, and i_l, i_r and i_p are the indices of the most left, most right and maximum, respectively, bin of the Doppler peak. In this study, Z_e, W and σ are called *lower* moments in contrast to the *higher* moments Sk, Ku, S_l, and S_r (even though the slopes are technically not moments).

While Sk has already been exploited for the detection of drizzle onset by *Kollias et al.* (2011), the potential of higher moments for observations of ice clouds is investigated in Publication III and Additional Study II.

Part B

KEY ISSUE I:
ENHANCED SNOWFALL OBSERVATIONS

4

PUBLICATION I: IMPROVED DOPPLER SPECTRA PROCESSING

IMPROVED MICRO RAIN RADAR SNOW MEASUREMENTS USING DOPPLER SPECTRA POST-PROCESSING

Maahn, M. and Kollias, P. (2012). Improved micro rain radar snow measurements using doppler spectra post-processing. *Atmospheric Measurement Techniques*, 5(11):2661–2673, doi:10.5194/amt-5-2661-2012.

Atmos. Meas. Tech., 5, 2661–2673, 2012
www.atmos-meas-tech.net/5/2661/2012/
doi:10.5194/amt-5-2661-2012

Atmospheric Measurement Techniques

Improved Micro Rain Radar snow measurements using Doppler spectra post-processing

M. Maahn[1] **and P. Kollias**[2]

[1]Institute for Geophysics and Meteorology, University of Cologne, Cologne, Germany
[2]Department of Atmospheric and Oceanic Sciences, McGill University, Montreal, Quebec, Canada

Correspondence to: M. Maahn (mmaahn@meteo.uni-koeln.de)

Received: 31 May 2012 – Published in Atmos. Meas. Tech. Discuss.: 12 July 2012
Revised: 4 October 2012 – Accepted: 13 October 2012 – Published: 12 November 2012

Abstract. The Micro Rain Radar 2 (MRR) is a compact Frequency Modulated Continuous Wave (FMCW) system that operates at 24 GHz. The MRR is a low-cost, portable radar system that requires minimum supervision in the field. As such, the MRR is a frequently used radar system for conducting precipitation research. Current MRR drawbacks are the lack of a sophisticated post-processing algorithm to improve its sensitivity (currently at +3 dBz), spurious artefacts concerning radar receiver noise and the lack of high quality Doppler radar moments. Here we propose an improved processing method which is especially suited for snow observations and provides reliable values of effective reflectivity, Doppler velocity and spectral width. The proposed method is freely available on the web and features a noise removal based on recognition of the most significant peak. A dynamic dealiasing routine allows observations even if the Nyquist velocity range is exceeded. Collocated observations over 115 days of a MRR and a pulsed 35.2 GHz MIRA35 cloud radar show a very high agreement for the proposed method for snow, if reflectivities are larger than −5 dBz. The overall sensitivity is increased to −14 and −8 dBz, depending on range. The proposed method exploits the full potential of MRR's hardware and substantially enhances the use of Micro Rain Radar for studies of solid precipitation.

1 Introduction

The study of snow fall using radars and in situ techniques is challenging (Leinonen et al., 2012; Rasmussen et al., 2011). The particle backscattering cross section depends on its shape and mass while their terminal velocity requires information on their projected area. For observations at K-band, absorption is negligible in ice, thus, the use of attenuation-based technique is not feasible. Despite recent advancements in sensor technology, in situ measurements of snow particles from aircraft (Baumgardner et al., 2012) and ground-based imagers (Battaglia et al., 2010) contain large uncertainties. The uncertainty also extends to snowfall rate measurements using traditional gauges due to biases introduced by wind undercatch and blowing snow (Yang et al., 2005). While the aforementioned challenges are active research topics, a larger gap exists in our ability to have basic information about snowfall occurrence and intensity over large areas in the high latitudes. This gap needs to be imperatively closed in order to evaluate the representation of snow processes in numerical models. Better observations at high latitudes would also help to investigate and monitor the water cycle, which is especially complex in polar regions. Due to the high impact of snow coverage on the radiation budget, better monitoring is also crucial for climate studies. A network of small, profiling radars can be part of the answer to address this fundamental gap by providing information on snow event occurrence, morphology and intensity.

The Micro Rain Radar 2 (MRR) is a profiling Doppler radar (Klugmann et al., 1996) originally developed to measure precipitation at buoys in the North Sea without being affected by sea spray. It is easy to operate due to its compact, light design and plug-and-play installation and is increasingly used for monitoring purposes and for studying liquid precipitation (Peters et al., 2002, 2005; Yuter et al., 2008). In addition to that, MRRs were used to study the bright band (Cha et al., 2009) and supported the passive microwave radiometer ADMIRARI in partitioning cloud and rain liquid water (Saavedra et al., 2012).

Its potential for snow fall studies was recently investigated by Kneifel et al. (2011b, KN in the following). They found sufficient agreement between a MRR and a pulsed MIRA36 35.5 GHz cloud radar, if reflectivities exceed 3 dBz. However, Kulie and Bennartz (2009) showed that approximately half of the global snow events occur at reflectivities below 3 dBz, thus MRRs are only of limited use for snow climatologies. KN attributed the poor performance of the MRR below 3 dBz to the real time signal processing algorithm. However, the lack of available raw measurements (radar Doppler spectra) prohibited KN from validating this assumption. In addition, MRR can be affected by Doppler aliasing effects due to turbulence as shown for rain by Tridon et al. (2011).

This study proposes a new data processing method for MRR. The method is based on non noise-corrected raw MRR Doppler spectra and features an improved noise removal algorithm and a dynamic method to dealiase the Doppler spectrum. The new proposed method provides effective reflectivity (Z_e), Doppler velocity (W) and spectral width (σ) besides other moments. The proposed method is evaluated by a comparison with a MIRA35 cloud radar using observations of solid precipitation. The dataset was recorded during a four month period at the Umweltforschungsstation Schneefernerhaus (UFS) close to the Zugspitze in the German Alps at an altitude of 2650 m above sea level.

2 Instrumentation and data

2.1 MRR

The MRR, manufactured by Meteorologische Messtechnik GmbH (Metek), is a vertically pointing Frequency Modulated Continuous Wave (FMCW) radar (Fig. 1, left) operating at a frequency of 24 GHz ($\lambda = 1.24$ cm). It uses a 60 cm offset antenna and a low power (50 mW) solid state transmitter. This leads to a very compact design and a low power consumption of approximately 25 W. To avoid snow accumulation on the dish, a 200 W dish heating system has been installed.

The MRR records spectra at 32 range gates. The first one (range gate no. 0) is rejected from processing, because it corresponds to 0 m height. The following two range gates (no. 1, 2) are affected by near-field effects and are usually omitted from analysis. The last range gate (no. 31) is usually excluded from analysis as well, since it is too noisy. Hence, 28 exploitable range gates remain, which leads to an observable height range between 300 and 3000 m when a resolution of 100 m is used. The peak repetition frequency of 2 kHz results in a Nyquist velocity of $\pm 6\,\mathrm{m\,s^{-1}}$. From this, the unambiguous Doppler velocity range between 0 and $12\,\mathrm{m\,s^{-1}}$ is derived, because Metek assumes only falling particles (see Sect. 3.1). This velocity range cannot be changed by the user, however, Metek offers MRR also with a customised velocity range.

Fig. 1. Micro Rain Radar 2 (MRR) (left) and MIRA35 cloud radar (right) at the UFS Schneeferenerhaus.

The standard product, *Processed Data*, provides, amongst others, rain rate (R), radar reflectivity (Z) and Doppler spectra density (η) with a temporal resolution of 10 s (see Sect. 3.1). *Averaged Data* is identical to *Processed Data*, but averaged over a user-selectable time interval (> 10 s). Doppler spectra densities without noise and height corrections are available in 10 s resolution in the product *Raw Spectra*. On average, 10 s data consist of 58 independently recorded spectra. In this study, *Averaged Data* is used with a temporal resolution of 60 s.

2.2 MIRA35

Metek's MIRA35 is a pulsed radar with a frequency of 35.2 GHz ($\lambda = 8.5$ mm) and a dual-polarized receiver (Fig. 1, right)[1]. Due to its Doppler capabilities it can detect particles within its Nyquist velocity of $\pm 10.5\,\mathrm{m\,s^{-1}}$. The system has a vertical range resolution of 30 m, covering a range between 300 m and 15 km above ground. Due to a very high sensitivity of -44 dBz at 5 km height it is even possible to detect thin ice clouds (Melchionna et al., 2008; Löhnert et al., 2011). To ensure optimal performance and thermal stability, the radar transmitter and receiver were installed in an air-conditioned room. To avoid snow accumulation on the dish, a dish heating system was installed.

The Doppler moments used in this study, Z_e, W, σ, are taken from the standard MIRA35 product. For better comparison with MRR, the MIRA35 data was averaged over 60 s as well and rescaled to the MRR height resolution of 100 m. Due to the near field of MIRA35, all data below 400 m was discarded. As for the MRR, Z_e was not corrected for

[1] Specification sheet available at http://metekgmbh.dyndns.org/mira36x.html.

attenuation, because attenuation effects can be neglected for snow observations at K-band (Matrosov, 2007).

While the MRR is the same instrument as used in KN, the originally used MIRA36 radar was replaced by a – now permanently installed – MIRA35 instrument with a slightly different operation frequency of 35.2 GHz instead of 35.5 GHz. For a tabular comparison of MIRA35 and MRR, see Table 1.

2.3 Data availability and quality control

In this study, coincident measurements of MRR and MIRA35 are analysed for a four-month period (January–April 2012). For this period, the data availability from MRR and MIRA35 was 98 % and 91 %, respectively. 15 % of the MIRA35 data were rejected from the analysis, because the antenna heating of MIRA35 turned out to be working insufficiently as can be seen from Fig. 2. The first panel shows Z_e measured by MRR (using the new method proposed in Sect. 3.3), whereas the second panel presents Z_e measured by MIRA35. The third panel features the dual wavelength difference $Z_e^{MRR} - Z_e^{MIRA35} = \Delta Z_e$. By comparison with the dish heating operation time (grey, at bottom of third panel), it is apparent that the lamellar pattern of ΔZ_e is related to the operation time of the heating. The maximum of ΔZ_e occurs always shortly after the heating was turned on. This is probably caused by snow which accumulates on the dish while the heating is turned off. Since snow attenuates the radar signal at K-band much stronger if the snow is wet, this is only visible shortly after the heating is turned on and the snow on the dish starts to melt. Little shifts in the pattern of ΔZ_e can be explained by the fact that the heating status information is recorded only every 3–4 min. All data showing this lamellar pattern of ΔZ_e was removed from the dataset by hand. Mainly observations featuring reflectivities larger than 5 dBz were affected by this and consequently only few observations with larger Z_e remain. However, the suitability of MRR for observation of snow at higher reflectivities was already shown by KN. The MIRA36 used in their study had a different dish heating system and was less affected by dish heating problems.

Furthermore, the MRR dish heating probably has problems in melting snow sufficiently fast, as can be seen in Fig. 2 around 16:15 UTC. However, this happens less often than for MIRA35. Nevertheless, 4 % of MRR data had to be removed from the dataset by manual quality checks due to dish heating problems. In the future, the installation of monitoring cameras is planned to supervise the antennas of both instruments. For the comparison presented in this study, about 1338 h of coincident observations by both instruments with precipitation remain after quality control.

In addition, the observations of this particular MRR are disturbed by interference artefacts of unknown origin, which are much more clearly visible if the new noise processing method is used instead of Metek's method. The interferences occurred approximately 50 % of the time, feature a Z_e of approximately −5 dBz and contaminate 1–2 range bins

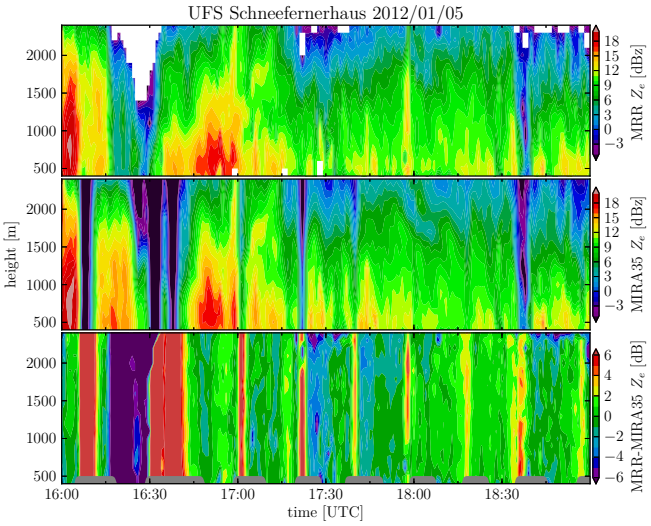

Fig. 2. Time-height effective reflectivity plot of MRR Z_e (top), MIRA35 Z_e (centre) and their dual wavelength difference ΔZ_e (bottom). The presented data is already corrected for constant calibration offsets. The operation time of MIRA35's heating is marked in grey in the bottom panel.

at varying heights greater than 1600 m. These interferences would bias comparisons of MRR and MIRA35, especially if a cloud is observed by MIRA35, which cannot be detected by MRR due to its lower sensitivity, but interference is present at the same range gate. To exclude these cases, all observations at heights exceeding 1600 m featuring a difference in observed Doppler velocity greater than 1 m s^{-1} are excluded from the analysis. This removes about 85 % of the interferences because of their random Doppler velocity. However, this filtering was done after the general agreement of observed Doppler velocities of MRR and MIRA35 had been found to be very good (compare with Sect. 4.2) and it was made sure that only falsely detected interference shows higher deviations of Doppler velocity.

We found a calibration offset between MRR and MIRA35 of 8.5 dBz. KN measured for the same MRR instrument a calibration offset of −5 dBz, thus we corrected our MRR dataset accordingly. The remaining difference of 3.5 dBz was attributed to MIRA35; its dataset was corrected accordingly.

3 Methodology

3.1 Standard analysing method by Metek

To derive the moments available in Metek's standard product *Averaged Data* (amongst other things reflectivity Z, Doppler velocity W and precipitation rate R), the observed Doppler spectra are noise corrected: first, the noise level is determined. For this, the most recent version of Metek's real-time processing tool (Version 6.0.0.2) uses the method by Hildebrand and Sekhon (1974), HS in the following. The HS

Table 1. Comparison of MIRA35 and MRR.

	MRR	MIRA35
Frequency (GHz)	24	35.2
Radar type	FMCW	Pulsed
Transmit power (W)	0.05	30 000 (peak power)
Receiver	Single polarisation	Dual polarisation
Radar Power consumption (W)	25	1000
System power consumption (incl. antenna heating) (W)	225	2000
No. of range gates	31	500
Range resolution (m)	10–200	15–60
Range resolution used in this study (m)	100	30
Resulting measuring range (km)	3	15
Antenna diameter (m)	0.6	1.0
Beam width (2-way, 6 dB)	1.5°	0.6°
Nyquist velocity range ($m\,s^{-1}$)	$\pm$6.0 (0 to +11.9)	$\pm$10.5
No. of spectral bins	64	256
Spectral resolution ($m\,s^{-1}$)	0.19	0.08
Averaged Spectra (Hz)	5.8	5000

algorithm sorts a single Doppler spectrum by amplitude and removes the largest bin until the following condition is fulfilled:

$$E^2/V \geq n \quad (1)$$

with E the average of the spectrum, V the variance and n is the number of temporal averaged spectra. For MRR, n is usually 58 for 10 s *Raw Spectra*. The bin, at which the loop stops, is identified as the noise limit, which is subtracted from the observed Doppler spectral densities[2].

After noise removal, the spectrum should fluctuate around zero, if no peak (i.e. backscatter by hydrometeors) is present and if noise removal is done correctly. We cannot verify, however, whether the noise fluctuates around zero in reality as well, because the spectra in *Averaged Data* are saved in logarithmic scale. Therefore, only positive values are available to the user even though negative values are used internally to derive the Doppler moments. Nevertheless, exemplary spectra of *Averaged Data* (Fig. 3, left panel) reveal that parts with negative (i.e. line not present) and positive (line present) noise values are not equally distributed. This indicates a malfunction of the noise removal method and as a consequence Metek's algorithm will lead to Doppler moments from hydrometeor-free range gates.

Velocity folding (aliasing) occurs when the observed Doppler velocity exceeds the Nyquist velocity boundaries ($\pm 6\,m\,s^{-1}$) of the MRR (fixed). The recorded raw MRR Doppler spectra have a velocity range from 0 to $+12\,m\,s^{-1}$. Thus, by default, the MRR real-time processing software assumes the absence of updrafts (negative velocity) and that all negative velocities are from hydrometeors with terminal

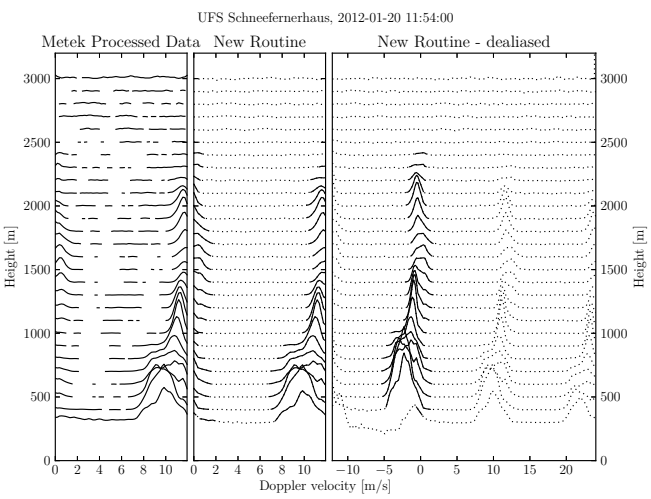

Fig. 3. Waterfall diagram of the recorded spectral reflectivities of the Doppler spectrum at 20 January 2012 11:54:00 UTC from 300 to 3000 m. Metek's *Averaged Data* is presented left, the state of the spectra after noise removal by the proposed method is shown in the middle; the state after dealiasing is shown as well and can be seen at the right. The *Averaged Data* provides only spectral reflectivity densities exceeding zero (see text); the new algorithm distinguishes between noise (dotted) and peak (solid).

velocities that exceed $+6\,m\,s^{-1}$. This is an assumption that will work reasonably in liquid precipitation. In the example shown in Fig. 3, we have a snow event. Typical snow particles do not exceed terminal velocities of $2\,m\,s^{-1}$. Thus, the observed velocities around $+10\,m\,s^{-1}$ can't be explained by particle fall velocities and imply the presence of a weak updraft that lifts the hydrometeors (negative velocities) and that the real-time software converts to very high positive velocities. This can be seen from Fig. 4, which shows the spectra

[2]For a detailed description, see: METEK GmbH, MRR Physical Basics, Version of 13 March 2012, Elmshorn, 20 pp., 2012.

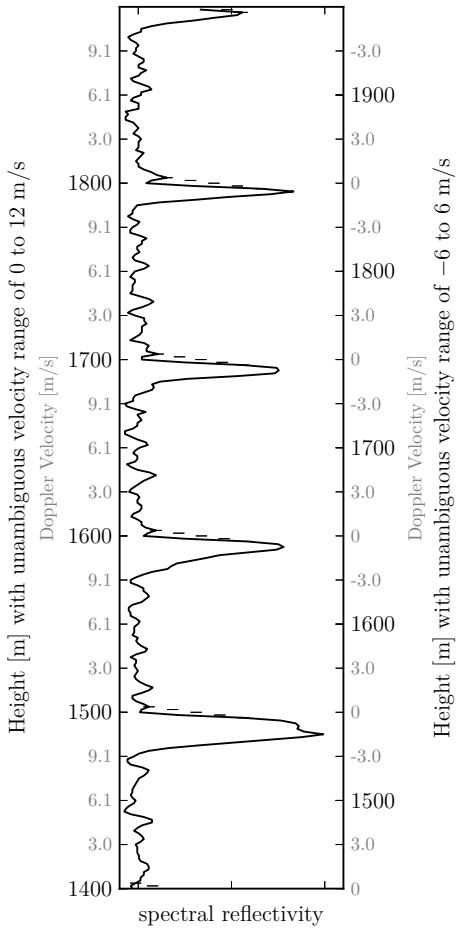

Fig. 4. Doppler spectra of several heights connected to each other as they are seen by a FMCW radar. The left scale shows the height levels (black) if an Nyquist Doppler velocity range of 0 to 12 $\mathrm{m\,s^{-1}}$ is chosen (grey scale). If, instead, the unambiguous Doppler velocity range is set to the Nyquist velocity $\pm 6\,\mathrm{m\,s^{-1}}$ (right, grey scale), the height of the peaks changes (right, black scale). The dashed lines indicate interpolations because of disturbances around $0\,\mathrm{m\,s^{-1}}$.

of five range gates connected to each other as they are seen by a FMCW radar. The peaks appear at Doppler velocities around $11\,\mathrm{m\,s^{-1}}$ (left scale), even though a Doppler velocity of $-1\,\mathrm{m\,s^{-1}}$ would be much more realistic for snow. In addition, the figure makes clear that the particles also appear in another range gate for FMCW radars (Frasier et al., 2002). I.e. upwards (strongly downwards) moving particles appear in the next lower (higher) range gate for MRR. If the Nyquist velocity range of -6.06 to $5.97\,\mathrm{m\,s^{-1}}$ were to be assumed instead (right scale), the peaks would be detected at the correct height for updrafts. In addition, the wrong height correction is applied to aliased peaks, thus dealiasing is mandatory for snow observations by MRR, even if only reflectivities are discussed.

It is important to note that the radar reflectivity Z, available in *Averaged Data*, is not derived directly by integration of the Doppler spectrum η as it is done by MIRA35 for effective reflectivity Z_e. Instead, the observed Doppler spectral densities are converted from dependence on Doppler velocity $\eta(v)$ to dependence on hydrometeor diameter $\eta(D)$ using an idealised size-fall velocity relation for rain by Atlas et al. (1973). Then, the particle-size distribution $N(D)$ is derived from $\eta(D)$ using Mie theory (Peters et al., 2002) to calculate the backscattering cross section for rain particles. Z is eventually gained by integrating $N(D)$ as it is actually customary for disdrometers (e.g. Joss and Waldvogel, 1967):

$$Z = \int N(D) D^6 \mathrm{d}D. \tag{2}$$

Instead of deriving the precipitation rate R by applying an empirical Z–R relation, R is derived from $N(D)$ as well:

$$R = \frac{\pi}{6} \int N(D) D^3 v(D) \mathrm{d}D. \tag{3}$$

This concept works – in the absence of turbulence – sufficiently well for rain and gives a much more accurate R than a weather radar, because it bypasses the uncertainty of the Z-R relation introduced by the unknown $N(D)$. For snow, however, the resulting Z and R are highly biased for several reasons (see also KN): first, the size-fall velocity relationship for snow is different and has a much higher uncertainty depending on particle type. Second, the fall velocity of snow is much more sensitive to turbulence. Third, the backscatter cross section of frozen particles is different from liquid drops and depends heavily on particle type and shape (e.g. Kneifel et al., 2011a). Thus, Z and R are suitable only for liquid precipitation and must not be used for snow observations.

3.2 Method by Kneifel et al. (2011b)

Instead of deriving Z and R via $N(D)$, KN (Kneifel et al., 2011b) calculated the effective reflectivity (Z_e) and other moments by directly integrating the Doppler spectrum:

$$Z_\mathrm{e} = 10^{18} \cdot \frac{\lambda^4}{\pi^5} |K|^2 \int \eta(v) \mathrm{d}v \tag{4}$$

with λ the wavelength in m, $|K|^2$ the dielectric factor, v the Doppler velocity in $\mathrm{m\,s^{-1}}$ and η is the spectral reflectivity in $\mathrm{s\,m^{-2}}$. In the case of MRR, the integrals are reduced to a summation over all frequency bins of the identified peak. Then, the snow rate (S) can be derived from Z_e by applying one of the numerous Z_e–S relations (e.g. Matrosov, 2007).

The η used in Eq. (4) is available in Metek's *Averaged Data*. In this product, η is already noise corrected by the method presented in Sect. 3.1. Thus, the incomplete noise removal also disturbs this approach. The dataset available to KN contained, however, no *Raw Spectra*.

To overcome the limitations of the unambiguous Doppler velocity range of 0 to $11.93\,\mathrm{m\,s^{-1}}$, they assumed that dry

snow does not exceed a velocity of $5.97\,\mathrm{m\,s^{-1}}$ and the corresponding spectrum is transferred to the negative part of the spectrum -6.06 to $-0.19\,\mathrm{m\,s^{-1}}$ (i.e. they used the Nyquist velocity range of $\pm 6\,\mathrm{m\,s^{-1}}$ as indicated by the right scale of Fig. 4) and corrected the height of the dealiased peaks accordingly.

Due to the FMCW principle, signals with independent phase need to be filtered. These filters disturb observations of MRR with a Doppler velocity of approximately $0\,\mathrm{m\,s^{-1}}$, which can be seen from the gaps in the peaks in Fig. 4. Thus the original bins 1, 2 and 64 were filled by linear interpolation (dashed line).

For this study their method was applied to our new dataset. In contrast to KN, an updated version of Metek's standard method (Version 6.0.0.2) was used to gain *Averaged Data*, which, in our experience, enhanced MRR's sensitivity by approximately 5 dBz. We did not implement a Z_e threshold to exclude noisy observations.

3.3 Proposed new method

In contrast to Metek's standard method, the new proposed MRR processing method determines the *most significant peak* including its borders and identifies the rest of the spectrum as noise. After that, the dealiasing routines corrects for aliased data. An overview of the method is presented in Fig. 5.

The proposed method is based on the spectra available in MRR *Raw Spectra*, which is the product with the lowest level available to the user. To save processing time, only spectra which pass a certain variance threshold are further examined, all other are identified to be noise. The threshold is defined as:

$$V_T = 0.6/\sqrt{\Delta t} \tag{5}$$

with V_T the normalized standard deviation of a single spectrum, and Δt is the averaging time. The threshold is defined very conservatively, because false positives are rejected later by post processing qualitative checks.

3.3.1 Noise removal

The objective determination of the noise level is the first step for the derivation of unbiased radar Doppler moments. Since the noise level can vary with time, it has to be calculated dynamically. The dynamic detection of the noise floor at each range gate allows for the detection of weak echoes and the elimination of artefacts caused by radar receiver instabilities. Similar to Metek's method, the determination of the noise level is based on HS (see Sect. 3.1).

The estimated noise level describes the spectral average of the noise, thus single bins of noise exceed the noise level. If the noise level is simply subtracted from the spectrum (as it is done by Metek's method), these bins would still be present and contribute to the calculated moments. Instead,

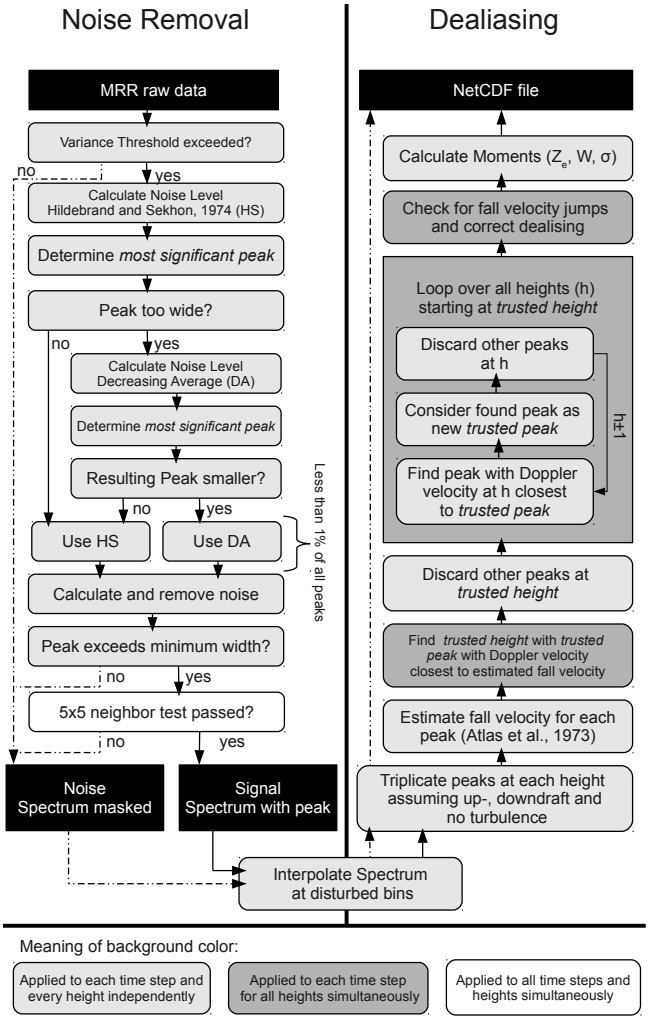

Fig. 5. Flow chart diagram of noise removal and dealiasing of the proposed MRR processing method.

the method determines the most significant peak with its borders. This peak is defined as the maximum of the spectrum plus all adjacent bins which exceed the identified noise level. All other peaks in the spectrum are discarded. Hence, secondary order peaks are completely neglected, but a clearly separated bimodal Doppler spectrum (i.e. with noise in between both peaks) is very rare for MRR since its sensitivity is too low to detect cloud particles.

In rare cases, the HS algorithm fails for MRR data and the noise level is determined as too low, which results in a peak covering the whole spectrum. To make the HS algorithm more robust, only bins exceeding 1.2 times the noise level identified by HS are initially added to the peak. One more bin at each side of the peak is added, if it is above the unweighted HS noise level. This prevents large parts of the spectrum from being falsely added to the peak, if the identified HS noise level is only slightly too low.

If more than 90 % of the spectrum are marked as a peak, the *decreasing average* (DA) method is applied additionally to HS to achieve the noise level: starting at the maximum of the spectrum, directly adjacent bins to the maximum are removed as long as the average of the rest of the spectrum is decreasing. As soon as it increases again, the borders of the peak are determined.

The DA method, however, can be spoiled by bimodal distributions and is less reliable than the HS method. It is only applied to the spectrum if the resulting peak is smaller than the one of the HS method. For the dataset presented in this study, DA was applied to less than 1 % of all peaks.

After the peak and its borders are determined, the noise is calculated as the average of the remaining spectrum. This is different to Metek's approach, which gains the noise level directly from HS. Figure 3 (middle) presents the spectra after subtraction of the noise. The proposed method detects the peaks correctly (solid) and separates them from the noise (dotted).

It is also visible that the algorithms, HS and DA, are able to detect peaks around $0\,\mathrm{m\,s^{-1}}$, which lie at both ends of the spectrum. Since aliasing moves the peak to another range gate, both "halves" of a peak actually originate from different heights, even though they are processed together. Due to the low variability of the Doppler velocity between two neighbouring range gates, this strategy fails only in very rare cases. This approach has to be chosen, because (i)the noise level is different at each range; and (ii) before the dealiasing routine can rearrange observations recorded at different heights, noise must be subtracted. Otherwise, artificial steps would be visible in dealiased spectra. Thus, dealiasing cannot take place before noise removal.

To clean up the spectrum of falsely detected peaks, two conditions are checked: first, peaks less than 3 bins wide (corresponding to a Doppler range of $0.75\,\mathrm{m\,s^{-1}}$) are removed. Second, it is checked whether the neighbours in time and height of the identified peaks contain a peak as well (Fig. 6). For this, a 5 by 5 box in the time-range domain is checked (Clothiaux et al., 1995): if less than 11 of all 24 neighbouring spectra contain a peak as well, the peak is masked. Only if a peak was found at least in 11 of 24 neighbours, is the peak confirmed. To make the test by Clothiaux et al. (1995) more robust, the method also checks the coherence of the position of the maxima of the spectrum. Only if the position of the neighbouring maxima are within $\pm 1.89\,\mathrm{m\,s^{-1}}$ distance of the maximum of the to-be-tested peak, are they included in the test. If a very strict clutter removal is more important than an enhanced sensitivity, the minimum peak width can be set to 4 instead of 3 bins, which reduces the sensitivity by about 4 dBz.

Due to the FMCW principle, signals with independent phase (e.g. due to non–moving targets) need to be filtered. These filters disturb the Doppler velocity bins 1, 2 and 64, which are excluded from the routine presented before. Instead, the bins 1, 2 and 64 are filled by linear interpolation after noise removal and peaks are, based on the found noise level, extended to the interpolated part of the spectrum. Even though Fig. 4 shows that peaks look more realistic due to interpolation (dashed line), a closer look at the middle panel of Fig. 3 reveals that the interpolation of the disturbed bins can also introduce small artefacts. E.g. at 1600 m, the top of the peak is cut. Thus, the resulting moments Z_e, W and σ might by slightly biased and peaks stretching across the interpolated area are registered in the quality array.

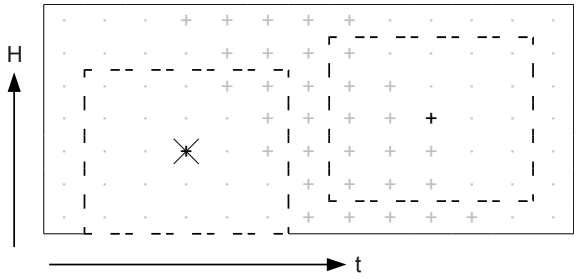

Fig. 6. Time-height plot of radar observations without (·) and with identified peak (+). While the left peak, marked with a black +, is removed because only 4 of 24 neighbours (dashed box) contain a peak as well, the right black + is confirmed as a peak, because 11 of 24 neighbours contain a peak as well.

3.3.2 Dealiasing of the spectrum

As already discussed, peaks which exceed (fall below) the unambiguous Doppler velocity range of 0 to $12\,\mathrm{m\,s^{-1}}$ appear at the next upper (lower) range gate at the other end of the velocity spectrum. The dealiasing method presented here aims to correct for this and is applied to every time step independently. In contrast to the method used by KN, the spectra are not statically but dynamically dealiased to work for both, exceeding and falling below the unambiguous Doppler velocity range.

For this, every spectrum is triplicated, i.e. it's velocity range is increased to -12 to $24\,\mathrm{m\,s^{-1}}$ by adding the spectra from the range gates above and below to the sides of the original spectrum (Fig. 3, right panel). As a consequence, every spectrum can contain up to three peaks with three different Doppler velocities: one peak assuming dealiasing by updrafts, one assuming no dealiasing and finally one assuming dealiasing by downdrafts. To find the correct peak of the corresponding height, a preliminary Z_e is determined (using the non dealiased spectrum) and converted to an expected fall velocity using the relations

$$v = 0.817 \cdot Z_\mathrm{e}^{0.063} \tag{6}$$

for snow and

$$v = 2.6 \cdot Z_\mathrm{e}^{0.107} \tag{7}$$

for rain (Atlas et al., 1973). Due to the high uncertainty of these relations and since the phase of precipitation is not

always known, the average of both relations is used. The peak with the smallest difference to the expected fall velocity is considered as the most likely one. This can, however, be spoiled due to strong turbulence and therefore the wrong peak might be chosen. Turbulence rarely occurs, however, in the complete vertical column simultaneously with the same extent. Thus, the peak of the column, which features the smallest difference to the expected fall velocity, is chosen by the algorithm. This peak is considered as the *trusted peak* at the *trusted height*. To make this approach more robust, the smallest 10 % of all peaks at a time step are usually not considered for the choice of the *trusted peak*.

Based on the *trusted peak* and its Doppler velocity, the most likely peaks of the spectra at the neighbouring heights are determined by using the velocity of the *trusted peak* as the new reference. The algorithm iterates through all heights, always using the most likely Doppler velocity of the previous height as a reference to find the peak of the current height. All other peaks of the triplicated spectrum are masked. The spectra, which are saved to file, keep, however, the triple width. Placing more than one peak in one range gate is not permitted and it is also ensured that every peak appears unmasked exactly once after triplication and dealiasing. As can be seen from the right panel of Fig. 3, the proposed method is able to determine the most likely height/Doppler velocity combination for each peak and masks the remaining peaks accordingly.

This routine works as long as the Doppler velocity of at least one peak is less than $6\,\mathrm{m\,s^{-1}}$ different of its expected fall velocity. For stronger turbulence, the algorithm fails. As a result, Doppler velocity jumps appear between time steps. Thus, a quality check searches for strong jumps (more than $8\,\mathrm{m\,s^{-1}}$) of the Doppler velocity averaged over all heights. If two jumps follow on each other shortly (i.e. within three time steps), the algorithm removes the jumps. Otherwise, the data around the jumps (± 10 min) is marked in the quality array. For the dataset presented in this study, 2 % of the data was marked due to velocity jumps.

Because range gate no. 2 (31) is not used for data processing, dealiasing due to updrafts (downdrafts) is not applied to range gate no. 3 (30). Peaks which stretch to the according borders are marked in the quality array, because they might be incomplete. This can be also seen form the lowest peak in Fig. 3 (right).

3.4 Calculation of the moments

From the noise corrected and dealiased spectrum, the according moments are calculated

$$Z_\mathrm{e} = 10^{18} \cdot \frac{\lambda^4}{\pi^5} |K|^2 \int \eta(v) \mathrm{d}v \tag{8}$$

$$W = \frac{\int \eta(v) v \, \mathrm{d}v}{\int \eta(v) \mathrm{d}v} \tag{9}$$

$$\sigma^2 = \frac{\int \eta(v)(v-W)^2 \, \mathrm{d}v}{\int \eta(v) \mathrm{d}v}, \tag{10}$$

with λ the wavelength in m, $|K|^2$ the dielectric factor, v the Doppler velocity in $\mathrm{m\,s^{-1}}$ and η is the spectral reflectivity in $\mathrm{s\,m^{-2}}$. In the case of MRR, the integrals are reduced to a summation over all frequency bins of the identified peak. In addition to the parameters presented here, the routine also calculates the third moment (skewness), fourth moment (kurtosis), and the left and right slope of the peak as proposed by Kollias et al. (2007). The peak mask, the borders of the peaks, the signal-to-noise ratio and the quality array are recorded as well.

The presented algorithm is written in Python and publicly available as *Improved MRR Processing Tool* (IMProToo) at http://gop.meteo.uni-koeln.de/software under the GPL open source license. Besides the new algorithm, the package also contains tools for reading Metek's MRR data files and for exporting the results to NetCDF files.

4 Results

To assess the suitability of MRR for snow observations and to demonstrate the improvements of the new method, observations of MRR and MIRA35 are compared. For MIRA35, the standard product is used and for MRR, all three presented variations of post-processing methodologies are applied: Metek's *Averaged Data*, the method after KN and the proposed method presented above. All reflectivities are corrected by the discussed calibration offsets.

4.1 Comparison of reflectivity

The scatterplot of Z derived from Metek's *Averaged Data* and Z_e from MIRA35 (Fig. 7, left) shows a general agreement between both data sets for Z_e exceeding 5 dBz, but a very high spread which we attribute to the different methods to derive the reflectivity. Noise is not completely removed in the MRR *Averaged Data*, thus the distribution departs from the 1 : 1 line for $Z_\mathrm{e} < -5\,\mathrm{dBz}$. Below -10 dBz, the MRR observations are completely contaminated by noise.

Even though the spread of the distribution is much less, if the algorithm developed by KN is applied (Fig. 7, centre), the insufficient noise removal of Meteks's standard method causes also here a rather constant noise level of -8 dBz. To cope with this, KN derived an instrument-dependent noise threshold from clear sky observations and discarded all Z_e below that noise threshold. Even though this was not implemented in this study, the figure indicates that this threshold would be around -4 dBz for the dataset presented here. But also for Z_e larger than the noise level, the observations are biased and the core area of the distribution is slightly above

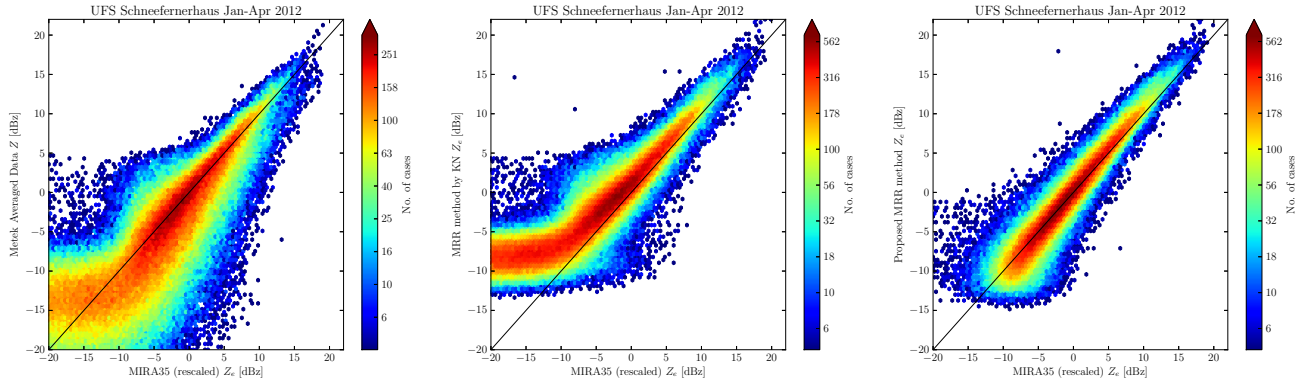

Fig. 7. Scatterplot comparing effective reflectivity (Z_e) of MIRA35 with D^6-based radar reflectivity (Z) derived by Metek's standard MRR product (left), with effective reflectivity (Z_e) of MRR using the method by KN (centre) and with Z_e of MRR using the new proposed MRR method (right). The black line denotes the 1 : 1 line.

the 1 : 1 line. For higher Z_e, this difference is due to the fact that in this study, the MRR's Z_e is not converted to a 35 GHz equivalent effective reflectivity (as carried out by KN) by modelling idealised snow particles, because the difference for $Z_e < 5\,\mathrm{dBz}$ is assumed to be less than 1 dB. For lower Z_e, however, the offset indicates that noise is not properly removed from the signal, even if the noise threshold is exceeded.

The new proposed method (Fig. 7, right) shows a much better agreement with the MIRA35 observations both for low and high Z_e. In contrast to the methods presented above, noise is also properly removed from clear sky observations. Thus, the distribution does not continue horizontally for small reflectivities. Only for $Z_e < -7\,\mathrm{dBz}$, MRR underestimates Z_e slightly, because these low reflectivities are always accompanied by very low SNRs. The small increasing offset towards higher Z_e is probably attributed to the different observation frequencies of the radars as already discussed. The remaining spread can most likely be explained by the different beam geometries which result in different scattering volumes and by the different spatial and/or temporal averaging strategies (i.e. averaging before vs. after noise correction). This explanation is supported by the fact that a closer examination of single events revealed that the spread is larger for events with a high spatial and/or temporal variability. The increase of the spread with decreasing reflectivity is most likely related to the logarithmic scale of the reflectivity unit. The outliers at the left side of the plot are related to the mentioned interference artefacts, which is a feature of the MRR used in this study and unfortunately cannot be removed in all cases. This interference can be also seen in Fig. 7 (left and centre), above the noise level.

Frequency by altitude diagrams (CFAD) of MIRA35 and the new MRR method are presented in Fig. 8. While MIRA's sensitivity limit is out of the range of the plot, MRRs sensitivity is between −14 and −8 dBz, depending on height. Both instruments show almost identical patterns for $Z_e > 0\,\mathrm{dBz}$. For smaller Z_e values, however, MIRA35 detects more cases. The percentage of snow observations which were not detected by MRR but by MIRA35 increases from 2 % at 0 dBz to 8 % at −5 dBz and to 53 % at −10 dBz. A closer look at single events reveals that mostly events with a very high spatial and/or temporal variability are observed with different Z_e. A possible explanation for this might be that the "11 of 24 neighbour spectra check" (see Sect. 3.3.1), which removes clutter from observations, is too rigid and removes sometimes true observations. For even smaller Z_e ($<-5\,\mathrm{dBz}$), the majority of the missing observations is likely caused by MRR's weaker sensitivity.

In comparison with the method of KN, the sensitivity of MRR was increased from 3 dBz to −5 dBz. This corresponds to an increase of the minimal detectable snow rate by the MRR from 0.06 to 0.01 $\mathrm{mm\,h^{-1}}$, if the exemplary Z_e–S relation from Matrosov (2007) (converted to 35 GHz by KN) is used:

$$Z_e = 56 \cdot S^{1.2} \tag{11}$$

4.2 Comparison of Doppler velocity

The Doppler velocity observed by MIRA35 (using the standard product) is compared to the Doppler velocity measured by MRR using the methodologies described previously: Metek's *Averaged Data*, the method of KN and the proposed method.

Metek's MRR software assumes only falling particles and thus no dealiasing is applied to the spectrum. This can be clearly seen from the comparisons of W between Metek's *Averaged Data* and MIRA35 (Fig. 9, left). Velocities below $0\,\mathrm{m\,s^{-1}}$ appear at the other end of the spectrum at very high Doppler velocities. Due to the insufficient noise removal, a cluster of randomly distributed Doppler velocities is visible around $0\,\mathrm{m\,s^{-1}}$. This cluster is attributed to cases, when MIRA35 detects a signal which is below MRR's sensitivity

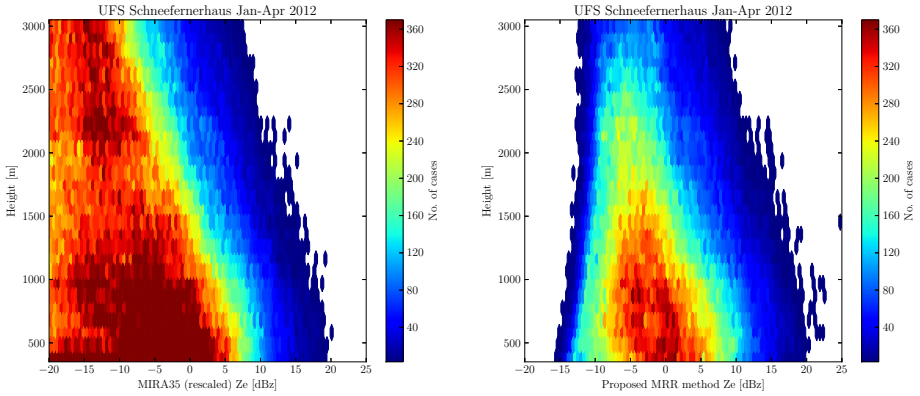

Fig. 8. Frequency by altitude diagram (CFAD) for Z_e of MIRA35 (left) and for Z_e of MRR using the new proposed method (right).

(e.g. clouds), but MRR detects only noise featuring a random velocity.

This cluster can also be seen in Fig. 9 (centre), in which MIRA35 is compared to the method of KN. Their simple dealiasing algorithm dealiases the spectra successfully, which results in the absence of artefacts. However, the spread remains very high due to the insufficient noise removal.

For the new proposed method, the observed Doppler velocities agree very well with MIRA35 (Fig. 9, right). Due to the dynamic dealiasing method, MRR can also detect upwards moving particles reliably and is not limited to its unambiguous Doppler velocity range of 0 to 12 m s^{-1}. The small offset of the spread with MRR (MIRA) detecting slightly larger values for positive (negative) Doppler velocities is most likely related to the coarser spectral resolution of MRR.

4.3 Comparison of spectral width

The Doppler spectrum width σ is not operationally provided by Metek's standard method or the procedure proposed by KN. Hence, only the new proposed method is compared with MIRA35. Observations of both instruments are exemplified for an altitude of 1000 m in Fig. 10 (left) and show a high agreement. The small offset from the 1 : 1 line can be explained by two factors: first, the spectral resolution of MRR is less than half of the spectral resolution of MIRA35 (0.19 vs. 0.08 m s^{-1}). Thus, all peaks detected by MRR feature a minimum [σ] of 0.17 m s^{-1}, even though their σ might be smaller according to MIRA35. Second, the difference in the antenna beam width (0.6° for MIRA 35 vs. 1.5° for MRR) results in different turbulence broadening contributions from the same atmospheric volume. To estimate the expected offset, it is assumed that the observed σ^2 is given by

$$\sigma^2 = \sigma_d^2 + \sigma_s^2 + \sigma_t^2, \tag{12}$$

where σ_d^2 is the variance of the Doppler velocity caused by the microphysics, σ_s^2 is the beam broadening term due to contribution of cross beam wind and wind shear within the radar sampling volume, and σ_t^2 is the variance due to turbulence (Kollias et al., 2001). Assuming that the difference between both radars of detection of σ_s^2 due to wind shear is small, the dependence of σ_t^2 on the beam width geometry causes the offset between both instruments. σ_t^2 can be expressed as

$$\sigma_t^2 = \int_{k_1}^{k_2} a\epsilon^{2/3} k^{-5/3} \mathrm{d}k \tag{13}$$

(Kollias et al., 2001) with a a universal dimensionless constant set to 1.6 (Doviak and Zrnic, 1993), k the wavenumber and ϵ is the dissipation rate. ϵ can have values between 0.01 and 800 cm^2 s^{-3} (Gultepe and Starr, 1995). The lower limit of the wavenumber, k_2, is defined by wavelength of the radar. k_1, instead, is determined by the scattering volume dimension. The difference in σ_t^2 can be determined by integrating Eq. (13) from k_1^{MRR} to k_1^{MIRA35}, because the wavelength of both radars is of the same magnitude. k_1 of MRR and MIRA35 can be derived from the scattering volume V_s with

$$k_1 = 2\pi / \sqrt[3]{V_s} \tag{14}$$

and

$$V_s = \pi H^2 (0.7532\theta)^2 \Delta H \tag{15}$$

with H the range, ΔH the range resolution, and θ is the 6 dB two-way beam width (Lhermitte, 2002).

The expected offset of σ between MRR and MIRA35 is calculated for $\epsilon = 0.3$ (solid), 3.0 (dashed), 10.0 (dash-dotted) and 30.0 cm^2 s^{-3} (dotted) and marked in Fig. 10 (left) exemplary for a height of 1000 m. Apparently, the prevailing dissipation rate was 3.0 cm^2 s^{-3} during the four-month observation period. Thus, the combination of MIRA35 and MRR can be used for observations of the dissipation rate.

This is presented in Fig. 10 (right) for an exemplary case. While ϵ is below 3 cm^2 s^{-3} at heights of 800 m and more, values of ϵ can reach 100 cm^2 s^{-3} and more closer to the ground

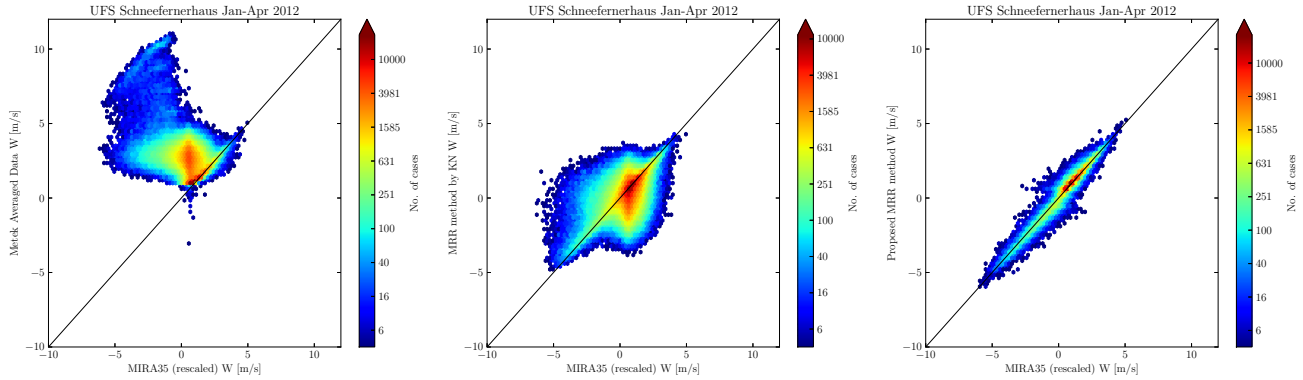

Fig. 9. Scatterplot comparing Doppler velocity (W) of MIRA35 with W of Metek's standard MRR product (left), with W of MRR using the method by KN (centre) and with W of MRR using the new proposed MRR method (right). The black line denotes the 1 : 1 line.

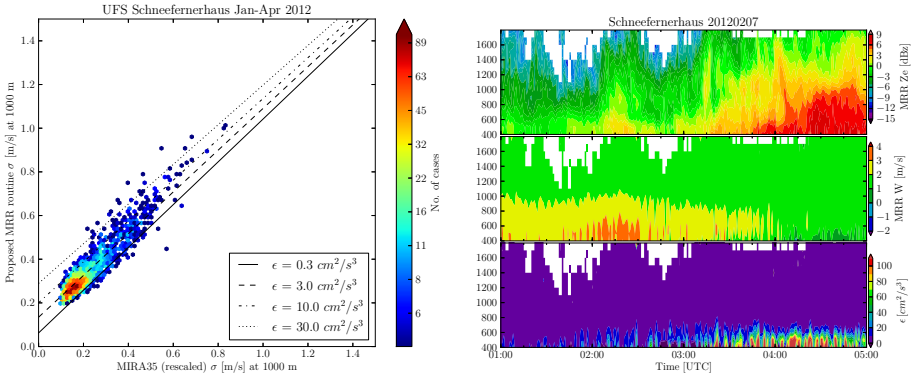

Fig. 10. Left: scatterplot comparing spectral width (σ) of MRR and MIRA35. The lines indicate the expected offset due to the different beam widths caused by a dissipation rate of $\epsilon = 0.3$ (solid), 3.0 (dashed), 10.0 (dash-dotted) and 30.0 $\mathrm{cm^2\,s^{-3}}$ (dotted). Right: time-height plot showing Z_e (top) and W (centre) measured by MRR using the proposed method. The bottom panel features the dissipation rate (ϵ) derived from comparison of σ of MRR and MIRA35.

due to stronger friction. As expected, the temporal variability is rather high. Interestingly, if observations close to the ground at 02:15 UTC are compared with 04:15 UTC, it is apparent that W of the latter is less even though Z_e is larger. This is most likely caused by a small updraft, which reduces the fall velocity. This is also confirmed by increased σ values at 04:15 UTC indicating stronger turbulence.

5 Conclusions

In this study, a new method for processing MRR raw Doppler spectra is introduced, which is especially suited for snow observations. The method corrects the observed spectra for noise and aliasing effects and provides effective reflectivity (Z_e), Doppler velocity (W) and spectral width (σ). Furthermore, the new post-processing procedure for MRR removes signals from hydrometeor-free range gates and thus improves the detection of precipitation echoes, especially at low signal-to-noise conditions.

By comparison with a MIRA35 K-band cloud radar, the performance of the proposed method is evaluated. The dataset contains 116 days from 1 January to 24 April 2012 recorded at the UFS Schneefernerhaus in the German Alps. Due to insufficiently working dish heatings, 15 % (4 %) of MIRA35 (MRR) data had to be excluded. Thus, both instruments need an improved dish heating for the future to ensure continuous observations.

For Z_e, the agreement between MIRA35 and the new proposed method for MRR is very satisfactory and MRR is able to detect precipitation with Z_e as low as -14 dBz. However, due to MRR's limited sensitivity, the number of observations is reduced for $Z_\mathrm{e} < -5$ dBz. Depending on the used Z_e–S relation, this corresponds to a precipitation rate of 0.01 $\mathrm{mm\,h^{-1}}$. This is a great enhancement in comparison to the results from KN (Kneifel et al., 2011b), who recommended using MRR only for observations of snow fall exceeding 3 dBz. The main reason is an enhanced noise removal which does not create artificial clear sky echos, as they are present if Metek's standard method or the method by KN is used.

Also for W, the agreement between MIRA35 and the new proposed method for MRR is very satisfactory. The new dealiasing routine corrects reliably for aliasing artefacts as they are present in Metek's standard method. As a consequence, observations are also possible if the Nyquist velocity range is exceeded. The variance between W observations of MRR and MIRA35 is drastically decreased because of the improved noise correction, which removes clear sky echoes completely. The developed dealiasing routine could be also used to correct aliasing effects during rain events as they were observed by Tridon et al. (2011), because the routine is designed to work for both, up- and downdrafts.

The comparison of σ reveals an offset of approximately $0.1\,\mathrm{m\,s^{-1}}$. This offset is, however, unbiased, but related to the different beam widths of MRR and MIRA35. The larger beam width of the MRR results to higher spectral broadening contribution. The difference in spectrum width measurements between the MRR and the MIRA35 can be used to extract the turbulence dissipation rate.

The presented methodology extracts atmospheric returns at low signal-to-noise conditions. The MRR performance is close to optimum and further improvements will require hardware changes. The current MMR processor has a data efficiency of 60 % (ratio of pulses digitized and used for moment estimation to number of pulses transmitted) due to its inability to receive and transfer data at the same time. Thus, the data acquisition is intermitted. A better digital receiver with 100 % data efficiency will improve our ability to extract weak SNR signals by 2–2.5 dBz. Additional sensitivity can be acquired by further averaging (post-processing) of the recorded radar Doppler spectra. However, this should be subject to the scene variability. Finally, a higher number of FFT points (e.g. 256) will enable better discrimination of radar Doppler spectra peaks and better higher moment estimation, e.g. Doppler spectra skewness (Kollias et al., 2011).

For monitoring precipitation over long time periods, high standards in radar calibration are a key requirement. This can be accomplished with the use of an internal calibration loop to calibrate the radar receiver, monitoring of the transmitted power or the use of an independent measurement of precipitation intensity coincident to the MRR system (e.g. precipitation gauge). Furthermore, the dish heating of MRR (and of MIRA35) needs enhancements to guarantee year-round observations. In case of snow observations, it is desirable that a narrow Nyquist interval can be selected to increase the velocity resolution of the Doppler spectra.

The presented study suggests that proper post-processing of the MRR raw observables can lead to high quality radar measurements and detection of weak precipitation echoes. In comparison to a cloud radar (e.g. MIRA35), dimensions, weight, power consumption and costs for MRR are small, which makes MRR easier to deploy and operate especially in remote areas.

Acknowledgements. The MIRA35 presented in this study is property of the Umweltforschungsstation Schneefernerhaus (UFS), the MRR is property of the German Aerospace Center (DLR) in Oberpfaffenhofen. We thank Martin Hagen and Kersten Schmidt of DLR for operating the radars and providing data and pictures. We would also like to thank Ulrich Löhnert, Stefan Kneifel, and Clemens Simmer for their detailed comments and corrections. This study was carried out within the project ADMIRARI II supported by the German Research Association (DFG) under research grant number LO901/5-1.

Edited by: F. S. Marzano

References

Atlas, D., Srivastava, R. C., and Sekhon, R. S.: Doppler radar characteristics of precipitation at vertical incidence, Rev. Geophys., 11, 1–35, doi:10.1029/RG011i001p00001, 1973.

Battaglia, A., Rustemeier, E., Tokay, A., Blahak, U., and Simmer, C.: PARSIVEL snow observations: a critical assessment, J. Atmos. Ocean. Tech., 27, 333–344, doi:10.1175/2009JTECHA1332.1, 2010.

Baumgardner, D., Avallone, L., Bansemer, A., Borrmann, S., Brown, P., Bundke, U., Chuang, P. Y., Cziczo, D., Field, P., Gallagher, M., Gayet, J., Heymsfield, A., Korolev, A., Krämer, M., McFarquhar, G., Mertes, S., Möhler, O., Lance, S., Lawson, P., Petters, M. D., Pratt, K., Roberts, G., Rogers, D., Stetzer, O., Stith, J., Strapp, W., Twohy, C., and Wendisch, M.: In situ, airborne instrumentation: addressing and solving measurement problems in ice clouds, B. Am. Meteorol. Soc., 93, ES29–ES34, doi:10.1175/BAMS-D-11-00123.1, 2012.

Cha, J., Chang, K., Yum, S., and Choi, Y.: Comparison of the bright band characteristics measured by Micro Rain Radar (MRR) at a mountain and a coastal site in South Korea, Adv. Atmos. Sci., 26, 211–221, doi:10.1007/s00376-009-0211-0, 2009.

Clothiaux, E. E., Miller, M. A., Albrecht, B. A., Ackerman, T. P., Verlinde, J., Babb, D. M., Peters, R. M., and Syrett, W. J.: An evaluation of a 94-GHz radar for remote sensing of cloud properties, J. Atmos. Ocean. Tech., 12, 201–229, doi:10.1175/1520-0426(1995)012<0201:AEOAGR>2.0.CO;2, 1995.

Doviak, R. J. and Zrnic, D. S.: Doppler Radar & Weather Observations, 2nd Edn., Academic Press, 1993.

Frasier, S. J., Ince, T., and Lopez-Dekker, F.: Performance of S-band FMCW radar for boundary layer observation, in: Preprints, 15th Conf. on Boundary Layer and Turbulence, Vol. 7, Wageningen, The Netherlands, 2002.

Gultepe, I. and Starr, D. O.: Dynamical structure and turbulence in cirrus clouds: aircraft observations during FIRE, J. Atmos. Sci., 52, 4159–4182, doi:10.1175/1520-0469(1995)052<4159:DSATIC>2.0.CO;2, 1995.

Hildebrand, P. H. and Sekhon, R. S.: Objective determination of the noise level in Doppler spectra, J. Appl. Meteorol., 13, 808–811, doi:10.1175/1520-0450(1974)013<0808:ODOTNL>2.0.CO;2, 1974.

Joss, J. and Waldvogel, A.: Ein Spektrograph für Niederschlagstropfen mit automatischer Auswertung, Pure Appl. Geophys., 68, 240–246, doi:10.1007/BF00874898, 1967.

Klugmann, D., Heinsohn, K., and Kirtzel, H.: A low cost 24 GHz FM-CW Doppler radar rain profiler, Contr. Atmos. Phys., 69,

247–253, 1996.

Kneifel, S., Kulie, M. S., and Bennartz, R.: A triple-frequency approach to retrieve microphysical snowfall parameters, J. Geophys. Res., 116, D11203, doi:10.1029/2010JD015430, 2011a.

Kneifel, S., Maahn, M., Peters, G., and Simmer, C.: Observation of snowfall with a low-power FM-CW K-band radar (Micro Rain Radar), Meteorol. Atmos. Phys., 113, 75–87, doi:10.1007/s00703-011-0142-z, 2011b.

Kollias, P., Albrecht, B. A., Lhermitte, R., and Savtchenko, A.: Radar observations of updrafts, downdrafts, and turbulence in fair-weather cumuli, J. Atmos. Sci., 58, 1750–1766, doi:10.1175/1520-0469(2001)058<1750:ROOUDA>2.0.CO;2, 2001.

Kollias, P., Clothiaux, E. E., Miller, M. A., Luke, E. P., Johnson, K. L., Moran, K. P., Widener, K. B., and Albrecht, B. A.: The atmospheric radiation measurement program cloud profiling radars: second-generation sampling strategies, processing, and cloud data products, J. Atmos. Ocean. Tech., 24, 1199–1214, doi:10.1175/JTECH2033.1, 2007.

Kollias, P., Remillard, J., Luke, E., and Szyrmer, W.: Cloud Radar Doppler Spectra in Drizzling Stratiform Clouds. Part I: Forward Modeling and Remote Sensing Applications, J. Geophys. Res., 116, D13201, doi:10.1029/2010JD015237, 2011.

Kulie, M. S. and Bennartz, R.: Utilizing spaceborne radars to retrieve dry snowfall, J. Appl. Meteorol. Clim., 48, 2564–2580, doi:10.1175/2009JAMC2193.1, 2009.

Leinonen, J., Kneifel, S., Moisseev, D., Tyynel, J., Tanelli, S., and Nousiainen, T.: Evidence of nonspheroidal behavior in millimeter-wavelength radar observations of snowfall, J. Geophys. Res., 117, D18205, doi:10.1029/2012JD017680, 2012.

Lhermitte, R.: Centimeter and Millimeter Wavelength Radars in Meteorology, Roger Lhermitte, Miami, FL, 2002.

Löhnert, U., Kneifel, S., Battaglia, A., Hagen, M., Hirsch, L., and Crewell, S.: A multisensor approach toward a better understanding of snowfall microphysics: the TOSCA project, B. Am. Meteorol. Soc., 92, 613–628, doi:10.1175/2010BAMS2909.1, 2011.

Matrosov, S. Y.: Modeling backscatter properties of snowfall at millimeter wavelengths, J. Atmos. Sci., 64, 1727–1736, doi:10.1175/JAS3904.1, 2007.

Melchionna, S., Bauer, M., and Peters, G.: A new algorithm for the extraction of cloud parameters using multipeak analysis of cloud radar data – first application and preliminary results, Meteorol. Z., 17, 613–620, doi:10.1127/0941-2948/2008/0322, 2008.

Peters, G., Fischer, B., and Andersson, T.: Rain observations with a vertically looking Micro Rain Radar (MRR), Boreal Environ. Res., 7, 353–362, 2002.

Peters, G., Fischer, B., Münster, H., Clemens, M., and Wagner, A.: Profiles of raindrop size distributions as retrieved by Microrain Radars, J. Appl. Meteorol., 44, 1930–1949, doi:10.1175/JAM2316.1, 2005.

Rasmussen, R., Baker, B., Kochendorfer, J., Meyers, T., Landolt, S., Fischer, A. P., Black, J., Theriault, J., Kucera, P., Gochis, D., Smith, C., Nitu, R., Hall, M., Cristanelli, S., and Gutmann, E.: The NOAA/FAA/NCAR winter precipitation test bed: how well are we measuring snow?, B. Am. Meteorol. Soc., 93, 811–829, doi:10.1175/BAMS-D-11-00052.1, 2011.

Saavedra, P., Battaglia, A., and Simmer, C.: Partitioning of cloud water and rainwater content by ground-based observations with the Advanced Microwave Radiometer for Rain Identification (ADMIRARI) in synergy with a micro rain radar, J. Geophys. Res., 117, D05203, doi:10.1029/2011JD016579, 2012.

Tridon, F., Baelen, J. V., and Pointin, Y.: Aliasing in Micro Rain Radar data due to strong vertical winds, Geophys. Res. Lett., 38, L02804, doi:201110.1029/2010GL046018, 2011.

Yang, D., Kane, D., Zhang, Z., Legates, D., and Goodison, B.: Bias corrections of long-term (1973–2004) daily precipitation data over the northern regions, Geophys. Res. Lett., 32, 19501, doi:10.1029/2005GL024057, 2005.

Yuter, S. E., Stark, D. A., Bryant, M. T., Colle, B. A., Perry, L. B., Blaes, J., Wolfe, J., and Peters, G.: Forecasting and characterization of mixed precipitation events using the MicroRainRadar, in: 5th European Conference on Radar in Meteorology and Hydrology, Helsinki, Finland, 2008.

5

PUBLICATION II: EXPLORING RADAR-BASED SNOWFALL STATISTICS

HOW DOES THE SPACEBORNE RADAR BLIND ZONE AFFECT DERIVED SURFACE SNOWFALL STATISTICS IN POLAR REGIONS?

Maahn, M., Burgard, C., Crewell, S., Gorodetskaya, I. V., Kneifel, S., Lhermitte, S., Van Tricht, K., and van Lipzig, N. P. M. (2014). How does the spaceborne radar blind zone affect derived surface snowfall statistics in polar regions? *Journal of Geophysical Research: Atmospheres*, 119(24):13604–13620 doi:10.1002/2014JD022079.

See Section 5.1 for supplementary material.

AGU PUBLICATIONS

JGR

Journal of Geophysical Research: Atmospheres

RESEARCH ARTICLE

10.1002/2014JD022079

Key Points:
- CloudSat blind zone effects were investigated using Micro Rain Radar profiles
- Blind zone can lead to underestimation of reflectivity and precipitation amount
- Reducing the blind zone by 50% does not improve results in all aspects

Supporting Information:
- Readme
- Figures S1–S3

Correspondence to:
M. Maahn,
mmaahn@meteo.uni-koeln.de

Citation:
Maahn, M., C. Burgard, S. Crewell, I. V. Gorodetskaya, S. Kneifel, S. Lhermitte, K. Van Tricht, and N. P. M. van Lipzig (2014), How does the spaceborne radar blind zone affect derived surface snowfall statistics in polar regions?, *J. Geophys. Res. Atmos.*, *119*, 13,604–13,620, doi:10.1002/2014JD022079.

Received 27 MAY 2014
Accepted 23 OCT 2014
Accepted article online 27 OCT 2014
Published online 16 DEC 2014

How does the spaceborne radar blind zone affect derived surface snowfall statistics in polar regions?

Maximilian Maahn[1], Clara Burgard[1], Susanne Crewell[1], Irina V. Gorodetskaya[2], Stefan Kneifel[3], Stef Lhermitte[2], Kristof Van Tricht[2], and Nicole P. M. van Lipzig[2]

[1]Institute for Geophysics and Meteorology, University of Cologne, Cologne, Germany, [2]Department of Earth and Environmental Sciences, KU Leuven, Leuven, Belgium, [3]Department of Atmospheric and Oceanic Sciences, McGill University, Montreal, Quebec, Canada

Abstract Global statistics of snowfall are currently only available from the CloudSat satellite. But CloudSat cannot provide observations of clouds and precipitation within the so-called blind zone, which is caused by ground-clutter contamination of the CloudSat radar and covers the last 1200 m above land/ice surface. In this study, the impact of the blind zone of CloudSat on derived snowfall statistics in polar regions is investigated by analyzing three 12 month data sets recorded by ground-based Micro Rain Radar (MRR) at the Belgian Princess Elisabeth station in East Antarctica and at Ny-Ålesund and Longyearbyen in Svalbard, Norway. MRR radar reflectivity profiles are investigated in respect to vertical variability in the frequency distribution, changes in the number of observed snow events, and impacts on total precipitation. Results show that the blind zone leads to reflectivity being underestimated by up to 1 dB, the number of events being altered by ±5% and the precipitation amount being underestimated by 9 to 11 percentage points. Besides investigating a blind zone of 1200 m, the impacts of a reduced blind zone of 600 m are also analyzed. This analysis will help in assessing future missions with a smaller blind zone. The reduced blind zone leads to improved representation of mean reflectivity but does not improve the bias in event numbers and precipitation amount.

1. Introduction

As an integral part of the water cycle in polar regions, snowfall is extremely difficult to capture at the relevant spatial scale and with sufficient accuracy [*Levizzani et al.*, 2011]. Surface observations by in situ sensors are sparse and available only over land [*Schneider et al.*, 2014], and snowfall measurements in polar regions are particularly affected by wind-induced errors such as undercatch or overcatch from blowing snow [*Yang et al.*, 1999; *Knuth et al.*, 2010].

An important source of spatially extensive measurements of snowfall are remote sensing observations from space, such as microwave radiometer [*Levizzani et al.*, 2011] or the radar of the CloudSat satellite [*Stephens et al.*, 2008]. CloudSat allowed snowfall climatologies for polar regions up to 82°N/S to be derived for the first time [*Liu*, 2008a; *Kulie and Bennartz*, 2009; *Palerme et al.*, 2014]. However, accurately determining the snowfall rate (S) from the observed profile of the equivalent radar reflectivity factor (Z_e) is challenging due to the microphysical and microwave scattering uncertainties in the conversion of Z_e to S [e.g., *Hiley et al.*, 2011] and the inability to reliably measure Z_e close to the surface when using satellite radar systems. Our research addresses this latter point by studying how this "blind zone" affects observations and what impact a reduced blind zone would have.

The vertical extent of this blind zone is largely determined by the surface type and is smaller over the ocean and larger over land or sea ice [*Durden et al.*, 2011a]. For CloudSat, it has been shown that over land, the received signal is free from ground clutter only from the fifth range bin above ground level (1200 m agl, hereafter $H_{CS} = H_{CloudSat}$) [*Marchand et al.*, 2008]. New spaceborne radars such as the recently launched dual-frequency radar on board the Global Precipitation Measurement (GPM) Core Observatory [*Hou et al.*, 2014] or the Cloud Profiling Radar (CPR) on board the upcoming Earth Clouds, Aerosols, and Radiation Explorer (EarthCARE) mission [*Gelsthorpe et al.*, 2010; *Donovan et al.*, 2013] are expected to achieve smaller blind zones ranging between 600 m and 1000 m above surface (depending on radar operation mode). Other proposed missions such as the Polar Precipitation Measurement Mission [*Joe et al.*, 2010] or the Aerosol/Cloud/Ecosystems (ACE) mission [*Durden et al.*, 2011b] are heading to blind zones in the order of 100 to 200 m.

These observational blind zones are likely to introduce errors in the derived statistics of snowfall frequency and *S* for surface level if the snowfall properties are significantly altered within the blind zone. For example, snowfall might be underestimated or completely missed, if the snow cloud is shallow. The opposite extreme of snowfall overestimation would be snowfall that is detected at the top of the blind zone but completely sublimates on its way down to the surface. Besides these extreme scenarios, the snowfall properties observed at the top of the blind zone might also be altered within the blind zone due to microphysical processes or wind shear. For midlatitude systems, a general increase of the radar reflectivity factor toward the ground in the range of 3 to 7 dB km^{-1} was found and has been associated to aggregation and depositional growth [*Fabry and Zawadzki*, 1995; *Liu*, 2008a; *Matrosov and Battaglia*, 2009; *Wolfe and Snider*, 2012]. While there is large variability, reflectivity gradients are found to generally increase with higher temperatures. *Henson et al.* [2011] and *Stewart et al.* [2004] studied ground-based radar data for the Canadian Arctic region and found radar reflectivity in the lowest 2 km above ground to be nearly constant. However, some cases revealed increasing as well as decreasing radar reflectivities in the range of 5 dB km^{-1} toward ground depending on the thermodynamic structure of the lowest layers and the intensity of snowfall. Despite its blind zone limitations, CloudSat still detects significantly more light snowfall than the ground-based precipitation radar networks do because of its higher sensitivity [*Smalley et al.*, 2014].

The goal of this paper is to investigate the impact of the blind zone on snowfall statistics at three polar sites and to estimate whether statistics derived from observations above the blind zone are biased in comparison to statistics taken at the surface. One way of investigating the impact of the blind zone is to directly compare CloudSat overpasses over a site where the lower reflectivity profile is measured with results from a ground-based cloud radar. However, these direct comparisons can be strongly affected by the difference in observed radar volumes or the horizontal displacement of the satellite overpass from the location of the ground-based radar. These complications can be avoided by statistically comparing satellite and ground-based radar observations [*Protat et al.*, 2009, 2010]. Alternatively, variations of radar reflectivity within the blind zone using only ground-based observations can be investigated. We use the observations at the top of the blind zone from the ground-based radars as a reference for the statistics that a theoretically perfect overpassing and volume-matched satellite radar would provide. In this way, we avoid any approximation due to temporal, spatial, or radar volume mismatch while the generally expected changes (e.g., underestimation/overestimation of snowfall) within the blind zone are assumed to appear in both the real satellite observations and the ground-based measurements.

In this study, we apply this method to long-term radar observations from observational sites in Antarctica and Svalbard. These ground-based observations were carried out using the Micro Rain Radar (MRR), a compact and lightweight 24 GHz frequency-modulated continuous wave (FMCW) radar [*Klugmann et al.*, 1996].

2. Study Area

We use column measurements from the Princess Elisabeth station (PE) in East Antarctica and from Ny-Ålesund (NÅ) and Longyearbyen (LY) in Svalbard, Norway, as exemplary data sets for polar regions. To the authors' knowledge, no other ground-based precipitation radar is currently operating in Antarctica and the data sets from NÅ and LY are the first of their kind in Svalbard. Because the setup and the results in LY were similar to NÅ and both sites are only 110 km apart, results for LY are only presented in the supporting information. Nevertheless, comparison of both sites is important when assessing how representative the study is.

2.1. Princess Elisabeth Station, East Antarctica

The only current precipitation radar over the Antarctic ice sheet is installed as part of the meteorological-cloud-precipitation observatory that has been operating at the PE station since February 2010 [*Gorodetskaya et al.*, 2014a] (http://ees.kuleuven.be/hydrant). The station is built on Utsteinen Ridge located north of the Sør Rondane Mountains in the eastern part of Dronning Maud Land (DML) at the ascent to the East Antarctic plateau (71°57'S, 23°21'E, 1392 m above mean sea level (amsl), 173 km from the coast, Figure 1a). Together with other remote sensing instruments, the MRR precipitation radar is installed on the roof of the PE station about 10 m above the snow surface (Figure 2a). An automatic weather station providing meteorological data is located 300 m east of the PE base [*Gorodetskaya et al.*, 2013]. In this study, we use year-round measurements available for the full year 2012.

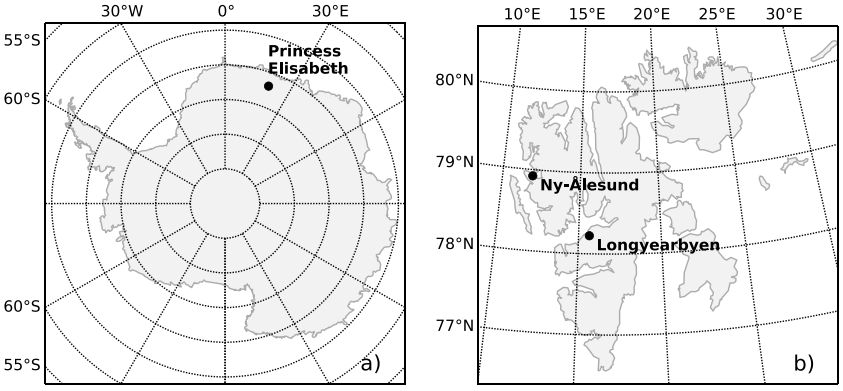

Figure 1. Map of the location of Princess Elisabeth station in (a) East Antarctica and (b) of Ny-Ålesund and Longyearbyen in Svalbard, Norway.

The PE site is characterized by a relatively mild climate, mainly due to the favorable location for warm air advection associated with local intense cyclonic activity and a lack of drainage of cold air from the high plateau due to shelter from the Sør Rondane Mountain [*Gorodetskaya et al.*, 2013]. Two main meteorological regimes govern the weather at PE—the cold katabatic regime and the warm/transitional synoptic regime [*Gorodetskaya et al.*, 2013]. The katabatic regime is characterized by low wind speeds of predominantly south-southeasterly direction, strong near-surface temperature inversions, low specific humidity, and low incoming longwave fluxes indicative of clear skies. The synoptic regime at PE is in turn associated with the Southern Ocean cyclones passing near DML and bringing heat and moisture advection into the Antarctic ice sheet [*Noone et al.*, 1999; *Schlosser et al.*, 2010]. Precipitation at PE (only as snowfall) mainly occurs during synoptic regimes. The largest snowfalls observed at PE have been associated with narrow bands of enhanced moisture amounts (atmospheric rivers) directed into DML and surrounding sectors [*Gorodetskaya et al.*, 2014b]. Such rare large snowfall events contribute significantly to the total yearly snow accumulation and can explain the high interannual variability of snow accumulation at the PE site (from 23 up to 230 mm water equivalent per year [*Gorodetskaya et al.*, 2014a, 2014b]) and entire DML [*Boening et al.*, 2012; *Lenaerts et al.*, 2012].

2.2. Ny-Ålesund, Svalbard

Measurements in the Arctic were taken in NÅ (78.92°N, 11.93°E, 8 m amsl) on Spitsbergen, the largest island of the archipelago of Svalbard, Norway (Figure 1b). The climate in Svalbard is strongly influenced by the West Spitsbergen Current, which flows from the North Atlantic along the west coast of Spitsbergen and provides the largest input of sensible heat into the Arctic Ocean [e.g., *Gammelsrød and Rudels*, 1983]. Through mixing, some of this heat reaches the fjords in the west of the island and leads to a much milder climate

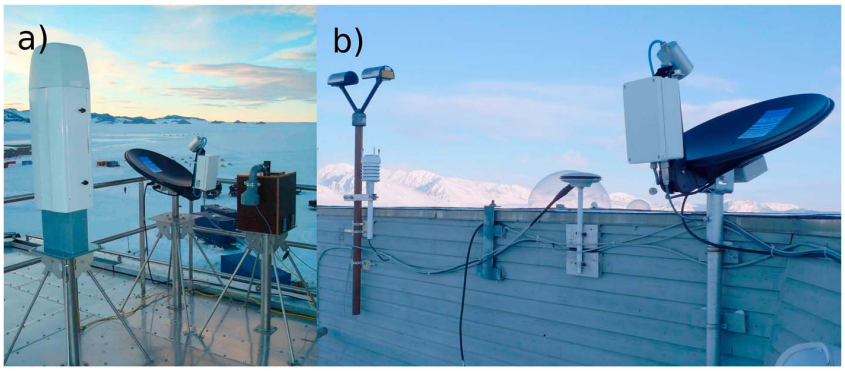

Figure 2. (a) Ceilometer (left), MRR (middle), and infrared pyrometer (right) on the roof of the Belgian Princess Elisabeth station in East Antarctica. (b) MRR (right) and Parsivel disdrometer on the roof of the Norwegian Polar Institute Sverdrup Station in Ny-Ålesund, Svalbard.

than in other locations at the same latitude (e.g., Greenland). Additionally, Svalbard lies in the North Atlantic storm track with general cyclogenesis and rapid cyclone deepening within the Icelandic Low and penetrating into the Arctic [*Serreze et al.*, 1997; *Tsukernik et al.*, 2007]. As a consequence, the atmospheric influence on the climate varies between moist and warm air masses coming from the Atlantic and dry and cold air masses coming from the Arctic. Precipitation in Svalbard can therefore be liquid as well as solid.

Ny-Ålesund lies at the shore of the Kongsfjord, which is 26 km long and up to 14 km wide. This position leads to a maritime climate, when the fjord is ice free, and higher precipitation, with an annual mean of 427 mm (for the period 1981–2010), than in the interior of Spitsbergen [*Førland et al.*, 2012]. The MRR was placed on the roof of the Sverdrup Research Station operated by the Norwegian Polar Institute (NP) in 8 m agl height (Figure 2b), 350 m away from the sea. Standard meteorological observations are taken from the weather station of the Norwegian weather service (World Meteorological Organization no. 01007, data available at http://eklima.met.no) located 100 m southeast of the NP station. Measurements were taken over a period of 1 year between 10 March 2010 and 15 March 2011.

2.3. Regime Classification

To investigate whether the impact of the blind zone on snowfall measurements depends on the type of snow event or ambient weather conditions such as stability or humidity, the data set is classified into different regimes. Sublimation of precipitation before reaching the surface (virga phenomenon) depends both on precipitation microphysical properties (such as particle size and terminal velocity) and on the ambient meteorological conditions [*Clough and Franks*, 1991; *Wang et al.*, 2004; *Campbell and Shiobara*, 2008; *Evans et al.*, 2011]. Dry meteorological conditions with a relatively warm subcloud layer will favor virga formation, whereas saturated and mixed subcloud layer will favor precipitation to the surface. The occurrence of either conditions was identified based on the classification of 3-hourly measurements of low-level temperature inversion (T_{inv}) and near-surface relative humidity with respect to ice (RH_i) in the vicinity of PE and NÅ stations.

Near-surface T_{inv} (°C m^{-1}) is calculated as the difference between the air temperature and the skin surface temperature of snow. The air temperature is measured at the variable height (within 2– 4 m) above the snow surface depending on snow accumulation. Surface temperature is calculated using measurements of outgoing and incoming longwave radiative fluxes (see *Gorodetskaya et al.* [2013] for details).

Prior to regime classification, the data were deseasonalized and standardized by subtracting monthly mean values and calculating *z* scores; the classification is based on hierarchical cluster analysis of RH_i and T_{inv} following *Gorodetskaya et al.* [2013]. Two main regimes were identified: the *dry stable regime* characterized by low RH_i and high T_{inv}, which represents 27% (41%) of all observations at PE (in NÅ), and for all other events the *wet unstable regime* with high RH_i and near-zero T_{inv}. MRR observations are grouped according to the two regimes. The regime classification was not applied to the data set in LY because no weather station was available in the immediate vicinity.

3. Radar Observations of Snowfall

In this study, MRR data are used to mimic CloudSat measurements (Table 1) while investigating how radar observations are altered in the blind zone.

3.1. CloudSat

CloudSat, which is part of the A-train satellite constellation, carries the Cloud Profiling Radar (CPR) operating at a frequency of 94.05 GHz (wavelength $\lambda = 3.2$ mm) [*Stephens et al.*, 2008; *Tanelli et al.*, 2008; *L'Ecuyer and Jiang*, 2010]. The raw measured return power is provided in the level 1 data product (1B-CPR) and converted into equivalent attenuated reflectivity factor, included in the 2B-GEOPROF data product [*Tanelli et al.*, 2008]. Near the surface, the reflectivity product is contaminated by ground clutter leading to significant power returns not related to hydrometeor occurrence [*Marchand et al.*, 2008; *Tanelli et al.*, 2008]. Although the latest 2B-GEOPROF version has a clutter reduction procedure, this procedure is less effective over land than over ocean and is particularly ineffective over mountainous terrain [*Mace*, 2006]. Consequently, snowfall rates at the surface derived from truncated 2B-GEOPROF profiles need to be approximated by snowfall rates at an elevated height of 1200 m (H_{CS}) above the surface, introducing an effective blind zone of 1200 m agl over land. To ensure equal processing of MRR and CloudSat (see section 3.3), Z_e data of the 2B-GEOPROF product are used even though a CloudSat snowfall product (2C-SNOW-PROFILE) [*Wood*, 2011; *Wood et al.*, 2013]

Table 1. Comparison of MRR and CloudSat's CPR

	MRR	CPR
Frequency (GHz)	24.23	94.05
Radar type	FMCW	Pulsed
Transmit power (W)	0.05	1820 (peak power)
Radar Power consumption (W)	25	–
Number of range gates	31	125
Range resolution (m)	100/60[a]	485, resampled to 240
Measuring range (km)	0–3/0–1.8[a]	0–25
Lowest usable range gate (m)	400/240[a]	1200
Antenna diameter (m)	0.6	1.85
Beam width (two-way, 6 dB)	1.5°	0.12°
Minimum detectable Z_e (dBz)	−5 at 1200 m agl	−30
Integration time (s)	300	0.16
Cross-track resolution (km)	–	1.4
Along-track resolution (km)	–	1.8

[a]Depending on configuration.

based on 2B-GEOPROF has recently been released. CloudSat is said to be overpassing a station if its nadir view is within a radius of 100 km. Based on this radius, we found 899 overpasses for the PE study area and 1579 overpasses for the NYA study area in the period between 2006 and 2013. Reflectivities of the lowest clutter-free range gate at H_{CS} as reported by the 2B-GEOPROF product are analyzed for each overpass.

3.2. Micro Rain Radar

The MRR (Micro Rain Radar) is a vertically pointing frequency-modulated continuous wave (FMCW) radar manufactured by METEK GmbH, Germany, [*Klugmann et al.*, 1996] operating at a frequency of 24 GHz ($\lambda = 1.24$ cm). Its low power consumption of only 25 W makes it particularly suitable for remote areas with limited power supply. The MRR was originally developed to measure rain [*Peters et al.*, 2002, 2005; *Tridon et al.*, 2011], but recent modifications in the MRR data processing [*Maahn and Kollias*, 2012] and comparisons to cloud radar observations [*Kneifel et al.*, 2011] have revealed that the MRR can also be used to study snowfall [*Stark et al.*, 2013; *Gorodetskaya et al.*, 2014a].

The MRRs were equipped with a 200 W antenna heating, but the heating was only used in NÅ when temperatures were around the melting point. At lower temperatures, the heating is unable to completely melt the snow, which causes the dish to glaciate resulting in a disturbance of the measurements. Presence of a thin layer of dry snow, instead, does not contaminate the measurements because attenuation by dry snow is very weak at K-band [*Matrosov*, 2007] and the snow is easily blown away by the ambient wind before a large layer can accumulate. The antenna dish of the MRR in NÅ was checked daily by the station staff to avoid glaciation of the dishes. The MRR at PE was regularly checked by the staff in summer and additionally supervised via webcam to check the status of the instrument during the unmanned period.

The MRR provides data at 31 range gates with a resolution of 100 m agl (60 m agl) at PE (in NÅ). The first two and the last range gate are extremely noisy and removed from the analysis. Because MRR's original software was designed for rain only, the alternative software package IMProToo designed for observations of snowfall by *Maahn and Kollias* [2012] has been used for this study. Due to the fixed MRR Doppler velocity range of 0 to 12 m/s, aliasing effects might occur at upward or very low fall velocities (as is common for snow). These effects can be corrected by IMProToo for all but the third MRR range bin (see *Maahn and Kollias* [2012] for details). Therefore, the third bin has also been excluded from the analysis so that an effective measurement range of 400 to 3000 m agl for PE (240 to 1800 m agl for NÅ) remains. Hereafter, the altitude of the lowest observation of the MRR will be called $H_{SF} = H_{SurFace}$. A contamination of the measurements due to blowing snow is unlikely at H_{SF} and above [*Xiao et al.*, 2000].

To increase MRR's sensitivity to around −10 dBz (−12 dBz) at PE (in NÅ), MRR data were averaged to 300 s. Even though this averaging reduces temporal and horizontal resolution (due to stronger advection effects), this reduction is justified as convective events with high temporal variability are rare at polar sites. Unfortunately, MRR's noise level varies significantly between different instruments and can vary by more than 5 dB in time, which leads to temporary lower sensitivities. To exclude the impact of a varying sensitivity on

Table 2. Equivalent Reflectivity-Snowfall Rate (Z_e-S) Relations From *Kulie and Bennartz* [2009] and Derived Conversion for Z_e From 35 GHz to 94 GHz

Particle Habit	Z_e (35 GHz)	Z_e (94 GHz)	Z_e Converted From 35 to 94 GHz
Three bullet rosette (LR3)	$24.04S^{1.51}$	$13.16S^{1.40}$	$0.69Z_e^{0.93}$
Aggregates (HA)	$313.29S^{1.85}$	$56.43S^{1.52}$	$0.50Z_e^{0.82}$
Snow (SS)	$19.66S^{1.74}$	$2.19S^{1.20}$	$0.28Z_e^{0.69}$

the presented analyses, MRR data with $Z_e < -5$ dBz are discarded. This Z_e value corresponds to 0.02 to 0.09 mm/h depending on how Z_e varies with snowfall rate (see section 3.3).

To exclude rainfall events in Svalbard from the analysis, data from temperatures above −2°C were removed. Note that liquid precipitation events were used to verify the calibration of the MRR by comparing it with the reflectivity measured by an optical Parsivel disdrometer [*Löffler-Mang and Joss*, 2000]. No significant offset was found, so the calibration of the MRR in NÅ is expected to be correct within ±1 dB. No calibration reference is available for PE, but a calibration offset would only affect absolute values and not the profile structure.

3.3. Estimating Precipitation Rates From Radar Measurements

To convert the equivalent radar reflectivity factor Z_e into snowfall rates S, a power law relation is usually used:

$$Z_e = a \cdot S^b. \tag{1}$$

The parameters a and b depend on several assumptions, e.g., on the assumed particle habit, density, orientation, and particle size distribution. Backscattering properties of snow particles are increasingly affected by non-Rayleigh effects if the snowflake size is in the range of the radar wavelength. In addition, the natural variability of snowfall properties introduces a large uncertainty for any Z_e-S relation. Most Z_e-S relations for cloud radars have been derived for 35 GHz or 94 GHz, but not for 24 GHz. Calculations using an extended and updated version of the scattering database for snow particles [*Liu*, 2008b] revealed that the difference between backscattering at 24 GHz and at 35 GHz is below 0.5 dB, and hence, the 35 GHz Z_e-S relation is applied to MRR observations at 24 GHz in this study. Note that *Kneifel et al.* [2011] came to a different result because of interpolation effects across frequency: at that time, the database of *Liu* [2008b] did not include scattering estimations for 24 GHz.

To take the uncertainty of a Z_e-S relation into account, we use three Z_e-S relations from *Kulie and Bennartz* [2009], which are available for both 94 and 35 GHz (Table 2). These relations have been derived from aircraft measurements of particle size distribution and a large set of snow particle habits and their associated scattering properties. While the conversion of Z_e to S is necessary to illustrate the impact on snow amount at the surface, most analyses are performed in Z_e space in order to confine uncertainties to the vertical structure.

Note that due to increasing non-Rayleigh effects with increasing particle size, Z_e measured by MRR can be larger than that measured by CloudSat. To estimate this effect, a correction term

$$Z_{e\,(94\,\mathrm{GHz})} = \alpha \cdot Z_{e\,(35\,\mathrm{GHz})}^{\beta} \tag{2}$$

is derived by solving each pair of 35/94 GHz Z_e-S relations presented above for S (see Table 2). In Figure 3, the resulting differences for a Z_e range of −10 to 30 dBz are presented. It shows a significant decrease of Z_e with a high spread due to particle type. For example, an MRR measurement of ∼10 dBz corresponds to CloudSat measurements between 1.4 and 7.7 dBz. In the following, the conversion for aggregates is used as an average of the different relations.

4. Comparison of MRR and CloudSat Above the Blind Zone

For our assumption that the MRR observations below the blind zone can be used to investigate the changes in Z_e within CloudSat's blind zone, we first have to investigate whether MRR generally reproduces the Z_e statistics measured by CloudSat above the blind zone. Because Z_e from both instruments cannot be directly

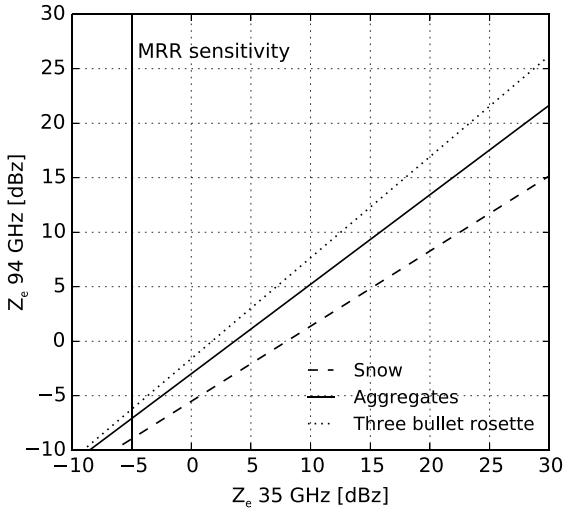

Figure 3. Conversion of reflectivity Z_e from 35 GHz to 94 GHz for snow (dashed), aggregates (solid), and three bullet rosettes (dotted) derived from the Z_e-S relations of *Kulie and Bennartz* [2009].

compared due to the different radar frequencies, the comparison is performed in terms of S using the Z_e-S relations introduced in section 3.3.

For this, we also applied the MRR sensitivity threshold to CloudSat data. The −5 dBz threshold of the MRR corresponds to −7.10 dBz at 94 GHz assuming aggregates for equation (2) (−8.97 dBz for snow and −6.25 dBz for three bullet rosettes). In comparison to the snowfall threshold of −10 dBz defined by *Liu* [2008a], this threshold reduced the number of events by 6 to 24%, depending on assumed particle type. Because these events only weakly contribute to total precipitation, snow mass is only reduced by 1 to 5%. Consequently, we can assume that the MRR is able to capture the majority of snowfall.

The comparison of the frequency distributions of derived snowfall rate S at H_{CS} for both PE and NÅ stations (Figure 4) reveals the generally strong similarity between CloudSat and MRR data at H_{CS} despite the different radar and data sampling characteristics. However, some differences between the CloudSat and MRR snowfall rate distribution occur particularly at PE, where CloudSat shows a broader frequency distribution shifted to higher S. Note that this discrepancy disappears if the MRR data are modified by an assumed calibration offset of +2 dB. Although we are currently unable to properly correct the calibration for the MRR at PE, such a constant bias would not affect the results of this study since we are using the same instrument for different heights and only analyze their relative differences. Attenuation effects might also lead to an offset between

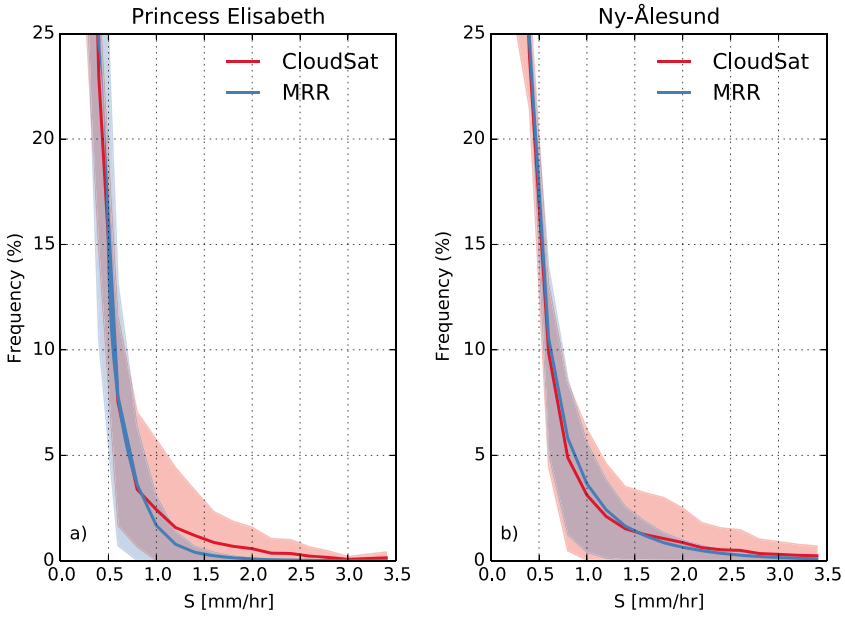

Figure 4. Frequency distribution of snowfall rates S for CloudSat (red) and MRR (blue) data at 1200 m agl (H_{CS}) for the (a) Princess Elisabeth and (b) Ny-Ålesund stations, where snowfall rate was determined by the range of Z_e-S relationships in *Kulie and Bennartz* [2009]. The line/polygon represents the mean/range of S for these Z_e-S relationships.

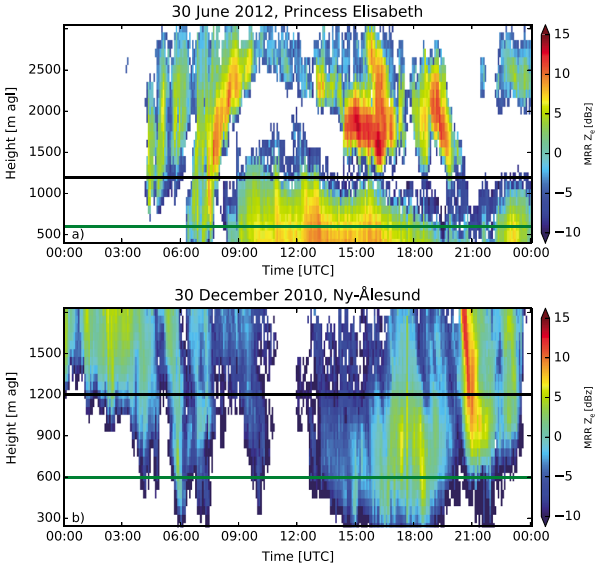

Figure 5. Time-height plots of reflectivity Z_e for two cases at (a) Princess Elisabeth and (b) Ny-Ålesund. CloudSat's blind zone of 1200 m agl (H_{CS}) and a reduced blind zone of 600 m agl (H_{FM}) are denoted by a black and green line, respectively.

CloudSat and MRR because attenuation at 94 GHz is 1 order of magnitude larger than at 35 GHz, as shown by *Matrosov* [2007]. However, they found that attenuation is only relevant for higher-precipitation rates and thick snow layers, where attenuation can exceed 1 dB. In addition, attenuation is partly compensated for by multiple scattering effects in heavier snowfall [*Matrosov and Battaglia*, 2009]. Attenuation due to supercooled liquid water can be neglected at 24 GHz and is below 1 dB at 94 GHz for liquid water paths of less than 100 g m^{-2} [e.g., *Kneifel et al.*, 2014].

Further, the wide range of occurrences for a specific S (e.g., between 0 and 5% for $S = 1$ mm h^{-1} for CloudSat at PE) demonstrates that the uncertainty in S due to the use of different Z_e-S relationships associated with varying snow microphysical characteristics is much larger than the difference between MRR and CloudSat data.

5. Analysis of the Blind Zone

Based on our comparison of MRR and CloudSat at H_{CS} in the previous section, we can assume that the MRR observations within CloudSat's blind zone can be used to investigate the impact of the blind zone on snowfall frequency and snowfall rate estimation. In the following, we will also include a blind zone height of 600 m ($H_{FM} = H_{FutureMission}$ hereafter) in the analysis. This height represents the most optimistic estimation of the blind zone of future satellite missions.

The different possible errors introduced by assigning the reflectivities at H_{CS} to the surface level can be identified in Figure 5 showing example days of the observed, rather complex but typical, precipitation structures. In the example at PE (Figure 5a), two precipitation layers can be identified during the day. They appear to be disconnected when observed with an MRR: a high-precipitation layer with high Z_e values does not necessarily imply that precipitation reaches the ground. For the NÅ case (Figure 5b), the effect of sublimating precipitation or virga is even more pronounced with precipitation sometimes reaching surface levels but most of the time sublimating aloft. Consequently, in these cases, the blind zone would lead to an overestimation of snowfall on the surface (hereafter referred to as *commission error*). At PE, the opposite effect can also be seen: shallow precipitation that would be potentially missed by a satellite radar and thus resulting in an underestimation of snowfall on the ground (hereafter called *omission error*).

In the following subsections, we analyze the ground-based data sets focusing on different aspects: what is the impact of the blind zone on the climatology of observations in respect to (1) Z_e distribution, (2) number of events, and (3) single events? Finally, we discuss the effect of the blind zone by considering precipitation amount.

5.1. Impact on Z_e Distribution

In the following, we investigate whether the vertical distribution of Z_e is affected by virga, shallow precipitation or microphysical processes such as sublimation, riming, and aggregation. For this investigation, reflectivity versus altitude 2-D histograms (2-DH) of observed reflectivities for the complete observation period of 1 year are shown in Figures 6b and 7b for PE and NÅ, respectively. To enable a better interpretation of the MRR statistics in terms of CloudSat observations, results are shown for both 24 GHz Z_e and converted to 94 GHz assuming aggregates (see Figure 3 for the impact of assuming other snow types). For both sites, the 2-DH is very homogeneous between H_{SF} and H_{CS}. The median of reflectivity is constant with altitude

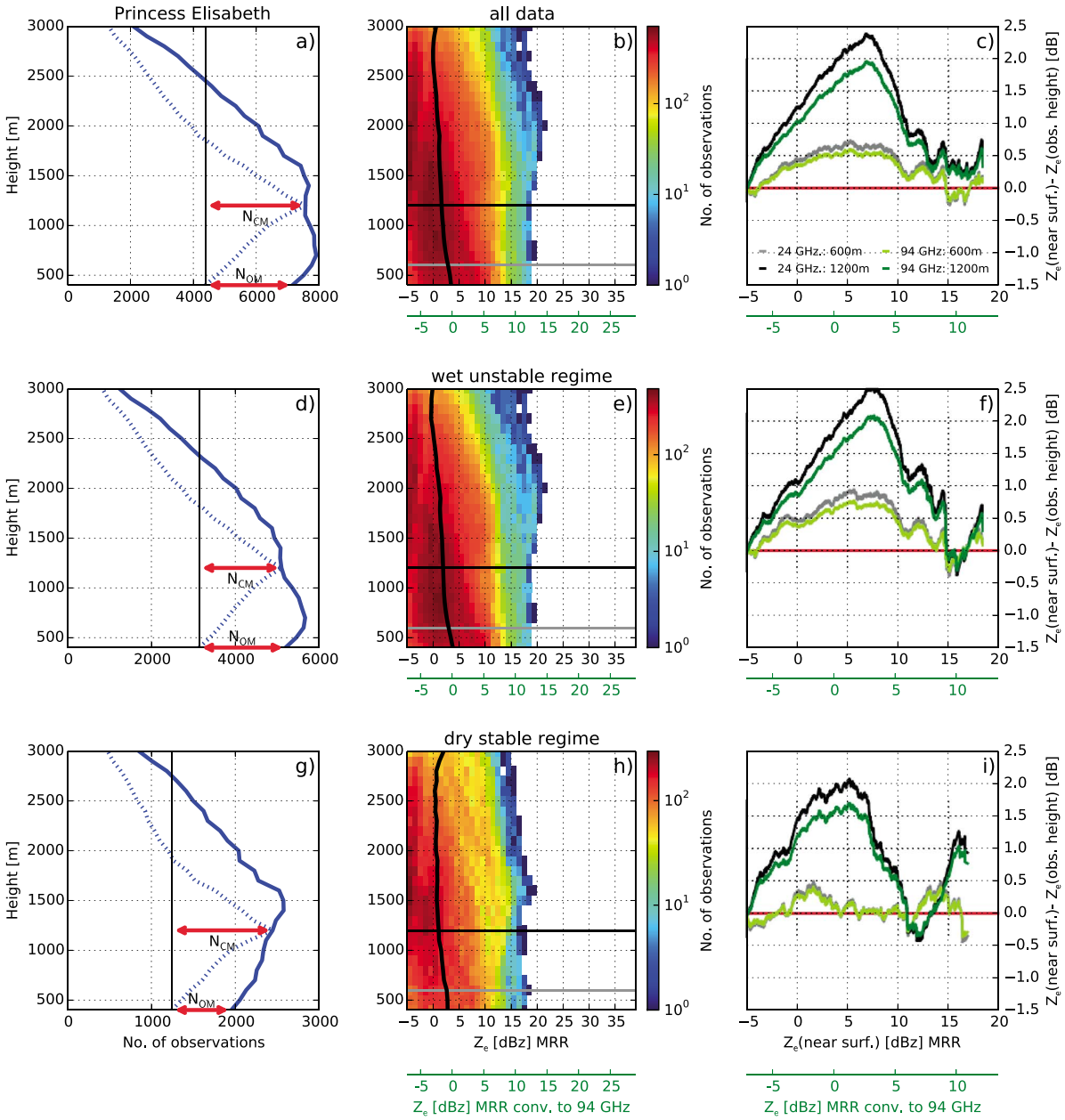

Figure 6. (a) Total number of observations N with Z_e of MRR observations at Princess Elisabeth station, East Antarctica, larger than −5 dBz (solid blue line) are compared with profiles $\hat{N}$, which also contain snowfall at 1200 m agl (dashed blue line) for the complete data set. Commission and omission errors (N_{CM} and N_{OM}) are marked with red arrows. (b) Reflectivity versus altitude 2-D histograms (2-DH) of observed MRR reflectivities. The median profile is denoted by the black solid line. The horizontal, black line denotes H_{CS}. A reduced blind zone of 600 m agl (H_{FM}) of a future satellite mission is marked with a horizontal, gray line. An estimate for the corresponding Z_e at 94 GHz using the coefficients for aggregates is indicated by the additional, green scale. (c) Detrended Quantile-Quantile (DQQ) plots of the reflectivity observations close to the surface (H_{SF}) in comparison to H_{CS} (black) and in comparison to H_{FM} (gray) as well as after conversion to 94 GHz (green and light green lines). In contrast to a Quantile-Quantile plot, only the differences between quantiles of Z_e at H_{CS} (or H_{FM}) and H_{SF} are shown for the ordinate, i.e., a value of zero means perfect agreement. (d–f) Same as Figures 6a–6c, but only for the *wet unstable regime*. (g–i) Same as Figures 6a–6c, but only for the *dry stable regime*.

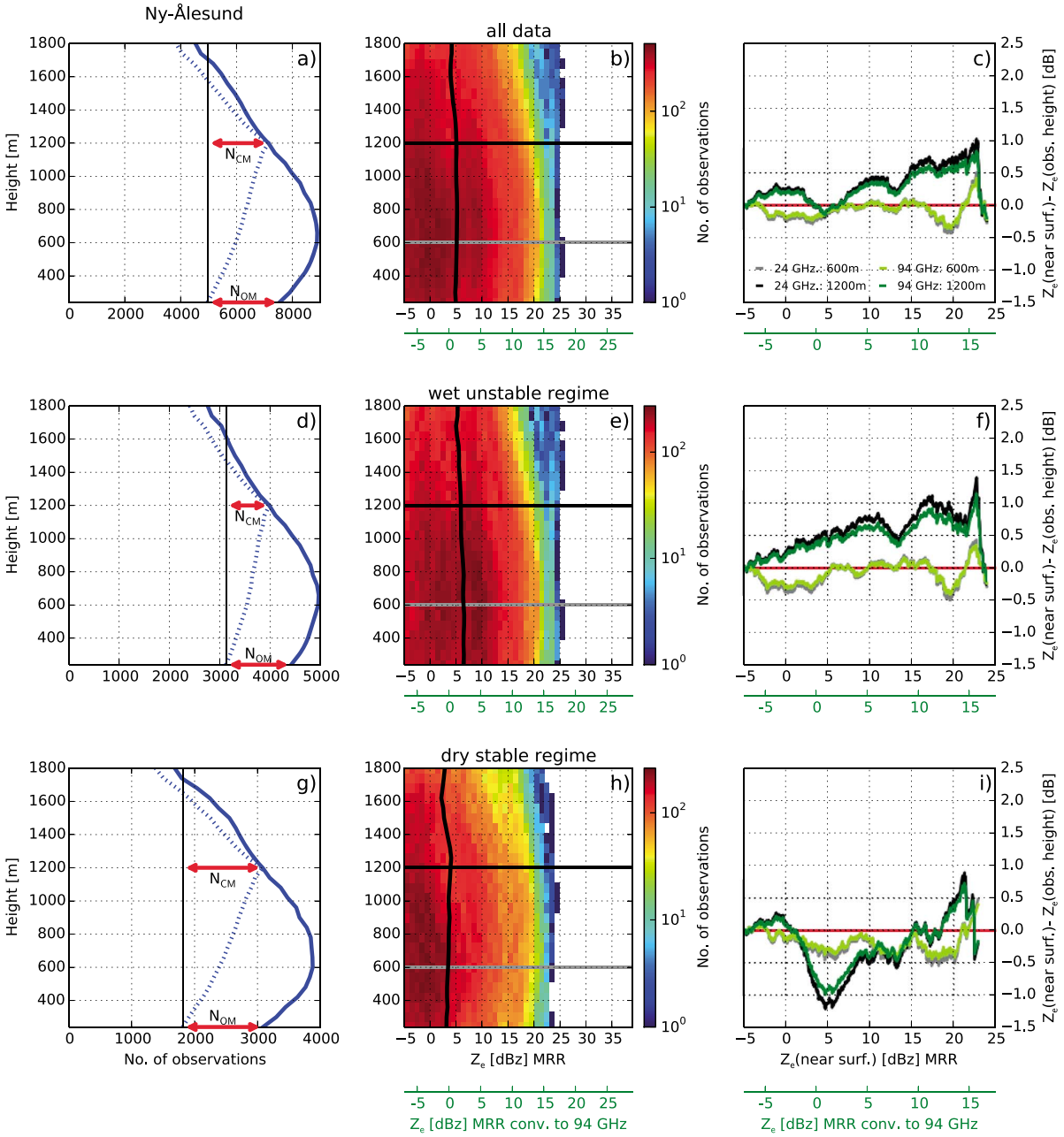

Figure 7. Same as Figure 6 but for Ny-Ålesund, Svalbard.

in NÅ and shows only a weak increase of 1–2 dB toward the surface at PE. This low-reflectivity gradient is highly consistent with the findings of an almost constant Z_e profile found by *Henson et al.* [2011] for the Canadian Arctic.

The distribution of reflectivity measurements at H_{CS} and H_{SF} is also compared using Detrended Quantile-Quantile (DQQ) [*Thode*, 2002] plots (Figures 6c and 7c). For this, both series of Z_e are divided into n_Z quantiles where n_Z is the length of the shorter Z_e series. Then, the quantiles are sorted and the quantiles of H_{CS} and H_{SF} are subtracted from each other. This difference of quantiles is plotted against the quantiles for Z_e at H_{SF}. By this, the distribution of Z_e at H_{CS} can be directly compared to the distribution at H_{SF} and even small

differences between these distributions become visible. In contrast to the analysis of vertical gradients of individual profiles, this method has the advantage that it is not influenced by changes of the Z_e profile due to, e.g., advection or temporal evolution. For PE, the distribution of Z_e at H_{CS} is shifted toward smaller reflectivities by a maximum of 2.3 dB in the medium Z_e range. The agreement of distributions increases for Z_e values larger than 10 dBz, indicating more similar distributions for stronger events. However, due to the relatively small number of events in this high-reflectivity region, a more extended data set would be necessary for a clear conclusion. For NÅ, agreement of Z_e distributions is better, and the shift between distributions at H_{CS} and H_{SF} is mostly below 1 dB, often below 0.5 dB with a slight increase toward larger Z_e. Performing the comparison with MRR data converted to 94 GHz has only minor impact on the results.

To investigate whether the found changes in statistics depend on the regime classification, the analysis is repeated for the two synoptic regimes. For the *wet unstable regime* (Figures 6e, 6f, 7e, and 7f), only small differences to the complete data set are visible in the 2-DH and the DQQ plot. However, the *dry stable regime* (Figures 6h, 6i, 7h, and 6i) features, on average, lower reflectivities for both sites, especially at the levels below H_{CS} because moisture supply for particle growth in the near-surface layers is low while temperatures are relatively high, favoring particle sublimation. In NÅ, the distribution of Z_e at H_{CS} is shifted by up to −1 dB in comparison to HSF for the *dry stable regime*, which is probably related to sublimation effects (Figure 7i). For PE, the shift of the distribution is similar to the one using the complete data set—except for rare values exceeding 10 dBz. Sublimation effects lead to a reduction of the shift of Z_e distributions by 0.3 dB (Figure 6i).

To investigate the impact of a reduced blind zone, DQQ plots are also presented for an observation height of 600 m agl (H_{FM}, Figures 6c, 6f, 6i, 7c, 7f, and 7i). For NÅ, this results in a significantly better statistical agreement of H_{FM} and H_{SF}. The offset is only ±0.5 dB for all regimes. For PE, the agreement of Z_e distributions is improved and the offset of the distributions is below ±1 dB and only for the *dry stable regime* (Figure 6i) is the offset negligible and below ±0.5 dB. In summary, a reduction of the blind zone by 50% significantly improves the agreement of the Z_e distributions at H_{SF} and the observation altitude. We expected the impact on Z_e distribution to still be underestimated for H_{CS} and H_{FM} at PE because H_{SF} is at an altitude of 400 m agl and processes between the surface and H_{SF} are not considered. In NÅ, H_{SF} is at 240 m agl, so the underestimation is expected to be less. The results for LY, which are very similar to NÅ, can be found in Figure S1 in the supporting information.

5.2. Impact on the Number of Snowfall Events

To investigate the impact of the blind zone on the total number of observed precipitation events, N—defined as the number of observations greater than −5 dBz—is calculated as a function of height (Figures 6a and 7a). By restricting the number of events in one height to those with snowfall at H_{CS} ($\hat{N}$ in Figures 6a and 7a), the number of shallow events (omission error, N_{OM}) can be estimated by the difference between N and $\hat{N}$. At PE (NÅ), 38.7% (34.1%) of 7153 (7537) observations are classified as omission errors because they are present at H_{SF} but not at H_{CS} above. For PE, this number might even be too low if shallow events occur below H_{SF} of 400 m agl.

Virga events that sublimate and do not reach H_{SF}, although they are present at H_{CS} (commission error, N_{CM}), can be estimated by the decrease of $\hat{N}$ relative to its maximum at H_{CS}. As a result, 44.4% (28.9%) of the events observed at H_{CS} do not reach the surface at PE (in NÅ). So N_{OM} is similar for PE and NÅ, while N_{CM} is not.

It is important to note that N_{OM} and N_{CM} not only contain shallow and sublimating precipitation events but are also affected by advection and shear effects as well as by the terminal fall velocity of snow, which also causes slanting of the observed snowfall profiles. When a cloud starts to precipitate, particles need up to 20 min from H_{CS} to the surface assuming a mean fall velocity for snow of 1 m s^{-1}. During these first 20 min, the event will be classified as a commission error. On the other hand, if the cloud stops precipitating, the last 20 min of the event will be classified as an omission error. Although N_{CM} and N_{OM} might be overestimated, they are affected in the same way in the long term. Thus, the difference between both errors is expected not to be biased by the slanting of the profiles. If advection of precipitation is assumed to be homogeneously distributed, advection effects are also expected to cancel each other out.

The difference between N_{OM} and N_{CM} is equal to the difference of N between the altitudes at H_{CS} and H_{SF}. For PE, N is reduced by 5.7% from H_{CS} toward the surface (Figure 6a). In contrast, N increases by 5.2% at the surface for NÅ (Figure 7a). Interestingly, the increase toward the surface is not monotonic, but the vertical distribution of N is "belly shaped" with a maximum at H_{FM}. Since the decrease toward H_{SF} is smaller than the

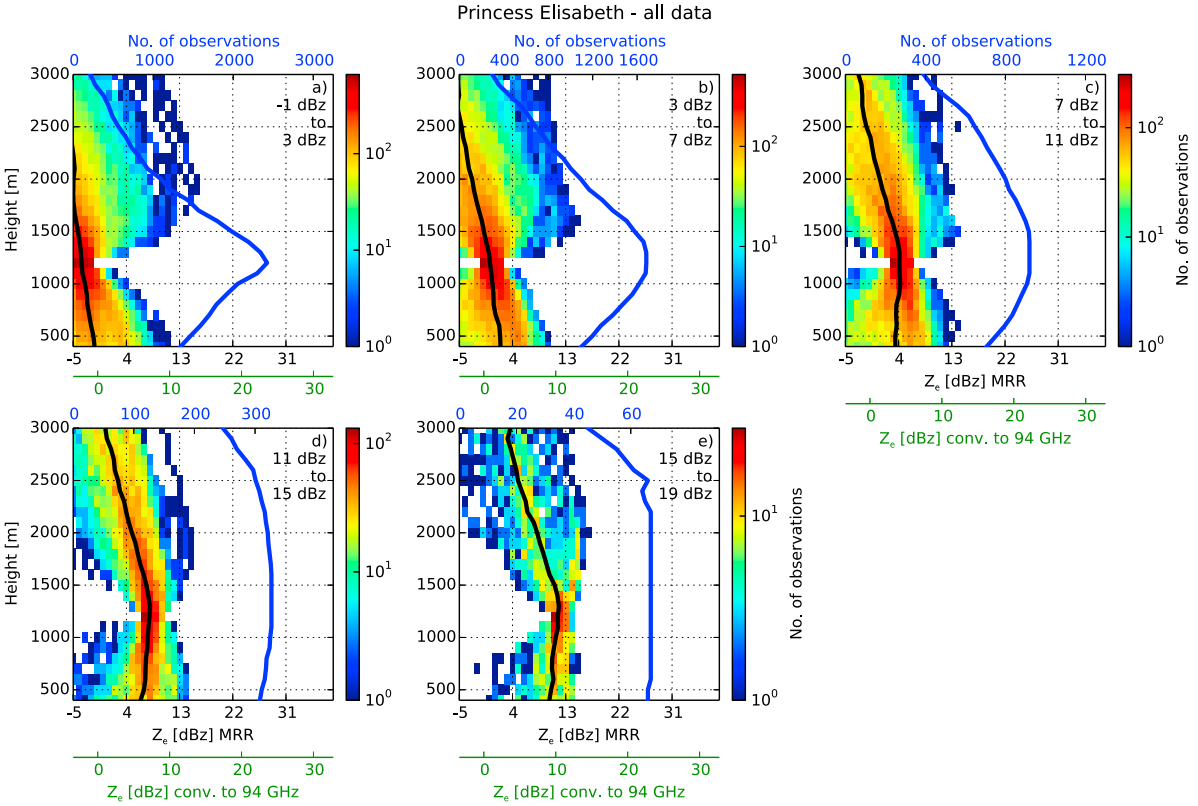

Figure 8. Reflectivity versus altitude 2-D histogram (2-DH) of MRR observations at Princess Elisabeth station, East Antarctica. The presented data set is limited to profiles which are within a certain reflectivity threshold at the CloudSat reference height of 1200 m agl (H_{CS}). (a) Only profiles that are between −1 and 3 dBz at the reference height. (b–e) Limited to reflectivities of −5, 9, 13, and 17±2 dBz, respectively. The median is denoted in black, the total number of observation greater −5 dBz per height in blue. An estimate for the corresponding Z_e at 94 GHz using the coefficients for aggregates is indicated by the additional, green scale.

increase to H_{CS}, a net increase of N occurs at NÅ. In other words, at PE, virga events are more frequent than shallow precipitation (Figure 6a), whereas at NÅ, shallow precipitation occurs more frequently (Figure 7a).

In NÅ, the maximum occurs at H_{FM}, which implies that a reduced blind zone with H_{FM} would lead from an underestimation of N to an overestimation by 17.8%. For PE, the overestimation of N would only slightly change from 5.7% to 8.5%. This deterioration is in contrast to the finding that the statistical representation of Z_e is improved for a lower blind zone (Figures 6c and 7c). Apparently, the combination of virga and shallow precipitation leads to a local maximum of occurrence between H_{FM} and H_{CS}.

While there is a clear tendency toward larger N below H_{CS} for the *wet unstable regime* indicating more frequent shallow precipitation (Figures 6d and 7d), a stronger decrease of snow events can be observed for the *dry stable regime* at both sites (but more pronounced at PE, Figures 6g and 7g). This stronger decrease might be attributable to strong sublimation and virga formation.

5.3. Impact on Individual Snowfall Events

While the previous sections investigated the mean occurrence of snow characteristics, we now highlight the large spread if single events are considered. This procedure is important because the 16 day repeat cycle of CloudSat means that a particular precipitation event is usually only observed once and temporal evolution cannot be measured. For this investigation, we sort the profiles with respect to their Z_e values at H_{CS}; the resulting 2-DH diagrams for the different Z_e intervals at H_{CS} are shown in Figure 8 for PE and Figure 9 for NÅ for the original measurement and also converted to 94 GHz. While events with Z_e of up to 7 dBz at H_{CS} tend to increase toward the surface on average by 0.5 to 3 dB, events with larger Z_e decrease by up to 3 dB. Transferred to a CloudSat observation, this result means that CloudSat would tend to underestimate weaker

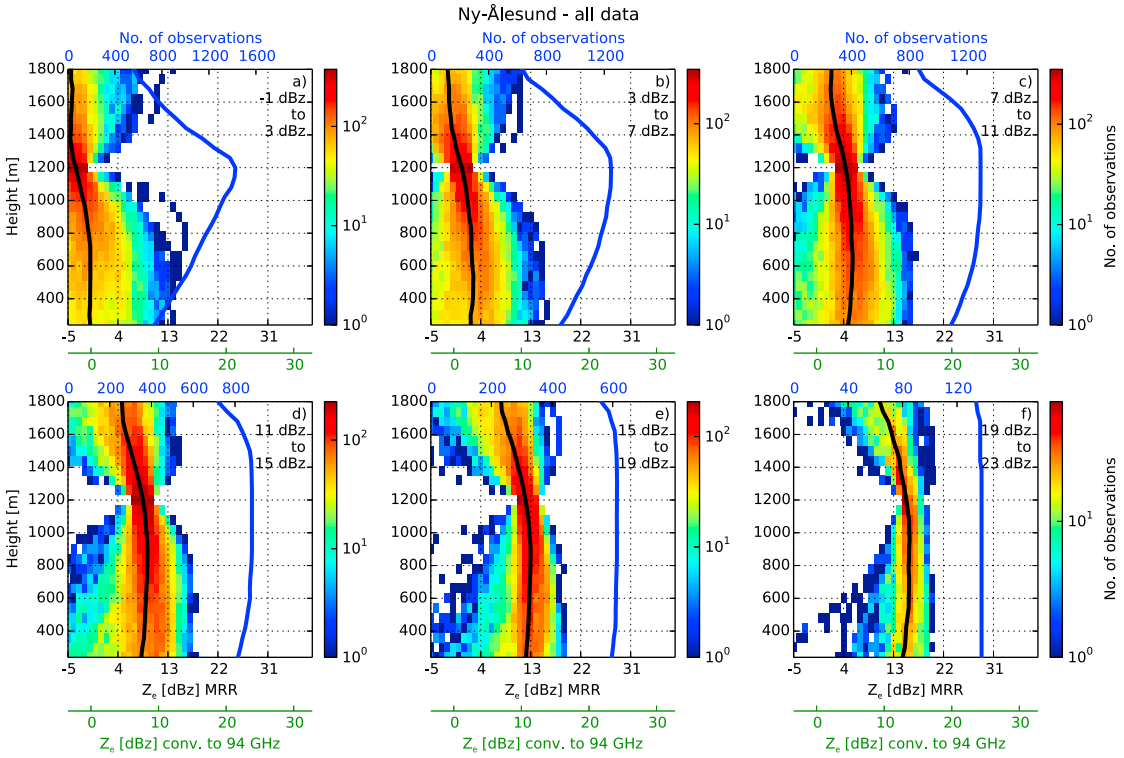

Figure 9. (a–e) Same as Figure 8 but for Ny-Ålesund with (f) an additional panel for the 19 to 23 dBz interval.

precipitation events while it would overestimate stronger events. This finding also holds for LY, and the corresponding plot can be found in the supporting information (Figure S2).

While for lower Z_e up to 3 dBz, this finding is consistent with our findings in section 5.1, for higher Z_e, an analysis of the DQQ plots revealed a shift of the Z_e distribution to higher reflectivities at H_{CS} in comparison to at H_{SF} (Figures 6c and 7c). This result highlights the vertical inhomogeneity of precipitation events at a single time step, and it can be also seen in the large spread of observations at H_{SF} for a single Z_e interval being larger for NÅ than for PE.

5.4. Impact on the Total Mass Flux

The hydrological cycle is driven by the flux of precipitation to the surface. To investigate the impact of the blind zone on mass flux, Figure 10 presents an estimation of the snowfall rate profile for PE and NÅ. The figure reveals how the different reflectivity values contribute to the total precipitation as a function of height using the Z_e-S relation for *snow* presented in section 3.3. The total liquid equivalent snowfall amount of the 12 month data set derived from MRR is roughly 200 mm at PE and 320 mm in NÅ, although uncertainty of the absolute values is large due to the application of the Z_e-S relation. Hence, we normalized the precipitation amount at every height with respect to the total precipitation amount at H_{SF}, resulting in a reduced sensitivity of the precipitation amount profile to uncertainties in the Z_e-S relation.

The vertical changes of Z_e are a combination of changes in the reflectivity distribution (section 5.1) and the variation of N with height (section 5.2). In general, events with reflectivities between 0 and 10 dBz (corresponding to 0.2 and 0.7 mm/h, respectively, using the Z_e-S relation for snow) contribute most to the total precipitation amount at PE (Figure 10a), underlining the need for a high radar sensitivity. This finding is in agreement with the results from *Kulie and Bennartz* [2009], who found that most precipitation in the northern periphery of Antarctica originates from precipitation rates of 0.2 to 1 mm/h and indicates that our data set is typical for Antarctica. Events with reflectivities larger than 15 dBz are so rare that they hardly contribute to the total precipitation amount. The contribution of the various classes of reflectivity is different for

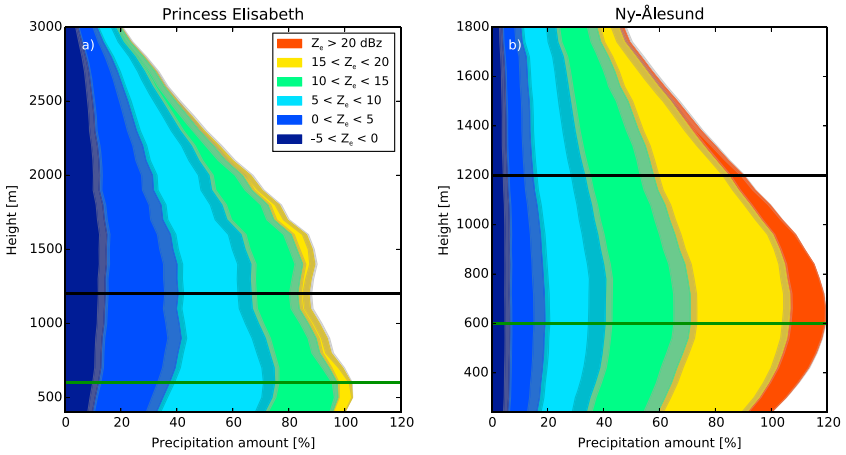

Figure 10. Contribution of various reflectivity intervals to the total precipitation amount in dependence on height for (a) Princess Elisabeth and (b) Ny-Ålesund. For the colored areas, the Z_e-S relation by *Kulie and Bennartz* [2009] for snow is used. Uncertainty of the borders between the different intervals due to the Z_e-S relations is estimated by the gray, shaded area, which is estimated by applying also Z_e-S relations for *three bullet rosettes* and *aggregates* by *Kulie and Bennartz* [2009]. The figures are normalized by total surface precipitation. CloudSat's blind zone of 1200 m agl (H_{CS}) and a reduced blind zone of 600 m agl (H_{FM}) are denoted by black and green lines, respectively.

NÅ (Figure 10b): most precipitation originates from events with reflectivities between 15 and 20 dBz, which is related to the, on average, warmer and moister climate in Svalbard.

The vertical development of the different reflectivity classes shows how behavior is different for NÅ and PE. For PE, the contribution of the 0 to 5 dBz interval and the 10 to 15 dBz interval changes little for the height between H_{CS} and H_{SF}. The contribution of the 5 to 10 dBz interval, however, increases toward the surface. At PE, the total mass flux at H_{CS} is underestimated by 11 percentage points of total precipitation in comparison to H_{SF}. At H_{FM}, this changes to an overestimation of 3 percentage points, but uncertainty is high because, for PE, observations below 400 m are not available and the further development toward the ground is unknown.

In NÅ, the contribution of the three intervals between 5 and 20 dBz is even more similar at H_{CS} and H_{SF}. For the range between H_{CS} and H_{SF}, however, all reflectivity intervals larger than 5 dBz contribute more to the total precipitation than at H_{CS} and H_{SF}. Apparently, omission and commission errors are competing but cancel out each other close to the surface. This result would also mean that a future satellite-based radar mission with a smaller blind zone would not improve the estimation of the total mass flux. Instead, at least for NÅ, total mass flux would be overestimated by 19 percentage points—in comparison to 9 percentage points underestimation at H_{CS}. The results are similar for LY (see Figure S3 in the supporting information) and prove that the belly shaped distribution is not a local effect.

These results are robust as demonstrated by using again the two other Z_e-S relations introduced in section 3.3 to estimate the uncertainty. As can be seen from Figure 10, applying a different Z_e-S relation has only a minor effect on the results and does not change the overall shape of the distribution. Even if the Z_e-S relation changes with height, the impact on the total precipitation distribution is less than 5%.

6. Summary and Conclusion

The impact of CloudSat's blind zone below 1200 m agl (H_{CS}) on snowfall statistics was investigated for three polar sites, the Belgian Princess Elisabeth station (PE) in East Antarctica and for Ny-Ålesund (NÅ) and Longyearbyen (LY, see supporting information for results) in Svalbard, Norway (Figure 1). To investigate the impact on a future satellite mission with a reduced blind zone, a blind zone of 600 m agl (H_{FM}) was also considered.

We used a ground-based Micro Rain Radar and compared with the lowest clutter-free CloudSat observation height H_{CS} (Figure 4). The MRR was found suitable because differences due to the different footprint

and temporal resolution were found to be less than the uncertainty caused by the applied Z_e-S relation. Consequently, we investigated the blind zone effects by comparing MRR observations at H_{CS} with MRR observations near surface (H_{SF}), assuming that MRR observations are representative of CloudSat observations. To our knowledge, the 12 month MRR data sets from NÅ and LY are the first precipitation radar observations available for Svalbard. The MRR at PE is currently the only ground-based precipitation radar in Antarctica.

The frequency distribution of MRR reflectivity changes between H_{CS} and H_{SF}. For PE (Figure 6c), the distribution of Z_e is shifted by up to 2.5 dB toward smaller values if measured at H_{CS}. For NÅ (Figure 7c), the shift is much smaller and below 1 dB. A reduction of the blind zone by 50% leads to a reduction of the offset by more than a factor of 2 for PE, and in NÅ the remaining shift is negligible.

The better agreement due to a reduction of the blind zone cannot be seen when analyzing the total number of observations N (Figures 6a and 7a): at H_{CS}, N is overestimated by 5.7% and underestimated by 5.2% for PE and NÅ, respectively. At H_{FM}, this result changes to overestimations of N of 8.5 and 17.8%. This change is more strongly pronounced at NÅ and most likely due to competing processes: virga and shallow precipitation.

Based on temperature inversion and relative humidity, the data set was divided into two regimes: the *dry stable* and the *wet unstable regime*, with the latter representing 73% and 59% of all precipitation events at PE and NÅ, respectively. For the *dry stable regime*, the overestimation of N at H_{CS} and H_{FM} is most pronounced and Z_e decreases toward the ground, i.e., virga effects dominate, as might be expected due to increased sublimation. For the *wet unstable regime*, agreement of N at the different levels is better. This indicates that for these regimes, which are more related to the influence of synoptic disturbances, the profiles are on average slightly more constant in the vertical. This classification might be exploited for mitigation strategies.

Agreement of observations between H_{CS} and H_{SF} is less when single events are considered (Figures 8 and 9) because precipitation intensity strongly varies with height due to the fall velocity of ice particles and due to advection effects. Hence, low-precipitation intensity gets generally enhanced and high-precipitation intensity becomes generally weaker.

The change in both N and Z_e contributes to the estimation of precipitation amount (Figure 10). For NÅ, the belly shape of N can be also seen in the total precipitation amount: at H_{CS}, total precipitation is underestimated by 9 percentage points, while at H_{FM}, it would be overestimated by 19 percentage points, which is mainly driven by events with $Z_e > 15$ dBz. For PE, such a belly shape cannot be clearly seen, but the underestimation of total precipitation of 11 percentage points at H_{CS} still changes to an overestimation of 3 percentage points at H_{FM} showing that virga and shallow precipitation effects are also partly overlapping at PE.

In general, our results are only valid for the vicinity around the station. However, due to the spatial homogeneity of surface properties in East Antarctica, we expect our findings to be representative of a much larger area. For Svalbard, orography is much more complex, limiting the spatial representativeness of this study. Because results for an identical setup in LY, located 110 km southeast of NÅ, are comparable (see supporting information), we are nevertheless confident that our results are representative at least for the western region of Svalbard.

In summary, shallow precipitation and virga effects are found to compete and lead to a change in the number of observed events and total mass flux of 9 to 11 percentage points, although the statistical distribution of Z_e changes only little. While the statistical agreement is enhanced with a potentially lower blind zone altitude, the difference in the number of observed events and total mass flux increases. Hence, a reduced blind zone would not improve snowfall observations in all aspects.

For the future, more radar observations would allow further investigation of this issue, also in other regions. Since heavy snowfall events are rare but contribute strongly to the total precipitation, longer time series are needed. The question of how total precipitation translates into snow accumulation at the surface is complex [*Gorodetskaya et al.*, 2014a, 2014b] and needs to be studied in more detail in the future. The MRR comprises a low-cost, low-maintenance alternative to more complex systems and has been successfully operated at PE during the unmanned winter period. It thus offers potential for investigating snowfall in other polar regions. Special care should be taken to configure the radar with a lower minimum

observation height, allowing observations as close to the surface as possible. Also, the use of a radar with a higher sensitivity is desirable so that the impact of the blind zone on events with reflectivities below −5 dBz can be investigated. For this, data from the North Slope of Alaska site of the Atmospheric Radiation Measurement Program in Barrow [*Mather and Voyles*, 2012], from the Summit Station in Greenland [*Shupe et al.*, 2013] or from the Zugspitze in the German Alps [*Löhnert et al.*, 2011], as well as possibly from other sites, could be used for future studies.

Acknowledgments

Part of this work was carried out under the HYDRANT project (http://ees.kuleuven.be/hydrant/) financed by the Belgian Science Policy (EA/01/04AB). MRR data are freely available upon request via the project website (PE) and from the corresponding author M. Maahn (NÅ, LY). CloudSat data were obtained from the CloudSat Data Processing Center (http://www.cloudsat.cira.colostate.edu). The authors would like to thank the International Polar Foundation for logistical support in Antarctica and the staff at the Princess Elisabeth station for supporting this project. We also thank Alexander Mangold (Belgian Royal Meteorological Institute) for help with the instrument maintenance on site. The field work in Svalbard was funded by the European Centre for Arctic Environmental Research (ARCFAC) under research grant ID2009-146 and by the German Academic Exchange Service (DAAD). The MRR in Ny-Ålesund was courtesy of Clemens Simmer, University of Bonn, and was kindly supervised by the team of the Sverdrup Station of the Norwegian Polar Institute. The MRR in Longyearbyen was courtesy of Chris Kidd, NASA Goddard, and was kindly supervised by Fred Sigernes, Niklas Gantert, and Benjamin Merkel (all University Centre in Svalbard). M. Maahn was supported by the project ADMIRARI II of the German Research Association (DFG, LO901/5-1). S. Lhermitte was funded as postdoctoral researcher and K. Van Tricht as aspirant by Fonds Wetenschappelijk Onderzoek-Vlaanderen. The work carried out by S. Kneifel was supported by the German Academic Exchange Service (DAAD), and I. Gorodetskaya was funded by the Belgian Science Policy (EA/01/04AB). The authors would like to thank the three anonymous reviewers for their valuable and constructive comments.

References

Boening, C., M. Lebsock, F. Landerer, and G. Stephens (2012), Snowfall-driven mass change on the East Antarctic ice sheet, *Geophys. Res. Lett.*, *39*, L21501, doi:10.1029/2012GL053316.

Campbell, J. R., and M. Shiobara (2008), Glaciation of a mixed-phase boundary layer cloud at a coastal arctic site as depicted in continuous lidar measurements, *Polar Sci.*, *2*(2), 121–127, doi:10.1016/j.polar.2008.04.004.

Clough, S. A., and R. A. A. Franks (1991), The evaporation of frontal and other stratiform precipitation, *Q. J. R. Meteorol. Soc.*, *117*(501), 1057–1080, doi:10.1002/qj.49711750109.

Donovan, D. P., H. W. Barker, R. J. Hogan, T. Wehr, M. Eisinger, D. Lajas, and A. Lefebvre (2013), Scientific aspects of the Earth clouds, aerosols, and radiation explorer (EarthCARE) mission, in *AIP Conference Proceedings*, vol. 1531, pp. 444–447, AIP, Melville, New York, doi:10.1063/1.4804802.

Durden, S., S. Tanelli, and G. Dobrowalski (2011a), CloudSat W-band radar measurements of surface backscatter, *IEEE Geosci. Remote Sens. Lett.*, *8*(3), 401–405, doi:10.1109/LGRS.2010.2079314.

Durden, S. L., et al. (2011b), *A Cloud and Precipitation Radar System Concept for the ACE Mission*, Jet Propulsion Laboratory, National Aeronautics and Space Administration, Pasadena, Calif., Vancouver, Canada.

Evans, E., R. E. Stewart, W. Henson, and K. Saunders (2011), On precipitation and virga over three locations during the 1999–2004 Canadian prairie drought, *Atmos. Ocean*, *49*(4), 366–379, doi:10.1080/07055900.2011.608343.

Fabry, F., and I. Zawadzki (1995), Long-term radar observations of the melting layer of precipitation and their interpretation, *J. Atmos. Sci.*, *52*(7), 838–851, doi:10.1175/1520-0469(1995)052<0838:LTROOT>2.0.CO;2.

Førland, E. J., R. Benestad, I. Hanssen-Bauer, J. E. Haugen, and T. E. Skaugen (2012), Temperature and precipitation development at Svalbard 1900–2100, *Adv. Meteorol.*, *2011*, 893790, doi:10.1155/2011/893790.

Gammelsrød, T., and B. Rudels (1983), Hydrographic and current measurements in the Fram Strait, August 1981, *Polar Res.*, *1*(2), 115–126, doi:10.1111/j.1751-8369.1983.tb00696.x.

Gelsthorpe, R. V., A. Heliere, A. Lefebvre, J. Lemanczyk, E. Mateu, A. Perez-Albinana, and K. Wallace (2010), Aspects of the EarthCARE satellite and its payload, in *Proc. SPIE 7826, Sensors, Systems, and Next-Generation Satellites XIV, 78260G (October 13, 2010)*, vol. 7826, pp. 78,260G–78,260G–11, SPIE, Bellingham.

Gorodetskaya, I. V., N. P. M. Van Lipzig, M. R. Van den Broeke, A. Mangold, W. Boot, and C. H. Reijmer (2013), Meteorological regimes and accumulation patterns at Utsteinen, Dronning Maud Land, East Antarctica: Analysis of two contrasting years, *J. Geophys. Res. Atmos.*, *118*, 1700–1715, doi:10.1002/jgrd.50177.

Gorodetskaya, I. V., S. Kneifel, M. Maahn, K. Van Tricht, J. H. Schween, S. Crewell, and N. P. M. Van Lipzig (2014a), Cloud and precipitation properties from ground-based remote sensing instruments in East Antarctica, *Cryosphere Discuss.*, *8*(4), 4195–4241, doi:10.5194/tcd-8-4195-2014.

Gorodetskaya, I. V., M. Tsukernik, K. Claes, M. F. Ralph, W. D. Neff, and N. P. M. Van Lipzig (2014b), The role of atmospheric rivers in anomalous snow accumulation in East Antarctica, *Geophys. Res. Lett.*, *41*, 6199–6206, doi:10.1002/2014GL060881.

Henson, W., R. Stewart, and D. Hudak (2011), Vertical reflectivity profiles of precipitation over Iqaluit, Nunavut during autumn 2007, *Atmos. Res.*, *99*, 217–229, doi:10.1016/j.atmosres.2010.10.009.

Hiley, M. J., M. S. Kulie, and R. Bennartz (2011), Uncertainty analysis for CloudSat snowfall retrievals, *J. Appl. Meteorol. Climatol.*, *50*(2), 399–418, doi:10.1175/2010JAMC2505.1.

Hou, A. Y., R. K. Kakar, S. Neeck, A. A. Azarbarzin, C. D. Kummerow, M. Kojima, R. Oki, K. Nakamura, and T. Iguchi (2014), The global precipitation measurement mission, *Bull. Am. Meteorol. Soc.*, *95*(5), 701–722, doi:10.1175/BAMS-D-13-00164.1.

Joe, P., et al. (2010), The polar precipitation measurement mission, *Proc. 6th European Conference on Radar Meteorology and Hydrology: Satellite Radar Measurements and Hydro-meteorological applications, Sibiu, Romania*, 6–10.

Klugmann, D., K. Heinsohn, and H.-J. Kirtzel (1996), A low cost 24 GHz FM-CW Doppler radar rain profiler, *Contrib. Atmos. Phys.*, *69*(1), 247–253.

Kneifel, S., M. Maahn, G. Peters, and C. Simmer (2011), Observation of snowfall with a low-power FM-CW K-band radar (Micro Rain Radar), *Meteorol. Atmos. Phys.*, *113*(1-2), 75–87, doi:10.1007/s00703-011-0142-z.

Kneifel, S., S. Redl, E. Orlandi, U. Löhnert, M. P. Cadeddu, D. D. Turner, and M.-T. Chen (2014), Absorption properties of supercooled liquid water between 31 and 225 GHz: Evaluation of absorption models using ground-based observations, *J. Appl. Meteorol. Climatol.*, *53*(4), 1028–1045, doi:10.1175/JAMC-D-13-0214.1.

Knuth, S. L., G. J. Tripoli, J. E. Thom, and G. A. Weidner (2010), The influence of blowing snow and precipitation on snow depth change across the Ross Ice Shelf and Ross Sea regions of Antarctica, *J. Appl. Meteorol. Climatol.*, *49*(6), 1306–1321, doi:10.1175/2010JAMC2245.1.

Kulie, M. S., and R. Bennartz (2009), Utilizing spaceborne radars to retrieve dry snowfall, *J. Appl. Meteorol. Climatol.*, *48*(12), 2564–2580, doi:10.1175/2009JAMC2193.1.

L'Ecuyer, T. S., and J. H. Jiang (2010), Touring the atmosphere aboard the A-Train, *Phys. Today*, *63*(7), 36–41, doi:10.1063/1.3463626.

Lenaerts, J. T. M., M. R. van den Broeke, W. J. van de Berg, E. van Meijgaard, and P. Kuipers Munneke (2012), A new, high-resolution surface mass balance map of Antarctica (1979–2010) based on regional atmospheric climate modeling, *Geophys. Res. Lett.*, *39*, L04501, doi:10.1029/2011GL050713.

Levizzani, V., S. Laviola, and E. Cattani (2011), Detection and measurement of snowfall from space, *Remote Sens.*, *3*(1), 145–166, doi:10.3390/rs3010145.

Liu, G. (2008a), Deriving snow cloud characteristics from CloudSat observations, *J. Geophys. Res.*, *113*, D00A09, doi:10.1029/2007JD009766.

Liu, G. (2008b), A database of microwave single-scattering properties for nonspherical ice particles, *Bull. Am. Meteorol. Soc.*, *89*(10), 1563–1570, doi:10.1175/2008BAMS2486.1.

Löffler-Mang, M., and J. Joss (2000), An optical disdrometer for measuring size and velocity of hydrometeors, *J. Atmos. Oceanic Technol.*, *17*(2), 130–139, doi:10.1175/1520-0426(2000)017<0130:AODFMS>2.0.CO;2.
Löhnert, U., S. Kneifel, A. Battaglia, M. Hagen, L. Hirsch, and S. Crewell (2011), A multisensor approach toward a better understanding of snowfall microphysics: The TOSCA project, *Bull. Am. Meteorol. Soc.*, *92*(5), 613–628, doi:10.1175/2010BAMS2909.1.
Maahn, M., and P. Kollias (2012), Improved Micro Rain Radar snow measurements using Doppler spectra post-processing, *Atmos. Meas. Tech.*, *5*(11), 2661–2673, doi:10.5194/amt-5-2661-2012.
Mace, G. G. (2006), Level 2 GEOPROF product process description and interface control document. [Available at http://www.cloudsat.cira.colostate.edu/ICD/2B-GEOPROF/2B-GEOPROF_PDICD_5.3.doc, Accessed 23 May 2014.]
Marchand, R., G. G. Mace, T. Ackerman, and G. Stephens (2008), Hydrometeor detection using *CloudSat*—An Earth-orbiting 94-GHz cloud radar, *J. Atmos. Oceanic Technol.*, *25*(4), 519–533, doi:10.1175/2007JTECHA1006.1.
Mather, J. H., and J. W. Voyles (2012), The ARM climate research facility: A review of structure and capabilities, *Bull. Am. Meteorol. Soc.*, *94*(3), 377–392, doi:10.1175/BAMS-D-11-00218.1.
Matrosov, S. Y. (2007), Modeling backscatter properties of snowfall at millimeter wavelengths, *J. Atmos. Sci.*, *64*(5), 1727–1736, doi:10.1175/JAS3904.1.
Matrosov, S. Y., and A. Battaglia (2009), Influence of multiple scattering on CloudSat measurements in snow: A model study, *Geophys. Res. Lett.*, *36*, L12806, doi:10.1029/2009GL038704.
Noone, D., J. Turner, and R. Mulvaney (1999), Atmospheric signals and characteristics of accumulation in Dronning Maud Land, Antarctica, *J. Geophys. Res.*, *104*(D16), 19,191–19,211, doi:10.1029/1999JD900376.
Palerme, C., J. E. Kay, C. Genthon, T. L'Ecuyer, N. B. Wood, and C. Claud (2014), How much snow falls on the Antarctic ice sheet?, *The Cryosphere*, *8*, 1577–1587, doi:10.5194/tc-8-1577-2014.
Peters, G., B. Fischer, and T. Andersson (2002), Rain observations with a vertically looking Micro Rain Radar (MRR), *Boreal Environ. Res.*, *7*(4), 353–362.
Peters, G., B. Fischer, H. Münster, M. Clemens, and A. Wagner (2005), Profiles of raindrop size distributions as retrieved by Microrain Radars, *J. Appl. Meteorol.*, *44*(12), 1930–1949, doi:10.1175/JAM2316.1.
Protat, A., D. Bouniol, J. Delano, E. O'Connor, P. T. May, A. Plana-Fattori, A. Hasson, U. Görsdorf, and A. J. Heymsfield (2009), Assessment of CloudSat reflectivity measurements and ice cloud properties using ground-based and airborne cloud radar observations, *J. Atmos. Oceanic Technol.*, *26*(9), 1717–1741, doi:10.1175/2009JTECHA1246.1.
Protat, A., J. Delano, E. J. O'Connor, and T. S. L'Ecuyer (2010), The evaluation of CloudSat and CALIPSO ice microphysical products using ground-based cloud radar and lidar observations, *J. Atmos. Oceanic Technol.*, *27*(5), 793–810, doi:10.1175/2009JTECHA1397.1.
Schlosser, E., K. W. Manning, J. G. Powers, M. G. Duda, G. Birnbaum, and K. Fujita (2010), Characteristics of high-precipitation events in Dronning Maud Land, Antarctica, *J. Geophys. Res.*, *115*, D14107, doi:10.1029/2009JD013410.
Schneider, U., A. Becker, P. Finger, A. Meyer-Christoffer, M. Ziese, and B. Rudolf (2014), GPCC's new land surface precipitation climatology based on quality-controlled in situ data and its role in quantifying the global water cycle, *Theor. Appl. Climatol.*, *115*(1-2), 15–40, doi:10.1007/s00704-013-0860-x.
Serreze, M. C., F. Carse, R. G. Barry, and J. C. Rogers (1997), Icelandic low cyclone activity: Climatological features, linkages with the NAO, and relationships with recent changes in the Northern Hemisphere circulation, *J. Clim.*, *10*(3), 453–464, doi:10.1175/1520-0442(1997)010<0453:ILCACF>2.0.CO;2.
Shupe, M. D., et al. (2013), High and dry: New observations of tropospheric and cloud properties above the Greenland Ice Sheet, *Bull. Am. Meteorol. Soc.*, *94*(2), 169–186, doi:10.1175/BAMS-D-11-00249.1.
Smalley, M., T. L'Ecuyer, M. Lebsock, and J. Haynes (2014), A comparison of precipitation occurrence from the NCEP stage IV QPE product and the CloudSat cloud profiling radar, *J. Hydrometeorol.*, *15*(1), 444–458, doi:10.1175/JHM-D-13-048.1.
Stark, D., B. A. Colle, and S. E. Yuter (2013), Observed microphysical evolution for two East Coast winter storms and the associated snow bands, *Mon. Weather Rev.*, *141*(6), 2037–2057, doi:10.1175/MWR-D-12-00276.1.
Stephens, G. L., et al. (2008), CloudSat mission: Performance and early science after the first year of operation, *J. Geophys. Res.*, *113*, D00A18, doi:10.1029/2008JD009982.
Stewart, R. E., J. E. Burford, D. R. Hudak, B. Currie, B. Kochtubajda, P. Rodriguez, and J. Liu (2004), Weather systems occurring over Fort Simpson, Northwest Territories, Canada, during three seasons of 1998–1999: 2. Precipitation features, *J. Geophys. Res.*, *109*, D22109, doi:10.1029/2004JD004929.
Tanelli, S., S. Durden, E. Im, K. Pak, D. Reinke, P. Partain, J. Haynes, and R. Marchand (2008), CloudSat's cloud profiling radar after two years in orbit: Performance, calibration, and processing, *IEEE Trans. Geosci. Remote Sens.*, *46*(11), 3560–3573, doi:10.1109/TGRS.2008.2002030.
Thode, H. C. (2002), *Testing for Normality*, Marcel Dekker, New York.
Tridon, F., J. Van Baelen, and Y. Pointin (2011), Aliasing in micro rain radar data due to strong vertical winds, *Geophys. Res. Lett.*, *38*, L02804, doi:10.1029/2010GL046018.
Tsukernik, M., D. N. Kindig, and M. C. Serreze (2007), Characteristics of winter cyclone activity in the northern North Atlantic: Insights from observations and regional modeling, *J. Geophys. Res.*, *112*, D03101, doi:10.1029/2006JD007184.
Wang, Z., K. Sassen, D. N. Whiteman, and B. B. Demoz (2004), Studying altocumulus with ice virga using ground-based active and passive remote sensors, *J. Appl. Meteorol.*, *43*(3), 449–460, doi:10.1175/1520-0450(2004)043<0449:SAWIVU>2.0.CO;2.
Wolfe, J. P., and J. R. Snider (2012), A relationship between reflectivity and snow rate for a high-altitude S-band radar, *J. Appl. Meteorol. Climatol.*, *51*(6), 1111–1128, doi:10.1175/JAMC-D-11-0112.1.
Wood, N. B. (2011), Estimation of snow microphysical properties with application to millimeter-wavelength radar retrievals for snowfall rate, PhD thesis, Colo. State Univ., Fort Collins. [Available at http://digitool.library.colostate.edu/R/?func=dbin-jump-full™amp;object_id=123397, Accessed 23 May 2014.]
Wood, N. B., T. S. L'Ecuyer, D. G. Vane, G. L. Stephens, and P. Partain (2013), Level 2C snow profile process description and interface control document. [Available at http://www.cloudsat.cira.colostate.edu/ICD/2C-SNOW-PROFILE/2C-SNOW-PROFILE_PDICD_P_R04.pdf, Accessed 23 Mai 2014.]
Xiao, J., R. Bintanja, S. J. Dry, G. W. Mann, and P. A. Taylor (2000), An intercomparison among four models of blowing snow, *Boundary Layer Meteorol.*, *97*(1), 109–135, doi:10.1023/A:1002795531073.
Yang, D., E. Elomaa, A. Tuominen, A. Aaltonen, B. Goodison, T. Gunther, V. Golubev, B. Sevruk, H. Madsen, and J. Milkovic (1999), Wind-induced precipitation undercatch of the Hellmann gauges, *Nordic hydrol.*, *30*(1), 57–80.

Additional Figures for the data obtained from March 2010 until March 2011 in Longyearbyen, Svalbard, Norway are presented here. The setup of the instruments was identical to the setup in Ny-Ålesund.

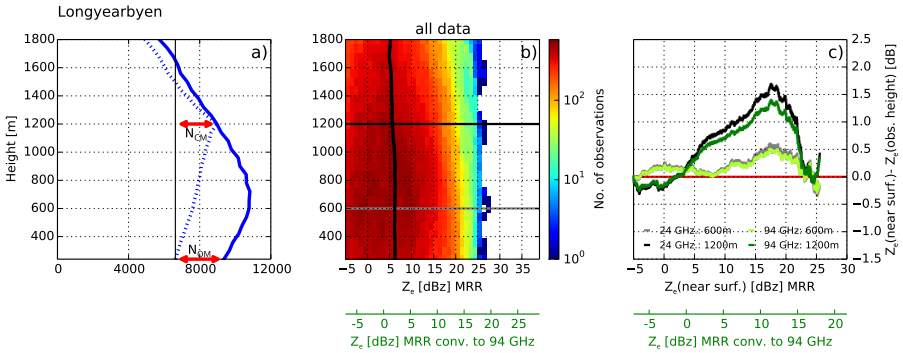

Figure S.1: Same as Figures 6.a-c of Publication III, but for Longyearbyen. The classification into different regimes was not applied to Longyearbyen.

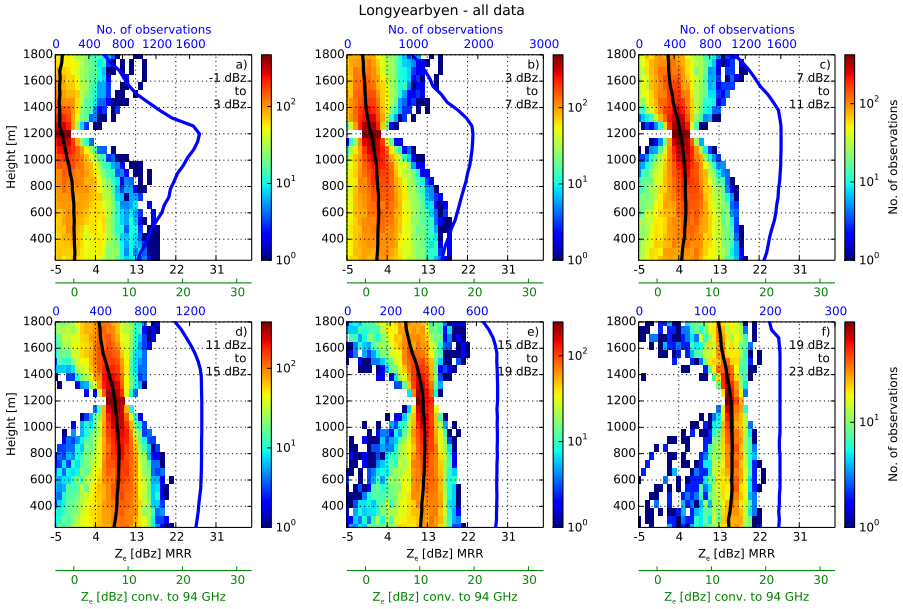

Figure S.2: Same as Figure 8 of Publication III, but for Longyearbyen.

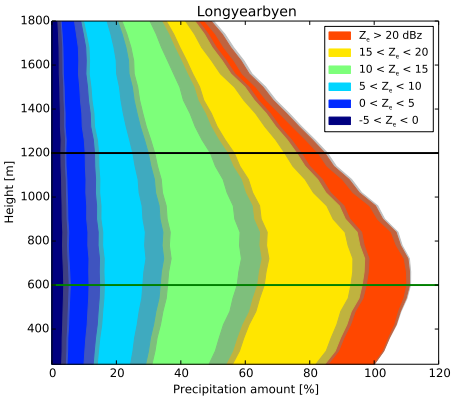

Figure S.3: Same as Figure 10 of Publication III, but for Longyearbyen.

Part C

KEY ISSUE II: EXPLOITING HIGHER MOMENTS

6

ADDITIONAL STUDY I: SPECTRAL RADAR SIMULATOR

This chapter introduces the PAMTRA (Passive and Active Microwave TRAnsfer) forward model for simulating passive and active microwave observations. The model is used in Publication III and in Additional Study II.

A detailed publication about PAMTRA is in preparation (Mech et al., 2015).

6.1 INTRODUCTION

During research, development and operation of microwave instruments such as radiometers or radars, forward models are required for sensitivity studies, maximizing the instrument's performance and to build retrievals to relate the measured quantities to the meteorological quantities of interest such as cloud properties.

PAMTRA is a FORTRAN90 model framework for the simulation of microwave observations in a plane-parallel, one-dimensional, and horizontally homogeneous atmosphere. In contrast to other models which are either designed for passive observations (e. g., *Czekala and Simmer*, 1998; *Saunders et al.*, 1999; *Rosenkranz*, 2002; *Eriksson et al.*, 2011) or active observations (e. g., *Capsoni et al.*, 2001; *Caumont et al.*, 2006; *Haynes et al.*, 2007; *Pfeifer et al.*, 2008; *Kollias et al.*, 2011), PAMTRA is able to simulate passive and active instruments including radar Doppler Spectra without beeing tailored to a specific mission (e. g., *Masunaga et al.*, 2010; *Bodas-Salcedo et al.*, 2011; *Hashino et al.*, 2013; *Matsui et al.*, 2013). Up- and down-welling radiation can be simulated at any height of the atmosphere and at any observation angle. PAMTRA has a modular structure combining modules by various authors in a consistent framework.

In the following, the model structure is presented with particular focus on the parts developed by the author, i. e., radar simulator and pyPAMTRA.

6.2 MODEL STRUCTURE

The overall modular structure of PAMTRA is summarized in Figure 8. PAMTRA needs several types of input data. First, the different hydrometeor species need to be defined with respect to phase, scattering properties, size distribution, discrete size bins, and—for the radar simulator—fall velocity model.

For each species, profiles of hydrometeor properties are needed. For forward simulations of in situ observations or NWP models with

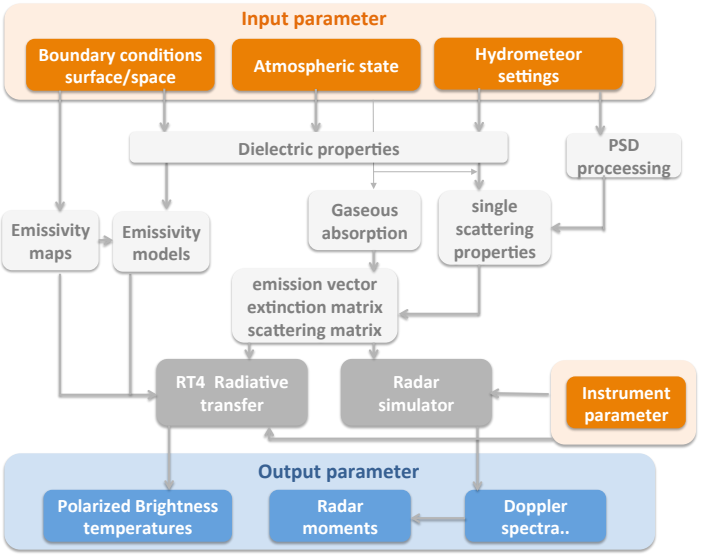

Figure 8: Flowchart of the steps performed during a PAMTRA simulation. Reddish areas describe input parameters given by the user, while the blue boxes are the model output (Figure courtesy of S. Crewell).

full bin micro-physics, the full $N(D)$ and—for ice—$m(D)$ as well as $A(D)$ can be provided. For coupling of NWP models with bulk microphysical schemes, it is possible to provide up to two moments of the particle size distribution, such as total particle number concentration (n_{tot}), effective radius (r_{eff}) or hydrometeor content (e. g., IWC). Then, the user can choose between different parameterizations for $N(D)$ e. g., (modified) gamma, exponential or log-normal distribution. In addition, atmospheric profiles of temperature T, pressure p and humidity q are needed. If the passive radiative transfer is used, additional assumptions about the surface type are required as well. The radar simulator needs a set of instrument specifications such as noise level or Nyquist interval.

In the following, the methodology to simulate radar and radiometer observations from hydrometeor profiles is briefly explained.

6.2.1 *Single scattering properties*

Single scattering properties such as scattering, extinction and emission are estimated for each hydrometeor species and for each discrete particle size bin separately. PAMTRA can be used for both, liquid and frozen hydrometeors. Partly melted particles (i. e. the melting layer) are currently not supported. Mie theory (*Mie*, 1908) is used to estimate the single scattering properties of liquid hydrometeors like cloud droplets, drizzle, or rain drops for each size bin. The user can chose between different models from *Ellison* (2007), *Liebe et al.*

(1991, 1993) and *Stogryn et al.* (1995) to estimate the refractive index of liquid water. While they agree for temperatures $> 0°C$, recent studies showed for the modeled refractive index of SCLW large differences. (*Cadeddu and Turner*, 2011; *Kneifel et al.*, 2014). A model consistent with observations for the whole range of microwave frequencies has yet to be found.

Due to the large variability in shape and density, estimating the scattering properties for frozen particles is more complex in PAMTRA. Frozen particles are modeled as "soft spheres" (*Marshall and Gunn*, 1952; *Liu*, 2004) which are spheres or spheroids composed of an ice-air mixture using the refractive index of pure ice estimated by *Warren and Brandt* (2008) and the mixing formula by *Garnett* (1904). The effective particle density ρ of the soft spheres is derived from the maximum dimension D, the aspect ratio AR and the particle mass m (*Bennartz and Petty*, 2001; *Petty*, 2001). Scattering properties are then estimated from T-Matrix Theory (*Mishchenko*, 2000) or—in case of AR equal to 1—Mie theory. Because the T-Matrix method is relatively expensive, scattering results can be cashed in a file-based database. While the soft sphere approach works reasonably well for particles smaller than the wavelength λ, this method becomes increasingly unable to consistently predict snow scattering properties affecting calculations for both, passive (e. g., *Petty and Huang*, 2010) and active instruments (e. g. *Kneifel*, 2011; *Leinonen et al.*, 2012). For the future, the inclusion of scattering databases (*Liu*, 2008b; *Petty and Huang*, 2010; *Tyynelä et al.*, 2011, 2014) is planned to describe the scattering properties of large ice particles more realistically.

6.2.2 *Gaseous Absorption*

Absorption by gases in the microwave range can be separated into contributions by lines and the continuum of atmospheric gases. In PAMTRA, they are either described by the Rosenkranz 98 model (*Rosenkranz*, 1998) with modifications proposed by *Turner et al.* (2009) and *Liljegren et al.* (2005) or by the MPM93 model developed by (*Liebe et al.*, 1993)

6.2.3 *Radar simulator*

After multiplying the single scattering properties of each hydrometeor species with the particle size distribution $N(D)$, the effective radar reflectivity factor Z_e can be obtained by integrating the backscattering cross sections over the whole size spectrum (e. g., like in QuickBeam, *Haynes et al.*, 2007). Z_e can be either non-polarized, HH (horizontal receive, horizontal transmit), or VV (vertical receive, vertical transmit) which allows also estimation of differential reflectivity $ZDR = Z_e^{HH}/Z_e^{VV}$. However, the full radar Doppler spectrum has to

A comprehensive version for liquid hydrometeors is available as McGill Radar Doppler Spectra Simulator (MRDSS) at http://www.clouds.mcgill.ca/Research/code_download_mrdss.htm.

be simulated if higher moments or the spectrum itself are of interest. The radar Doppler spectra simulator included in PAMTRA is based on the work of *Kollias et al.* (2011, 2013) and has been extended for polarized radiation and to treat not only liquid but also ice particles. The basic working principle is explained in the following.

To convert the back-scattering cross section $\sigma_B(D)$ of the individual particles in m^2 to the volumetric back-scattering in the unit of spectral radar reflectivity $mm^6m^{-3}m^{-1}$, several constants need to be applied to obtain the spectral reflectivity η_D:

$$\eta_D(D) = 10^{18}\sigma_B(D)\, N(D)\frac{\lambda^4}{\pi^5|K_w^2|} \tag{21}$$

where λ is the wavelength in m, $N(D)$ is the particle size distribution in m^{-4} and $|K_w^2|$ is the dielectric factor of water related to the refractive index. Similar to most cloud and precipitation radars, the refractive index values for liquid water at centimeter wavelengths are used ($|K^2| = 0.93$, *Ulaby et al.*, 1986) regardless of whether ice or liquid clouds are observed.

Attenuated $\eta_D(D)$ is obtained by subtracting the path integrated attenuation, which is estimated from extinction of gases and hydrometeors depending on measurement geometry (ground-based, airborne or space-based)

Because a Doppler spectrum is described as a function of velocity instead of particle size, the size descriptor of the spectral radar reflectivity η_D is changed from D to fall velocity v with

$$\eta_v(v) = \eta_D(D)\frac{\partial D}{\partial v} \tag{22}$$

To obtain the fall velocity v and $\frac{\partial D}{\partial v}$ depending on particle habit, the relation by *Heymsfield and Westbrook* (2010) is used for ice and snow particles, which accounts for particle shape by using particle size, mass, and area in addition to environmental conditions such as air density, temperature and pressure as input. For liquid drops, the relation provided by *Khvorostyanov and Curry* (2002) is used instead. For PAMTRA, v is defined such that positive values refer to particles falling towards the surface.

In addition to the particle fall velocities, vertical air motion V can be added to the velocity spectrum $\eta_v(v)$. V can be either fixed or described by a function (step, linear). $\eta_v(v)$ has a velocity resolution specified by the bin spacing of the particle size distribution. However, radar Doppler spectra have velocity boundaries v_{nyq} (Equation 14) and velocity resolution that is determined by the number of FFT points n_{fft} in the radar Doppler spectrum. These parameters are adjustable in the radar Doppler spectra simulator. $\eta_v(v)$ of all hydrometeors is then linearly interpolated onto the spectral resolution of the simulated radar. Furthermore, if the fall velocity (with or without air motion component) exceeds v_{nyq}, the simulator adds velocity folding effects.

The next step is to add the radar receiver noise power N_P (in units of mm^6/m^3 to be in accordance with Z_e) to the spectrum. To account for the decrease of radar sensitivity due to range, the noise level is artificially increased with range R

$$N_P = N_{1000} \cdot (R/1000)^2 \tag{23}$$

where R is range in meters and N_{1000} is the radar receiver noise power at $R = 1000$ m which is estimated either from the radar parameters or by fitting Equation 23 to radar receiver noise measurements at different ranges. Depending on the stability of the radar components, these parameters might change with time. Because the noise level is equally distributed to the complete spectrum (white noise), noise per spectral bin N_i is estimated with

$$N_i = \frac{N_P}{n_{fft} \cdot \Delta v} \tag{24}$$

where Δv is the Doppler spectrum bin resolution.

Kinematic broadening is assumed to have a Gaussian distribution with standard deviation σ_k, which is convoluted with $\eta_v(v)$ to simulate the broadening of the Doppler Spectrum (*Gossard and Strauch*, 1989). σ_k is the sum of several components (*Doviak and Zrnic*, 1993; *Shupe et al.*, 2008b):

$$\sigma_k^2 = \sigma_w^2 + \sigma_s^2 + \sigma_t^2 \tag{25}$$

where σ_w^2 is the variance due to the finite radar beam width, σ_s^2 is the beam broadening term due to contribution of wind shear, and σ_t^2 is the variance due to turbulence within the radar sampling volume. σ_w^2 and σ_s^2 can be estimated from the wind field (*Sloss and Atlas*, 1968; *Doviak and Zrnic*, 1993; *Nastrom*, 1997)

Wind shear of the horizontal wind is neglected here, see e. g., Shupe et al. (2008b).

$$\sigma_w^2 = U^2\theta^2/2.76 \tag{26}$$

$$\sigma_s^2 = k_v^2(\Delta R)^2/12 \tag{27}$$

with U is the horizontal wind, θ is the half-power half-width one-way radar beam width, k_v is the wind shear of the vertical wind V, and ΔR is the vertical radar resolution. σ_t^2 depends mostly on the Eddy dissipation rate ϵ

$$\sigma_t^2 = \int_{k_\lambda}^{k_s} a'\epsilon^{2/3}k^{-5/3}\,dk = \frac{3a'}{2}\left(\frac{\epsilon}{2\pi}\right)^{2/3}\left(L_s^{2/3} - L_\lambda^{2/3}\right) \tag{28}$$

where k is the wavenumber, a' is the Kolmogorov constant (chosen as 0.5 according to *Sreenivasan*, 1995), $L_\lambda = \lambda/2$ is the smallest length scale and L_s is the largest length scale observed by the radar. The latter is defined by

$$L_s = Ut + 2R\sin(\theta) \tag{29}$$

with t the observation time and R is the range. ϵ can be estimated in situ, but can also be obtained from radar observations (*Bouniol et al.*, 2003; *O'Connor et al.*, 2005; *Shupe et al.*, 2008b).

Finally, random perturbations are added to every bin i of the spectrum in order to account for random noise effects

$$\eta_{v,N}(i) = -\log(r(i)) \cdot (\eta_v(i) + N_i) \tag{30}$$

where $r(i)$ is a randomly distributed number between 0 and 1 (*Zrnić*, 1975). On the one hand, simulations by the radar simulator should be reproducible, on the other hand the perturbation applied to every spectrum should be different for each simulated profile to avoid artifacts in the statistics. In order to allow both applications, the random seed can be specified by the user. To account for temporal averaging, the spectrum is successively averaged n_{ave} times.

The moments of the simulated Doppler spectrum are estimated similar to a real radar data processing scheme (Publication I): firstly, the noise is removed from the spectrum, secondly the moments of the most significant peak, defined as peak containing the bin with the greatest power, are determined. The only difference to a real radar data processing scheme is that the noise N_i is known already in advance and does not need to be estimated e. g., using *Hildebrand and Sekhon* (1974). Besides the standard moments reflectivity Z_e, mean Doppler velocity W and Doppler spectrum width σ, PAMTRA estimates also the higher moments skewness Sk and kurtosis Ku as well as the left and the right slope of the spectrum (S_l and S_r) as proposed by *Kollias et al.* (2007a) and used by *Kollias et al.* (2011) and in Publication III. In addition, the left and right edges of the peak are provided. All radar observables are available non-polarized as well as for HH and VV polarizations.

6.2.4 *Radiative transfer for passive simulations*

PAMTRA can also simulate measurements of passive microwave radiometers. This part is based on the RT4 code provided by *Evans and Stephens* (1995b) which enables the user to perform polarized radiative transfer calculations for non-spherical and oriented particles. The earth's surface has to be taken into account as the lower boundary and can be modeled in PAMTRA either by an Lambertian or a Fresnel surface (e. g., *Mätzler*, 2006). The former is used for estimating the surface emissivity based on a database of angle and frequency dependent monthly mean emissivity values obtained from *Special Sensor Microwave Imager* (SSM/I) measurements (*Prigent et al.*, 1997). The latter is used for ocean surface together with a correction developed by *Liu et al.* (2011) to account for sea waves, parameterized as a function of the surface wind.

6.2.5 *pyPAMTRA*

pyPAMTRA adds a Python framework around the FORTRAN core which allows it to call PAMTRA directly from Python excluding the FORTRAN I/O routines. Consequently, pyPAMTRA is a more user-friendly way to access the PAMTRA model. It includes a collection of supporting routines, e. g., for importing model data or plotting. By pyPAMTRA, a local parallel execution of PAMTRA on multiprocessor computer systems is possible. Support for high-performance computer clusters such as the *Cologne High Efficient Operating Platform for Science* (CHEOPS) is provided by a client-server model. The server splits the PAMTRA input field into small chunks which are processed by the clients running on CHEOPS. When finished, the clients send back their results to the server for merging and further processing.

6.3 CONCLUSIONS

In this section, the microwave forward model PAMTRA was introduced. It is a radiative transfer model framework for the simulation of the one-dimensional radiative transfer in a plane-parallel atmosphere for passive and active applications. Unlike other models, active and passive observations by satellite, airborne, or ground-based instruments can be simulated with the same model. It is prepared for coupling with bulk and full-bin NWP models (see *Mech et al.*, 2014, for example applications), but can also be run using aircraft in-situ observations (see Publication III) and for retrieval development (see Additional Study I). Consequently, PAMTRA can be used in the future for several applications e. g., model evaluation, future instruments design or retrieval development. The modular design makes implementation of additional features simple, e. g., the integration of single scattering databases (*Liu*, 2008b; *Petty and Huang*, 2010; *Tyynelä et al.*, 2011, 2014) is planned for the future. This will improve the estimation of scattering properties, in particular for particles greater than the instrument wavelength. An extensive description of PAMTRA is in preparation (*Mech et al.*, 2015) and it is planned to release the source code of PAMTRA under an open source license.

7

PUBLICATION III: ICE CLOUD PARAMETERIZATIONS

DEVELOPING AND EVALUATING ICE CLOUD PARAMETERIZATIONS FOR FORWARD MODELING OF RADAR MOMENTS USING IN SITU AIRCRAFT OBSERVATIONS

Maahn, M., Löhnert, U., Kollias, P., Jackson, R. C., and McFarquhar, G. M. (2015). Developing and Evaluating Ice Cloud Parameterizations for Forward Modeling of Radar Moments Using In Situ Aircraft Observations. *Journal of Atmospheric and Oceanic Technology*, accepted.

Developing and Evaluating Ice Cloud Parameterizations for Forward Modeling of Radar Moments Using In Situ Aircraft Observations

MAXIMILIAN MAAHN AND ULRICH LÖHNERT

Institute for Geophysics and Meteorology, University of Cologne, Germany

PAVLOS KOLLIAS

Department of Atmospheric and Oceanic Sciences, McGill University, Montreal, Quebec, Canada

ROBERT C. JACKSON AND GREG M. MCFARQUHAR

Department of Atmospheric Sciences, University of Illinois at Urbana-Champaign, USA

SUBMITTED TO JOURNAL OF ATMOSPHERIC AND OCEANIC TECHNOLOGY

June 2014. Revised November 2014 and February 2015. Accepted February 2015

ABSTRACT

Observing ice clouds using zenith pointing millimeter cloud radars is challenging, because the transfer functions relating the observables to meteorological quantities are not uniquely defined. Here, we use a spectral radar simulator to develop a consistent data set containing particle mass, area and size distribution as functions of size. This is an essential prerequisite for radar sensitivity studies and retrieval development. The data are obtained from aircraft in situ, and ground-based radar observations during the Indirect and Semi-Direct Aerosol Campaign (ISDAC) campaign in Alaska. The two main results of this study are: 1) An improved method to estimate the particle mass–size relation as a function of temperature is developed and successfully evaluated by combining aircraft in situ and radar observations. The method relies on a functional relation between reflectivity and Doppler velocity. 2) The impact on the Doppler spectrum by replacing measurements of particle area and size distribution by recent analytical expressions is investigated. For this, higher order moments such as skewness and kurtosis as well as the slopes of the Doppler spectrum are also used as a proxy for the Doppler spectrum. For the area–size relation, it is found that a power law is not sufficient to describe particle area and small deviations from a power law are essential for obtaining consistent higher moments. For particle size distributions, the normalization approach for the gamma distribution of Testud et al. (2001), adapted to maximum diameter as size descriptor, is preferred.

1. Introduction

Ice clouds are ubiquitous throughout the Earth's atmosphere and play a key role in Earth's climate system (Waliser et al. 2009). Ice clouds influence the Earth's radiative budget, contribute to the dehydration of the upper atmosphere and are crucial for the global hydrological cycle (Curry et al. 1996; Morrison et al. 2012). At the same time, they present one of the largest uncertainties in general circulation models, because many of the processes of ice clouds are poorly understood, occur at sub-grid scale and observational constraints are limited (e. g., Zhang et al. 2005). Due to their ability to penetrate optically thick clouds and to detect even thin cirrus clouds, *cloud radars* have been increasingly used to study ice cloud microphysics (e. g., Brown et al. 1995; Benedetti et al. 2003; Matrosov et al. 2002).

One of the main challenges to measure ice clouds by remote sensing is that the transfer functions which relate the observables (e. g., radar Doppler spectrum) to cloud properties (e. g., ice water content IWC) are not uniquely defined (Szyrmer et al. 2012). To overcome this challenge, this study has two main objectives: 1) estimate a mass–size relation $m(D)$ from a combination of in situ and radar observations and 2) investigate the effect of describing particle area A and number concentration N as functions of size D on moments of the radar Doppler spectrum. Both parts together result in a consistent set of equations to describe $m(D)$, $A(D)$ and $N(D)$ for simulating the radar Doppler spectrum. Such a set of equations is an essential

prerequisite for sensitivity studies and the development of radar retrievals exploiting radar moments.

The first objective is investigated in this study, because $m(D)$ introduces one of the greatest uncertainties when relating remote sensing observables to meteorological quantities. At the same time, $m(D)$ is particularly difficult to measure in situ. It can be obtained by collecting and melting single particles at the ground, but sample sizes are often very small (Magono and Lee 1966; Locatelli and Hobbs 1974; Mitchell et al. 1990). From aircraft, only ice water content *IWC* can be measured directly by probes (Korolev et al. 1998; Noone et al. 1988) and $m(D)$ has to be estimated from closure studies (Brown and Francis 1995; Heymsfield et al. 2004). Another, yet rather indirect possibility is relating projected area (Schmitt and Heymsfield 2010) or particle shape (Jackson et al. 2012) as measured by particle imaging probes to $m(D)$. Most ice cloud retrievals using remote sensing instruments retrieve not $m(D)$, but *IWC* (e. g., Matrosov et al. 2002; Delanoë and Hogan 2008) and often need prior knowledge of $m(D)$ (e. g., Posselt and Mace 2014). In this study, we estimate $m(D)$ as a function of temperature by combining radar observations with aircraft in situ measurements. We use optimal estimation (Rodgers 2000) to find the pair of $m(D)$ coefficients such that the functional relation between effective radar reflectivity factor Z_e and Doppler velocity W observed by radar and forward modeled from in situ data match.

Knowledge of $m(D)$ enables us to investigate the second objective: similar to $m(D)$, $A(D)$ is commonly expressed by a power law. Gamma (Schneider and Stephens 1995) and exponential distributions (Gunn and Marshall 1958) are commonly used to describe $N(D)$ for snow and ice. More recently, Petty and Huang (2011) showed that they can be generalized for all particle size descriptors using the four-parameter modified gamma function. The use of log-normal distributions for describing cirrus clouds has also been described (Tian et al. 2010). The ISDAC data set with measured profiles of $A(D)$ and $N(D)$ allows us to investigate the impact of applying these functions on simulated radar observations. In addition, the sensitivity on assumed minimum and maximum particle size can be evaluated. For this, not only the standard moments Z_e, W and Doppler spectrum width σ are investigated, but also the use of higher moments of the Doppler spectrum, such as skewness (*Sk*, third moment) and kurtosis (*Ku*, fourth moment) together with left slope ("slow" side of the spectrum) and right slope ("fast" side of the spectrum) of the peak (S_l and S_r), is proposed as a proxy for the shape of the radar Doppler spectrum. For the following, we will call *Sk*, *Ku*, S_l and S_r *higher moments* even though the slopes are technically not moments. Consequently, Z_e, W and σ will be called *lower moments*. While the radar spectrum and higher radar moments have been used to estimate liquid water content (Babb et al. 1999) and precipitation rate (Atlas et al. 1973), to separate cloud drops from drizzle (Kollias et al. 2011b) and to locate supercooled liquid water (Shupe et al. 2004; Luke et al. 2010), no studies thus far have investigated the use of higher moments for studying ice clouds, and the radar spectrum has only been used for case studies (Verlinde et al. 2013).

In order to develop the set of parameters to describe $m(D)$, $A(D)$ and $N(D)$, we combined observations of the *MilliMeter wavelength Cloud Radar* (MMCR, Moran et al. 1998) at the *Atmospheric Radiation Measurement* (ARM) site *North Slope of Alaska* in Barrow with in situ aircraft data acquired during the *Indirect and Semi-Direct Aerosol Campaign* (ISDAC, McFarquhar et al. 2011). To convert the in situ observations into higher radar moments, we use the *Passive and Active microwave radiative TRAnsfer* (PAMTRA) radar simulator (Kollias et al. 2011a; Mech et al. 2015).

The observational data set and the radar simulator are described in Sec. 2. The novel method to estimate $m(D)$ is introduced and compared to other methods in Sec. 3. Higher moments are used to evaluate parameterizations of $A(D)$ and $N(D)$ in Sec. 4 and concluding remarks on the optimal set of ice cloud parameterization are provided in Sec. 5. See Appendix C for an overview of the most used abbreviations and symbols.

2. Data Set, Forward Operator, and Instruments

In this section, the ISDAC data set is introduced, and the forward operator PAMTRA is briefly described. In addition, the MMCR radar is presented and it is shown how both data sets are combined.

a. ISDAC

For this study, in situ aircraft data acquired during the *Indirect and Semi-Direct Aerosol Campaign* (ISDAC) campaign in April 2008 (McFarquhar et al. 2011) are used. The ISDAC data set contains observations of mostly stratocumulus ice and mixed-phase clouds featuring temperatures (T) between -40 and 5 °C. It is available at the website of the *US Department of Energy* ARM program (`http://www.arm.gov/campaigns/aaf2008isdac`). Best estimates of ice particle size distribution $N(D)$ and area vs. size $A(D)$—with D defined as the maximum dimension of the particle—are derived from a combination of the *2-D Stereo Probe* (2DS), *2-D Cloud Probe* (2DC), *Cloud Imaging Probe* (CIP), and *2-D Precipitation Probe* (2DP) using the methodology described in Jackson et al. (2012). The 2DC included a modified tip design to mitigate contamination due to shattered artifacts (Korolev et al. 2011, 2013a). The data are corrected for shattering effects using the inter-arrival time method (Field et al. 2006) and using the numbers, sizes and gaps between fragments in a single image (Korolev and Isaac 2005). Although this approach reduces

contributions from artifacts (Lawson 2011), shattered particles still contribute to $N(D)$ for $D < 0.5$ mm (Korolev et al. 2013b; Jackson et al. 2014). Jackson and McFarquhar (2014) showed for the 2DC that shattered particles made contributions of only about 15 to 20% to higher order moments of $N(D)$, such as *IWC* and total area, when probes without modified tips are used. Thus, contributions of shattered artifacts to the moments of the $N(D)$ of the ISDAC in situ data set are expected to be even less. As a consequence, particles with $D < 0.5$ mm are included for all approaches based on moments of $N(D)$, but removed for all least squares based methods to avoid artifacts due to shattering. In this study, ice particles are assumed to be larger than 50 μm, hence, smaller particles are discarded, because the uncertainty in their measured concentrations is high as shown by Jackson et al. (2012) for ISDAC.

Furthermore, the ISDAC data set contains bulk measurements such as T, humidity (q), pressure (p) and *IWC*. Due to technical problems with the Nevzorov and CSI probes associated with electrical interference, *IWC* is derived from a combination of the size distributions measured by the optical array probes and shape distributions from the habit identification scheme of Jackson et al. (2012). Eddy dissipation rate ε, which is a measure of turbulence, was estimated from measurements of the Tropospheric Aircraft Meteorological Data Reports (TAMDAR) system (Moninger et al. 2009). TAMDAR reports $\sqrt[3]{\varepsilon}$ at a low spatio-temporal resolution in only 27 discrete intervals. During ISDAC, ε was—with very few exceptions at very low altitudes—reported as the lowest measurement interval "00" which corresponds to $\sqrt[3]{\varepsilon} < 0.1$ m$^{2/3}$ s^{-1} for both, maximum and mean $\sqrt[3]{\varepsilon}$ within the measurement increment. This highlights the low turbulence conditions during ISDAC around Barrow and consequently, we assume an even lower, constant value of $\sqrt[3]{\varepsilon} = 0.01$ m$^{2/3}$ s^{-1} for the complete data set.

For this study, the integration time is increased from 1 s to 10 s to ensure that the number of detected particles represents a statistically significant sample. The impact of averaging time on the results is discussed in Appendix B3. Only particles classified as ice are considered in this study. In addition, ice particles obtained when more than than 0.01 g m^{-3} liquid water was detected by the King probe are not used in this study, representing 14% of the total data set. Assuming $D = 20$ μm, 0.01 g m^{-3} correspond to roughly -38 dBz which is close to the lowest values observed for Z_e observed in this study (Sec. 4d), so we consider an impact of remaining liquid on the analysis unlikely.

b. PAMTRA Radar Simulator

To convert the ISDAC in situ microphysical measurements into radar observables (forward modeled ISDAC observation are called F-ISDAC hereafter), the *Passive and Active microwave radiative TRAnsfer* (PAMTRA) model, developed at the University of Cologne, is used (Mech et al. 2015). The active part of PAMTRA is based on Kollias et al. (2011a)[1], but modifications to treat the microphysical and scattering properties of ice particles are necessary, as described below.

First, the backscattering cross sections for each size bin are calculated. For this, the T-Matrix method (Mishchenko 2000) is used assuming that the particles can be modeled as horizontally aligned, soft oblate spheroids with an aspect ratio (*AR*) of 0.6 (Hogan et al. 2012) defined as mixtures of ice and air (Petty 2001). To obtain the refractive index of soft spheres from the refractive index of solid ice (estimated using Warren and Brandt 2008), the mixing formula of Maxwell Garnett (1904) is used that depends on the effective particle density which follows from the mass-dimensional relationship and the specified spheroid. Even though databases based on realistic particle shapes using DDA (e. g., Liu 2008; Petty and Huang 2010; Tyynelä et al. 2011) are available, we prefer the T-Matrix method, because the databases publicly available do not cover all needed $A(D)$ and $m(D)$ relations. Several studies showed (e. g., Kneifel et al. 2011; Tyynelä et al. 2011; Hogan et al. 2012) that at 35 GHz, the T-Matrix approximation can be used at least for particles with $D <$ 5-10 mm. For the ISDAC data set, larger particles are rare (see Sec. 4c). The impact of assuming a fixed *AR* of 0.6 is discussed in Appendix B1. As attenuation is expected to be low for snow and ice at 35 GHz (Matrosov 2007), attenuation effects are ignored in this study.

The effective radar reflectivity factor Z_e can be obtained by integrating $\sigma(D) \cdot N(D)$ over D. If, however, higher radar moments need to be modeled, the Doppler spectrum has to be simulated which requires application of a particle fall velocity vs. diameter relationship $v(D)$. $v(D)$ is a function of particle habit and is estimated using the method proposed by Heymsfield and Westbrook (2010) which depends on the particle shape by using D, $m(D)$, and $A(D)$ in addition to environmental conditions such as air density, T and p as input. Here, positive values of v refer to particles which are falling towards the radar.

The contribution of the kinematic broadening to the radar Doppler spectrum is assumed to have a Gaussian distribution with standard deviation σ_k (m s^{-1}), which is convolved with the radar reflectivity spectrum (Gossard and Strauch 1989). σ_k is composed of (Shupe et al. 2008)

$$\sigma_k^2 = \sigma_w^2 + \sigma_s^2 + \sigma_t^2 \quad (1)$$

where σ_w^2 describes the contribution of the horizontal wind field to the radial velocity due to the finite radar beamwidth, σ_s^2 is the broadening term due to shear of

[1] A version of the *McGill Radar Doppler Spectra Simulator* (MRDSS) tuned for liquid particles is available at `http://www.clouds.mcgill.ca/Research/code_download_mrdss.htm`

the vertical wind, and σ_t^2 is the variance due to turbulence within the radar sampling volume. σ_w^2 is estimated by $\sigma_w^2 = U^2\theta^2/2.76$ with U the horizontal wind as measured by the aircraft and θ the half-power half-width one-way radar beam width in radians (Sloss and Atlas 1968; Nastrom 1997) which is 0.155° for the MMCR in Barrow. σ_s^2 is neglected in this study, because is is expected to be smaller than the other terms and gradients of vertical winds are not available from aircraft observations. σ_t^2 depends on the Eddy dissipation rate ε as measured by the aircraft with (Shupe et al. 2008)

$$\sigma_t^2 = \int_{k_\lambda}^{k_s} a' \varepsilon^{2/3} k^{-5/3}\,\mathrm{d}k = \frac{3a'}{2}\left(\frac{\varepsilon}{2\pi}\right)^{2/3}\left(L_s^{2/3} - L_\lambda^{2/3}\right) \tag{2}$$

where k is the wavenumber, a' is the Kolmogorov constant (chosen as 0.5 according to Sreenivasan 1995), $L_\lambda = \lambda/2$ is the smallest length scale and L_s is the largest length scale observed by the radar. The latter is defined by $L_s = Ut + 2z\sin(\theta)$ with t the observation time and z is the height.

Finally, noise is added to the simulated radar Doppler spectrum using the methodology proposed by Zrnić (1975). Then, the spectra are averaged n_{ave} times which reduces the noise variance by $\sqrt{n_{ave}}$. The moments of the simulated Doppler spectrum are estimated similar to a real radar data processing scheme (e. g., Maahn and Kollias 2012): First, the noise is removed from the spectrum, then the moments of the most significant peak, defined as peak containing the bin with the greatest power, are determined.

PAMTRA estimates not only the lower, but also the higher moments: the skewness *Sk* indicates whether the peak has more weight on the left ($Sk < 0$) or right side ($Sk > 0$) (Fig. 1a). The kurtosis *Ku* describes the shape of the peak (Fig. 1b): While *Ku* of a Gaussian is three, values below indicate a more round tip while larger values indicate a pointed tip. In addition to these higher moments, the slopes in dB s m^{-1} are estimated using the position of the left (right) edge of the spectrum, the mean noise power and the position as well as power of the spectral peak (Fig. 1c). In contrast to Z_e, higher moments do not depend on the absolute calibration of the radar. Furthermore, the mean vertical air motion shifts only the Doppler spectrum and W, but does not change the higher moments. Higher moments and the slopes in particular are, however, strongly influenced by atmospheric turbulence and depend on the signal-to-noise ratio of the radar.

c. MMCR

As a reference, the *MilliMeter wavelength Cloud Radar* (MMCR) of the *US Department of Energy ARM* program located in Barrow (71.32°N, 156.62°W, 8 m asl) at the *North Slope of Alaska* (NSA) is used. It is a vertical pointing pulsed radar system with a frequency of 35 GHz ($\lambda = 8.6$ mm) and can detect hydrometeors with Z_e as low as −50 dBz (Moran et al. 1998). For this study, the so called *boundary layer* mode is used (Kollias et al. 2007), since it provides the best sensitivity and the highest Doppler velocity resolution covering a height range up to 6 km with a vertical resolution of 43.7 m. The boundary layer mode uses 10 spectral averages and is available with an effective time resolution of 1.4 s. Protat et al. (2011) found a calibration offset of −9.8 dB through comparisons of MMCR data obtained between March and October 2008 and the CloudSat satellite (Stephens et al. 2008), so the data set is corrected accordingly.

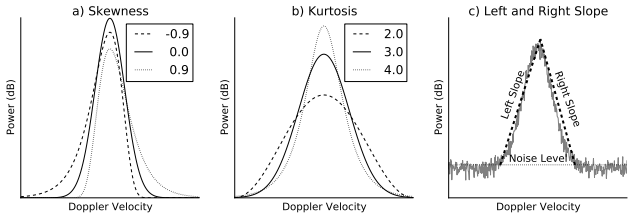

FIG. 1. Examples of idealized radar Doppler spectra for different values of (a) skewness *Sk*, (b) kurtosis *Ku* and (c) left S_l and right slope S_r. Positive values of Doppler velocity refer to particles which are falling towards the radar.

The presence of supercooled liquid water can influence the radar Doppler spectrum (Shupe et al. 2004; Luke et al. 2010). Consequently, observations with a liquid water path measured by a microwave radiometer of more than 0.1 kg m^{-2} are removed (15% of the radar data set). Assuming a cloud depth of 2.5 km, this corresponds to a mean reflectivity due to liquid of −32 dBz which can be neglected, because observations with $Z_e < -30$ dBz were rare during ISDAC (Sec. 4d). To reduce the impact of non-uniform beam filling effects near cloud edges, the MMCR observations at the boundaries of the observed hydrometeor layers are excluded in the analysis.

The synthetic radar Doppler spectra (forward modeled from the in situ measurements) and the MMCR recorded radar Doppler spectra (product *nsammcrspecmomC1*) are post-processed with the same moment estimators to ensure consistency between the two data sources. Ghost peaks in the Doppler spectrum mirrored at 0 m s^{-1}, which occur for high Z_e, are filtered by processing the most significant peak only. To remove rare cases where ghost and real peak are not clearly separated, peaks with the left edge of the peak below −0.5 m s^{-1} are also discarded.

Temperature profiles corresponding to the MMCR observations were obtained using the Merged Sounding product (ARM 1996) which is based on radiosonde observations interpolated with microwave radiometer measurements and model output of the European Centre for Medium Range Weather Forecasts (ECMWF). Data above 0 °C are discarded.

d. Combination of the data sets

Direct comparisons of aircraft and ground-based remote sensing instruments are challenging due to mismatches in time, space and sampling volumes. Thus, MMCR observations and F-ISDAC calculations can only be compared statistically. For this, only aircraft measurements within a radius of 10 km around Barrow are used. The size of the radius is a trade-off between the need for a sufficiently large data set and the requirement to have in situ measurements that are representative for the conditions around the ARM site and capture the small-scale variability (see Appendix B2 for discussion of the 10 km radius). The MMCR data set, in turn, is restricted to observations, where the aircraft was in a horizontal plane closer than 10 km, within 60 s and within an altitude of ±90 m (2 MMCR height bins). After filtering, around 2100 10 s-observations remained in the F-ISDAC data set and around 57200 observations remained in the MMCR data set.

3. Determination of the mass–size relation

No direct measurements of particle mass vs. diameter $m(D)$ are available for ISDAC, only IWC is included in the data set obtained from shape analysis. Thus, we need to estimate $m(D)$, which is the first objective of this study. In this section, a novel approach for determination of the coefficients a and b of the power law mass – size relation $m(D)$

$$m(D) = a \cdot D^b. \tag{3}$$

is presented and compared with other methods by application to the ISDAC data set.

a. Estimating the mass–size relation from the reflectivity–mean Doppler velocity relation

The new method to estimate the mass–size relation $m(D)$ is based on the relation between Z_e and W

$$W = e \cdot Z_e^{\,f} \tag{4}$$

where the coefficients e and f depend on microphysical conditions (Kalesse et al. 2013). Fig. 2 shows that for the MMCR data set, there is a clear correlation between Z_e and W even though there is a high spread. Although vertical air motions also contribute to W, we expect that they do not influence the least squares fit to determine the coefficients e and f and cancel out over time. Extreme outliers are manually removed (see Fig. 2).

All parameters needed to estimate Z_e and W with PAMTRA are contained in the ISDAC data set (see Fig. 3 for flow chart diagram) except for $m(D)$. Consequently, we choose $m(D)$ such that the functional relation between Z_e and W is maintained and e and f of the MMCR observations and F-ISDAC agree. Using $m(D)$ as a closure leads

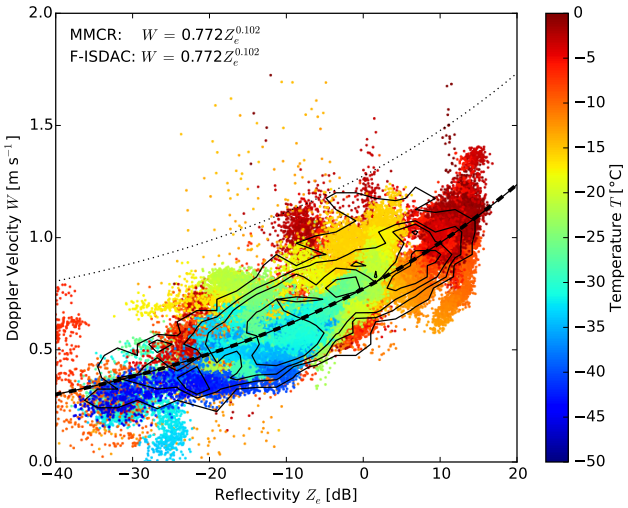

FIG. 2. Z_e vs. W as measured by MMCR with color showing temperature. The dashed line (mostly hidden by solid line) denotes the result of the least squares fit of the radar data. The dotted line is used to remove outliers. The contour plot shows F-ISDAC data for the retrieved $m(D)$ for the full data set and the resulting least squares fit (solid line).

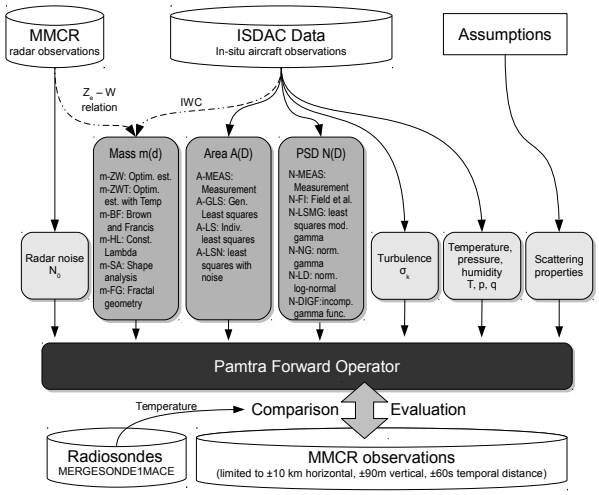

FIG. 3. Schematic overview of the forward modeling of the ISDAC data set and the comparison with MMCR observations.

to the fact that biases of the forward operator and especially the included $v(D)$ relation translate directly into biases of $m(D)$. As an advantage for remote sensing applications, $m(D)$ is estimated from the particle size range being most important most for radar observations (i. e., large particles). In situ observations of IWC are not required.

In order to find the optimal $m(D)$, we make use of the optimal estimation (OE) theory (Rodgers 2000). OE is a simplified Bayesian retrieval technique based on a Gaus-

TABLE 1. Coefficients e and f of the reflectivity – fall velocity ($Z_e - W$) relation (Eq. 4) and retrieved coefficients α, a, and b of the (normalized) mass-size relation $m(D)$ (Eqs. 3 and 10). All quantities are in SI-units, only temperature is in °C and Z_e is in mm^6 m^{-3}.

Temp. range	−40 to 0	−40 to −30	−30 to −25	−25 to −20	−20 to −15	−15 to −10	−10 to −5	−5 to 0
$Z_e - W$: e	0.772	0.680	0.760	0.714	0.820	0.717	0.779	0.883
$Z_e - W$: f	0.102	0.119	0.091	0.096	0.036	0.076	0.129	0.065
$m(D) : \alpha$	0.958	0.568	0.812	0.997	1.282	0.913	0.837	1.195
$m(D) : a$	0.093	0.053	0.042	0.013	0.001	0.020	0.074	0.120
$m(D) : b$	2.228	2.223	2.134	1.933	1.476	2.004	2.215	2.234

sian statistical model of the problem in addition to a priori information to estimate the state vector $\mathbf{x}$ with dimension N from the observation vector $\mathbf{y}$. The updated state vector $\mathbf{x}_{i+1}$ is obtained with

$$\mathbf{x}_{i+1} = \mathbf{x}_a + (\gamma_i \mathbf{S}_a^{-1} + \mathbf{K}_i^T \mathbf{S}_e^{-1} \mathbf{K}_i)^{-1} \mathbf{K}_i \mathbf{S}_e^{-1} \cdot [\mathbf{y} - P(\mathbf{x}_i) + \mathbf{K}_i (\mathbf{x}_i - \mathbf{x}_a)] \quad (5)$$

where $\mathbf{x}_a$ is the a priori assumption for $\mathbf{x}$, $\mathbf{S}_a$ is the a priori uncertainty expressed as the covariance matrix of $\mathbf{x}_a$, $\mathbf{S}_e$ is the uncertainty of $\mathbf{y}$ expressed as the measurement covariance matrix, and $\mathbf{K}_i$ is the Jacobian matrix of the forward model $P(\mathbf{x}_i)$, i. e., $\mathbf{K}_i = (\partial P(x_j)/\partial x_{j'})_{j,j'=1,\ldots,N}$ with x_j the elements of $\mathbf{x}_i$. γ_i is an additional factor following Turner and Löhnert (2014) to put a higher weight on $\mathbf{S}_a$ in the beginning of the retrieval in order to stabilize the retrieval in case of a bad first guess. Similarly, we use decreasing values of 10000, 3000, 1000, 300, 100, 30, 10, 3, 1, 1, ... for γ_i. Due to the Bayesian concept, the uncertainty of the retrieval solution can be easily estimated from the covariance matrix $\mathbf{S}_i$ of the problem

$$\mathbf{S}_i = \mathbf{B}_i^{-1} (\gamma_i^2 \mathbf{S}_a^{-1} + \mathbf{K}_i^T \mathbf{S}_e^{-1} \mathbf{K}_i) \mathbf{B}_i^{-1} \quad (6)$$

where

$$\mathbf{B}_i = (\gamma_i \mathbf{S}_a^{-1} + \mathbf{K}_i^T \mathbf{S}_e^{-1} \mathbf{K}_i). \quad (7)$$

The iteration is started with $\mathbf{x}_1 = \mathbf{x}_a$ and is stopped when $\gamma_i = 1$ and the convergence criteria

$$(\mathbf{x}_i - \mathbf{x}_{i+1})^T \mathbf{S}_i^{-1} (\mathbf{x}_i - \mathbf{x}_{i+1}) \ll N \quad (8)$$

is met.

In this study, the retrieval is not applied to individual profiles, but to the complete data set. Consequently, $\mathbf{y}$ does not consist of radar observables such as Z_e or W, but instead consists of the coefficients e, f of the $Z_e - W$ relation, whereby $\mathbf{x}$ consists of the parameters of the $m(D)$ relation. Thus, parameters of the $m(D)$ relation can be found such that F-ISDAC features a similar $Z_e - W$ relation as the reference MMCR data set. For the forward model P, we use the PAMTRA forward operator which is applied to all ISDAC profiles for every iteration step i. To ensure the stability of the retrieval, it is necessary to include median(Z_e) of the data set as a third variable of $\mathbf{y}$. This ensures that OE does not solve the problem by iterating to very small values of Z_e due to reducing $m(D)$ such that the majority of simulated Z_e observations is below the sensitivity threshold of the MMCR. In this case, the least squares fit of Eq. 4 could be easily solved because only few points would remain.

Eq. 3 depends strongly on changes in b which makes the retrieval unstable and makes convergence difficult to obtain. Hence, we used the normalization approach of Szyrmer et al. (2012); they defined a reference diameter D^* with a corresponding reference mass m^* given by

$$m^* = m(D^*) = a(D^*)^b \quad (9)$$

Together with Eq. 3, this leads to

$$m(D) = m^* (D/D^*)^b = \alpha C_0 (D/D^*)^b. \quad (10)$$

Here, m^* is expressed as an arbitrary reference mass C_0 and a dimensionless factor α. This form has the advantage that $m(D)$ has a less dependence on b if the reference size is representative of the observations. In other words, most of the variability is expressed by α while uncertainties in the estimate of b have little impact on derived particle mass. In accordance with Szyrmer et al. (2012), $D^* = 1.2$ mm and $C_0 = 3 \cdot 10^{-5}$ g are chosen. Hence, the state vector $\mathbf{x}$ of OE is composed of b and $\log_{10}(\alpha)$. The logarithm of α is used to prevent OE from iterating to negative values. OE requires the definition of an a priori value $\mathbf{x}_a$ for $\mathbf{x}$ and the uncertainties expressed as covariance matrices of a priori $\mathbf{S}_a$ and measurements $\mathbf{S}_e$. As a priori values, we chose $b = 2.1$, because it is a typical value for $m(D)$ relations, and $\alpha = 1$, since it corresponds to the m^* value proposed by Szyrmer et al. (2012). $\mathbf{S}_e$ is estimated from the uncertainty derived from the least squares fit to gain the coefficients e and f of the $Z_e - W$ relation, 1 dB is assumed as the variance VAR of median(Z_e), and off-diagonal entries are neglected. For the diagonal of $\mathbf{S}_a$, VAR($\log_{10} \alpha$) = 1.0 and VAR(b) = 0.5 are chosen as estimates for the natural variability, and off-diagonal entries are neglected as well.

Fig. 2 shows that there might be also a dependence of the $Z_e - W$ relation on T (see Table 1 for coefficients). To investigate this, the retrieval is also applied to data sub

sets defined by T intervals between -40 and 0 °C with 5 °C width. Only few observations are available for $T < -30$ °C and thus only one interval from -40 to -30 °C was used.

b. Retrieval results

For the complete data set, OE converges to $b = 2.23 \pm 0.002$ and $\alpha = 0.959 \pm 1.7\text{E-}6$ which corresponds to $a = 0.093 \pm 0.002$ kg m$^{-2.23}$. These are similar to the values found by Mitchell et al. (1990) for *aggregates of side planes* ($a = 0.083$, $b = 2.2$ in SI units). Applied to the F-ISDAC data set, the resulting $Z_e - W$ distribution is presented in Fig. 2 and shows good agreement with the least squares fits between MMCR and F-ISDAC. Note that the retrieval errors are extremely small because 1) any forward model errors are neglected and 2) α and b most likely vary from profile to profile, but only smoothed values are retrieved here. Hence, the values found for α and b might be representative for the entire data set, but their variability from profile to profile is not well represented by the retrieval errors.

The retrieval results for α, b and derived a as a function of T and the corresponding errors (if large enough to be visible) are shown in Fig. 4. The values for α, b and derived a vary with T from 0.57 to 1.28, 1.47 to 2.23 and from 0.001 to 0.120 in SI units, respectively (Table 1). b and a follow an U-shaped curve with values larger than 2.1 for $T < -25$ °C and $T > -10$ °C . We attribute this to the transition of the dominant shape of snow particles from compact, columnar polycrystals typical for cold temperatures, to more fluffy particles, such as aggregated crystals or stellar single crystals, to heavy, rimed particles for $T > -15$ °C (Magono and Lee 1966; Bailey and Hallett 2009). This can be also seen from five examples of $m(D)$ relations from prior studies which are also presented in Fig. 4. Note that the found decrease of a and b can—although to a lesser extent—also be seen in Fig. 12 of Heymsfield et al. (2013) who investigated the temperature dependence of a and b using a much larger data set composed of several campaigns.

While a and b are correlated as expected (e. g., Heymsfield et al. 2010; Szyrmer et al. 2012), α shows a different trend: Generally, α increases with increasing T, but the trend is interrupted by a minimum between -15 °C and -5 °C . Note that α is proportional to the reference effective density ρ^* of a particle with size D^* and mass $m^* = \alpha C_0$ as defined by Szyrmer et al. (2012)

$$\rho^* = \frac{6}{\pi} \alpha C_0 (D^*)^3 (AR)^{-1}. \tag{11}$$

Consequently, we can explain the minimum of α between -15 °C and -5 °C with a minimum of ρ^*. This is most likely related to the occurrence of low density particles such as e. g. stellar crystals. For this particle shape,

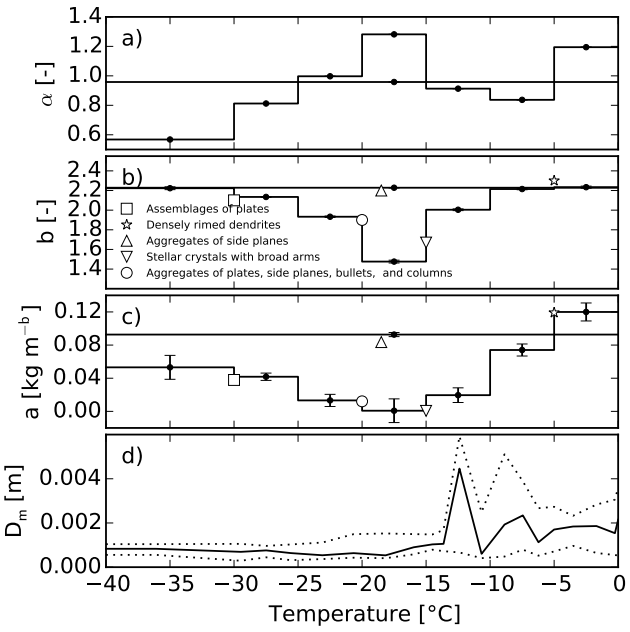

FIG. 4. (a) Retrieved α and (b) b as well as (c) derived a coefficients in dependence on temperature in comparison to (d) the 10, 50 and 90% quantiles of the "mass–weighted" mean diameter D_m (see Sec. 4b) for definition). The retrieval result for α, b and a for the complete data set are marked with a solid, straight line. For comparison, various $m(D)$ relations from literature are presented at arbitrary, but typical temperatures: radiating assemblages of plates (Mitchell et al. 1990), densely rimed dendrites (Locatelli and Hobbs 1974), aggregates of side planes, (Mitchell et al. 1990), stellar crystals with broad arms (Mitchell 1996) and aggregates of unrimed radiating assemblages of plates, side planes, bullets, and columns (Locatelli and Hobbs 1974) which is the $m(D)$ relation used by Brown and Francis (1995) as well.

Mitchell (1996) reported very similar coefficients for a and b (Fig. 4). Ground-based in situ observations found a secondary maximum of aggregation growth at temperatures between -10 and -15 °C (Hobbs et al. 1974; Löhnert et al. 2011) and also laboratory measurements of particle density of idealized ice crystals found a minimum around -15 °C (Fukuta and Takahashi 1999) where the difference in saturation pressure over liquid and over ice is largest (Libbrecht 2005). The larger size of the particles in this interval can be also seen from the median of the "mass–weighted" mean diameter D_m (see Sec. 4b for definition), which has a clear maximum around -14 °C (Fig. 4).

c. Reference methods for determination of $m(D)$

The novel methods based on the $Z_e - W$ relation with and without considering T (called m-ZW and m-ZWT, respectively, hereafter) are compared with various other methods to estimate $m(D)$, which are described below.

The widely used $m(D)$ relationship by Brown and Francis (1995) (m-BF hereafter) expresses m as a function of

the mean particle diameter D_{mean}. Hogan et al. (2012) converted it to a relation in terms of maximum particle dimension D, where (in SI-units)

$$m(D) = 0.0121 \cdot D^{1.9}. \tag{12}$$

Heymsfield et al. (2004) proposed a method (constant Λ m-CL) to estimate the coefficients of the $m(D)$ relation by testing different values for b from 1.7 to 2.7 in increments of 0.05 and estimated the corresponding a by comparison to the measured mean IWC

$$a = \frac{\overline{IWC}}{\overline{\sum N(D) \cdot D^b \Delta D}} \tag{13}$$

where ΔD is the size bin width. In order to find a, b most consistent with the measured IWC, the ratio between measured IWC and IWC estimated from a and b is calculated for every profile. The selected pair of a, b coefficients is the one that demonstrates the least sensitivity on the shape of $N(D)$ which is characterized by the gamma distribution parameter Λ (see Sec. 4b, Eq. 30 for definition). Using this method, the following coefficients (in SI-units) are found for the limited bulk mass data available in ISDAC:

$$m(D) = 0.0428 \cdot D^{2.1} \tag{14}$$

Jackson et al. (2012) estimated $m(D)$ for ISDAC by shape estimation (m-SA). They determined particle type by an automated habit identification scheme and applied the corresponding $m(D)$ relationships (i. e. Brown and Francis 1995; Mitchell 1996) of nine particle habits: spheres, columns, plates, stellars, dendrites, rosettes, budding rosettes, small irregulars, and big irregulars.

Schmitt and Heymsfield (2010) proposed a method based on fractal geometry (m-FG) which makes it possible to derive the exponent of the power law $m(D)$ relation for every profile individually. They found for mid-latitude regions that the exponent of the area–size relation

$$A = c \cdot D^d \tag{15}$$

is related to the exponent of the $m(D)$ relation with $b = 1.25 \cdot d$. In order to obtain the coefficients of the $A(D)$ relation, the least squares fit presented in Sec. 4a is used. After obtaining b, a is chosen in such a way that the measured IWC is conserved similar to Eq. 13, but for every profile individually. This method has the drawback that it is only applicable to profiles where a good fit of Eq. 15 to the observed values can be made. Hence, profiles with less than five size bins with $N(D)\Delta D > 10$ m^{-3} or with an explained variance R^2 below 0.7 are excluded from the analysis.

Based on this method, (Heymsfield et al. 2013) developed temperature T dependent (m-TD) estimates for a and b from 10 different field campaigns obtained in different regions from $-12°$ to $71°$ latitude. They found (converted to SI units)

$$b = 2.31 + 0.0054\,T \tag{16}$$

$$a = 0.0081 e^{0.0131\,T} 10^{2b-3}. \tag{17}$$

d. Comparison to MMCR

To investigate the impact of the various $m(D)$ parameterizations on the radar moments, F-ISDAC is calculated for each method, and compared against MMCR observations with histograms and medians of the radar moments Z_e, W and σ (Fig. 5, columns 1-3). To compare the distributions more quantitatively, we use the Kolmogorov – Smirnov statistic (d_α) (Massey 1951). Lower values indicate better agreement with $d_\alpha = 0$ for samples originating from equal distributions. Note that we use d_α only as a degree of agreement and not to test whether the two underlying probability distributions differ. Here and for all following comparisons, the MMCR data set is also restricted to periods where the F-ISDAC data are available (i. e., where$N(D)\Delta D > 10$ m^{-3} and $R^2 > 0.7$). Consequently, the size of the MMCR data set is different for each comparison.

The new methods m-ZW and m-ZWT of finding the coefficients of the $m(D)$ relation based on the $Z_e - W$ relation lead to a high agreement of MMCR and F-ISDAC observations. Since only Z_e and W are used to derive the coefficients of the $m(D)$ relation, agreement of σ is as an independent test, because Z_e, W and σ depend all differently and nonlinearly on $m(D)$. This and the good agreement to reported values of a and b, leads to the conclusions that uncertainties in the forward model or vertical air motion do not contribute to the bias in the retrieved a and b coefficients. For m-ZWT, d_α is smaller than 0.09 for all moments. The offset of Z_e is -1.9 dB, which is within the uncertainty range of Z_e, given the large calibration offset of the MMCR of -9.8 dB found by Protat et al. (2011). For the retrieval without considering temperature m-ZW, agreement for Z_e decreases to -2.7 dB and the offset for σ increases significantly from 0.002 to 0.02. As a consequence, it is concluded that one $m(D)$ relation is not sufficient for forward modeling the complete data set and variability due to temperature has to be accounted for. Z_e of MMCR shows a bi-modal distribution and the larger peak around 10 dBz cannot be fully reproduced by F-ISDAC when using m-ZWT. A reason for that could be the reduced accuracy of the T-Matrix approach for larger particles leading to decreased backscattering. Some studies suggested also that the exponent of the $m(D)$ relation is different for larger particles (e. g., Matrosov 2007; Mitchell 1996). This, however, cannot be investigated with the given data set.

Z_e is correlated to W and σ and it is investigated in Fig. 5 (columns 4-5) whether this functional relationship

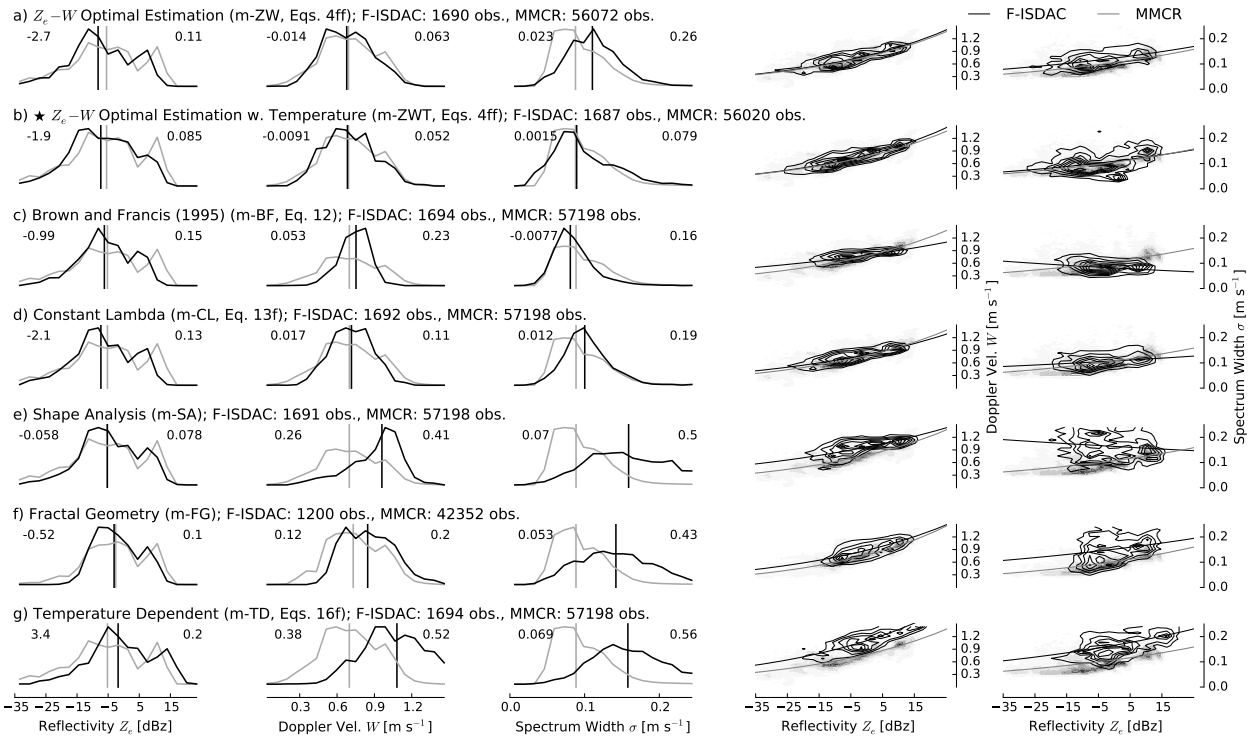

FIG. 5. Normalized 1-D (columns 1–3) and 2-D (columns 4–5) histograms of radar moments (columns) effective reflectivity factor Z_e, Doppler velocity W and spectrum width σ of MMCR observations (gray lines (1-D) and filled contour plot (2-D), respectively) and forward modeled ISDAC observations (F-ISDAC, black lines (1-D) and contour plot with lines (2-D), respectively) for miscellaneous mass parameterizations presented in Sec. 3 (rows). $N(D)$ and $A(D)$ of the particles are taken from measurements. For each data set, the number of cases is given. For 1-D plots, the vertical lines denote the median of the distributions, the difference between both medians is denoted in the upper left corner and the Kolmogorov – Smirnov statistic d_α is presented in the upper right corner of each panel. For 2-D plots, a least squares power fit is shown for MMCR (gray) and F-ISDAC (black).

can be reproduced by F-ISDAC. For m-ZW and m-ZWT it can be seen that we can reproduce the $Z_e - W$ relation, which is the basis for the retrieval used. In addition, the $Z_e - \sigma$ relation—which follows a similar power law—is reproduced with less difference for Z-ZWT compared to Z-ZW. Similar to the 1-D histogram for σ, this is an important closure indicating that the derived $m(D)$ is consistent with the observations.

Comparison to the reference methods for $m(D)$ reveals that the other methods cannot reproduce the MMCR observations as well as m-ZWT. Even though the comparison of 1-D histograms reveals only minor offsets for m-BF (Fig. 5c), comparison of the $Z_e - \sigma$ relation shows that σ is negatively correlated to Z_e instead of positively (Fig. 5c, last column). The performance of m-CL is similar to m-ZWT with respect to the functional relations and to the offsets (Fig. 5d), but d_α is larger for all moments. Even though agreement of Z_e is almost perfect for m-SA, the other moments are highly biased for m-SA (Fig. 5e). Similarly, m-FG and m-TD lead to relatively large offsets for W and σ (Fig. 5f,g). Note that the methods m-CL and m-FG depend on IWC which had to be partly recovered from the m-SA method (Jackson et al. 2012) due to technical problems. Hence, the performance of m-CL and m-FG might be better for other campaigns with higher quality IWC measurements.

The fact that all methods for $m(D)$ are able to reproduce Z_e distributions very similar to the MMCR data set, even though some show offsets for W and even stronger for σ, underlines that investigation of Z_e alone is not sufficient to evaluate $m(D)$ relations. The results for m-BF show that even separate investigation of W and σ is not sufficient and the functional relationships among Z_e, W and σ have to be investigated as well.

4. Evaluating parameterizations for projected area and particle size distribution using higher moments

With the novel method for $m(D)$, the ISDAC data set contains all variables required by PAMTRA. In this section, the impact of replacing measurements of $A(D)$ and

$N(D)$ by corresponding parameterizations is evaluated using lower and higher moments of the Doppler spectrum (see Fig. 3 for schematic overview). Finally, the impact of truncation effects is investigated.

a. Methods to parametrize projected area

Particle area is usually parametrized using an exponential law (e. g., Mitchell 1996) as shown in Eq. 15. The uncertainty of measured $A(D)$ follows from the uncertainty of the total cross section area of all measured particles $A_{\text{tot}}(D) = A(D) \cdot N_{\text{true}}(D)$, which is described with $1/\sqrt{N(D)_{\text{true}}}$ (Hallett 2003) where $N(D)_{\text{true}}$ is the number of particles detected by the cloud probe not normalized by measurement volume and size bin width at a certain D.

First, a least squares fit is applied to the complete data set to estimate the coefficients of Eq. 15 (A-GLS). In order to avoid biases due to shattering effects on the probe tips, only particles larger than 0.5 mm are taken into account. The derived $A(D)$ relation is (in SI-units)

$$A = 0.282 \cdot D^{1.949} \tag{18}$$

Second, the least squares fit is applied to every profile of the data set individually (A-LS), with the uncertainty of $A(D)$ still considered. Particles smaller than 0.5 mm and size bins where $N(D)\Delta D < 10\ \text{m}^{-3}$ are excluded from the fit. Profiles are completely discarded if R^2 of fit and observations is less than 0.7.

The fall velocity relation of Heymsfield and Westbrook (2010) used by PAMTRA depends on both m and A. If both relations are expressed by power laws in terms of D, the degrees of freedom of the fall velocity relation is reduced by one. In order to investigate whether this has any impact on the forward operator, random noise is added to the result of Eq. 15 as a third method (A-LSN)

$$A = c \cdot D^d \cdot 10^{r(D)} \tag{19}$$

where r is a random number dependent on particle size. For every profile, different random numbers are applied. r follows a Gaussian distribution with mean value of 0 and a spread derived from the standard deviation of $\log_{10}(A(D)_{\text{fitted}}/A(D)_{\text{measured}})$. As already discussed, shattering effects can occur for particles smaller than 0.5 mm. Consequently, for this part, the mean of the standard deviation for $D > 0.5$ mm is used. Values of the standard deviation vary between 0.08 and 0.51 with a mean value of 0.24.

b. Methods to parametrize particle size distribution

Similar to the area, the particle size distribution $N(D)$ is a direct measurement of the in situ probes. Hence, a reference is available to investigate the performance of the various methods. The uncertainty of the measurement of $N(D)$ is estimated with $1/\sqrt{N_{\text{true}}}$ (Hallett 2003).

Most of the formulas used to describe $N(D)$ can be related to the modified gamma distribution, which is usually expressed with

$$N(D) = N_0 \cdot D^{\mu} \exp(-\Lambda \cdot D^{\gamma}). \tag{20}$$

where N_0 describes the overall scaling and μ, Λ and γ control the shape. The gamma distribution, which has only three parameters, can be obtained by setting $\gamma = 1$. If, additionally, $\mu = 0$ is applied, the result is the two-parameter exponential distribution. An extensive review of the modified gamma distribution and its derivatives is given by Petty and Huang (2011).

Alternatively, a log-normal distribution can be used to describe $N(D)$, which is defined as

$$N(D) = \frac{N_T}{\sqrt{2\pi} \cdot s \cdot D} \exp\left(-\frac{\ln^2(D/D_T)}{2s^2}\right) \tag{21}$$

where N_T describes the overall scaling, and s and D_T are the shape parameters.

The parameters of Eqs. 20 and 21 can be obtained using miscellaneous methods, either by fits or by moment matching. In this section, various approaches are presented. For all presented methods, only profiles where the R^2 of fit and measurement is greater than 0.7 are investigated.

As an independent reference, which does not depend on the hydrometeor measurements of ISDAC, the method of Field et al. (2005) is presented (hereafter N-FI), which was obtained from measurements of stratiform ice cloud around the British Isles and is used widely in models. They showed that N_0 of the exponential distribution can be given by

$$N_0 = 5.65 \cdot 10^5 \cdot \exp(-0.107 \cdot T) \tag{22}$$

where T is the ambient air temperature T in °C. Thereafter, Λ of the exponential distribution is derived from the total number of particles N_{tot} with $\Lambda = N_0/N_{\text{tot}}$

The easiest way to find the coefficients of a modified gamma distribution is to apply a least squares fit (N-LSMG). Here, it is only applied to the modified gamma distribution, since gamma and exponential distribution are special cases.

The concept of normalizing $N(D)$ was introduced by Testud et al. (2001) for liquid clouds and by Delanoë et al. (2005, 2014) for ice clouds (N-NG). The normalized $N(D)$ is defined as

$$N(D) = N_0^* F(D/D_m) \tag{23}$$

where D_m is the "mass–weighted" scaling parameter for the particle size and $F(D/D_m)$ is the normalized function. This formulation has the advantage that scaling of the distribution in direction of N is clearly separated from scaling in the direction of D and a change of N_0^* has only an effect on the total number of particles, whereas a modified

D_m changes only the size of the particles. Delanoë et al. (2014) found that normalization works best on the basis of modified and non-modified gamma distributions with only little difference between both variants. Thus, we use the gamma distribution for simplicity and to keep the number of variables at a minimum. In contrast to Delanoë et al. (2005, 2014), we chose the particle's maximum dimension D instead of the equivalent melted diameter D_{melt} as the size descriptor. Therefore, we have to rephrase most the formulas used for the normalization. In Appendix A, it is described in detail how defining D_m as "mass–weighted" mean diameter and N_0^* with

$$D_m = \frac{M_{b+1}}{M_b} \tag{24}$$

$$N_0^* = \frac{M_b^{b+2}}{M_{b+1}^{b+1} C}. \tag{25}$$

leads to a conservation of IWC and to the definition of the normalization function

$$F(D/D_m) = \frac{(b+\mu+1)^{b+\mu+1}\Gamma(b+1)}{\Gamma(b+\mu+1)(b+1)^{b+1}} \left(\frac{D}{D_m}\right)^{\mu} \cdot \exp(-(b+\mu+1)D/D_m) \tag{26}$$

where b is the exponent of the $m(D)$ relation, M_j is the jth moment of $N(D)$, μ describes the shape of the distribution and C is an arbitrary constant. With $b = 3$ like for a water drop, these equations collapse into the corresponding ones of Testud et al. (2001) and Delanoë et al. (2005). Using Equations 24 and 25, D_m and N_0^* can be directly calculated from the measured, truncated moment $\hat{M}_j$ as a replacement for the theoretical M_j defined from 0 to ∞. For μ, Delanoë et al. (2005) suggested a value of 3, but they used the equivalent melted diameter as the size descriptor and thus we cannot transfer that value to our study. Instead, we use a least squares fit to find a best estimate of μ for every measured $N(D)$. Defining D_m and N_0^* such that they depend on the exponent b of the $m(D)$ relation, means that their definition might change with changing b. At first sight, this might appear counterintuitive, but it is important to note that the original studies by Delanoë et al. (2005, 2014) had a similar drawback by using the melted equivalent diameter as a size descriptor. I. e., the $m(D)$ relation was implicitly included in the size parameter.

Tian et al. (2010) presented another approach for normalizing $N(D)$ for exponential, gamma and log-normal distributions. Here, only the latter (N-LD) is investigated, because it performed best for the data set used by Tian et al. (2010) containing convective cirrus clouds. For N-LD, they used the first, second and fourth moment to define the parameters of

$$D_T = \frac{(M_2/M_1)^2}{\sqrt{M_4/M_2}} \tag{27}$$

$$s = \sqrt{\ln\left(\frac{(M_4/M_1)^{1/3}}{(M_2/M_1)}\right)} \tag{28}$$

$$N_T = M_1 \frac{(M_4/M_1)^{1/3}}{(M_2/M_1)^2} \tag{29}$$

The characteristic feature of the parameterization by Tian et al. (2010) is that they force all distributions to collapse onto the same function. The presented equations are based on the assumption that the corresponding particle size functions describe all particles from zero size to infinity. In reality, however, particle sizes are limited from a certain minimum to maximum diameter (D_{min} and D_{max}), so that the real measured moment $\hat{M}_j$ is different from the moment M_j defined from zero to infinity. The proposed correction by Tian et al. (2010) is used here.

We also use the *discrete incomplete gamma fitting* (N-DIGF) introduced by Freer and McFarquhar (2008) and extended by McFarquhar et al. (2014). They normalize the gamma distribution partly by introducing D_* which ensures that N_0 has the same unit as $N(D)$.

$$N(D) = N_0 \cdot \left(\frac{D}{D_*}\right)^{\mu} \exp(-\Lambda \cdot D). \tag{30}$$

Because SI units are chosen in this study, we chose $D_* = 1$ m. The coefficients N_0, μ and Λ are found by minimizing

$$\chi^2 = \sum_{j=1,2,6} \left(\frac{M_j - \hat{M}_j}{\sqrt{M_j \hat{M}_j}}\right) \tag{31}$$

using the method of Byrd et al. (1995) where $j = 1,2,6$ indicates the three moments used in the normalization. The advantage of the DIGF, the provision of an uncertainty range for the found parameters, is not exploited in this study.

c. Intercomparison of Parameterizations

Here, the impact of the different parameterizations of $A(D)$ and $N(D)$ on the dreived radar moments is examined. Only in situ data obtained within a 10 km radius around Barrow are analyzed (see Sec. 2d for details). To investigate the numerical stability of the derived parameterizations, they are not only applied to the size bins where the parameterizations are derived from (i. e., measurements are available and $N(D) > 0$), but also to the full range of D from 0.05 to 12.8 mm as determined by the in situ particle probes.

Frequency distributions of A vs. D are presented in Fig. 6. For A-MEAS, the step in spread of the distribution due to the different probes can be clearly seen around

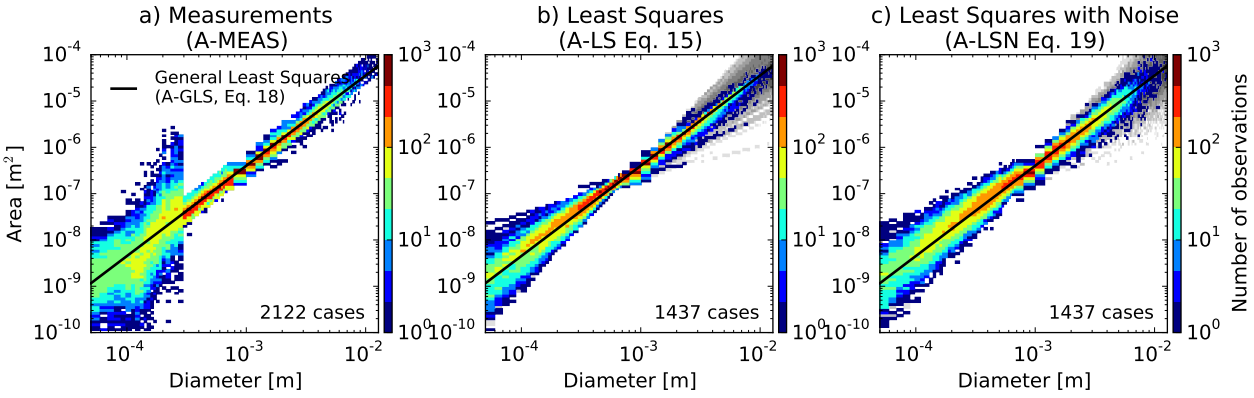

FIG. 6. Comparison of (a) measured area with (b–c) the various methods for area estimation presented in Sec. 4a. The *general least squares fit* (A-GLS) over all ISDAC data is shown by a black line on top of all plots. The other methods are presented using 2-D plots where the color scale corresponds to the number of observations. $A(D)$ is limited to profiles with measured $N(D)\Delta D > 0$. The gray contour-plot in the background corresponds to the number of observations without this limitation (i. e. extrapolated $A(D)$).

0.3 mm. For particles larger than 0.3 mm, a power law with two coefficients seem sufficient to describe $A(D)$, because the spread (a factor of ≈ 2.5) is evenly distributed around the A-GLS line. The scatter is slightly reduced if A-LS instead of A-MEAS is used. Application of A-LSN, instead, leads to scatter of the same order as for A-MEAS for medium size particles, but leads to overestimation of scatter for larger particles. Additional scatter on the order of up to one magnitude occurs for larger particles, if $A(D)$ is extrapolated until the maximum diameter of 12.8 mm. Note that application of the least squares fit reduces the number of profiles from 2122 to 1437. The reduction mainly occurs because many profiles with too few measurements with $N(D)\Delta D > 10$ m^{-3} are available for the least squares fit, i. e. mostly profiles with very low number concentrations are affected.

For $N(D)$, frequency distributions of the various methods are presented in Fig. 7. In contrast to $A(D)$, N-MEAS does not follow a straight line and has a much wider spread of two to three orders of magnitude indicating high variability of the observed $N(D)$. Similar to A-MEAS, the transition between the different in situ probes is clearly visible around 0.3 and 0.8 mm. Application of N-FI and N-LSMG leads to strong differences to N-MEAS in the shape of the 2-D distribution. In particular, particles larger than 1 mm and extrapolation to even higher diameters lead to artificially high particle size distributions which might cause biases in Z_e due to the strong scattering of large particles. As an advantage, the total number of observations is constant for N-FI and is reduced only to 1698 and 1762 cases for N-LSMG and N-NG. Application of N-DIGF and N-LN, instead, leads to a stronger reduction of the number of observations to 1260 and 830 cases, respectively, due to application of the fits and the R^2 test. Consequently, the latter, N-LN, is excluded from further analysis. Regarding the frequency distribution, N-NG and N-DIGF show highest similarities to N-MEAS with the latter having more outliers. Both methods lead to small $N(D)$ if extrapolated to D up to 12.8 mm.

d. Comparison to MMCR

In this section, F-ISDAC and MMCR data are compared using the various methods to describe $A(D)$ and $N(D)$. The evaluation is carried out in two steps: the method, which performs best for $A(D)$ is also used during the evaluations of the methods describing $N(D)$. Similar to Sec. 3d the Kolmogorov – Smirnov statistic (d_α) (Massey 1951) and the median are used as a measure of similarity. For the analysis, we consider not only the standard, lower moments, but also the higher moments of the Doppler spectrum.

For $A(D)$, Fig. 8 shows comparisons between MMCR and F-ISDAC for A-MEAS and the corresponding parameterizations. m-ZWT is used for $m(D)$ and hence the data shown in Fig. 8a is identical to Fig. 5b. The lower moments Z_e, W and σ show only little variation between A-MEAS and the other parameterizations. Hence, higher moments of the Doppler spectrum are also used for evaluation. Note that functional relations between higher moments and Z_e are not as pronounced as for lower moments and hence not analyzed here. Fig. 8a shows that for A-MEAS the agreement of higher moments is also high when using m-ZWT for $m(D)$. A major offset is only visible for S_r, which is shifted towards steeper slopes and has a wider spread. This is most likely related to sampling problems of fast-falling, large, and rare particles which are insufficiently sampled by the in situ sensors (Korolev and Isaac 2005). In addition, the accuracy of the T-Matrix approximation of the scattering properties is decreasing

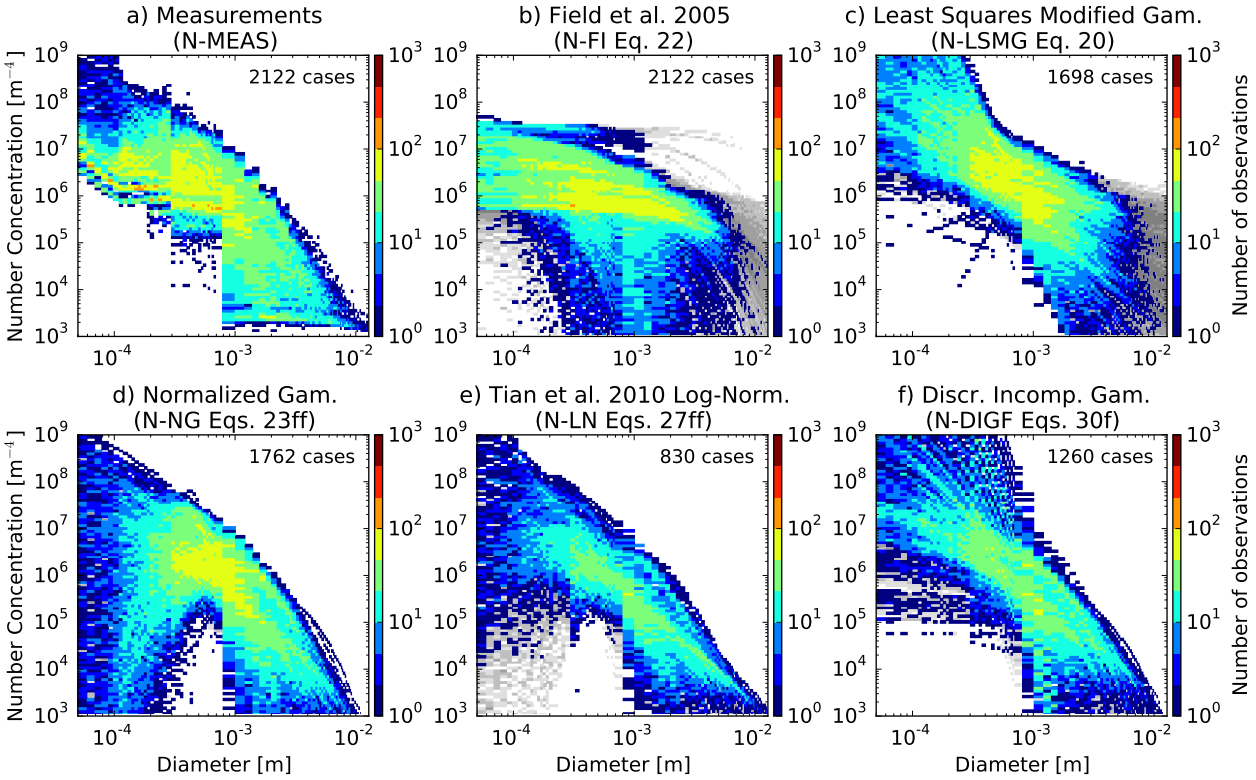

FIG. 7. Similar to Fig. 6, but for comparison of (a) the measured $N(D)$ with (b–f) the methods presented in Sec. 4b to parametrize $N(D)$ from the ISDAC observations.

with increasing particle size due to resonance effects reducing the backscattered power (Kneifel et al. 2011). Consequently, the right, fast tail of the Doppler peak is cut and the slope is too steep. Because the slopes are derived from the Doppler spectrum in log-scale, the impact of small perturbations at the borders of the peak on the slopes is rather high even though these perturbations hardly influence the moments which are derived using linear units. Only *Sk* is shifted towards negative values in comparison to MMCR by 0.17 due to the truncation of the right, fast tail of the Doppler spectrum.

A-GLS and A-LS lead to very similar results, indicating the low variability of the $A(D)$ relation during ISDAC, d_α values are even slightly better for A-GLS than for A-LS for all moments but σ and *Sk*. For all least squares fits, particles with $D < 0.5$ mm are ignored to remove shattering artifacts (Sec. 2a), but from the fact that agreement of S_l (which is partly determined by small particles) is not decreasing from A-MEAS to A-GLS and A-LS, it can be assumed that representation of A for particles < 0.5 mm is good even though they are excluded form the least squares fit or that they have only minor impact on the radar moments.

Strikingly, the offsets of *Sk* and *Ku* are increased for A-GLS and A-LS in comparison to A-MEAS and MMCR. This is most likely—again—related to problems at the right, fast side of the Doppler spectrum, because the offset of S_r increases from -23 dB s m^{-1} to -40 to -38 dB s m^{-1} as well. Since at the same time, W and σ change only little, the peak becomes more asymmetric and *Sk* is biased. Methods to express $A(D)$ by a gamma relation (similar to Eq. 20, but with $\gamma = 1$) or by two different sets of power law coefficients depending on D did not lead to a significant improvement (not shown).

To investigate whether the offset of *Sk* is caused by a certain part of the size spectrum, A-LS is applied only to parts of the spectrum and measurements are used otherwise. As a result, the offset of *Sk* is reduced to -0.12 for $D < 0.3$ mm and to -0.14 for $0.3 < D < 1$ mm, but is increased to -0.22 for $D > 1$ mm (not shown). Hence, the effect is caused by particles larger 1 mm.

However, if noise (A-LSN) is added to $A(D)$ estimated with A-LS so that the scatter of $A(D)$ around the A-GLS line is increased (see Fig. 6c), the offsets are reduced and d_α-values for *Sk* and *Ku* are in the same order as for A-MEAS (Fig. 8d). Only σ is slightly increased—especially for larger Z_e values (not shown). We conclude that small,

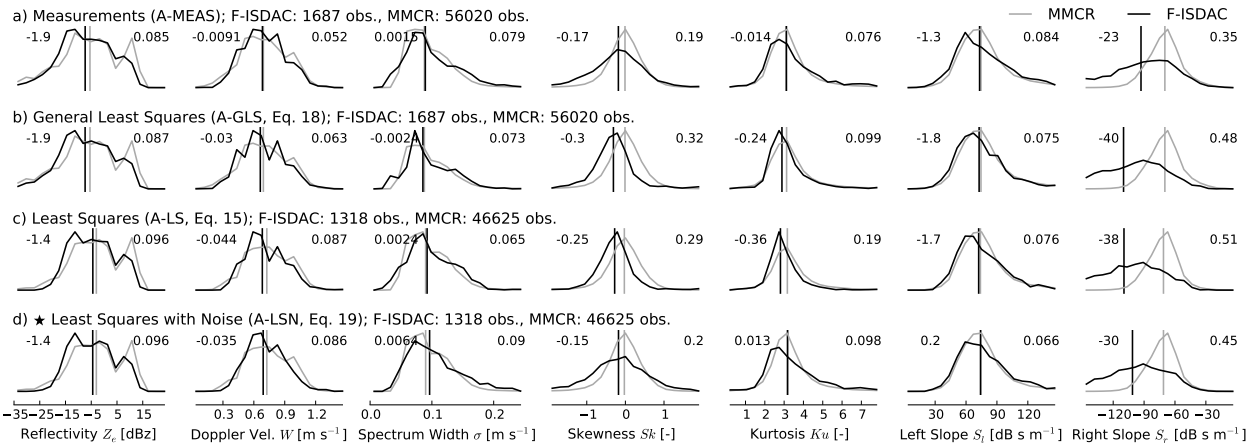

FIG. 8. Normalized histograms of the radar moments (columns) of MMCR observations (gray lines) and forward modeled ISDAC observations (F-ISDAC, black lines) for various methods to describe $A(D)$ (rows) when forward modeling ISDAC data. $N(D)$ is taken from measurements, $m(D)$ is always approximated using the $Z_e - W$ *optimal estimation with temperature* (m-ZWT) method. For each data set, the number of cases is given. The vertical lines denote the median of the distributions, the difference between both medians is denoted in the upper left corner and the Kolmogorov – Smirnov statistic d_α is presented in the upper right corner of each panel.

random deviations from the power law are mandatory to reproduce realistic distributions of Sk. A variation of the coefficients c or d, instead, is not sufficient because otherwise, the difference between A-GLS and A-LS would be larger. A possible reason could be that if both, A and m, are expressed by power laws, the degrees of freedom of the fall velocity relation is reduced because both, A and m, can be expressed in terms of D. This could lead to a reduced variability of $v(D)$ which apparently becomes most evident for larger particles. Consequently, we use A-LSN as the preferred method for $A(D)$ in the following.

Fig. 9 shows the comparison of F-ISDAC and MMCR using lower and higher moments for the various methods to describe $N(D)$. For all methods, m-ZWT and A-LSN are used to estimate $m(D)$ and $A(D)$, respectively.

For N-FI (Fig. 9b), agreement of the lower moments is similar to N-MEAS, but the offsets for Sk, Ku and S_r are increased. This highlights the need for also investigating higher moments when comparing $N(D)$ parameterizations. N-LSMG leads to increased offsets for all moments (Fig. 9c). N-NG shows (Fig. 9d) that this is most likely related to the fit type instead of being related to the use of a gamma distribution to describe $N(D)$. For all moments, offsets and d_α values are almost identical for N-MEAS and N-NG. We attribute this to the combination of the least squares fit and the conservation of PSD moments of the N-NG method. N-DIGF, which is also designed to conserve moments, leads to increased offsets especially for the lower moments (Fig. 9e). In addition, the number of profiles are reduced by 1/3 for this method, mostly due to the $R^2 > 0.7$ condition.

e. Truncation Effects

Finally, the best methods for $A(D)$ and $N(D)$ are used to investigate whether the minimum and/or maximum detected particle diameter $D_{\min}$ and $D_{\max}$ have to be a treated as additional parameters or whether a fixed value for $D_{\min}$ and $D_{\max}$ is sufficient (Fig. 10).

To investigate how truncation effects have to be handled, the minimum and maximum observed diameters of the distribution $D_{\min}$ and $D_{\max}$ are estimated. Then, a) the method applied so far (i. e., application of the parameterizations for $m(D)$, $A(D)$ and $N(D)$ only if measured $N(D) > 0$ to ensure equal treatment of measurements and parameterizations) is compared with b) applying $D_{\min}$ and $D_{\max}$ instead (i. e., interpolating gaps in-between), c) applying only $D_{\max}$ and using a fixed value of 0.05 mm for $D_{\min}$ and d) using also a fixed value of 12.8 mm for $D_{\max}$ (i. e., extrapolation) which is the maximum of the measurement range of the in situ probe. The difference of F-ISDAC of b) and c) to a) are negligible. Omission of $D_{\min}$ leads to only slightly increased (i. e., steeper) values for S_l. Hence, we conclude that smaller particles and gaps of the particle spectrum have little impact on the radar moments. For d), agreement of F-ISDAC to MMCR is actually better than for a): the offset of Sk is decreased from -0.2 to -0.08 and—even more strongly pronounced—the offset of S_r is reduced from -31 to -6 (even though the shape of distribution still cannot be captured correctly and d_α is only 0.21). This indicates that the problems with the right, fast side of the spectrum were partly caused by problems with measuring rare, fast particles with in situ probes. As a disadvantage, agreement of σ and S_l decrease slightly.

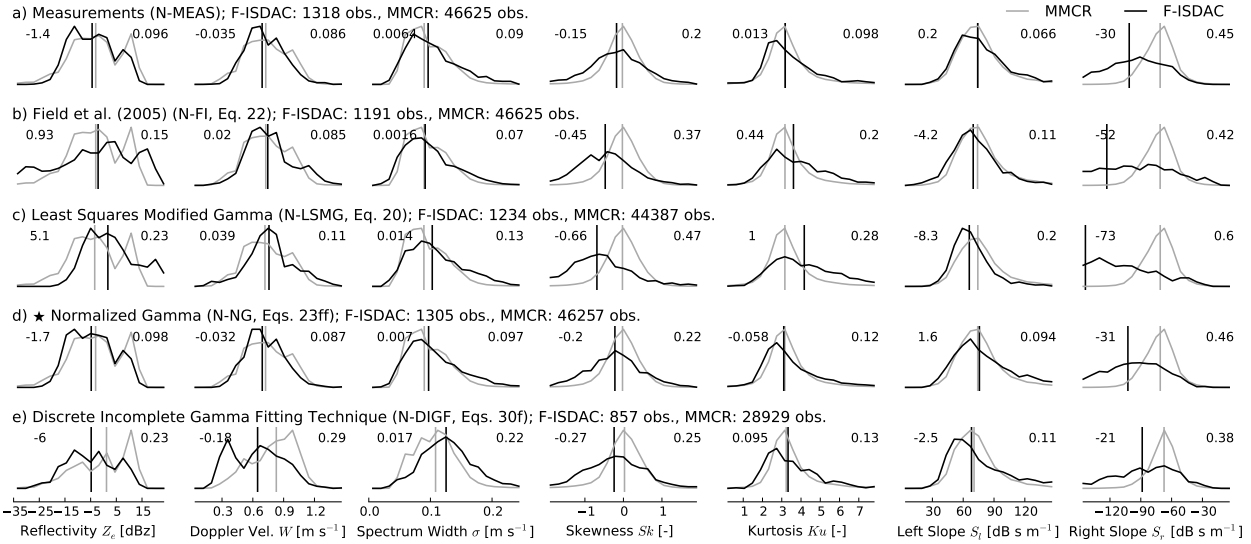

FIG. 9. Comparison of MMCR observations and various methods to represent $N(D)$ for ISDAC data, similar to Fig. 8. $m(D)$ is always approximated using the $Z_e - W$ *optimal estimation with temperature* (m-ZWT) method, for $A(D)$, the *least squares with noise* (A-LSN) method is used.

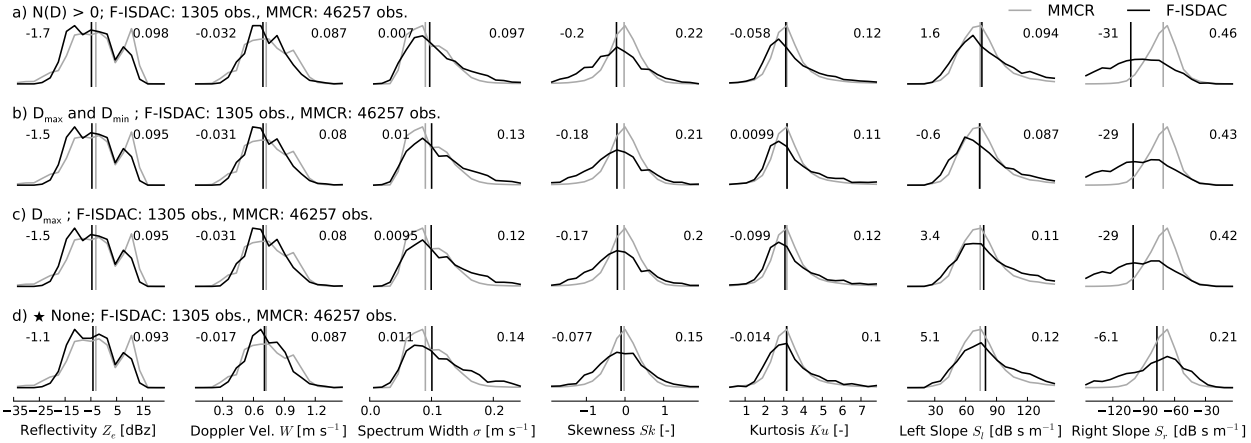

FIG. 10. Same as Fig. 8, but for truncation effects of particle size distribution. While (a) shows only data where measured $N(D) > 0$, (b) uses minimum and maximum detected particle size ($D_{\min}$ and $D_{\max}$), for (c) $D_{\min}$ is replaced by a fixed value of 0.05 mm. Finally, (d) a fixed value of 12.8 mm is used also for $D_{\max}$. $m(D)$ is always approximated using the $Z_e - W$ *optimal estimation with temperature* (m-ZWT) method. For $A(D)$, the *least squares with noise* (A-LSN) method is used. $N(D)$ is estimated using the *normalized gamma* (N-NG) approach.

The fact that omission of $D_{\max}$ does not lead to decreased results can be explained by the shape of $N(D)$: for N-NG, $N(D)$ is strongly decreasing for larger particles and consequently $N(D)$ is small, even for a fixed $D_{\max} = 12.8$ mm. If a method without this property would be used for $N(D)$, e. g., N-FI, Z_e would increase by around 10 dB for a fixed $D_{\max}$ of 12.8 mm (not shown). In conclusion, for the presented data set with the chosen parameterizations, it is not necessary to keep $D_{\min}$ and/or $D_{\max}$ as additional parameters in the forward model. However, an investigation is recommended for every data set.

5. Conclusions

In situ aircraft and MMCR radar observations obtained during the ISDAC campaign around Barrow, Alaska, were used to develop a consistent data set of stratocumulus ice cloud properties such as mass $m(D)$, area $A(D)$ and particle size distribution $N(D)$. For m(D), a novel method

to derive the power law coefficients based on the functional relation between effective reflectivity factor Z_e and Doppler velocity W was developed and compared to other methods. Then, the effect of applying various parameterizations to $A(D)$ and $N(D)$ on radar simulated observations was investigated. For this, higher moments such as Skewness *Sk*, Kurtosis *Ku* and the slopes (S_l, S_r) were also used as a proxy for the radar Doppler spectrum. The principal conclusions of this study are as follows:

1. $m(D)$ can be successfully obtained from a combination of in situ and radar observations by choosing $m(D)$ with optimal estimation such that the $Z_e - W$ relations of radar and forward modeled in situ data match (Fig. 2). The found, temperature dependent, $m(D)$ relations are in high agreement with relations reported in literature (Fig. 4) and also lead to a high agreement of Z_e to Doppler spectrum width (σ) relations between observation and model (Fig. 5). From this, we conclude that the potentially large errors in $m(D)$ due to forward model uncertainties can be neglected.

2. Even though other methods to describe $m(D)$ lead to similar Z_e as observed by the MMCR, they cannot reproduce the functional relations $Z_e - W$ and—even more pronounced—$Z_e - \sigma$. From this, it is concluded that analyzing Z_e, W and σ independently is not sufficient when analyzing $m(D)$ relations (Fig. 5).

3. The presented forward model PAMTRA is able to simulate lower and higher moments consistently on the basis of aircraft in situ observations and the novel method to derive $m(D)$ (Fig. 8a). We attribute a small offset for *Sk* (-0.17) and larger offsets for S_r (-22 dB s m^{-1}) to in situ sampling issues of rare, large, and fast-falling particles as well as to the decreasing accuracy of T-Matrix scattering calculations for larger particles.

4. Even though power law fits are well suited to describe $A(D)$ (Fig. 6) and lead to a high agreement of lower moments, consistent results for higher moments can be only obtained if an additional, size dependent noise factor is applied to the result of the power law (Fig. 8). We conclude that small deviations from the power law for single parts of $A(D)$ are essential to obtain realistic Doppler spectra.

5. For the description of $N(D)$, most consistent results are found for a gamma distribution, if the coefficients are estimated using a moment preserving approach (Fig. 9). Of these, the normalized gamma distribution approach by Testud et al. (2001), which was modified to work with maximum dimension as size descriptor, is identified to work best for the ISDAC data set. The use of higher moments was also found to be a valuable addition.

6. For the investigated data set, the minimum and maximum measured particle size do not have to be passed to the radar simulator as additional parameters (Fig. 10) and fixed boundaries can be assumed instead. Extrapolating the particle size distribution to the maximum diameter of 12.8 mm removes the offset for *Sk* found before and improves the agreement of S_r.

These results are robust with respect to uncertainties in the aspect ratio as shown in Appendix B1, but the large calibration offset of the MMCR of -9.8 dB prevents more detailed analysis of this. While the estimation of scattering properties with T-Matrix is sufficient for this study, more sophisticated methods need be used for observations of larger snowflakes and/or with radars using smaller wavelengths. The data set investigated in this study is rather small and consists of only 1690 profiles. In this study, the data set cannot be extended, because no other data sets with observations of ice clouds are available to the authors knowledge in the vicinity of a cloud radar and where modified probe tips were used which reduce the impact of shattering. Thus, more aircraft campaigns in the vicinity of super sites instrumented with cloud radars are desirable to extend the data set, to confirm the results and to investigate how the found results depend on temperature or geographical location. In addition, the maximum distance between aircraft and radar for the comparison could be decreased to enhance agreement of cloud characteristics. A larger data set would also potentially increase the spread of observed $A(D)$, which does show only small variability in this study, and would allow a more thorough investigation of the temperature dependence of the mass – size relation. Better measurements of ice water content *IWC* would be also an additional, independent test of the found $m(D)$ relation. Analysis of S_r showed that better measurements of rare, large particles by aircraft in situ probes are also desirable for the future.

The presence of more modern cloud radars such as the *Ka-band ARM zenith radar* (KAZR, Lamer et al. 2014) or the MIRA cloud radar (Melchionna et al. 2008), which are available at numerous ground-based sites today, can also lead to better possibilities for the exploration of higher moments and the Doppler spectrum due to their better sensitivity and larger spectral resolution. The question of why deviations from the $A(D)$ power law for particles greater 1 mm are essential to obtain consistent results for the higher moments has to be investigated in greater detail in the future. The impact of supercooled liquid water on the Doppler spectrum e. g., via riming of ice particles, also has to be included in future studies.

This study shows that higher radar moments are a valuable addition to the set of radar observables and should

be exploited more often in the future. The advantage of using higher moments is—besides increasing the number of observables—that they are neither affected by calibration issues (as Z_e) nor biased by vertical air motions (as W). Furthermore, higher moments can be also used as an independent closure test for evaluating numerical weather models or ice cloud retrievals by forward modeling their output and comparing modeled and observed higher moments. Turbulence was very low during ISDAC and had hence only little impact on the Doppler spectrum via kinematic broadening. Because turbulence tends to make radar Doppler spectra more Gaussian, sensitivity studies are needed to investigate whether higher moments can be still exploited in more turbulent conditions.

This study developed a consistent set of parameterizations to describe $m(D)$, $A(D)$, and $N(D)$ which can be used in combination with the presented PAMTRA model to investigate the potential for a retrieval of microphysical ice cloud properties based on lower and higher moments. Assuming that the ability to simulate higher moments indicates also the ability to simulate the full Doppler spectrum consistently (except for the fastest particles), this also allows for investigating the potential of using the full Doppler spectrum for retrievals. Then, the information content, which higher moments or the full radar Doppler spectrum can provide to ice cloud retrievals can be estimated using inverse retrieval methods, such as optimal estimation (Rodgers 2000). In addition, the impact of using an optimized radar configuration or the addition of additional observation frequencies can be investigated.

Acknowledgments. The authors would like to thank Edward Luke from Brookhaven National Laboratory for providing MMCR data and supporting us with their use, Daniel Mulally for supporting us with decoding TAMDAR data, and Wanda Szyrmer for her detailed comments regarding the used parameterizations. Data were obtained from the Atmospheric Radiation Measurement (ARM) Program sponsored by the U.S. Department of Energy (DOE), Office of Science, Office of Biological and Environmental Research (BER), Climate and Environmental Sciences Division. This study was carried out within the project ADMIRARI II supported by the German Research Association (DFG) under research grant number LO901/5-1. Pavlos Kollias is supported by funding from the DOE Atmospheric System Research (ASR) program. The work of Greg M. McFarquhar and Robert C. Jackson was supported by the BER DOE grants DE-SC00001279 and DE-SC0008500. Computing time was gratefully allocated by the Cologne High Efficiency Operating Platform for Sciences (CHEOPS) at the University of Cologne. The authors would like to thank the three reviewers for their valuable and constructive comments.

APPENDIX A

Normalization of the Gamma Distribution with Maximum Dimension D as Size Descriptor

According to Testud et al. (2001) and Delanoë et al. (2005), the normalized $N(D)$ is defined as

$$N(D) = N_0^* F(D/D_m) \tag{A1}$$

or with $X = D/D_m$

$$N(X) = N_0^* F(X) \tag{A2}$$

where N_0^* is the scaling parameter in the direction of the concentration axis and D_m is the scaling parameter for the particle size.

In contrast to Delanoë et al. (2005, 2014), we chose the ice particle's maximum dimension instead of the equivalent melted diameter as the size descriptor. Therefore, we have to rephrase most the formulas used for the normalization.

We begin with the constraint that the normalized $N(D)$ is supposed to be mass consistent:

$$IWC = \int m(D)N(D)dD \tag{A3}$$

Assuming a $m(D)$ relation of $m = aD^b$ and using equation A2 we get

$$IWC = \int aD^b N(D)dD = aD_m^{b+1} N_0^* \int X^b F(X)dX \tag{A4}$$

The term $\int X^b F(X)dX$ is supposed to be constant to put all the variability of IWC into D_m and N_0^*. Hence, we define

$$D_m = \frac{M_{b+1}}{M_b} \tag{A5}$$

where M_j is the jth moment of the distribution defined as $M_j = \int N(D)D^j dD$. This yields to:

$$D_m = \frac{\int N(D)D^{b+1}dD}{\int N(D)D^b dD} = \frac{D_m^{b+2}\int F(X)X^{b+1}dX}{D_m^{b+1}\int F(X)X^b dX} \tag{A6}$$

using Eq. A2. Since this equation has to be valid for all X and $F(X)$ we can follow

$$\int F(X)X^{b+1}dX = \int F(X)X^b dX = C \tag{A7}$$

where C is an arbitrary constant. Using C, Eq. A4 becomes

$$IWC = aD_m^{b+1} N_0^* C \tag{A8}$$

$$\Leftrightarrow N_0^* = \frac{IWC}{aD_m^{b+1}C} \tag{A9}$$

Using Eq. A5 and knowing that $IWC = aM_b$, N_0^* becomes

$$N_0^* = \frac{M_b^{b+2}}{M_{b+1}^{b+1}C}. \tag{A10}$$

In principle, C can be chosen arbitrarily and so far the derived equations are valid for all kinds of distributions. We follow Delanoë et al. (2005), which chose C in such a way that N_0^* is equal to N_0 of the exponential distribution. The ith moment of an exponential distribution is defined as

$$M_j = N_0 \frac{\Gamma(j+1)}{\Lambda^{j+1}} \tag{A11}$$

Inserting this in A5 yields to

$$D_m = \frac{\Gamma(b+1)}{\Lambda} \tag{A12}$$

This is used to rephrase Eq. A10 which results in

$$N_0^* = N_0 \frac{\Gamma(b+1)}{(b+1)^{(b+1)} C} \tag{A13}$$

Requiring $N_0^* = N_0$ we get

$$C = \frac{\Gamma(b+1)}{(b+1)^{b+1}}. \tag{A14}$$

However, Delanoë et al. (2005) showed that an exponential distribution is not sufficient to to give a realistic approximation of $N(D)$ for ice, instead, they suggested a modified or non-modified gamma distribution. Since they found only little difference between both variants, we decided to use a gamma distribution for simplicity and to keep the number of variables smaller. The definition of C is simply overtaken from the exponential distribution.

For the gamma distribution, the jth moment is defined as

$$M_j = N_0 \frac{\Gamma(j+\mu+1)}{\Lambda^{j+\mu+1}}. \tag{A15}$$

Inserting this in A5 yields to

$$D_m = \frac{b+\mu+1}{\Lambda} \tag{A16}$$

These two equations are used to rephrase Eq. A10

$$N_0^* = \frac{M_b^{b+2}}{M_{b+1}^{b+1}} \frac{(b+1)^{b+1}}{\Gamma(b+1)} = N_0 D_m^{\mu} \frac{\Gamma(b+\mu+1)(b+1)^{b+1}}{(b+\mu+1)^{b+\mu+1}\Gamma(b+1)} \tag{A17}$$

Therefore, the gamma distribution

$$N(D) = N_0 D^{\mu} \exp(-\Lambda D) \tag{A18}$$

can be normalized by inserting Eq. A17 for N_0 and Eq. A16 for Λ

$$N(D) = N_0^* \frac{(b+\mu+1)^{b+\mu+1}\Gamma(b+1)}{\Gamma(b+\mu+1)(b+1)^{b+1}} \left(\frac{D}{D_m}\right)^{\mu} \cdot \exp(-(b+\mu+1)D/D_m) \tag{A19}$$

If the $m(D)$ relation of water spheres is used ($a = \pi\rho/6$ and $b = 3$), these equations collapse into the corresponding ones of Testud et al. (2001) and Delanoë et al. (2005).

APPENDIX B

Sensitivity to Model and Data Processing Assumptions

Here, we motivate why we 1) use an $AR = 0.6$ for estimating the scattering properties, 2) limit the aircraft to a radius of 10 km around the ARM NSA site in Barrow and 3) why we average aircraft data to 10 s. For this, F-ISDAC data are statistically compared with MMCR using different aspect ratios, maximum radii and averaging times (Fig. B1). $m(D)$ is estimated with m-ZWT, which was found to work best in Sec. 4d, and $A(D)$ and $N(D)$ are taken from the measurements.

B1. Sensitivity to Aspect Ratio

Unfortunately, we cannot estimate AR from ISDAC data directly, because D_{short}, defined as the particle extent perpendicular to D (see Hogan et al. 2012), is not available in the data set. Other studies found typical mean AR in ice clouds of 0.6 (see Korolev and Isaac 2003; Hogan et al. 2012) or 0.65 - 0.7 (Tyynelä et al. 2011). If we approximate AR from $A(D)$ and D of the ISDAC data set, we find $AR = 0.5$ on average. With this method, however, we underestimate AR, because $A(D)$ is usually smaller than the corresponding cross section of an ellipsoid (Hogan et al. 2012) which would be required to estimate the correct AR. Consequently, the measurements indicate that AR is > 0.5 also for the ISDAC data set.

To investigate the sensitivity of the higher moments to AR, AR values between 1.0 and 0.4 are applied to the ISDAC data set in steps of 0.2 and compared to MMCR measurements (Fig. B1). For 1.0, scattering is estimated with Mie instead with T-Matrix. With decreasing AR, the offset of Z_e is also decreasing, because smaller AR lead to larger particle density due to the smaller particle volume. The secondary peak of Z_e can only be reproduced by $AR \leq 0.6$. For all other moments, the impact of AR is surprisingly low. Apparently, AR has only minor influence on all radar moments except Z_e. Results for AR of 0.4 and 0.6 are most consistent with MMCR observations, but the value of 0.6 is chosen for the rest of the study to be in accordance with literature and observations.

B2. Sensitivity to Maximum Distance to Barrow

If the maximum distance between the aircraft and the radar observations is chosen too large, the data sets are not comparable due to the spatial variability. X-band radar observations of the stratocumulus sampled during ISDAC showed small-scale structure and inhomogeneities in the microphysical structure on scales on the order of 2 to 3 km (McFarquhar et al. 2011). Choosing a too small distance, instead, leads to a too little number of observations prohibiting statistical comparisons. Fig. B1 presents histograms of the radar moments of F-ISDAC and MMCR observations for a maximum radius of 10, 5 and 1 km. A

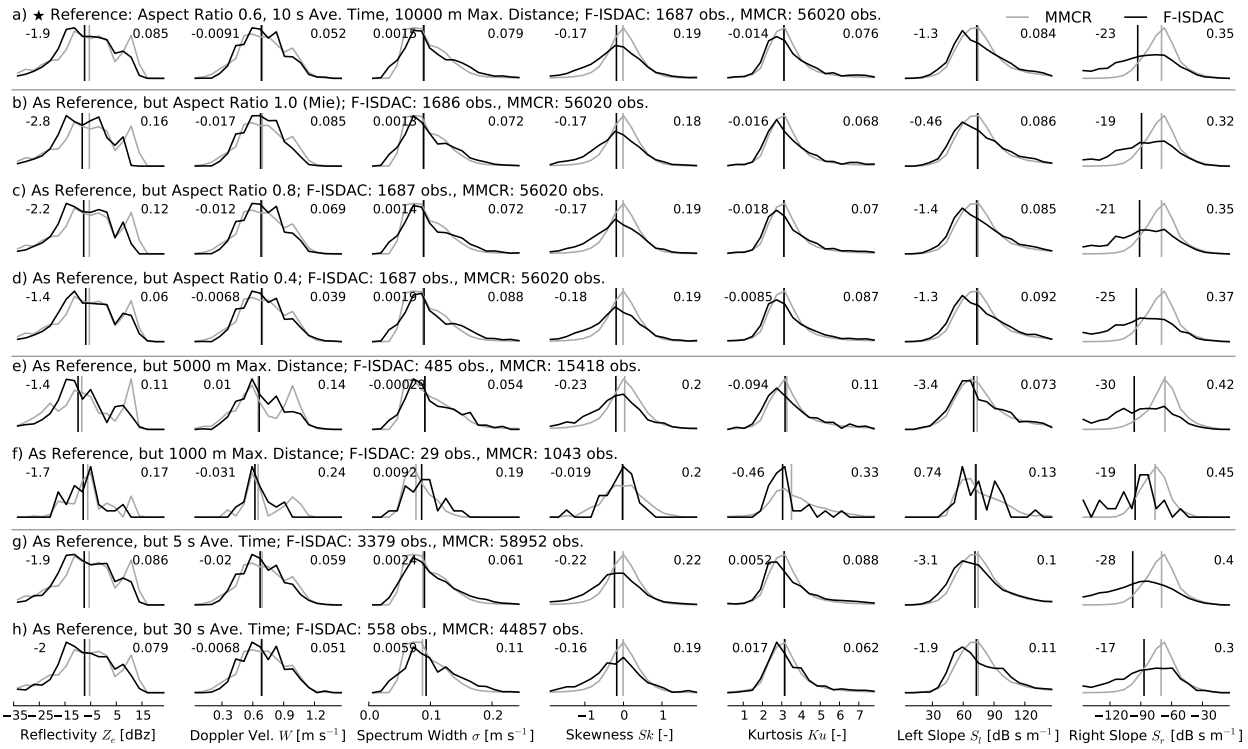

FIG. B11. Dependence of F-ISDAC on aspect ratio for values of (a) 0.6 vs. (b) 1.0, (c) 0.8, and (d) 0.4; on the maximum distance of the aircraft to Barrow for radii of (a) 10 km, (e) 5 km, and (f) 1 km; and on ISDAC averaging time for (a) 10 s, (g) 5 s, and (h) 30 s. $m(D)$ is estimated using $Z_e - W$ *optimal estimation with temperature* (m-ZWT), and measurements are used for $A(D)$ and $N(D)$.

reduction of the radius from 10 to 5 km leads to a decrease of the number of observations by three quarters. However, a significant change in the distribution of the moments cannot be seen. A further reduction to 1 km radius reduces the number of observations to only 29. Slightly increases offsets for σ and Ku are most likely related to the sample size.

B3. Sensitivity to in situ Data Averaging Time

Averaging of the 1-s ISDAC data is required to improve the representation of rare, large particles. A too long averaging time, however, might smooth out small scale ice cloud variability. To investigate which averaging time is appropriate, averaging times of 5, 10 and 30 s are compared (Fig. B1). The number of observations does, as expected, scale with the inverse of the averaging time. The better representation of larger particles can be seen from the better agreement of S_r: The offset is reduced from around -23 dB s m^{-1} to -17 dB s m^{-1} for 30 s data, but the greater width of S_r of F-ISDAC still indicates noisy sampling of larger particles. σ, on the other hand is represented best with 5 s and 10 s data (offset $\sim$0.002 m s^{-1}) while for 30 s, there is an slightly increased offset of 0.006 m s^{-1} which is probably related to smoothing effects. Consequently, 10 s is found as a compromise between sufficient sample size and agreement of σ and S_r.

APPENDIX C

List of Symbols

A	(projected) particle area
a	pre-factor of mass–size relation
A-GLS	general least squares fit applied to the complete data set
A-LS	least squares fit applied to every profile individually
A-LSN	least squares fit applied to every profile individually with additional noise factor
A-MEAS	area from in situ measurements
AR	aspect ratio
α	mass–size reference factor
b	exponent of mass–size relation
c	pre-factor of area–size relation
D	maximum particle dimension

d	exponent of area–size relation
d_α	Kolmogorov Smirnov statistic
ΔD	particle size bin width
e	pre-factor of reflectivity-Doppler velocity relation
f	exponent of reflectivity-Doppler velocity relation
IWC	ice water content
Ku	kurtosis
Λ	shape coefficient of exponential and (modified) gamma distribution
m	particle mass
m-BF	mass–size relation by Brown and Francis (1995)
m-CL	constant Λ method by Heymsfield et al. (2004)
m-FG	fractal geometry method by Schmitt and Heymsfield (2010)
m-SA	shape analysis data of Jackson et al. (2012)
m-ZW	optimal estimation method using $Z_e - W$ relation
m-ZWT	optimal estimation method using $Z_e - W$ relation and temperature
M_j	jth moment of a distribution
$\hat{M}_j$	jth measured moment of a distribution
N	particle size distribution
N-DIGF	discrete incomplete gamma fitting technique by Freer and McFarquhar (2008)
N-FI	method by Field et al. (2005) to estimate $N(D)$ from temperature
N-LD	normalized log-normal distribution approach by Tian et al. (2010)
N-LSMG	least squares method to estimate coefficients of the modified gamma distribution
N-MEAS	particle size distribution from in situ measurements
N-NG	normalized gamma distribution approach by Testud et al. (2001)
N_{true}	sample size detected by cloud probe
R^2	correlation coefficient
Sk	skewness
S_l	left slope
S_r	right slope
σ	Doppler spectrum width
T	temperature
W	mean Doppler velocity (positive means towards the ground)
Z_e	effective radar reflectivity factor

References

ARM, 1996: Merged sounding (MERGESONDE1mace). URL http://dx.doi.org/10.5439/1034922, 2008-04-01 to 2008-04-30, 71.323 N 156.609 W: North Slope Alaska (NSA) Central Facility, Barrow AK (C1). Compiled by D. Troyan and M. Jensen. Atmospheric Radiation Measurement (ARM) Climate Research Facility Data Archive: Oak Ridge, Tennessee, USA., doi:10.5439/1034922.

Atlas, D., R. C. Srivastava, and R. S. Sekhon, 1973: Doppler radar characteristics of precipitation at vertical incidence. *Rev. Geophys.*, **11 (1)**, 1–35, doi:10.1029/RG011i001p00001.

Babb, D. M., J. Verlinde, and B. A. Albrecht, 1999: Retrieval of cloud microphysical parameters from 94-GHz radar Doppler power spectra. *J. Atmos. Oceanic Technol.*, **16 (5)**, 489–503, doi:10.1175/1520-0426(1999)016⟨0489:ROCMPF⟩2.0.CO;2.

Bailey, M. P., and J. Hallett, 2009: A comprehensive habit diagram for atmospheric ice crystals: Confirmation from the laboratory, AIRS II, and other field studies. *J. Atmos. Sci.*, **66 (9)**, 2888–2899, doi:10.1175/2009JAS2883.1.

Benedetti, A., G. L. Stephens, and J. M. Haynes, 2003: Ice cloud microphysics retrievals from millimeter radar and visible optical depth using an estimation theory approach. *J. Geophys. Res.*, **108 (D11)**, 4335, doi:10.1029/2002JD002693.

Brown, P. R. A., and P. N. Francis, 1995: Improved measurements of the ice water content in cirrus using a total-water probe. *J. Atmos. Oceanic Technol.*, **12 (2)**, 410–414, doi:10.1175/1520-0426(1995)012⟨0410:IMOTIW⟩2.0.CO;2.

Brown, P. R. A., A. J. Illingworth, A. J. Heymsfield, G. M. McFarquhar, K. A. Browning, and M. Gosset, 1995: The role of spaceborne millimeter-wave radar in the global monitoring of ice cloud. *J. Appl. Meteor.*, **34 (11)**, 2346–2366, doi:10.1175/1520-0450(1995)034⟨2346:TROSMW⟩2.0.CO;2.

Byrd, R., P. Lu, J. Nocedal, and C. Zhu, 1995: A limited memory algorithm for bound constrained optimization. *SIAM J. Sci. Comput.*, **16 (5)**, 1190–1208, doi:10.1137/0916069.

Curry, J. A., J. L. Schramm, W. B. Rossow, and D. Randall, 1996: Overview of Arctic cloud and radiation characteristics. *J. Climate*, **9 (8)**, 1731–1764, doi:10.1175/1520-0442(1996)009⟨1731:OOACAR⟩2.0.CO;2.

Delanoë, J., and R. J. Hogan, 2008: A variational scheme for retrieving ice cloud properties from combined radar, lidar, and infrared radiometer. *J. Geophys. Res.*, **113 (D7)**, D07 204, doi:10.1029/2007JD009000.

Delanoë, J., A. Protat, J. Testud, D. Bouniol, A. J. Heymsfield, A. Bansemer, P. R. A. Brown, and R. M. Forbes, 2005: Statistical properties of the normalized ice particle size distribution. *J. Geophys. Res.*, **110 (D10)**, D10 201, doi:10.1029/2004JD005405.

Delanoë, J. M. E., A. J. Heymsfield, A. Protat, A. Bansemer, and R. J. Hogan, 2014: Normalized particle size distribution for remote sensing application. *J. Geophys. Res.*, **119 (7)**, 4204–4227, doi:10.1002/2013JD020700.

Field, P. R., A. J. Heymsfield, and A. Bansemer, 2006: Shattering and particle interarrival times measured by optical array probes in ice clouds. *J. Atmos. Oceanic Technol.*, **23 (10)**, 1357–1371, doi:10.1175/JTECH1922.1.

Field, P. R., R. J. Hogan, P. R. A. Brown, A. J. Illingworth, T. W. Choularton, and R. J. Cotton, 2005: Parametrization of ice-particle size distributions for mid-latitude stratiform cloud. *Quart. J. Roy. Meteor. Soc.*, **131 (609)**, 1997–2017, doi:10.1256/qj.04.134.

Freer, M., and G. M. McFarquhar, 2008: Development and comparison of cloud particle size distribution fitting and analysis techniques. *Proceedings of 18th ARM Science Team Meeting*, Norfolk, Virginia, [Available online at http://www.arm.gov/publications/proceedings/conf18/poster/P00090.pdf.].

Fukuta, N., and T. Takahashi, 1999: The growth of atmospheric ice crystals: A summary of findings in vertical supercooled cloud tunnel studies. *J. Atmos. Sci.*, **56 (12)**, 1963–1979, doi:10.1175/

1520-0469(1999)056⟨1963:TGOAIC⟩2.0.CO;2.

Garnett, J. C. M., 1904: Colours in metal glasses and in metallic films. *Phil. Trans. Roy. Soc. London*, **203**, 385–420.

Gossard, E. E., and R. G. Strauch, 1989: *Further Guide for the Retrieval of Dropsize Distributions in Water Clouds with a Ground-based Clear-air-sensing Doppler Radar*. NASA STI/Recon Technical Report N, U.S. Department of Commerce, National Oceanic and Atmospheric Administration, Environmental Research Laboratories.

Gunn, K. L. S., and J. S. Marshall, 1958: The distribution with size of aggregate snowflakes. *J. Meteor.*, **15 (5)**, 452–461, doi:10.1175/1520-0469(1958)015⟨0452:TDWSOA⟩2.0.CO;2.

Hallett, J., 2003: Measurement in the atmosphere. *Handbook of Weather, Climate, and Water*, T. D. Potter, and B. R. Colman, Eds., John Wiley & Sons, Inc., 711–720.

Heymsfield, A. J., A. Bansemer, C. Schmitt, C. Twohy, and M. R. Poellot, 2004: Effective ice particle densities derived from aircraft data. *J. Atmos. Sci.*, **61 (9)**, 982–1003, doi:10.1175/1520-0469(2004)061⟨0982:EIPDDF⟩2.0.CO;2.

Heymsfield, A. J., C. Schmitt, and A. Bansemer, 2013: Ice cloud particle size distributions and pressure-dependent terminal velocities from in situ observations at temperatures from 0° to 86°C. *J. Atmos. Sci.*, **70 (12)**, 4123–4154, doi:10.1175/JAS-D-12-0124.1.

Heymsfield, A. J., C. Schmitt, A. Bansemer, and C. H. Twohy, 2010: Improved representation of ice particle masses based on observations in natural clouds. *J. Atmos. Sci.*, **67 (10)**, 3303–3318, doi:10.1175/2010JAS3507.1.

Heymsfield, A. J., and C. D. Westbrook, 2010: Advances in the estimation of ice particle fall speeds using laboratory and field measurements. *J. Atmos. Sci.*, **67 (8)**, 2469–2482, doi:10.1175/2010JAS3379.1.

Hobbs, P. V., S. Chang, and J. D. Locatelli, 1974: The dimensions and aggregation of ice crystals in natural clouds. *J. Geophys. Res.*, **79 (15)**, 2199–2206, doi:10.1029/JC079i015p02199.

Hogan, R. J., L. Tian, P. R. A. Brown, C. D. Westbrook, A. J. Heymsfield, and J. D. Eastment, 2012: Radar scattering from ice aggregates using the horizontally aligned oblate spheroid approximation. *J. Appl. Meteor. Climatol.*, **51 (3)**, 655–671, doi:10.1175/JAMC-D-11-074.1.

Jackson, R. C., and G. M. McFarquhar, 2014: An assessment of the impact of antishattering tips and artifact removal techniques on bulk cloud ice microphysical and optical properties measured by the 2D Cloud Probe. *J. Atmos. Oceanic Technol.*, doi:10.1175/JTECH-D-14-00018.1.

Jackson, R. C., G. M. McFarquhar, J. Stith, M. Beals, R. A. Shaw, J. Jensen, J. Fugal, and A. Korolev, 2014: An assessment of the impact of anti-shattering tips and artifact removal techniques on cloud ice size distributions measured by the 2D Cloud Probe. *J. Atmos. Oceanic Technol.*, doi:10.1175/JTECH-D-13-00239.1.

Jackson, R. C., and Coauthors, 2012: The dependence of ice microphysics on aerosol concentration in Arctic mixed-phase stratus clouds during ISDAC and M-PACE. *J. Geophys. Res.*, **117 (D15)**, D15 207, doi:10.1029/2012JD017668.

Kalesse, H., P. Kollias, and W. Szyrmer, 2013: On using the relationship between Doppler velocity and radar reflectivity to identify microphysical processes in midlatitudinal ice clouds. *J. Geophys. Res.*, **118 (21)**, 12,168–12,179, doi:10.1002/2013JD020386.

Kneifel, S., M. S. Kulie, and R. Bennartz, 2011: A triple-frequency approach to retrieve microphysical snowfall parameters. *J. Geophys. Res.*, **116 (D11)**, doi:10.1029/2010JD015430.

Kollias, P., E. E. Clothiaux, M. A. Miller, E. P. Luke, K. L. Johnson, K. P. Moran, K. B. Widener, and B. A. Albrecht, 2007: The atmospheric radiation measurement program cloud profiling radars: Second-generation sampling strategies, processing, and cloud data products. *J. Atmos. Oceanic Technol.*, **24 (7)**, doi:10.1175/JTECH2033.1.

Kollias, P., J. Rmillard, E. Luke, and W. Szyrmer, 2011a: Cloud radar Doppler spectra in drizzling stratiform clouds: 1. Forward modeling and remote sensing applications. *J. Geophys. Res.*, **116 (D13)**, D13 201, doi:10.1029/2010JD015237.

Kollias, P., W. Szyrmer, J. Rmillard, and E. Luke, 2011b: Cloud radar Doppler spectra in drizzling stratiform clouds: 2. Observations and microphysical modeling of drizzle evolution. *J. Geophys. Res.*, **116 (D13)**, D13 203, doi:10.1029/2010JD015238.

Korolev, A., E. Emery, and K. Creelman, 2013a: Modification and tests of particle probe tips to mitigate effects of ice shattering. *J. Atmos. Oceanic Technol.*, **30 (4)**, 690–708, doi:10.1175/JTECH-D-12-00142.1.

Korolev, A., and G. Isaac, 2003: Roundness and aspect ratio of particles in ice clouds. *J. Atmos. Sci.*, **60 (15)**, 1795–1808, doi:10.1175/1520-0469(2003)060⟨1795:RAAROP⟩2.0.CO;2.

Korolev, A., and G. A. Isaac, 2005: Shattering during sampling by OAPs and HVPS. Part I: Snow particles. *J. Atmos. Oceanic Technol.*, **22 (5)**, 528–542, doi:10.1175/JTECH1720.1.

Korolev, A. V., E. F. Emery, J. W. Strapp, S. G. Cober, and G. A. Isaac, 2013b: Quantification of the effects of shattering on airborne ice particle measurements. *J. Atmos. Oceanic Technol.*, **30 (11)**, 2527–2553, doi:10.1175/JTECH-D-13-00115.1.

Korolev, A. V., E. F. Emery, J. W. Strapp, S. G. Cober, G. A. Isaac, M. Wasey, and D. Marcotte, 2011: Small ice particles in tropospheric clouds: Fact or artifact? Airborne icing instrumentation evaluation experiment. *Bull. Amer. Meteor. Soc.*, **92 (8)**, 967–973, doi:10.1175/2010BAMS3141.1.

Korolev, A. V., J. W. Strapp, G. A. Isaac, and A. N. Nevzorov, 1998: The Nevzorov airborne hot-wire LWC-TWC probe: Principle of operation and performance characteristics. *J. Atmos. Oceanic Technol.*, **15 (6)**, 1495–1510, doi:10.1175/1520-0426(1998)015⟨1495:TNAHWL⟩2.0.CO;2.

Lamer, K., A. Tatarevic, I. Jo, and P. Kollias, 2014: Evaluation of gridded scanning ARM cloud radar reflectivity observations and vertical Doppler velocity retrievals. *Atmos. Meas. Tech.*, **7 (4)**, 1089–1103, doi:10.5194/amt-7-1089-2014.

Lawson, R. P., 2011: Effects of ice particles shattering on the 2D-S probe. *Atmos. Meas. Tech.*, **4 (7)**, 1361–1381, doi:10.5194/amt-4-1361-2011.

Libbrecht, K. G., 2005: The physics of snow crystals. *Rep. Prog. Phys.*, **68 (4)**, 855, doi:10.1088/0034-4885/68/4/R03.

Liu, G., 2008: A database of microwave single-scattering properties for nonspherical ice particles. *Bull. Amer. Meteor. Soc.*, **89 (10)**, 1563–1570, doi:10.1175/2008BAMS2486.1.

Locatelli, J. D., and P. V. Hobbs, 1974: Fall speeds and masses of solid precipitation particles. *J. Geophys. Res.*, **79 (15)**, 2185–2197, doi:10.1029/JC079i015p02185.

Löhnert, U., S. Kneifel, A. Battaglia, M. Hagen, L. Hirsch, and S. Crewell, 2011: A multisensor approach toward a better understanding of snowfall microphysics: The TOSCA project. *Bull. Amer. Meteor. Soc.*, **92 (5)**, 613–628, doi:10.1175/2010BAMS2909.1.

Luke, E. P., P. Kollias, and M. D. Shupe, 2010: Detection of supercooled liquid in mixed-phase clouds using radar Doppler spectra. *J. Geophys. Res.*, **115 (D19)**, D19 201, doi:201010.1029/2009JD012884.

Maahn, M., and P. Kollias, 2012: Improved Micro Rain Radar snow measurements using Doppler spectra post-processing. *Atmos. Meas. Tech.*, **5 (11)**, 2661–2673, doi:10.5194/amt-5-2661-2012.

Magono, C., and C. W. Lee, 1966: Meteorological classification of natural snow crystals. *J Fac. Sci., Hokkaido Univ., Ser. 7*, **2 (4)**, 321–335.

Massey, F. J., Jr., 1951: The Kolmogorov-Smirnov test for goodness of fit. *J. Amer. Statist. Assoc.*, **46 (253)**, 68–78, doi:10.2307/2280095.

Matrosov, S. Y., 2007: Modeling backscatter properties of snowfall at millimeter wavelengths. *J. Atmos. Sci.*, **64 (5)**, 1727–1736, doi:10.1175/JAS3904.1.

Matrosov, S. Y., A. V. Korolev, and A. J. Heymsfield, 2002: Profiling cloud ice mass and particle characteristic size from Doppler radar

measurements. *J. Atmos. Oceanic Technol.*, **19 (7)**, 1003–1018, doi:10.1175/1520-0426(2002)019⟨1003:PCIMAP⟩2.0.CO;2.

McFarquhar, G., and Coauthors, 2011: Indirect and semi-direct aerosol campaign: The impact of Arctic aerosols on clouds. *Bull. Amer. Meteor. Soc.*, **92 (2)**, doi:10.1175/2010BAMS2935.1.

McFarquhar, G. M., T.-L. Hsieh, M. Freer, J. Mascio, and B. F. Jewett, 2014: The characterization of ice hydrometeor gamma size distributions as volumes in N0/Lambda/gamma phase space: implications for microphysical process modeling. *J. Atmos. Sci.*, doi:10.1175/JAS-D-14-0011.1.

Mech, M., M. Maahn, E. Orlandi, S. Kneifel, P. Kollias, S. Redl, and S. Crewell, 2015: PAMTRA - passive and active microwave radiative transfer model. *Atmos. Chem. Phys.*, **in preparation**.

Melchionna, S., M. Bauer, and G. Peters, 2008: A new algorithm for the extraction of cloud parameters using multipeak analysis of cloud radar data - first application and preliminary results. *Meteor. Z.*, **17 (5)**, 613–620, doi:10.1127/0941-2948/2008/0322.

Mishchenko, M. I., 2000: Calculation of the amplitude matrix for a nonspherical particle in a fixed orientation. *Appl. Opt.*, **39 (6)**, 1026–1031, doi:10.1364/AO.39.001026.

Mitchell, D. L., 1996: Use of mass- and area-dimensional power laws for determining precipitation particle terminal velocities. *J. Atmos. Sci.*, **53 (12)**, 1710–1723, doi:10.1175/1520-0469(1996)053⟨1710:UOMAAD⟩2.0.CO;2.

Mitchell, D. L., R. Zhang, and R. L. Pitter, 1990: Mass-dimensional relationships for ice particles and the influence of riming on snowfall rates. *J. Appl. Meteor.*, **29 (2)**, 153–163, doi:10.1175/1520-0450(1990)029⟨0153:MDRFIP⟩2.0.CO;2.

Moninger, W. R., S. G. Benjamin, B. D. Jamison, T. W. Schlatter, T. L. Smith, and E. J. Szoke, 2009: Evaluation of regional aircraft observations using TAMDAR. *Wea. Forecasting*, **25 (2)**, 627–645, doi:10.1175/2009WAF2222321.1.

Moran, K. P., B. E. Martner, M. J. Post, R. A. Kropfli, D. C. Welsh, and K. B. Widener, 1998: An unattended cloud-profiling radar for use in climate research. *Bull. Amer. Meteor. Soc.*, **79 (3)**, 443–455, doi:10.1175/1520-0477(1998)079⟨0443:AUCPRF⟩2.0.CO;2.

Morrison, H., G. de Boer, G. Feingold, J. Harrington, M. D. Shupe, and K. Sulia, 2012: Resilience of persistent Arctic mixed-phase clouds. *Nat. Geosci.*, **5 (1)**, 11–17, doi:10.1038/ngeo1332.

Nastrom, G. D., 1997: Doppler radar spectral width broadening due to beamwidth and wind shear. *Annales Geophysicae*, **15 (6)**, 786–796, doi:10.1007/s00585-997-0786-7.

Noone, K. J., J. A. Ogren, J. Heintzenberg, R. J. Charlson, and D. S. Covert, 1988: Design and calibration of a counterflow virtual impactor for sampling of atmospheric fog and cloud droplets. *Aerosol Sci. Technol.*, **8 (3)**, 235–244, doi:10.1080/02786828808959186.

Petty, G. W., 2001: Physical and microwave radiative properties of precipitating clouds. Part II: a parametric 1D rain-cloud model for use in microwave radiative transfer simulations. *J. Appl. Meteor.*, **40 (12)**, 2115–2129, doi:10.1175/1520-0450(2001)040⟨2115:PAMRPO⟩2.0.CO;2.

Petty, G. W., and W. Huang, 2010: Microwave backscatter and extinction by soft ice spheres and complex snow aggregates. *J. Atmos. Sci.*, **67 (3)**, 769–787, doi:10.1175/2009JAS3146.1.

Petty, G. W., and W. Huang, 2011: The modified gamma size distribution applied to inhomogeneous and nonspherical particles: Key relationships and conversions. *J. Atmos. Sci.*, **68 (7)**, 1460–1473, doi:10.1175/2011JAS3645.1.

Posselt, D. J., and G. G. Mace, 2014: MCMC-based assessment of the error characteristics of a surface-based combined radar-passive microwave cloud property retrieval. *J. Appl. Meteor. Climatol.*, **53 (8)**, 2034–2057, doi:10.1175/JAMC-D-13-0237.1.

Protat, A., D. Bouniol, E. J. O'Connor, H. Klein Baltink, J. Verlinde, and K. Widener, 2011: CloudSat as a global radar calibrator. *J. Atmos. Oceanic Technol.*, **28 (3)**, 445–452, doi:10.1175/2010JTECHA1443.1.

Rodgers, C. D., 2000: *Inverse Methods for Atmospheric Sounding : Theory and Practice*. World Scientific Publishing Company.

Schmitt, C. G., and A. J. Heymsfield, 2010: The dimensional characteristics of ice crystal aggregates from fractal geometry. *J. Atmos. Sci.*, **67 (5)**, 1605–1616, doi:10.1175/2009JAS3187.1.

Schneider, T. L., and G. L. Stephens, 1995: Theoretical aspects of modeling backscattering by cirrus ice particles at millimeter wavelengths. *J. Atmos. Sci.*, **52 (23)**, 4367–4385, doi:10.1175/1520-0469(1995)052⟨4367:TAOMBB⟩2.0.CO;2.

Shupe, M. D., P. Kollias, S. Y. Matrosov, and T. L. Schneider, 2004: Deriving mixed-phase cloud properties from Doppler radar spectra. *J. Atmos. Oceanic Technol.*, **21 (4)**, 660–670, doi:10.1175/1520-0426(2004)021⟨0660:DMCPFD⟩2.0.CO;2.

Shupe, M. D., P. Kollias, M. Poellot, and E. Eloranta, 2008: On deriving vertical air motions from cloud radar Doppler spectra. *J. Atmos. Oceanic Technol.*, **25 (4)**, 547–557, doi:10.1175/2007JTECHA1007.1.

Sloss, P. W., and D. Atlas, 1968: Wind shear and reflectivity gradient effects on Doppler radar spectra. *J. Atmos. Sci.*, **25 (6)**, 1080–1089, doi:10.1175/1520-0469(1968)025⟨1080:WSARGE⟩2.0.CO;2.

Sreenivasan, K. R., 1995: On the universality of the Kolmogorov constant. *Phys. Fluids*, **7 (11)**, 2778–2784, doi:10.1063/1.868656.

Stephens, G. L., and Coauthors, 2008: CloudSat mission: Performance and early science after the first year of operation. *J. Geophys. Res.*, **113 (D8)**, D00A18, doi:10.1029/2008JD009982.

Szyrmer, W., A. Tatarevic, and P. Kollias, 2012: Ice clouds microphysical retrieval using 94-GHz Doppler radar observations: Basic relations within the retrieval framework. *J. Geophys. Res.*, **117 (D14)**, D14 203, doi:10.1029/2011JD016675.

Testud, J., S. Oury, R. A. Black, P. Amayenc, and X. Dou, 2001: The concept of normalized distribution to describe raindrop spectra: A tool for cloud physics and cloud remote sensing. *J. Appl. Meteor.*, **40 (6)**, 1118–1140, doi:10.1175/1520-0450(2001)040⟨1118:TCONDT⟩2.0.CO;2.

Tian, L., G. M. Heymsfield, L. Li, A. J. Heymsfield, A. Bansemer, C. H. Twohy, and R. C. Srivastava, 2010: A study of cirrus ice particle size distribution using TC4 observations. *J. Atmos. Sci.*, **67 (1)**, 195–216, doi:10.1175/2009JAS3114.1.

Turner, D. D., and U. Löhnert, 2014: Information content and uncertainties in thermodynamic profiles and liquid cloud properties retrieved from the ground-based atmospheric emitted radiance interferometer (AERI). *J. Appl. Meteor. Climatol.*, **53 (3)**, 752–771, doi:10.1175/JAMC-D-13-0126.1.

Tyynelä, J., J. Leinonen, D. Moisseev, and T. Nousiainen, 2011: Radar backscattering from snowflakes: Comparison of fractal, aggregate, and soft spheroid models. *J. Atmos. Oceanic Technol.*, **28 (11)**, 1365–1372, doi:10.1175/JTECH-D-11-00004.1.

Verlinde, J., M. P. Rambukkange, E. E. Clothiaux, G. M. McFarquhar, and E. W. Eloranta, 2013: Arctic multilayered, mixed-phase cloud processes revealed in millimeter-wave cloud radar Doppler spectra. *J. Geophys. Res.*, **118 (23)**, 2013JD020 183, doi:10.1002/2013JD020183.

Waliser, D. E., and Coauthors, 2009: Cloud ice: A climate model challenge with signs and expectations of progress. *J. Geophys. Res.*, **114 (D8)**, D00A21, doi:10.1029/2008JD010015.

Warren, S. G., and R. E. Brandt, 2008: Optical constants of ice from the ultraviolet to the microwave: A revised compilation. *J. Geophys. Res.*, **113 (D14)**, D14 220, doi:10.1029/2007JD009744.

Zhang, M. H., and Coauthors, 2005: Comparing clouds and their seasonal variations in 10 atmospheric general circulation models with satellite measurements. *J. Geophys. Res.*, **110 (D15)**, D15S02, doi:10.1029/2004JD005021.

Zrnić, D. S., 1975: Simulation of weatherlike Doppler spectra and signals. *J. Appl. Meteor.*, **14 (4)**, 619–620, doi:10.1175/1520-0450(1975)014⟨0619:SOWDSA⟩2.0.CO;2.

8

ADDITIONAL STUDY II: RETRIEVAL POTENTIAL

Here, the forward operator presented in Additional Study I is used together with the data set developed in Publication III to investigate the potential of higher radar moments for enhancing ice cloud retrievals. The data set contains parameterizations and corresponding coefficients of ice clouds.

8.1 INTRODUCTION

Even though radars offer great potential for observing ice clouds due to their ability to penetrate ice clouds, the desired cloud properties cannot be measured directly. Instead, radar measurements need to be transferred from measurement space into the desired state space using a retrieval. Commonly, radar measurements do not contain sufficient information to constrain the state space unambiguously, resulting in large uncertainties of radar retrievals. For example, this can be seen from the great spread of empirically and theoretically derived reflectivity-ice water content relations (Figure 5). Different strategies are used to increase the number of independent information pieces: some studies used radar-microwave radiometer combinations (*Grecu and Olson*, 2008; *Posselt and Mace*, 2014), radar-lidar combinations (*Intrieri et al.*, 1993; *Delanoë and Hogan*, 2008), or multiple radars operating at different frequencies (*Hogan et al.*, 2000; *Kulie et al.*, 2014). For single instrument retrievals, studies propose to exploit not only radar reflectivity Z_e, but also mean Doppler velocity W (*Matrosov et al.*, 2002; *Szyrmer et al.*, 2012) and Doppler spectrum width σ (*Mace et al.*, 2002; *Deng and Mace*, 2006) of zenith pointing radars.

In this study, reflectivity Z_e, mean Doppler velocity W, and Doppler spectrum width σ are called lower moments while skewness Sk, kurtosis Ku and left S_l and right slope S_r are referred to as higher moments even though the slopes are technically no moments.

This study goes one step further and investigates the potential of adding the higher radar moments skewness Sk and kurtosis Ku as well as the left slope S_l and the right slope S_r to the retrieval (see Section 3.3.4 for definitions). In contrast to reflectivity Z_e, higher moments do not depend strongly on radar calibration, and in contrast to mean Doppler velocity W, they are not biased by the vertical wind. Higher moments are, however, highly shaped by turbulence which needs to be considered.

The structure of this chapter is as follows: firstly, the response functions of lower and higher moments to quantities describing ice cloud microphysics are analyzed. Secondly, the number of independent information pieces which higher moments can add to an ice cloud retrieval is estimated. These analyses are performed for different turbulence strengths, radar configurations, and sets of radar moments.

8.2 RESPONSE FUNCTIONS

In order to investigate the impact of the microphysical properties on the radar moments, response functions are estimated for all radar moments and slopes. For this, the parameterizations, coefficients, and data sets developed in Publication III are used. Hereby, the focus is more on a qualitative than on a quantitative analysis in order to get an "idea" of how radar moments depend on the various ice cloud properties.

8.2.1 *Data set*

The particle size distribution $N(D)$ is estimated using the normalized gamma distribution approach by *Testud et al.* (2001) and *Delanoë et al.* (2005) with maximum dimension D as size descriptor as introduced in Publication III

$$N(D) = N_0^* \frac{(b+\mu+1)^{b+\mu+1}\Gamma(b+1)}{\Gamma(b+\mu+1)(b+1)^{b+1}} \left(\frac{D}{D_m}\right)^{\mu} e^{-(b+\mu+1)D/D_m} \quad (31)$$

where N_0^* is the intercept parameter, D_m is the mass–weighted scaling parameter, μ describes the shape of the distribution, Γ is the gamma function, and b is the exponent of the mass-size relation. Note that in the following, μ is replaced by $\mu^* = \mu + 1 + b$ to increase the numerical stability of the gamma function when using it within a retrieval. Particle mass is expressed by a normalized power law as proposed by *Szyrmer et al.* (2012)

$$m(D) = \alpha\, C_0\, (D/D^*)^b \quad (32)$$

where D^* and C_0 describe a reference particle size and mass, respectively, and α is a dimensionless factor. In accordance with *Szyrmer et al.* (2012) and Publication III, D^* and C_0 are set to 1.2 mm and 3×10^{-5} g, respectively. In comparison to the common power law formulation of the mass-size relation, the normalized version is more robust to variations of the parameters, but still has two degrees of freedom. The projected area $A(D)$ is described with a power law

$$A(D) = c \cdot D^d \quad (33)$$

with pre-factor c and exponent d. Additional noise—as proposed in Publication III—is not applied for the sake of convenience and because it is expected that the additional noise has only minor impact on the response functions.

The response functions are analyzed for the seven coefficients of the parameterizations of $N(D)$ (N_0, D_m, μ^*), $A(D)$ (c, d) and $m(D)$ (α, b). As an eighth quantity, the effect of aspect ratio AR is studied. The boundaries of the particle size distribution D_{min} and D_{max} are fixed to

0.05 mm and 12.8 mm, respectively, because it is found in Publication III that variable boundaries are not required.

The response functions of the coefficients of $N(D)$ and $A(D)$ are estimated for a range of ± 1 standard deviation around the mean value of values found in the ISDAC data set presented in Publication III. The coefficients of $m(D)$ are perturbed according to the range of temperature-dependent coefficients found in Publication III, and aspect ratio AR is varied from 0.4 to 0.8. To obtain the radar moments, the PAMTRA model (Additional Study I) is configured based on the technical specifications of the MMCR radar in Barrow (*Moran et al.*, 1998).

The kinematic broadening of the radar spectrum σ_k has high impact on the higher moments (Equation 25). For the response functions, σ_k is estimated assuming a constant horizontal wind of $10\,m\,s^{-1}$ and—as found in Publication III based on aircraft measurements—a fixed Eddy dissipation rate ϵ of $10^{-6}\,m^2s^{-3}$ (corresponding to a turbulence broadening σ_k of $0.01\,m\,s^{-1}$). In addition, also higher turbulence levels $1.25 \times 10^{-4}\,m^2s^{-3}$ and $10^{-3}\,m^2s^{-3}$ (corresponding to $\sigma_k = 0.06\,m\,s^{-1}$ and $\sigma_k = 0.11\,m\,s^{-1}$, respectively) are investigated. Though all three turbulence levels are comparatively small (*Gultepe and Starr*, 1995), they are within the range $10^{-7}\,m^2s^{-3}$ to $10^{-3}\,m^2s^{-3}$ found by *Shupe et al.* (2012) for the *Mixed-Phase Arctic Cloud Experiment* (MPACE, *Verlinde et al.*, 2007). This campaign also took place around Barrow and featured cloud types similar to the ones found for ISDAC. In the following, the three turbulence levels are described as "low", "medium" and "large", even though this applies only to Arctic stratocumulus clouds and much higher turbulence levels can occur for e. g., convective clouds (*Gultepe and Starr*, 1995).

8.2.2 *Results*

The response functions showing the impact of the parameters on the higher moments are presented in Figures 9 and 10 for the three turbulence levels. To assess their uncertainty and to investigate whether the moments are stable with respect to radar noise, the analysis is repeated 1000 times. The resulting uncertainty range indicated by the 10% and 90% percentiles is shown in addition to the median value. Reflectivity Z_e (Figures 9.a and 10.a) depends strongly on D_m and N_0^*, but not on the shape parameter μ^* and not on the coefficients of the area-size relation, because the latter only influences the fall velocity relation, but not the scattering of the particles. Furthermore, Z_e is affected by the coefficients of the normalized mass-size relation α and b. The aspect ratio AR has only a very small influence on Z_e (less than 1 dB difference between 0.4 and 0.8) which confirms the result of Publication III (Appendix B1) that a fixed aspect ratio can be assumed.

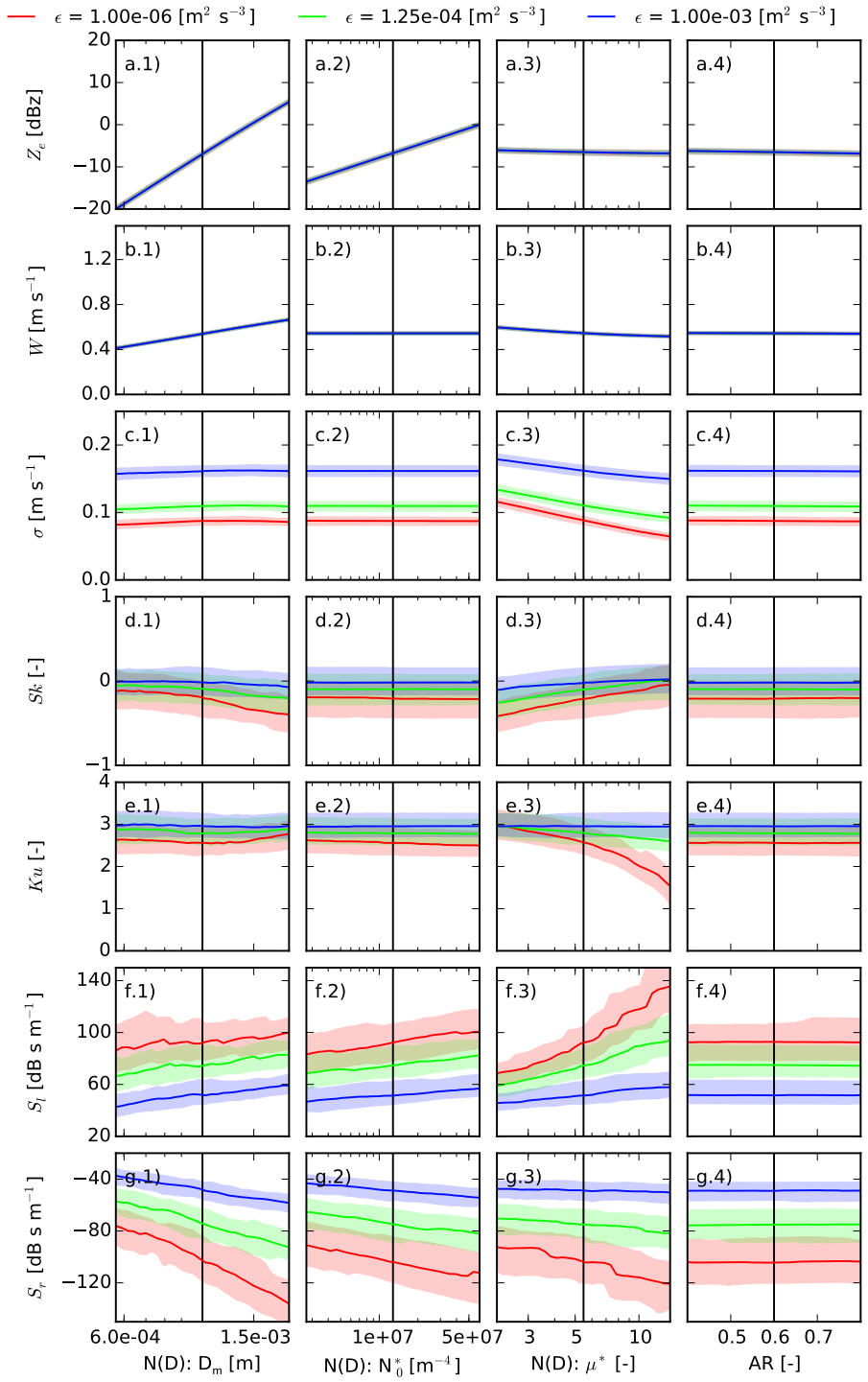

Figure 9: Impact of the parameters D_m, N_0^*, and μ^* of the normalized gamma distribution for $N(D)$ and the aspect ratio AR (columns) on MMCR moments (rows) for the turbulence levels 10^{-6} m²s^{-3} (red), 1.25×10^{-4} m²s^{-3} (green), and 10^{-3} m²s^{-3} (blue). If large enough, the uncertainties of the higher moments (10% and 90% percentiles) caused by radar noise are indicated as colored area around the median values. The black vertical line denotes the mean value of the coefficients found in Publication III.

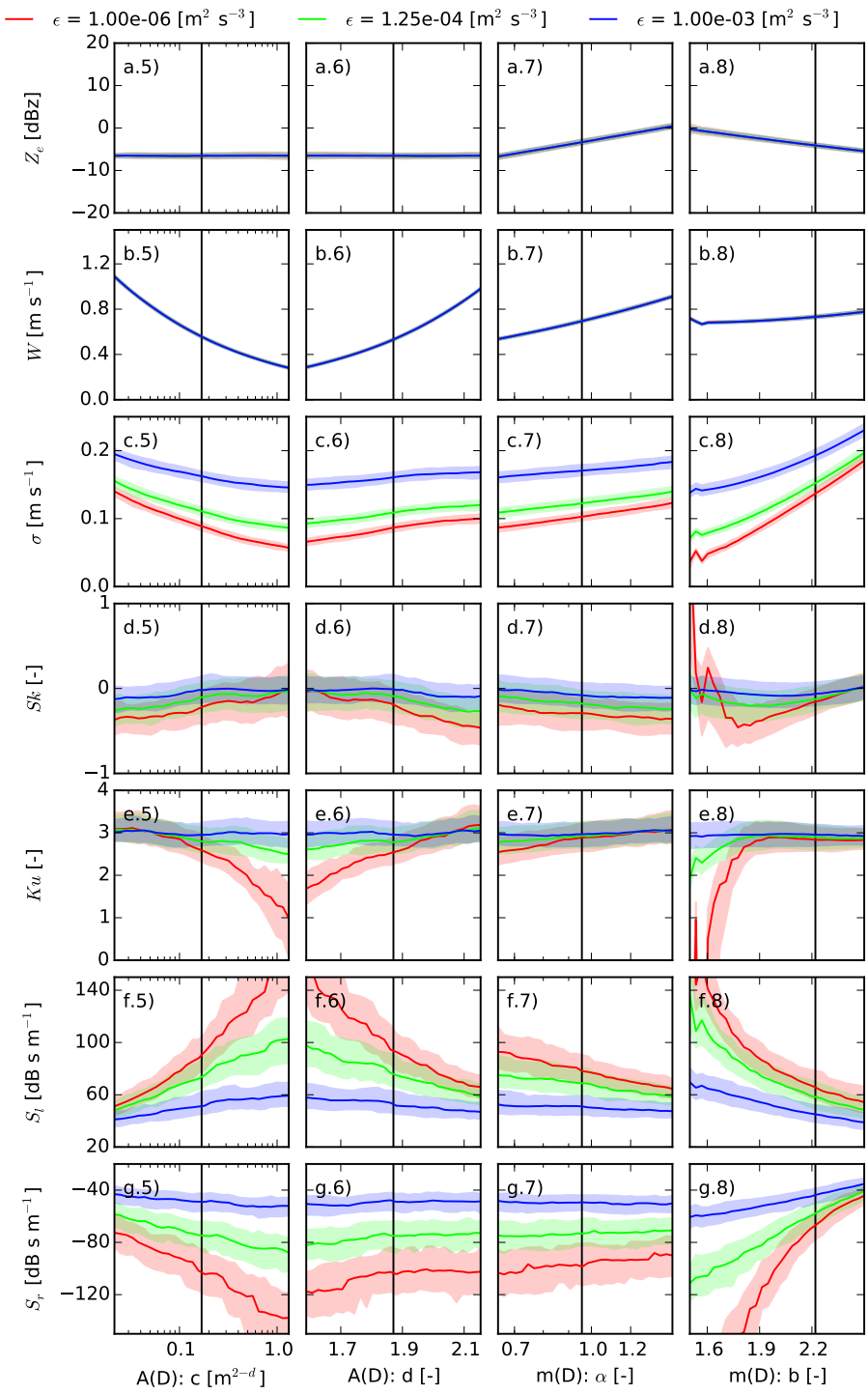

Figure 10: Same as Figure 9, but for c and d of the area-size relation as well as for α and b^* of the normalized mass-size relation. For $A(D)$, the black vertical line denotes the mean value of the coefficients found in Publication III and for $m(D)$ the line denotes the coefficients found in Publication III for the complete data set without considering temperature.

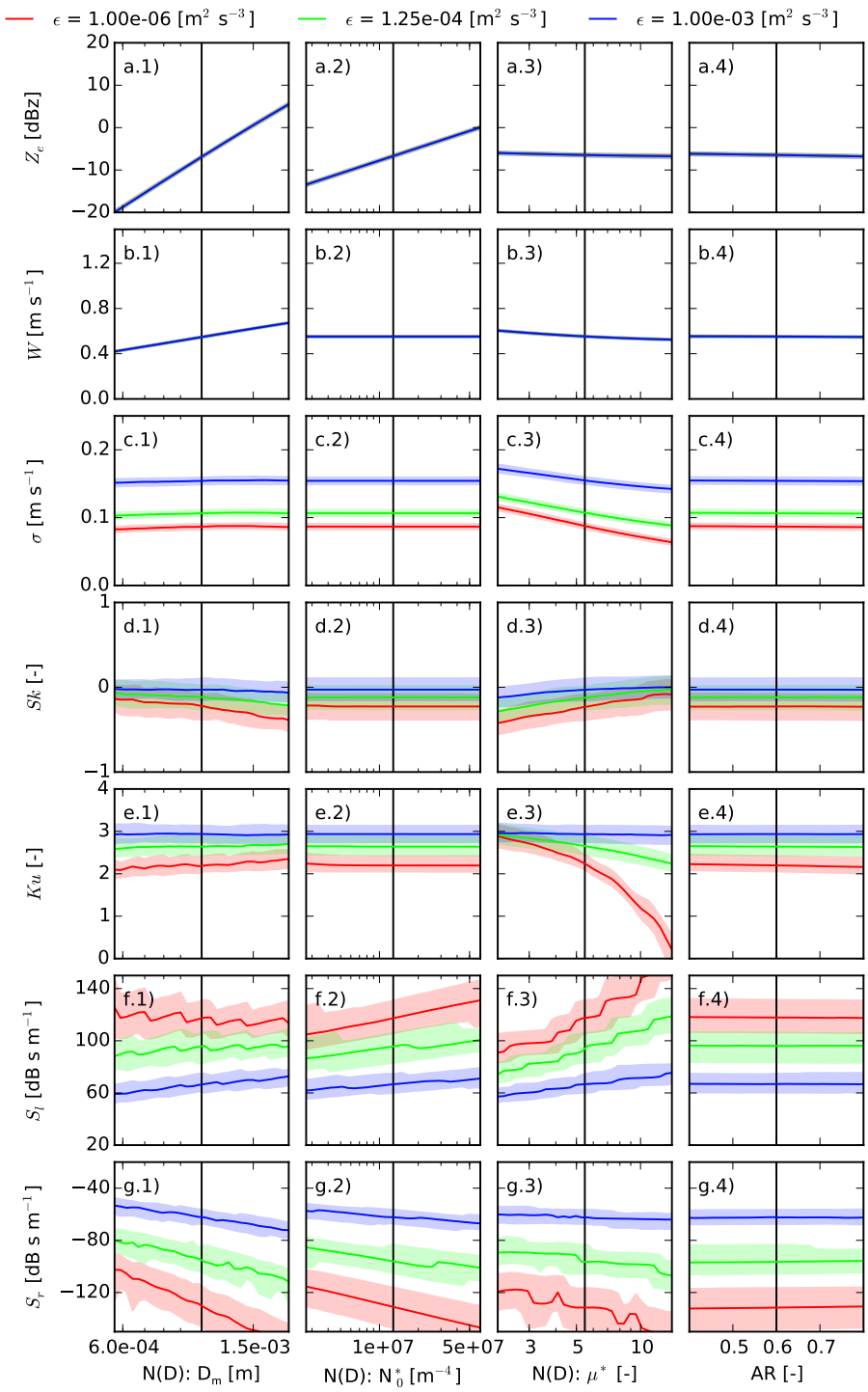

Figure 11: Same as Figure 9, but for the KAZR.

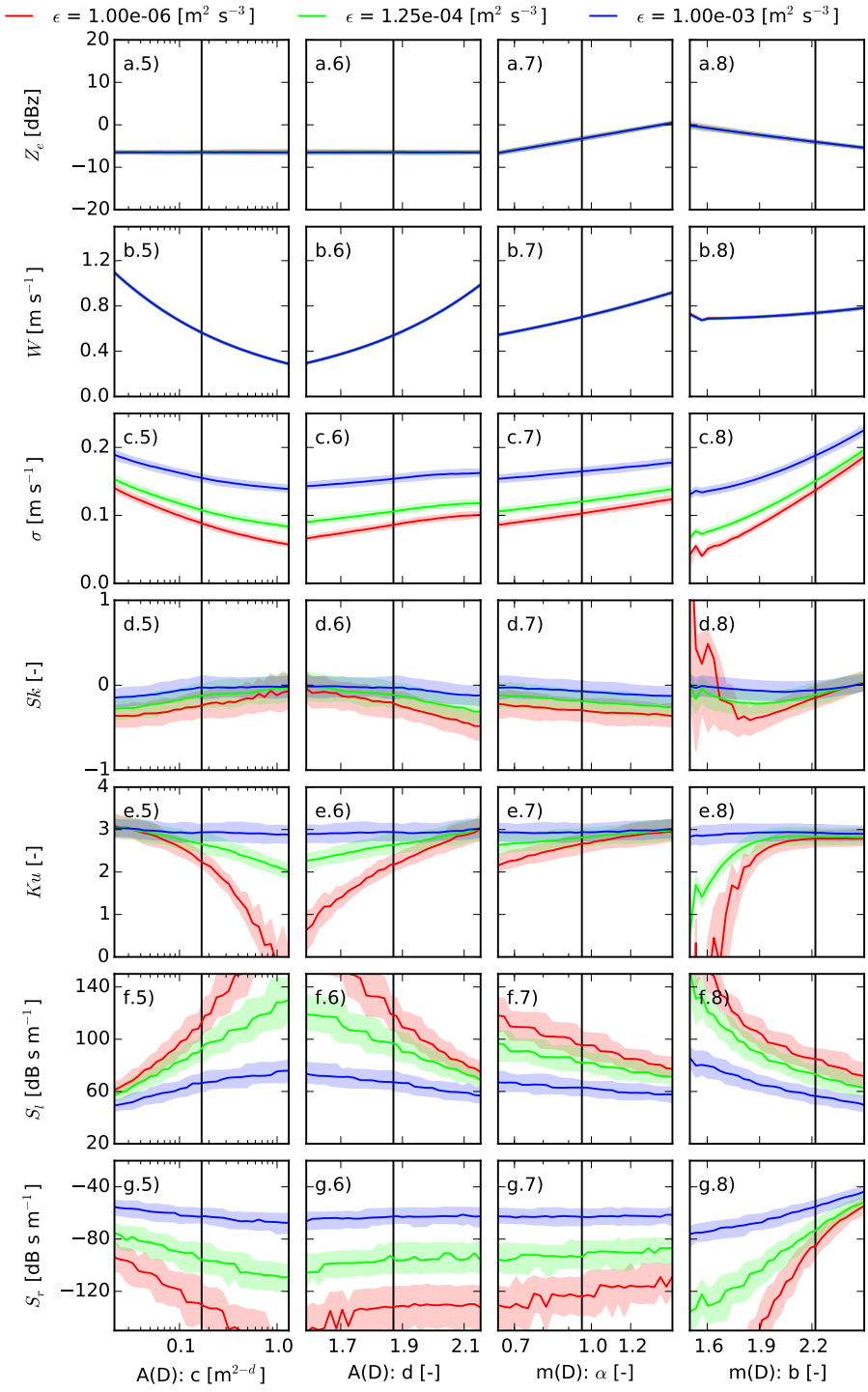

Figure 12: Same as Figure 10, but for the KAZR.

Because the influence of AR on the other radar moments is even less, it is not further discussed.

Mean Doppler velocity W (Figures 9.b and 10.b) depends on both mass-size and area-size coefficients via the fall velocity relation. The response of W to the area-size coefficients is particularly strong, but this can be considered as an artifact, because c and d are strongly correlated, which in reality partly compensates the change of W. To account for this, it would be possible to develop a normalized area-size relation similar to the concept of *Szyrmer et al.* (2012) for the mass-size relation. Regarding $N(D)$, W depends only on D_m, but not on N_0^*, because scaling in the direction of number concentration and particle size are clearly separated when using the normalized gamma distribution approach (Publication III, Appendix A). The shape parameter μ^* has only little impact on W.

In contrast to Z_e and W, Doppler spectrum width σ (Figures 9.c and 10.c) depends strongly on the assumed turbulence level, which causes an offset of σ, but has only little influence on the response functions of the various microphysical parameters. Apart from the coefficients of the area-size and mass-size relation, σ also depends on the shape parameter μ^*, but not on D_m and N_0^*.

While the response functions of the lower radar moments to ice cloud properties have already been exploited by other studies (e. g., *Mace et al.*, 2002; *Matrosov et al.*, 2002), to the author's knowledge the use of higher moments has not yet been investigated.

Skewness (Figures 9.d and 10.d) is influenced by all parameters but N_0^*. However, the response is rather small (with the exception of b) in comparison to the other radar moments and the interval of estimated uncertainty (~0.25) is often of similar size as the response. Only for b, the response is greater than 1, but also very non-linear and not monotonic. Because increasing turbulence leads to a more Gaussian shape of the peak with values around zero for Sk, the response functions are reduced for the medium turbulence level. For the high turbulence level, the response is less than the estimated uncertainty range for all parameters even though the uncertainty of Sk is reduced.

Kurtosis Ku (Figures 9.e and 10.e) is mainly determined by the shape parameter μ^* and the coefficients of the area-size and mass-size relations leading to a response of up to 3. This is larger than the uncertainty of Ku (~0.4). The response to b is, however, saturated for values greater than 1.9. Similar to Sk, the response of Ku is reduced for the medium turbulence level. For the highest turbulence level, Ku has—like a Gaussian distribution—generally a value of 3 and the response functions are greatly reduced and smaller than the uncertainties.

The left slope S_l (Figures 9.f and 10.f) responds to all parameters, but only for μ^*, b, c, and d, the response is greater than the uncertainty estimate of up to $20\,\mathrm{dB\,s\,m^{-1}}$. In comparison to Sk and Ku, the

uncertainty appears larger, because the slopes are obtained from the Doppler spectrum in logarithmic scale which increases the impact of the radar noise. The "real" moments, contrary, are estimated from the spectrum in linear scale. The steps in the response function are caused by the discrete Doppler velocity bins of the radar resulting in "jumps" of the left and right edge of the detected Doppler peak. Similar to Sk and Ku, the response functions are reduced for the medium and high turbulence intervals and often within or close to the noise estimate. The uncertainty estimate is, however, reduced for the higher turbulence and hence, S_l might even be better exploitable by a retrieval in higher turbulence conditions despite the smaller response functions.

The response functions of the right slope S_r (Figures 9.g and 10.g), which is mainly determined by the fastest falling particles, are similar to S_l with respect to noise and with respect to steps. For the lowest turbulence level, the response outweighs the noise for D_m, b, and c. For the latter, the response is significant also for the highest turbulence level.

8.2.3 *Results for a more advanced radar*

In order to investigate whether the uncertainty of the higher moments can be reduced when using a more advanced radar, the response functions are estimated using the technical specifications of the *K_a-band ARM Zenith Radar* (KAZR) instead of the MMCR. The KAZR replaced the MMCR in Barrow in 2011 and features a noise level reduced by approximately 18 dB. In addition, the spectrum is expected to be more smooth, because the KAZR spectrum is averaged 20 as opposed to of 10 times (Table 2) even though its effective integration time is reduced from 1.4 s to 1 s in comparison to the MMCR. This limits the impact of turbulent broadening onto the radar spectrum (Equation 29).

The response functions based on the KAZR settings are shown in Figures 11 and 12. While the new radar settings have no impact on the lower moments (Figures 11.a-c and 12.a-c), the uncertainty estimates of skewness Sk and kurtosis Ku are reduced and the corresponding response functions are enlarged (Figures 11.d-e and 12.d-e). As a consequence, it is expected that Sk and Ku are more useful for ice cloud retrievals when using a more advanced radar. Only for the response of Sk to b, the uncertainty estimate is strongly increased for the KAZR which requires further investigations. In comparison to Sk and Ku, the slopes are enhanced less with respect to uncertainty and the response functions (Figures 11.f-g and 12.f-g), but an improvement is visible. As a disadvantage, the steps in the response functions of the slopes caused by the "jumps" of the edges of the peak are more strongly pronounced—probably because they are less "hidden" by the reduced noise level of the KAZR.

Table 2: Specifications of the boundary layer mode of the MMCR and KAZR radars. Information obtained from *Moran et al.* (1998), *Kollias et al.* (2007a), and *P. Kollias* (personal communication).

	MMCR	KAZR
Frequency [GHz]	35	35
Nyquist velocity [$m\,s^{-1}$]	5.27	5.96
Noise level at 1 km [dB]	-32	-50
Number of spectral averages	10	20
Number of FFT points	256	256
Effective integration time [s]	1.4	1

8.3 DEGREES OF FREEDOM FOR SIGNAL

Following the quantitative analysis presented above, optimal estimation theory (*Rodgers*, 2000) is used here in order to quantify qualitatively how much information lower and higher moments can contribute to ice cloud retrievals.

8.3.1 *Retrieval setup*

Optimal estimation is a Bayesian retrieval technique based on a Gaussian statistical model which combines the observation vector $\mathbf{y}$ of length M with prior information to estimate the state vector $\mathbf{x}$ of dimension N. Optimal estimation requires that the forward operator P is moderately linear and that the probability density distributions of state vector $\mathbf{x}$ and the errors of the observation vector $\mathbf{y}$ follow a Gaussian shape. Then, the optimal solution of $\mathbf{x}$ can be found by an iterative procedure where the updated state vector $\mathbf{x}_{i+1}$ is obtained with

$$\mathbf{x}_{i+1} = \mathbf{x}_a + (\gamma_i \, \mathbb{S}_a^{-1} + \mathbb{K}_i^T \mathbb{S}_e^{-1} \mathbb{K}_i^T)^{-1} \mathbb{K}_i \, \mathbb{S}_e^{-1} [\mathbf{y} - P(\mathbf{x}_i) + \mathbb{K}_i (\mathbf{x}_i - \mathbf{x}_a)] \tag{34}$$

where $\mathbf{x}_a$ is the a priori assumption for $\mathbf{x}$, $\mathbb{S}_a$ is the a priori uncertainty expressed as the covariance matrix of $\mathbf{x}_a$, $\mathbb{S}_e$ is the uncertainty of $\mathbf{y}$ expressed as the measurement covariance matrix, and $\mathbb{K}_i$ is the Jacobian matrix, which linearizes the forward model $P(\mathbf{x}_i)$. $\mathbb{K}_i$ is evaluated for every iteration i with

$$\mathbb{K}_i = \left(\frac{\partial P(x_j)}{\partial x_{j'}} \right)_{j,j'=1,\ldots,N} \tag{35}$$

with x_j the elements of $\mathbf{x}_i$. Following *Turner and Löhnert* (2014), an additional decreasing factor $\gamma_i = 10000, 3000, 1000, 300, 100, 30, 10, 3,$

1, 1, ... is used which enhances the stability of the retrieval: in case of a bad first guess, γ_i adjusts these elements of the state vector first which can be obtained best from the observation. Due to the Bayesian concept, the uncertainty of the optimal solution can be estimated from

$$\mathbb{S}_i = \mathbb{B}_i^{-1}(\gamma_i^2 \mathbb{S}_a^{-1} + \mathbb{K}_i^T \mathbb{S}_e^{-1} \mathbb{K}_i)\mathbb{B}_i^{-1} \tag{36}$$

where

$$\mathbb{B}_i = (\gamma_i \mathbb{S}_a^{-1} + \mathbb{K}_i^T \mathbb{S}_e^{-1} \mathbb{K}_i). \tag{37}$$

The prior value $\mathbf{x}_a$ is used as starting value $\mathbf{x}_1$ and the iteration is stopped when $\gamma_i = 1$ and the convergence criteria

$$(\mathbf{x}_i - \mathbf{x}_{i+1})^T \mathbb{S}_i^{-1} (\mathbf{x}_i - \mathbf{x}_{i+1}) \ll N \tag{38}$$

is met. Then, the degrees of freedom for signal d_f, which describe the number of independent pieces of information that can be obtained from the measurement, can be estimated from the trace of the averaging kernel

$$\mathbb{A}_i = \mathbb{B}_i^{-1} \mathbb{K}_i^T \mathbb{S}_e^{-1} \mathbb{K}_i \tag{39}$$

after convergence. Usually, d_f is less than the number of observations M, because the elements of $\mathbf{y}$ share redundant information.

It is shown in Publication III, that the following parameters obtained from in situ observations are required to forward model a Doppler spectrum:

1. The three coefficients of the normalized gamma particle size distribution $N(D)$ (D_m, N_0^*, and μ^*, Equation 31).
2. The two coefficients of the normalized mass-size relation $m(D)$ (α and b, Equation 32).
3. The two coefficients of the power law area-size relation with additional noise $A(D)$ (c and d, Equation 40).
4. The kinematic broadening of the Doppler spectrum σ_k depending on the Eddy dissipation rate ϵ and the horizontal wind field U (Equation 25).

Hence, these eight parameters are chosen as elements of the state vector $\mathbf{x}$. Similar to Section 8.2, the boundaries of the particle size distribution D_{min} and D_{max} are set to 0.05 mm and to 12.8 mm, respectively. Even though the Eddy dissipation rate is fixed to $10^{-6}\,m^2s^{-3}$, as found in Publication III, the kinematic broadening σ_k still varies because it also depends on the horizontal wind U measured by aircraft probes (Equation 25).

The a priori $\mathbf{x}_a$ and the corresponding covariance $\mathbb{S}_a$ are estimated from the means and the covariance, respectively, of the coefficients of the data set obtained in Publication III for a radius of 10 km around the location of the MMCR radar in Barrow. Optimal estimation requires the *probability density functions* (PDF) of $\mathbf{x}$ to follow a normal distribution, but the elements D_m, N_0^*, μ^*, α, c, and σ_k of the state vector $\mathbf{x}$ can be better described with a log-normal distribution. Hence, the natural logarithms of these quantities are used as elements of $\mathbf{x}$ instead.

Because an idealized retrieval is investigated, no real radar measurements but simulated measurements are used for the observations $\mathbf{y}$. This has the advantage that convergence of the retrieval is less obstructed by forward model errors and/or instrument biases. In addition, the radar configuration can be easily changed to test the impact of using e. g., additional frequencies. The measurement uncertainty $\mathbb{S}_e$ is estimated from running the forward model 1000 times with different random perturbations (see Additional Study I) for an exemplary profile with average characteristics. This has the advantage that also the off-diagonal entries of the measurement uncertainty matrix $\mathbb{S}_e$ can be estimated. Because the impact of a potential instability of the radar calibration, and the impact of vertical wind on $\mathbb{S}_e$ are neglected as well as other uncertainty sources, this results likely in too small elements of the measurement uncertainty matrix $\mathbb{S}_e$. Because there is no information available about additional sources of uncertainty, the variability among the 1000 runs of the same profile is increased by applying Gaussian noise to $A(D)$ when simulating the measurement as proposed in Publication III (see below).

The response functions (Section 8.2) confirm that the aspect ratio AR has only very little influence on the radar moments. Therefore, AR is set to 1.0 allowing the use of much quicker Mie instead of T-Matrix routines for the retrieval.

It is found in Publication III that random perturbations $r(D)$ need to be applied to the area-size relation $A(D)$ to achieve consistent results

$$A = c \cdot D^d \cdot 10^{r(D)} \tag{40}$$

where $r(D)$ is obtained from a random Gaussian distribution with mean zero and standard deviation $A_{std}(D)$. $A_{std}(D)$ is taken from the standard deviation per size bin D of the logarithmic ratio between fitted $A(D)$ and measured $A(D)$

$$A_{std}(D) = \mathrm{std}(\log_{10}(A(D)_{fitted}/A(D)_{measured})). \tag{41}$$

For simulating the measurement, $r(D)$ is obtained from a random number generator for every profile separately, i. e., every profile of $A(D)$ is disturbed differently. When including the forward model into the retrieval, the noise $r(D)$ applied to the area-size relation and furthermore the random perturbations required for simulation of the

radar spectrum itself (Additional Study I) can cause problems: for observation quantities with small response functions but a large uncertainty, the corresponding elements of the Jacobian matrix $\mathbb{K}_i$ might be random as well. This would make convergence of the retrieval difficult and might lead to results that cannot be reproduced. Therefore, the random perturbations of the radar spectrum are fixed during the retrieval. For $A(D)$, an alternative method is proposed here in order to apply fixed pseudo-random noise to the area-size power law: Instead of obtaining $r(D)$ from a random Gaussian distribution, it is proposed to use a sinus function instead to obtain $r(D)$

$$r(D) = \sin(D/D_{max}\,\Phi\,2\pi) \cdot A_{std}(D) \tag{42}$$

where Φ is the number of periods between 0 and D_{max}, which is fixed to 12.8 mm. Due to the non-evenly distributed size bins used in this study (originating from the bin sizes of the particle probes), this results in a quasi-random disturbance of $A(D)$ obtained from the least squares fit if $\Phi = 2000$ is chosen. This allows reproducibility and the performance of this approach can be tested in advance as it was done for the other parameterizations of $A(D)$ in Publication III: the new method is applied to the ISDAC data set and the forward modeled ISDAC data set is compared to MMCR observations (Figure 13.c). For comparison, the corresponding histograms for the standard least squares fit (Figure 13.a) and the least squares fit with Gaussian noise (Figure 13.b—identical to Figure 10.d of Publication III) are also presented. For the sinus method, the Kolmogorov–Smirnov statistic d_α (*Massey*, 1951), which describes the agreement of the distributions, is equal or even better for all moments appart from mean Doppler velocity W and left slope S_l in comparison to the method using Gaussian noise. As a consequence, the sinus method is used as an alternative to the Gaussian method for the idealized retrieval.

For every tenth profile of the ISDAC data set (~130 profiles), the degrees of freedom d_f are calculated using different retrieval configurations. Three different sets of radar moments are used for the observation vector :

1. Only reflectivity Z_e and mean Doppler velocity W.
2. Only Doppler spectrum width σ, skewness Sk, kurtosis Ku, and left as well as right slope S_l, S_r (σ and higher moments).
3. All radar moments including the slopes.

Note that this is not equal to the "lower" and "higher" moments classification used elsewhere where σ belongs to the "lower" moments.

While the first set is similar to other studies using reflectivity and mean Doppler velocity (e. g., *Matrosov et al.*, 2002; *Szyrmer et al.*, 2012), the second set is chosen in order to evaluate whether reflectivity (sensitive to radar calibration) and mean Doppler velocity (sensitive to vertical air motions) can be excluded from the retrieval. The radar simulator is configured in accordance to the specifications of the more

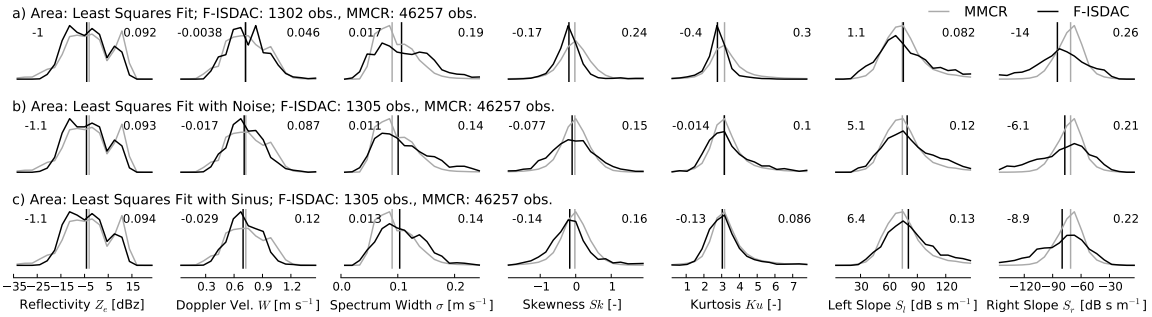

Figure 13: Normalized histograms of the radar moments (columns) of MMCR observations (gray lines) and forward modeled ISDAC observations (F-ISDAC, black lines) for various methods to describe projected area $A(D)$ (rows) when forward modeling ISDAC data: a) least squares fit, b) least squares fit with Gaussian random noise, and c) least squares fit with quasi-random noise using the sinus function. $N(D)$ is estimated using the normalized gamma approach, $m(D)$ is retrieved from the functional relation between Z_e and W as proposed in Publication III, and all parameterizations are applied to the full particle size range. For each data set, the number of cases is given. The vertical lines denote the median of the distributions, the difference between both medians is denoted in the upper left corner and the Kolmogorov–Smirnov statistic d_α is presented in the upper right corner of each panel.

When using the MMCR configuration, the retrieval does not converge in most cases (not shown).

advanced KAZR featuring enhanced response functions (Section 8.2) instead of the MMCR used during ISDAC.

Some studies suggest to combine reflectivity measurements at different frequencies to increase the number of observables (e. g., *Hogan et al.*, 2000; *Kneifel et al.*, 2011a). In order to investigate whether additional frequencies can also contribute additional information when using higher moments, the impact of adding observations at 13 GHz (K_u-band) and at 94 GHz (W-band) to the K_a-band observation at 35 GHz is investigated as well as using all three frequencies together. Note that estimating the scattering properties at 94 GHz with the Mie (or T-Matrix) method leads to an underestimation of backscattering cross section for particles larger than ~3 mm (see Section 3.2 for discussion). For a real-world retrieval, a more sophisticated scattering model has to be used for 94 GHz. For simplicity, the KAZR radar settings are also applied to the other frequencies.

8.3.2 *Results*

The percentage of the approximately 130 investigated ISDAC profiles which converge successfully to a solution is presented in Figure 14.a. The value varies between 40% and 75%. A profile does not converge if either the convergence criteria (Equation 38) is not met within 30

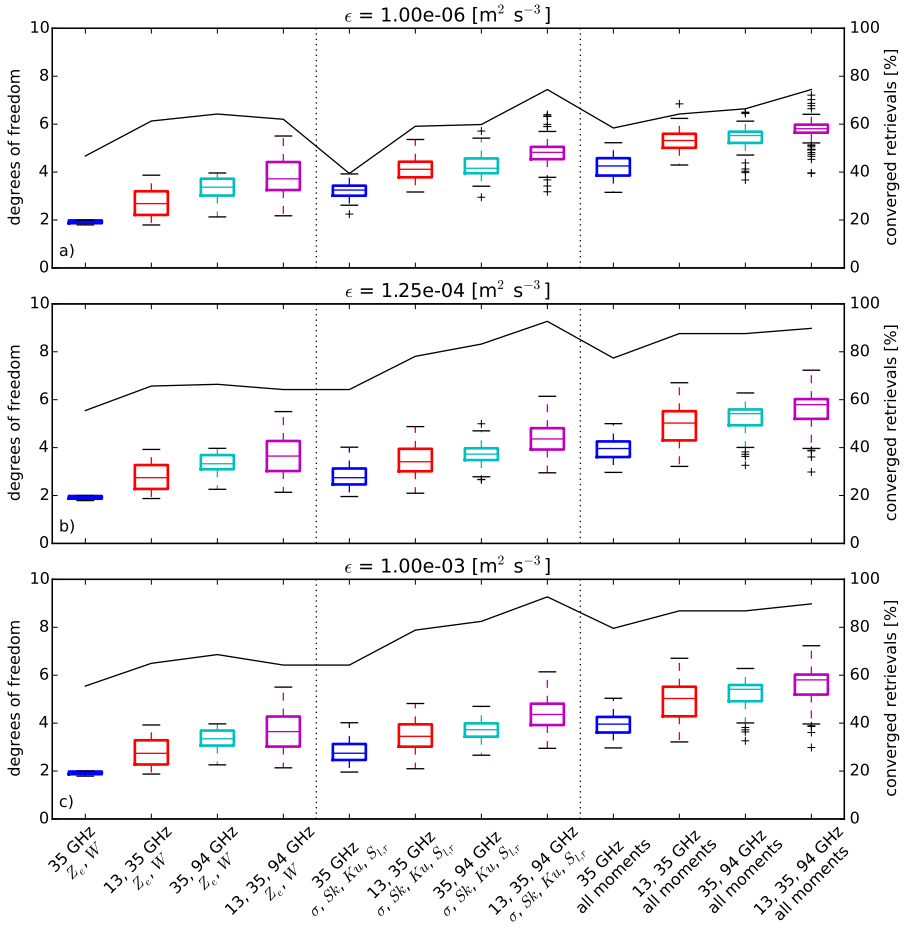

Figure 14: Box and whisker plots showing the degrees of freedom for signal d_f obtained for the investigated ~130 ISDAC profiles depending on retrieval configuration for three fixed Eddy dissipation rates ϵ. The colors correspond to sets of frequencies. The solid black line denotes the percentage of retrievals which converge successfully.

iteration steps or if the retrieval iterates to a state which is either below radar sensitivity or physically inconsistent (e. g., ice crystals with density greater than pure ice) and which cannot be forward modeled. Note that in general, the single-frequency retrieval is the least converging retrieval configuration. Apparently, the information contained in a single-frequency observations is often insufficient to find a solution when including all eight quantities into the state vector $\mathbf{x}$. In this case, additional constrains might be required.

The degrees of freedom for signal d_f obtained for the successfully converged profiles are also presented in Figure 14.a for the various retrieval configurations. The spread of d_f is also indicated, because d_f varies from profile to profile. Note that the largest possible value of d_f is equal to the length of the observation vector $\mathbf{y}$ and varies with retrieval configuration.

When using only Z_e and W, d_f varies between 2 for the single-frequency and 4 ± 1.5 for the triple-frequency configuration. For two frequencies, d_f is 2.8 ± 1 and 3.4 ± 1 for the 13 GHz & 35 GHz and the 35 GHz & 94 GHz configuration, respectively. This shows that also the combination of 13 GHz & 35 GHz is feasible even though both frequencies are similar. In contrast to 94 GHz, using 13 GHz has the advantage that the scattering properties are easier to estimate for a real-world retrieval (Section 3.2).

It is shown that the combination of σ, Sk, Ku, S_l, and S_r of a single frequency can already provide as many degrees of freedom for signal d_f (3.4 ± 0.5) as a dual-frequency combination of Z_e and W. The observation vector $\mathbf{y}$ of this configuration contains, however, more redundant information, because only 3.4 of the largest possible value of 5 d_f can be obtained, while for the dual-frequency configuration using Z_e and W, up to 3.4 of 4 possible d_f can be exploited. However, only 40% of the retrievals converge, which is 20 percentage points less than for Z_e and W and two frequencies. When using additional frequencies for the combination of σ and higher moments, the obtained d_f and the percentage of converged retrievals increase to up to 4.8 ± 0.2 and to 75%, respectively, for three frequencies.

When using all moments together, d_f varies between 4.2 ± 0.5 and 5.8 ± 0.2, depending on the used set of moments. The percentage of converged profiles increases from 48% to 75% with increasing number of frequencies.

Increasing the broadening of the Doppler spectrum by using larger values of Eddy dissipation rate ϵ reduces the response functions of the higher moments. To investigate the effect of this reduction on the retrieval, increased values of $1.25 \times 10^{-4}\,m^2s^{-3}$ (Figure 14.b) and $10^{-3}\,m^2s^{-3}$ (Figure 14.c) are also used for ϵ. While this—as expected—has no impact on the retrievals using only Z_e and W, it reduces d_f by 0.2 to 0.3 for the medium turbulence level and by approximately twice the value for the larger turbulence level. In addition, the spread of d_f is increased for the medium and high turbulence level in comparison to the low turbulence level. Surprisingly, the percentage of converging retrievals is increased by 15 to 20 percentage points in comparison to the lower turbulence level. A possible explanation for this could be the reduced uncertainty of the response functions for higher turbulence levels. Another reason could be problems with the assumed a priori uncertainty S_a which might contain some rather strong correlations between the elements of $\mathbf{x}$ caused by the limited size of the data set. Because the impact of the quantities which describe the cloud microphysics is reduced for the larger turbulence levels, it is expected that problems with S_a have the largest impact for the lowest turbulence level.

8.4 SUMMARY AND DISCUSSION

The response functions and the degrees of freedom for signal d_f are studied to evaluate the potential of adding higher moments to radar retrievals. It is found that higher moments (including the slopes) depend on the parameters describing microphysical properties such as area $A(D)$, mass $M(D)$ and particle size distribution $N(D)$.

The response functions of skewness Sk and kurtosis Ku are rather small, noisy and strongly reduced for a larger Eddy dissipation rate. The response functions of the slopes S_l and S_r are more noisy, but in general also show larger gradients. Configuring the forward model in accordance with a more advanced radar such as the KAZR enhances the response functions. It is expected that future radar systems can achieve even lower noise levels thereby further enhancing the quality of the response functions. For example, the upcoming, second generation of the KAZR will feature a noise level reduced by 10 dB in comparison to the first KAZR generation (*P. Kollias*, personal communication). Increasing the number of fast Fourier transformation (FFT) points from 256 to 512 would reduce the steps which can be seen in the response functions of the slopes and an even stronger enhancement could be obtained by increasing the number of spectral averages to make the spectrum more smooth. This, however, requires in most cases longer integration times of the radar, which—as a drawback—increases the effect of turbulence onto the radar spectrum. As a consequence, sensitivity studies are recommended similar to the one presented here to find the optimal radar configuration for exploration of higher radar moments.

"Larger" Eddy dissipation rate refers here to conditions in arctic stratocumulus (Shupe et al., 2012). For example, for convective clouds, much larger values of ϵ have been found (Gultepe and Starr, 1995).

Analysis of the degrees of freedom for signal d_f using an optimal estimation-based retrieval shows—when configured in accordance with the more advanced KAZR radar—that despite the small response functions with large uncertainty, higher moments can add additional information to ice cloud retrievals. Even if only a single frequency is used, a retrieval exploiting only σ, Sk, Ku, S_l, and S_r can retrieve on average 3.4 d_f. This is more than for a dual-frequency retrieval using Z_e and W. If all moments are used, even 4 to 6 d_f can be retrieved depending on the number of used frequencies. Increasing the turbulence level decreases the obtained d_f only by 0.2 to 0.6. This highlights that despite the small response functions, higher moments can be exploited not only for very low Eddy dissipation rates, but also for larger Eddy dissipation rates.

Larger turbulence levels also increase the percentage of retrievals converging to a solution. This can be attributed to the reduced uncertainty of the response functions, but also too small errors of the a priori uncertainty S_a matrix. As a consequence, is has to be studied in the future how S_a can be obtained best. Furthermore, it was not evaluated whether skewness and kurtosis or the slopes contribute

most to the increased value of d_f, but this can be easily tested by removing one or two elements of the observation vector and evaluating the impact.

The next step required for evaluation of the idealized retrieval is to explore the error characteristics of the solution. This allows to investigate for which of the eight quantities of state $\mathbf{x}$ describing the microphysical parameterizations, the a posteriori uncertainty S_i has become significantly smaller than the a priori uncertainty S_a. If no or only little improvement can be achieved for individual quantities, it can be tested whether the retrieval becomes more stable by excluding these quantities from the retrieval. Further studies are also required to adapt the retrieval to less idealized conditions, and to increase the percentage of converged retrievals. To make the retrieval convergence more stable, a normalization approach similar to the one proposed by *Szyrmer et al.* (2012) for mass $m(D)$, could also be applied to the power law describing projected area $A(D)$ which would potentially account better for the high correlation between the coefficients of the area-size relation.

Note that the results presented here are based on an idealized retrieval and only testing the concept with real measurements can confirm that the information content found here for the higher moments can be exploited in real world as well. Even though is was found that the influence of aspect ratio AR is small, the application of the retrieval to real observations probably also requires the use of T-Matrix instead of Mie scattering calculations. For W-band, even more sophisticated methods need to be used which further increases the computational costs of the retrieval.

Unfortunately, it is unlikely that the retrieval can be applied successfully to the MMCR data obtained during ISDAC due to the rather noisy observations of the radar. The percentage of converged idealized retrievals was greatly reduced when configuring the radar simulator with respect to the technical specifications of the MMCR instead of the KAZR. To the author's knowledge, no other data set is available which features both, radar observations by a state-of-the-art cloud radar (e. g., KAZR) and aircraft observations of ice clouds using modified probe tips limiting shattering effects (*Korolev et al.*, 2013). A close candidate is the *Global Precipitation Mission* (GPM) *Cold-season Precipitation Experiment* (GCPEx, *Hudak et al.*, 2012) which took place around Egbert, Ontario, and contains aircraft observations and cloud radar observations. However, the zenith pointing radar of McGill university was operating at 94 GHz, which makes scattering calculations challenging, especially because the campaign was mainly targeted at observations of snowfall instead of ice clouds. In addition, the *Dual-Frequency Dual-Polarized Doppler Radar* (D3R *Chandrasekar et al.*, 2010) operating at 14 GHz and at 35 GHz was participating in GCPEx but its sensitivity was not sufficient for cloud detection at 35 GHz and fur-

thermore, the radar was scanning rapidly and no continuous zenith observations were obtained.

Future studies should aim at using a larger data set, because the ISDAC data set contains rather homogeneous cloud conditions and especially the coefficients of the area-size relation vary only little for the ISDAC data set (Publication III). This issue could be partly addressed for ISDAC by using not only aircraft observations obtained within a 10 km radius around Barrow as in Publication III, but exploiting the complete ISDAC data set for estimating the a priori information.

A further reason limiting the quality of the retrieval is that optimal estimation requires the forward model to be "moderately linear" (*Rodgers*, 2000) and that all uncertainties are described by Gaussian distributions. Being "moderately linear" requires that the model responds linear at least for the interval used to estimate the Jacobian matrix $\mathbb{K}$. In order to test whether this is the case for the perturbation of 0.5%, which is used to calculate $\mathbb{K}$ in this study, the linearity criteria proposed by *Rodgers* (2000, Section 5.1) can be used, which is related to the ratio of the error caused by linearization to the uncertainty of the measurement.

While the state vector $\mathbf{x}$ and the observation vector $\mathbf{y}$ can be well described by (log-)normal distributions, it can only be assumed that the uncertainty of the solution $\mathbb{S}_i$ can be described by a normal distribution as well. Multiple minima of $\mathbb{S}_i$ might exist for multiple solutions and it is not possible to investigate whether a local or global minimum is found when using optimal estimation.

An alternative to optimal estimation are Monte Carlo-based retrieval approaches which also rely on a Bayesian concept and which obtain the solution and the corresponding probability density function by random sampling of the state space. This allows the use of arbitrary and also non-linear forward models and the use of arbitrary PDFs to describe the error characteristics. The major disadvantage is that the random sampling of the Monte Carlo-based methods is much more expensive with respect to computing time than optimal estimation. There are various versions of Monte Carlo-based algorithms using different strategies to accelerate calculations. In atmospheric science, the use of *Markov chain Monte Carlo* (MCMC, *Metropolis et al.*, 1953) methods is proposed (*Posselt et al.*, 2008; *Posselt and Mace*, 2014) while some hydrology studies suggest to use the *Differential Evolution Adaptive Metropolis* (DREAM) variant of MCMC allowing massive parallelization (*Vrugt et al.*, 2008, 2009). Still, MCMC-based approaches are currently too expensive to develop an operational radar ice cloud retrieval, especially if more realistic particle types are to be used when estimating the scattering properties. MCMC, however, could be used for selected profiles in order to map the solution space (*Posselt and Mace*, 2014), in order to investigate whether optimal estimation con-

verges to a global or a local minimum, and in order to assess the information content d_f obtained from optimal estimation.

The agreement of the higher moments between forward model and radar observations as presented in Publication III can also be seen as a proxy indicating that the complete Doppler spectrum can be realistically forward modeled as well. Building up on this, the full Doppler spectrum could be used instead of radar moments for the observation vector $\mathbf{y}$ of the retrieval. Then, it could be tested whether this adds information to the retrieval which cannot be obtained from the radar moments. In the future, the use of the complete Doppler spectrum will be simplified by the advent of more advanced radar generations featuring even better spectral data quality.

Part D

DISCUSSION AND OUTLOOK

9 DISCUSSION OF THE STUDIES

In the following, the principal results of Key Issue I *Enhanced snowfall observations* (Publications I and II) and Key Issue II *Exploiting higher moments* (Publication III and Additional Studies I and II) are summarized and discussed.

9.1 PUBLICATION I: IMPROVED DOPPLER SPECTRA PROCESSING

In Publication I (*Maahn and Kollias*, 2012), a new data processing scheme for the *Micro Rain Radar* (MRR) is presented. In contrast to the standard MRR processing scheme, the proposed method estimates lower and higher radar moments directly from the observed Doppler spectrum. Furthermore, signals from hydrometeor-free range gates are removed and the MRR sensitivity is significantly enhanced. This improves the detection of hydrometeors at low signal-to-noise ratios (SNR). A dealiasing routine is developed to remove aliasing effects caused by particles exceeding the radar Nyquist velocity range. While the method published by *Kneifel et al.* (2011b) is based on the spectra which are processed by the standard MRR software, the proposed method relies on the non-processed raw spectra.

The method is evaluated by comparison to a K_a-band MIRA35 cloud radar (*Melchionna et al.*, 2008) using a data set containing 116 days in winter and spring 2012. A comparison of reflectivity of MRR and MIRA35 is shown in Figure 15 for the original MRR processing scheme, the method by *Kneifel et al.* (2011b), and the proposed scheme. In comparison to the two reference methods, firstly the offset between both instruments is reduced for the proposed method and secondly the "knee" at $-10\,\mathrm{dBz}$ and $-5\,\mathrm{dBz}$, caused by clear sky echoes due to insufficient noise removal, is removed. By this, the sensitivity of MRR for snowfall observations is improved from $+3\,\mathrm{dBz}$ (*Kneifel et al.*, 2011b) to $-5\,\mathrm{dBz}$ which corresponds to an enhanced minimal detectable snowfallrate S of $\sim 0.01\,\mathrm{mm\,h^{-1}}$ in comparison to $\sim 0.06\,\mathrm{mm\,h^{-1}}$ for *Kneifel et al.* (2011b) if the $Z_e - S$ relation by *Matrosov* (2007) is applied.

The improvement with respect to mean Doppler velocity W is even stronger, as shown in Figure 16. Because the standard scheme assumes a Nyquist velocity range of $0\,\mathrm{m\,s^{-1}}$ to $11.9\,\mathrm{m\,s^{-1}}$, the Doppler velocity of those hydrometeors which fall very slowly or even drift upwards (aliasing effect) is highly biased. The dealiasing routine of the proposed processing scheme can successfully correct for aliasing effects and the agreement of MRR to MIRA35 is distinctly improved.

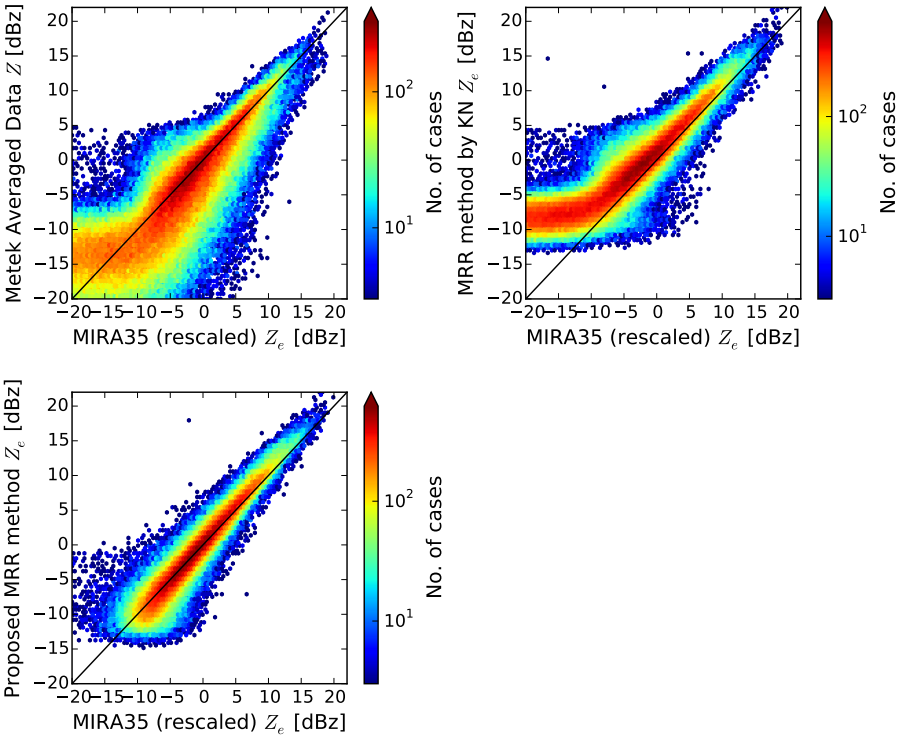

Figure 15: Scatter plots comparing effective reflectivity (Z_e) of MIRA35 with D^6-based radar reflectivity (Z) derived from Metek's standard MRR product (top left), with effective reflectivity (Z_e) of MRR using the method by *Kneifel et al.* (2011b) (KN, top right), and with Z_e of MRR using the new proposed MRR method (bottom). The black line denotes the 1 : 1 line. Adapted from *Maahn and Kollias* (2012).

Furthermore, the new processing scheme can also provide additional radar moments such as Doppler spectrum width σ, skewness Sk and Kurtosis Ku which are not available when using the standard MRR software.

The presented method exploits the full potential of MRR's hardware. A further increase requires modifications of the instrument design. Publication I shows that despite MRR's limitations due to its low-cost design, it features a performance similar to a K_a-band cloud radar concerning the observation of snowfall. In comparison to a cloud radar, MRR is easier to operate in remote areas due to its smaller dimensions, the low power consumption, and the little need for maintenance. The new processing scheme is released as *IMProToo* under an open source license online and has already been used in several other studies (*Stark et al.*, 2013; *Colle et al.*, 2014; *Garrett and Yuter*, 2014; *Gorodetskaya et al.*, 2015, 2014; *Misumi et al.*, 2014; *Pokharel et al.*, 2014).

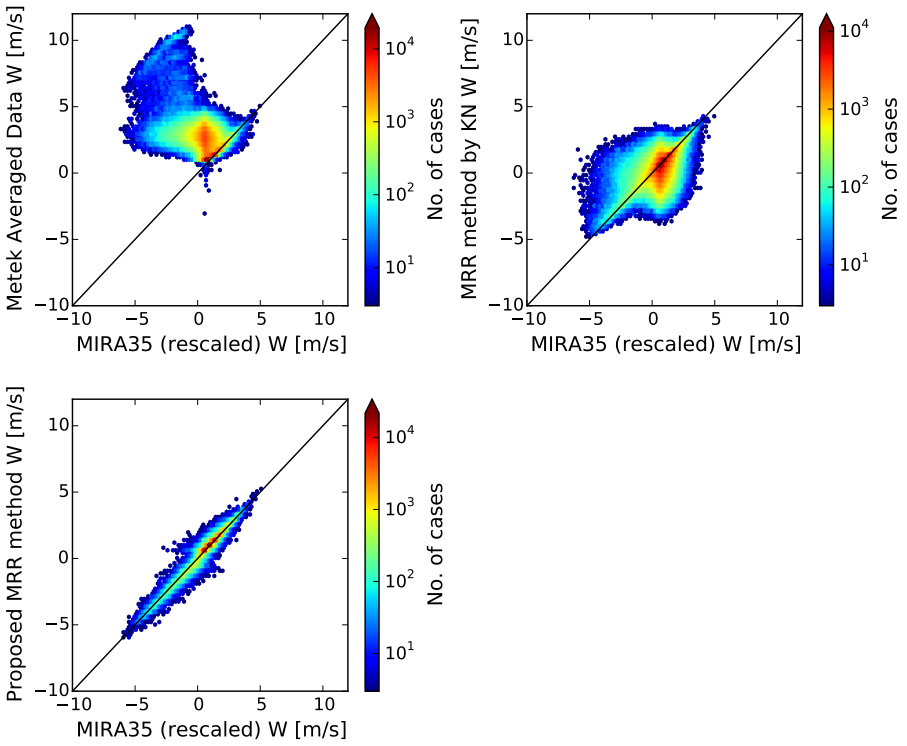

Figure 16: Same as Figure 15, but for Doppler velocity (W). Adapted from *Maahn and Kollias* (2012).

9.2 PUBLICATION II: EXPLORING RADAR-BASED SNOWFALL STATISTICS

In Publication II (*Maahn et al.*, 2014), the potential of the radar onboard the CloudSat satellite for surface snowfall detection is evaluated. For this, the effect of the CloudSat radar's blind zone is investigated based on MRR observations. The blind zone affects the lowest 1200 m above ground level (agl) and is caused by contamination of the radar observations with ground clutter. It is assumed that MRR can mimic CloudSat observations and hence vertical changes as found by MRR are representative for CloudSat. Consequently, the MRR processing scheme developed in Publication I is applied to one year of MRR observations at Ny-Ålesund in Svalbard, Norway (*Maahn*, 2010) and at the Belgian Princess Elisabeth station in East Antarctica (*Gorodetskaya et al.*, 2015). The MRR data set is analyzed for vertical changes within the blind zone. Because smaller blind zones are proposed for future satellite missions, also a reduced blind zone of 600 m agl is investigated. To account for the different operating frequencies of MRR and CloudSat, a power law correction is developed to convert MRR observations of Z_e at 24 GHz to CloudSat's 94 GHz from the combination of reflectivity-snowfall relations for both frequencies.

Results for the third site, Longyearbyen in Svalbard, can be found in the supporting information to Publication II.

Vertical changes in the Z_e distribution, the number of events, and the mass flux are investigated based on MRR data. 2-D histograms of

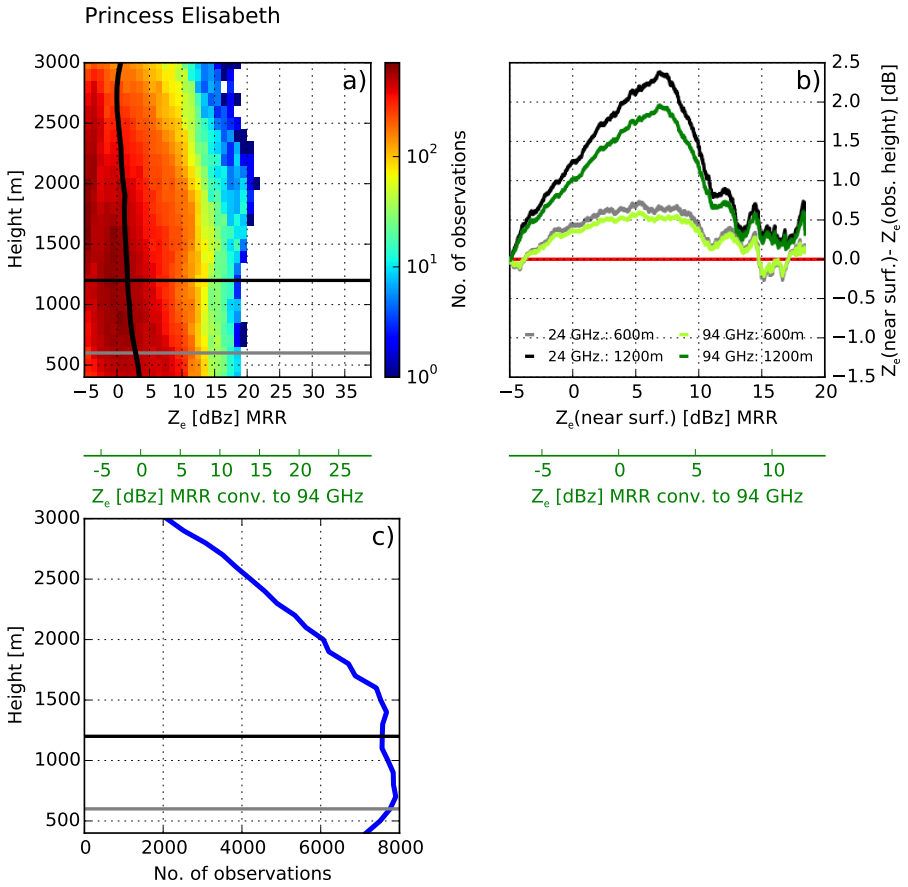

Figure 17: (a) Reflectivity vs. altitude 2D histograms (2D-H) of observed MRR reflectivities at Princess Elisabeth Station, East Antarctica. The median profile is denoted by the black solid line. The horizontal, black line denotes the CloudSat measurement height H_{CS}, the horizontal, gray line a reduced blind zone height H_{FM}. An estimate for the corresponding Z_e at 94 GHz using the coefficients for aggregates is indicated by the additional, green scale. (b) Detrended Quantile-Quantile (DQQ) plot of the reflectivity observations for 24 GHz close to the surface (H_{SF}) in comparison to H_{CS} (black) and in comparison to H_{FM} (gray) as well as after conversion to 94 GHz (green and light-green lines). (c) Total number of observations with Z_e of MRR observations larger than −5 dBz (solid blue line). Adapted from *Maahn et al.* (2014).

DQQ-plots (Thode, 2002) are similar to quantile-quantile (QQ) plots, but on the ordinate the difference between both quantiles is shown. This difference is equal to the distance of a standard QQ-plot to its 1:1 line.

the data sets (Figures 17.a and 18.a) reveal only small vertical changes. The Z_e distributions at the lowest CloudSat height (H_{CS}) and the MRR measurement height closest to the surface (H_{SF}) are compared using *Detrended Quantile-Quantile* (DQQ) plots (Figures 17.b and 18.b). They show that the shift of distributions is below 2.5 dB for Princess Elisabeth and below 1.0 dB for Ny-Ålesund. While the result is mainly the same after transformation from 24 to 94 GHz, a reduction of the blind zone to 600 m as proposed for future satellite missions (H_{FM}) reduces the shift in the distributions to 0.5 dB at Princess Elisabeth and to less than 0.5 dB in Ny-Ålesund.

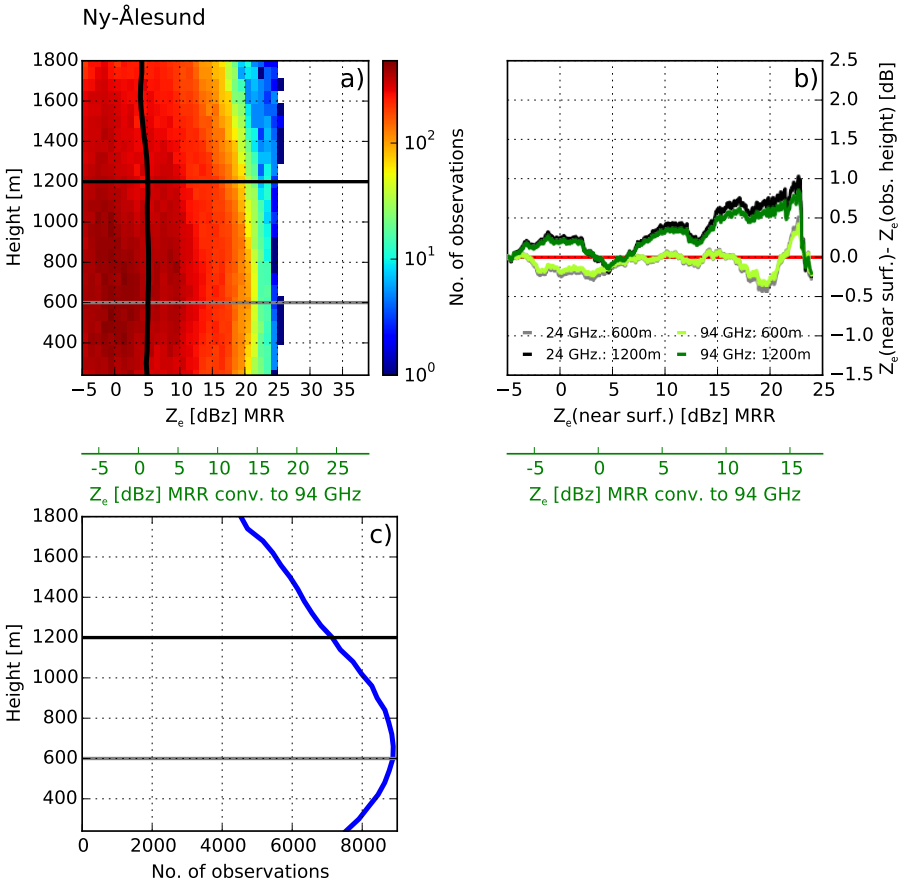

Figure 18: Same as Figure 17, but for Ny-Ålesund, Svalbard. Adapted from *Maahn et al.* (2014).

The analysis of the vertical change of number of precipitation events detected by MRR (greater −5 dBz) reveals that the number of observed profiles is increased at the CloudSat measurement height H_{CS} in comparison to the near-surface height H_{SF} by 5.7% for Princess Elisabeth (Figure 17.c), but reduced by 5.2% for Ny-Ålesund (Figure 18.c). In addition, the number of observed profiles follows a belly shaped curve for Ny-Ålesund between H_{SF} and H_{CS} with the maximum around H_{FM}. For Princess Elisabeth, the belly shape is reduced, but still visible. The belly shape is attributed to the competition between shallow precipitation and virga effects which overlap around the reduced blind zone height H_{FM}. This belly shape is even increased when considering the total precipitation flux (Figure 19) by applying reflectivity–snowfall rate relations by *Kulie and Bennartz* (2009). Then, the underestimation of total precipitation—normalized to observations at H_{SF}—changes from 11 percentage points at Princess Elisabeth and 9 percentage points at Ny-Ålesund at H_{CS} to an overestimation of 3 and 19 percentage points, respectively, at H_{FM}.

In general, the results are only valid for the vicinity of the sites. However, results for Ny-Ålesund are in agreement with results for

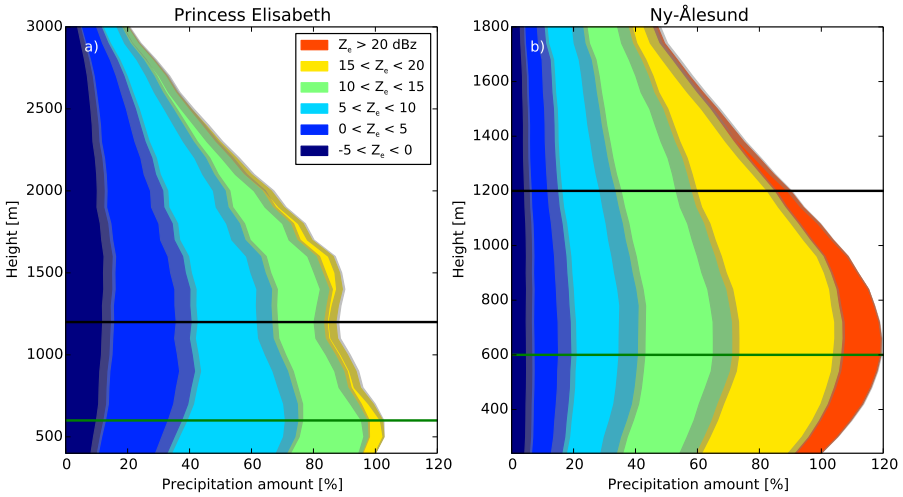

Figure 19: Contribution of various reflectivity intervals to the total precipitation amount in dependence on height for Princess Elisabeth and Ny-Ålesund. The figures are normalized by total surface precipitation. H_{CS} and H_{FM} are denoted by black and green lines, respectively. Figure taken from *Maahn et al.* (2014).

Longyearbyen which is located 110 km to the southeast (see supporting information to Publication II for figures), so it is expected that the results are at least representative for West-Svalbard. Due to the spatial homogeneity of East Antarctica, it is further assumed that the findings are representative for a larger region for Princess Elisabeth. Even though it is found that the agreement of precipitation statistics at the height of CloudSat observations H_{CS} and the near-surface height H_{SF} is relatively high, the agreement of the observed number of events and the total precipitation amount is reduced at the height of future missions H_{FM}. This indicates that not the *same* events are observed at H_{CS} and H_{SF} even though they share similar statistical properties. At the same time, this highlights that potential future precipitation radar missions do not feature improved estimates of surface precipitation per se by a reduction of the blind zone by 50%.

In the future, the analysis can also be applied to other ground-based radar observations, e. g., the Greenland summit station (*Shupe et al.*, 2013), the ARM site North Slope of Alaska (*Mather and Voyles*, 2012), or the UFS station in the German alps (*Löhnert et al.*, 2011).

9.3 ADDITIONAL STUDY I: SPECTRAL RADAR SIMULATOR

In Additional Study I, the PAMTRA forward model is introduced. The forward model was originally designed for passive microwave observations and is extended by a radar simulator which is capable of simulating the full radar Doppler spectrum (Figure 8). The routines developed in Publication I are used for estimating the radar moments from the simulated radar Doppler spectrum. PAMTRA is especially

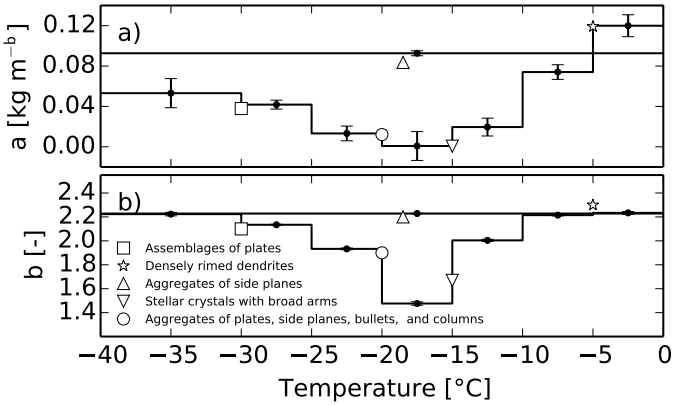

Figure 20: (a) a and (b) b coefficients of the mass-size relation as a function of temperature. The result for a and b for the complete data set is marked with a solid, straight line. For comparison, various $m(D)$ relations from literature are presented at arbitrary yet typical temperatures: radiating assemblages of plates (*Mitchell et al.*, 1990), densely rimed dendrites (*Locatelli and Hobbs*, 1974), aggregates of side planes, (*Mitchell et al.*, 1990), stellar crystals with broad arms (*Mitchell*, 1996), and aggregates of unrimed radiating assemblages of plates, side planes, bullets, and columns (*Locatelli and Hobbs*, 1974). Adapted from *Maahn et al.* (2015).

suited for combined radiometer-radar retrievals, but can also be used for coupling to NWP models and GCM (e. g., for evaluation), for development of future instruments, for the setup of radiative transfer databases, and for forward modeling in situ observations.

9.4 PUBLICATION III: ICE CLOUD PARAMETERIZATIONS

The aim of Publication III (*Maahn et al.*, 2015) is to develop a consistent set of parameterizations for describing the microphysical properties of ice clouds as it is required for retrieval studies. For this, in situ observations of ice cloud properties are obtained from the data set of the *Indirect and Semi-Direct Aerosol Campaign* (ISDAC, *McFarquhar et al.*, 2011). The data set is forward modeled using the radar simulator presented in Additional Study I. The study has two main results. Firstly, the mass-size relation $m(D)$ is retrieved from a combination of radar and in situ observations. Secondly, the optimal set of analytical expressions to express area A and particle size distribution N as functions of D are found for simulating radar observations. For this, higher radar moments are used which have not been used for ice cloud observations before.

The mass-size relation $m(D)$ is estimated first, because it is the only important parameter required for PAMTRA which is not included in the ISDAC data set. For estimating the coefficients of $m(D)$, a novel

method is developed based on the functional relation between Z_e and W, which is approximated by a power law

$$W = e\, Z_e^{f} \tag{43}$$

with the coefficients e and f obtained by a least squares fit. Temperature dependent values for e and f are obtained from combined *MilliMeter wavelength Cloud radar* (MMCR, *Moran et al.*, 1998) and radiosonde observations during ISDAC. Due to the low turbulence conditions it is expected that vertical air motions cancel out for the least squares fit and have only little impact on the coefficients of the $Z_e - W$ relation. In the forward model, the coefficients of $m(D)$ are chosen such that the $Z_e - W$ relation of the forward modeled ISDAC data matches the $Z_e - W$ relation of the MMCR observations. In order to find the optimal set of coefficients a and b for $m(D)$, optimal estimation (*Rodgers*, 2000) is used. That is, a and b are used as a closure to match MMCR and ISDAC observations.

The resulting coefficients a and b for the complete data set and as a function of temperature are presented in Figure 20. For comparison, pairs of a, b coefficients taken from literature (see caption) are included at arbitrary though typical temperatures as well. While the coefficients a and b found for the complete data set are very similar to the ones found for *aggregates of side planes* (*Locatelli and Hobbs*, 1974), the temperature-dependent coefficients reveal a clear transition with increasing temperature from plates and aggregates of columns and plates to more complex, stellar single crystals as they are typical for temperatures between $-20\,°C$ and $-10\,°C$. For higher temperatures, the coefficients equal the ones for rimed dendrites. This transition agrees well with ice habit diagrams published in literature (Section 3.1.2). Also, comparisons of 2-D histograms of Z_e to W, and—as an independent check—to spectrum width σ reveal a good agreement between MMCR and forward modeled ISDAC observations (see Figure 5 of Publication III). Even though other methods for estimating $m(D)$ can also lead to a good agreement of 1-D distributions of lower radar moments, they are unable to reproduce the functional relations $Z_e - W$ and $Z_e - \sigma$. Therefore, it is concluded that the proposed approach to use $m(D)$ as a closure leads to consistent results even though the approach is potentially affected by retrieval errors. Following up on this, it is recommended to investigate not only the lower radar moments separately, but also the functional relations among the moments when assessing mass-size relations.

ISDAC observations are forward modeled also for the second objective, the investigation of the impact of parameterizations on the forward model. Because higher moments are used for the evaluation of parameterizations, their performance is evaluated first. For this, higher moments are estimated using measured projected area $A(D)$, measured particle size distribution $N(D)$, and retrieved mass-size relation $m(D)$ as described above. Then, lower and higher moments

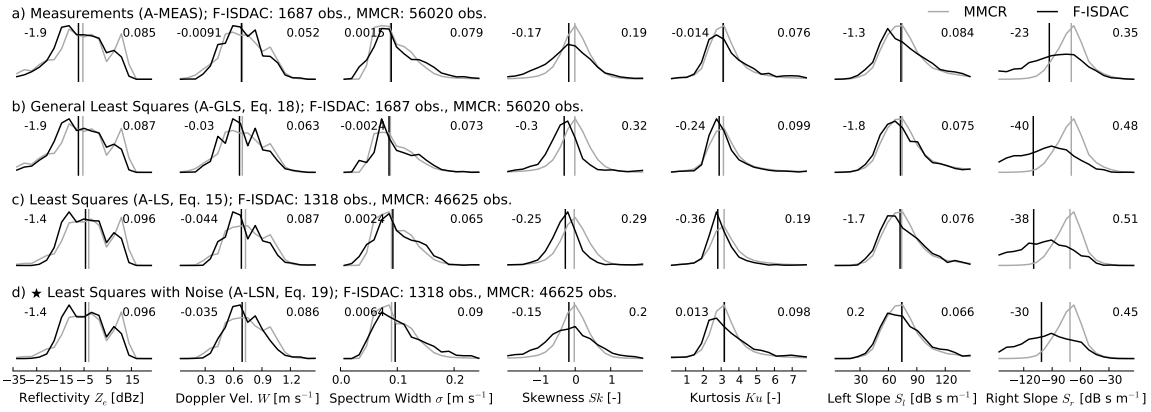

Figure 21: Normalized histograms of the radar moments (columns) of MMCR observations (gray lines) and forward modeled ISDAC observations (F-ISDAC, black lines) for various methods to describe $A(D)$ (rows) when forward modeling ISDAC data. For each method, the first (second) number denotes the number of cases in the F-ISDAC (MMCR) data set. The vertical lines denote the median of the distributions, the difference between both medians is denoted in the upper left corner and the Kolmogorov–Smirnov statistic d_α is presented in the upper right corner of each panel. Figure taken from *Maahn et al.* (2015).

of forward modeled ISDAC observations are statistically compared to MMCR observations (Figure 21.a). PAMTRA is able to produce consistent results for kurtosis Ku and left slope S_l, but a large offset for right slope S_r ($-22\,\mathrm{dB\,s\,m^{-1}}$) and a small offset for skewness Sk (-0.17) remains. This is attributed to problems with large, rare particles at the right (fast) side of the Doppler peak which are insufficiently sampled by in situ probes and where the scattering uncertainties are largest.

For area, the in situ measurements of projected area $A(D)$ are replaced by various parameterizations: the measured area-size relations $A(D)$ are fitted to a power law $A(D) = c\,D^d$ for both, the complete data set, and by applying the fit to each individual profile. Comparison to MMCR data shows that the parameterization of $A(D)$ has negligible impact on the lower moments (Figure 21.b and c). For the higher moments it is found that application of a least squares fit to measured $A(D)$, however, deteriorates the offsets of Sk and S_r. It is concluded that this is caused by small deviations from the power law which are required but missing after application of the fit. For this, the area–size power law is modified to include a size dependent noise term $r(D)$ determined from observations (see Publication III or Section 8.3 for details)

$$A = c \cdot D^d \cdot 10^{r(D)}. \tag{44}$$

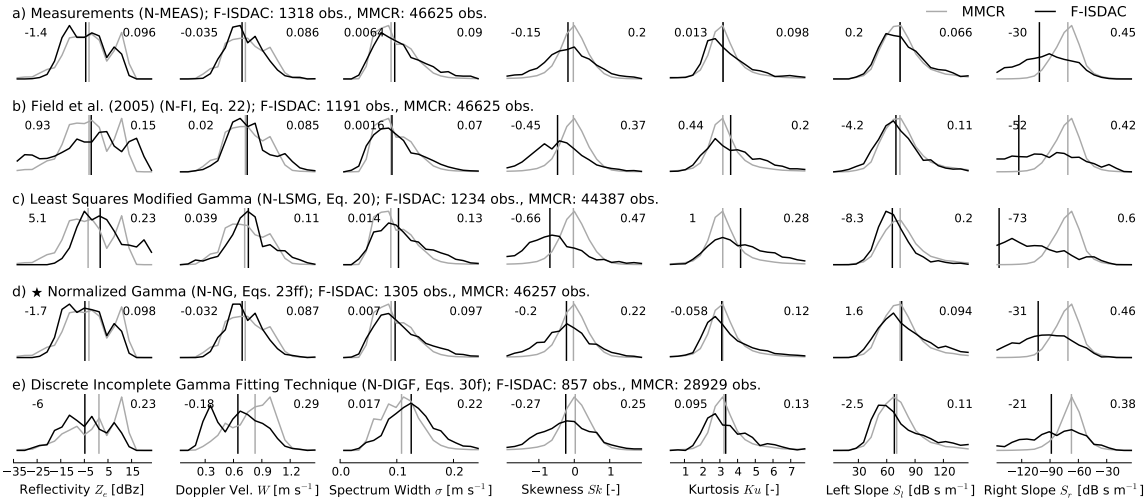

Figure 22: Comparison of MMCR observations and various methods to represent $N(D)$ for ISDAC data, similar to Figure 21. Figure taken from *Maahn et al.* (2015).

Application of $r(D)$ to the power law fit improves the agreement of the distributions of Sk and S_r between ISDAC and MMCR again (Figure 21.d). Hence, it is concluded that small deviations from the power law are mandatory for forward modeling of consistent higher moments and—if higher moments are seen as a proxy for the complete Doppler spectrum—the Doppler spectrum.

The particle size distribution $N(D)$ is analyzed in the same way as projected area $A(D)$ and different methods are applied to express $N(D)$ as a modified gamma distribution or a gamma distribution. A least squares fit to the modified gamma distribution is compared to two variants which use the gamma distribution, but preserve the moments of $N(D)$: Firstly, the normalization approach proposed by *Testud et al.* (2001) and, secondly the incomplete gamma method of *McFarquhar et al.* (2014). As an independent reference, the parameterization of *Field et al.* (2005) is used which relies on temperature and is also used in NWP models (*Reitter*, 2013). Comparison of forward modeled ISDAC and MMCR observations shows (Figure 22) that the parameterization of $N(D)$ has large impact on the distributions of lower and higher moments. Among the investigated methods, the normalized gamma approach is the only method which can reproduce results similar to measured $N(D)$ for all moments. In addition, this parameterization is found to be stable with respect to extrapolation beyond the largest measured diameter. As a consequence, the borders of $N(D)$ are fixed to 0.05 mm and 12.8 mm which are the smallest and largest size, respectively, of the in situ data set.

In Publication III, the normalization concept of Testud et al. (2001) is modified for the use with maximum dimension as size descriptor instead of melted-equivalent diameter. This enhances the applicability of the normalization greatly.

Both parts together form a consistent set of analytical expressions and coefficients to describe particle mass $m(D)$, projected area $A(D)$,

and particle size distribution $N(D)$ for forward modeling with the PAMTRA operator. The high agreement between MMCR and forward modeled ISDAC observations highlights the potential of the PAMTRA operator for simulating not only reflectivity Z_e, but also higher moments. The latter are found to be valuable additions to the conventional observables due to their high dependence on parameterizations. Parameterizations, coefficients and, forward model form the main ingredients required for a sensitivity study to test whether higher moments can also provide additional information for ice cloud retrievals.

However, there are also other applications for the methods developed in Publication II. The novel approach to retrieve the mass-size relation by combining aircraft in situ and ground-based radar measurements can also be applied to other data sets. Applications to other data sets would also allow to further investigate why small deviations from the power law area-size relation are required to obtain consistent results for $A(D)$. Also, novel parameterizations for $N(D)$ could be developed to test the possibility of parameterizations working even better for remote sensing applications.

9.5 ADDITIONAL STUDY II: RETRIEVAL POTENTIAL

The forward model developed in Additional Study I and the parameterized data set obtained in Publication III are used to analyze the potential of higher radar moments for ice cloud retrievals. The potential is investigated both quantitatively and qualitatively.

For the quantitative analysis, the response functions describing the dependence of the radar moments on the coefficients of the microphysical parameterizations are evaluated (Figures 9 and 10). They are analyzed for the coefficients of the particle size distribution $N(D)$ (N_0, D_m, and μ^* of the normalized gamma distribution, see Publication III, Appendix A), the normalized mass-size relation $m(D)$ (α and b, *Szyrmer et al.*, 2012), and the area-size relations $A(D)$ (c and d). In addition, the uncertainty of the estimates of the moments caused by radar noise are estimated by repeating the calculations to gain the response functions 1000 times.

For the lowest turbulence level, it is found that Doppler spectrum width σ depends on the size distribution shape parameter μ^* and the coefficients of the mass-size and area-size relations. The response for skewness Sk is mostly below 0.5, but depends on all ice cloud parameters apart from the intercept parameter N_0^*. For the exponent of the mass-size relation b, the response is larger than 1, but also nonlinear and not monotonically increasing. In general, the uncertainty of the response functions for Sk is rather high (~0.2) and is often larger than the found gradient itself. For kurtosis Ku, values between 0 and 3 are found. Similar to Sk, it depends on all coefficients but N_0^*. The

response to b is very strong, but also non-linear. For the dimensionless pre-factor of the mass-size relation α and the mass-weighted mean particle size D_m, the response is within the found uncertainty of ~0.4. The slopes S_l and S_r feature a comparatively strong, but also noisy and non-linear response to almost all parameters. More pronounced and less noisy response functions can be obtained when configuring the forward model in accordance to the more advanced KAZR radar (Figures 11 and 12). This highlights the importance of using advanced radars for obtaining higher moments.

Broadening due to turbulence leads to a more Gaussian shape of the Doppler velocity peak which might cover the response of Sk and Ku on cloud properties. Consequently, the analysis is repeated for two additional higher turbulence levels typical for Arctic stratocumulus clouds. Increasing the turbulence reduces the response functions of the higher moments and for the highest investigated turbulence level the response functions of the higher moments vanish almost completely. At the same time, higher turbulence levels smooth the spectrum as well resulting in less noisy estimates of the slopes, but also of Ku and Sk. This means that with increased turbulence levels, the usability of higher moments for retrieval applications might even be enhanced despite of the reduced response functions.

For the qualitative analysis, the parameters of the particle size distribution, area-size relation and mass-size relation are included in an idealized retrieval based on optimal estimation (*Rodgers*, 2000). Aspect ratio AR is fixed to 0.6, and the Eddy dissipation rate ϵ is set to the same three values as for analyzing the response functions. Because the broadening of the radar spectrum σ_k not only depends on ϵ, but also on the wind as measured by the aircraft, σ_k is not fixed and is included as additional quantity into the retrieval. To investigate the information content that higher moments can contribute, the retrieval is applied to approximately 130 profiles of the ISDAC data set and the degrees of freedom for signal d_f are estimated (Figure 14). It is shown that when using σ, Sk, Ku, S_l, and S_r of a single frequency, already approximately 3 d_f can be obtained which is similar to a dual-frequency retrieval using only Z_e and W. Adding further frequencies adds about 1 d_f per frequency when σ and the higher moments are used. Another additional degree is obtained when using all moments together. For a triple-frequency combination, almost 6 d_f can be obtained on average, which corresponds to 75% of the length of the state vector. Unfortunately, the percentage of successfully converging retrievals is only 40% to 75% for the lowest turbulence level. Even though d_f decreases by approximately 0.2 – 0.4 with increasing turbulence, the percentage of converging retrievals is increased to up to 60% to 90% already for the medium turbulence level. This is firstly attributed to the fact that higher moments are less noisy if turbulence

smooths the spectrum and secondly to small errors in the estimation of the prior uncertainty estimate.

The results have yet to be confirmed using real measurements, but for an idealized retrieval, higher moments are found to add significant information to ice cloud retrievals of Arctic stratocumulus clouds. Consequently, higher moments should be used more often when studying ice clouds.

10 OUTLOOK

In this chapter, a brief outlook is given for the two key issues discussed in this thesis (Figure 2).

10.1 KEY ISSUE I: ENHANCED SNOWFALL OBSERVATIONS

With the updated processing scheme, the *Micro Rain Radar* (MRR) was found to be valuable for observations of snowfall, also in remote regions. Even though uncertainties are high when converting reflectivity into precipitation rate, MRRs are not affected by blowing snow and wind undercatch as traditional precipitation gauges are. In addition, vertical profiles of Doppler velocity and spectrum width are also provided which can be used e. g., to investigate particle riming (*Colle et al.*, 2014) or to estimate turbulence (*Garrett and Yuter*, 2014). It would even be possible to combine MRR with ceilometer measurements (*Hogan et al.*, 2003) to develop a simple, low-cost combined radar-lidar product.

Ceilometer are low-cost lidars designed for cloud base height estimation.

Vertical profiles observed by MRR at sites in Antarctica and Svalbard were used to analyze the impact of the blind zone on snowfall measurements of the CloudSat satellite. Because the spatial variability of precipitation is high, additional studies are required to investigate the vertical variability for other regions, for example in the mid-latitudes. The analysis in not limited to MRR observations and also other vertically pointing radars can be used, too, for example the MIRA35 (*Melchionna et al.*, 2008; *Löhnert et al.*, 2011) or the KAZR radar of the ARM program (*Mather and Voyles*, 2012). The use of more advanced cloud radars has the advantage that these feature a better sensitivity for observation of weak precipitation and a higher spatio-temporal resolution. The spatio-temporal resolution and the sensitivity are the main weaknesses of MRR and an enhancement of the hardware would be desirable for the future.

10.2 KEY ISSUE II: EXPLOITING HIGHER MOMENTS

Due to the flexible design of the presented PAMTRA forward model, it can be used for many applications, e. g., online and offline coupling to various kinds of weather or climate models, from global to large eddy scale. Such forward operators are crucial for both kinds of model evaluation, model-to-observation evaluations in measurement space and—incorporated into a retrieval—observation-to-model evaluations in the model space. Due to its passive and active capabilities, PAMTRA is

especially suited for development, for sensitivity studies, and for retrievals of combined passive-active microwave instruments. For this, new instruments have become available recently, e. g., HAMP which is the active-passive microwave package of the new German *High Altitude and LOng range research aircraft* (HALO, *Mech et al.*, 2014) or the recently launched core satellite of the *Global Precipitation Measurement* (GPM) mission (*Hou et al.*, 2014) which carries a dual-frequency precipitation radar and a multi-channel (10–183 GHz) microwave imager. There is also an increasing number of ground-based sites (e. g., *Löhnert et al.*, 2011, 2014; *Mather and Voyles*, 2012; *Shupe et al.*, 2013) featuring radar-microwave radiometer combinations, amongst other instruments.

One particular application of PAMTRA was presented in this thesis: PAMTRA was used to forward model aircraft in-situ measurements of ice clouds. This resulted in the development of a novel method to estimate particle mass as a function of temperature. Subsequently, various methods were used to evaluate ice cloud parameterizations describing projected area and particle size distribution. For this, the higher moments of the radar Doppler spectrum were found to be an useful addition to the standard observables (i. e., the lower moments). Unfortunately, the used ISDAC data set is rather small and older data sets (e. g., MPACE, *Verlinde et al.*, 2007) cannot be used, because at that time aircraft in situ probes with the new modified tip design for avoiding particle shattering (*Korolev et al.*, 2013) were not yet available. Therefore, additional collocated radar–in situ measurements of ice clouds are needed for the future. This would e. g. allow to refine the dependence of particle mass on temperature using smaller temperature intervals. The availability of additional measurements could also be used to test the results for geographical dependence. The use of an airborne instead of a ground-based radar (*Wang et al.*, 2012) would lead to a better match of observed volumes, but at the same time, this would also make the measurement of the radar moments challenging due to the movement of the aircraft (*Mech et al.*, 2014).

Nevertheless, the found coefficients and analytical expressions can still be included in a retrieval framework to investigate the potential of higher radar moments for retrieving particle mass, projected area, and particle size distribution. Even though the response functions were found to be rather small, for an idealized retrieval it was found that higher moments can add significant, additional information at moderate turbulence levels as they are common for Arctic stratocumulus clouds. A retrieval based on lower and higher moments obtained at a single frequency can provide more information than a dual-frequency retrieval based only on radar reflectivity and mean Doppler velocity. These results highlight the great potential of higher moments which should be exploited more often in the future. The forward model was configured in accordance to the more advanced KAZR instead

of the older MMCR. For the latter, the retrieval was less successful. This highlights the great importance of the quality of radar measurements. In the future, advancements of radar technology will result in cleaner radar spectra less affected by noise and artifacts allowing better exploitation of the spectrum and higher moments.

As a next step, it is necessary to explore the error space of the obtained retrieval solutions in detail. This allows to investigate which of the parameters to describe particle mass, projected area, and particle ice distribution can be retrieved well and for which parameters the estimate cannot be significantly improved in comparison to the a priori uncertainty. With upcoming future radar generations, it is expected that the noise level is further reduced resulting in enhanced estimates of the higher moments making the retrieval more stable. In addition, the a priori description of the ice clouds needs to be improved, because for optimal estimation, it is of great importance to specify the error characteristics correctly (*Ebell et al.*, 2010). The description of the mass-size relation as a function of temperature using only seven different temperature intervals could lead to undesired correlations in the prior uncertainty matrix obstructing retrieval convergence. The retrieval could also be extended such that the observation vector is composed of the full Doppler spectrum in order to investigate whether this adds further information to the retrieval. Another approach would be using slanted measurements in order to exploit also polarimetric radar observations in addition to Doppler observations (*Spek et al.*, 2008; *Dufournet and Russchenberg*, 2011). This however, greatly enhances the impact of horizontal wind on the spectrum which probably prohibits the use of higher moments.

Also, the use of enhanced scattering models could improve the retrieval performance. Alternatives to the use of Mie and T-Matrix theories could be the Rayleigh-Gans theory (e. g., *Bohren and Huffman*, 1983) or database supported DDA calculations (*Liu*, 2008b; *Petty and Huang*, 2010; *Tyynelä et al.*, 2011, 2014). For the latter, however, the problem has yet to be solved how particle distributions following arbitrary mass-size and area-size relations (as it is required by retrievals) can be obtained from a database which contains only certain particle types with certain mass-size and area-size relations. One possibility to solve this issue would be to select different particles from the database (possibly in accordance with temperature) and mix them such that the mixture matches the required microphysical properties.

Finally, other Bayesian retrieval methods such as *Markov chain Monte Carlo* (MCMC) could be used (*Posselt et al.*, 2008; *Posselt and Mace*, 2014; *Vrugt et al.*, 2008, 2009). Even though they require much more resources with respect to computing time, they can handle non-linear forward models and arbitrary, non-Gaussian probability density functions and allow a detailed investigation of the solution space.

The found potential of higher moments for observing ice clouds has yet to be confirmed by application of the retrieval to real measurements. Unfortunately, it was found that a radar more advanced than the MMCR is required to develop a successful retrieval. However, to the author's knowledge no data set is currently available which contains both, state-of-the-art vertically pointing Doppler radar observations and in situ aircraft observations of stratus or stratocumulus clouds using already modified probe tips as proposed by *Korolev et al.* (2013). As a consequence, the realization of such a campaign is highly desirable for the future.

ABBREVIATIONS

2-D	2-Dimensional
3-D	3-Dimensional
AGL	Above Ground Level
ARM	Atmospheric Radiation Measurement program
CHEOPS	Cologne High Efficient Operating Platform for Science
D3R	Dual-frequency Dual-polarized Doppler Radar
DDA	Discrete Dipole Approximation method
DQQ	Detrended Quantile-Quantile plot
DREAM	Differential Evolution Adaptive Metropolis
FFT	Fast Fourier Transformation
FMCW	Frequency Modulated Continuous Wave
GCM	Global Climate Model
GCPEX	GPM Cold-season Precipitation EXperiment
GPM	Global Precipitation Mission
HALO	High Altitude and LOng range research aircraft
HAMP	HALO Microwave Package
IMPROTOO	Improved Mrr PROcessing TOOl
IPCC	Intergovernmental Panel on Climate Change
ISDAC	Indirect and Semi-Direct Aerosol Campaign
IWC	Ice Water Content
KAZR	K_a-band ARM Zenith Radar
LIDAR	LIght Detection and Ranging
MCMC	Markov Chain Monte Carlo
MPACE	Mixed-Phase Arctic Cloud Experiment
MRDSS	McGill Radar Doppler Spectra Simulator
MRR	Micro Rain Radar

NWP	Numerical Weather Prediction
PAMTRA	Passive and Active Microwave Radiative TRansfer model
PDF	Probability Density Function
RADAR	RAdio Detection and Ranging
PRF	Pulse Repetition Frequency
SCLW	SuperCooled Liquid Water
SNR	Signal-to-Noise Ratio
SSM/I	Special Sensor Microwave Imager
TAMDAR	Tropospheric Aircraft Meteorological Data Reports
USF	Umweltforschungsstation SchneeFernerhaus

A	Projected particle area
a	Pre-factor of the mass-size relation
a'	Kolmogorov constant
AR	Aspect Ratio
b	Exponent of the mass-size relation
c	Pre-factor of the area-size relation
C_0	Reference particle mass of the normalized mass-size relation
D	Particle size defined as maximum extend
d	Exponent of the area-size relation
D^*	Reference particle size of the normalized mass-size relation
d_f	degrees of freedom for signal
D_m	Mass-weighted mean diameter of the normalized gamma distribution
D_{max}	Upper boundary of the particle size distribution
D_{min}	Lower boundary of the particle size distribution
e	Pre-factor of the $Z_e - W$ relation
f	Exponent of the $Z_e - W$ relation
H_{CS}	CloudSat observation height
H_{FM}	Observation height of potential future satellite missions
H_{SF}	Near-surface observation height
k	Wave number
$\|K\|^2$	Dielectric factor
$\|K_w\|^2$	Dielectric factor for liquid water at cm wavelengths
$\mathbb{K}_i$	Jacobian matrix at iteration i
Ku	Kurtosis

L_s	Largest length scale observed by the radar
L_λ	Smallest length scale observed by the radar
m	Particle mass
N	Particle size distribution
N_0	Intercept parameter of the (modified) gamma distribution and exponential distribution
N_0^*	Intercept parameter of the normalized gamma distribution
n_{fft}	Number of FFT points and Doppler spectrum bins
N_i	Spectral radar receiver noise power
N_P	Radar receiver noise power
n_{tot}	Total number of particles
P	Forward model
p	Pressure
q	Humidity
R	Radar range
$\dot{R}$	Rainfall rate
r	randomly distributed number
r_{eff}	Effective particle radius
S	Snowfall rate
$\mathbb{S}_a$	Covariance of a priori state
$\mathbb{S}_e$	Covariance of measurements
$\mathbb{S}_i$	Covariance of solution at iteration i
S_r	Right slope
Sk	Skewness
S_l	Left slope
T	Temperature
U	Horizontal wind
V	Vertical wind
v	Particle fall velocity / spectral Doppler velocity

v_{nyq}	Nypuist velocity
W	Mean Doppler velocity
$\mathbf{x}$	State vector
$\mathbf{x}_a$	A priori state vector
$\mathbf{x}_i$	State vector at iteration i
$\mathbf{y}$	Observation vector
Z	Radar reflectivity factor
Z_e	Equivalent radar reflectivity factor (mostly called "reflectivity")
α	Dimensionless pre-factor of the normalized mass-size relation
γ	Shape parameter of the (modified) gamma distribution
ΔD	Particle size bin size
ΔR	Radar range resolution
η	Radar reflectivity
η_D	Spectral reflectivity as a function of D
η_v	Spectral reflectivity as a function of v
$\eta_{v,N}$	Spectral reflectivity as a function of v with noise
θ	Half-power half-width one-way radar beam width
Λ	Slope parameter of the (modified) gamma distribution and exponential distribution
λ	Wavelength
μ	Shape parameter of the modified gamma distribution and the normalized gamma distribution
μ^*	Stabilized shape parameter of the normalized gamma distribution
ρ	Effective particle density
σ	Doppler spectrum width
σ_B	Radar backscattering cross section
σ_k	Total, kinematic spectral broadening
σ_s	Spectral broadening due to wind shear

σ_t	Spectral broadening due to turbulence
σ_w	Spectral broadening due to horizontal wind

BIBLIOGRAPHY

For the references of the included articles, please refer to the corresponding bibliographies in Publications I, II, and III.

Adams, N. (2004), Precipitation forecasting at high latitudes, *Wea. Forecasting*, *19*(2), 456–472, doi:10.1175/1520-0434(2004)019<0456:PFAHL>2.0.CO;2.

AMS (2014), Glossary of meteorology, available online: http://glossary.ametsoc.org/wiki (Accessed 22. Nov 2014).

Arakawa, A. (2004), The cumulus parameterization problem: Past, present, and future, *J. Climate*, *17*(13), 2493–2525, doi:10.1175/1520-0442(2004)017<2493:RATCPP>2.0.CO;2.

Atlas, D. (1948), New techniques in quantitative radar analysis of rainstorms, *Proc. Inst. Radio Eng.*, *36*(3), 377–377, WOS:A1948UM88300108.

Atlas, D. (1990), *Radar in meteorology: Battan Memorial and 40th Anniversary Radar Meteorology Conference*, American Meteorological Society, Boston.

Atlas, D., R. C. Srivastava, and R. S. Sekhon (1973), Doppler radar characteristics of precipitation at vertical incidence, *Rev. Geophys.*, *11*(1), 1–35, doi:10.1029/RG011i001p00001.

Bailey, M., and J. Hallett (2012), Ice crystal linear growth rates from −20° to −70°C: Confirmation from wave cloud studies, *J. Atmos. Sci.*, *69*(1), 390–402, doi:10.1175/JAS-D-11-035.1.

Bailey, M. P., and J. Hallett (2009), A comprehensive habit diagram for atmospheric ice crystals: Confirmation from the laboratory, AIRS II, and other field studies, *J. Atmos. Sci.*, *66*(9), 2888–2899, doi:10.1175/2009JAS2883.1.

Baker, B., and R. P. Lawson (2006), Improvement in determination of ice water content from two-dimensional particle imagery. Part I: Image-to-mass relationships, *J. Appl. Meteor. Climatol.*, *45*(9), 1282–1290, doi:10.1175/JAM2398.1.

Battaglia, A., and J. Delanoë (2013), Synergies and complementarities of CloudSat-CALIPSO snow observations, *J. Geophys. Res. Atmos.*, *118*(2), 721–731, doi:10.1029/2012JD018092.

Baumgardner, D., et al. (2012), In situ, airborne instrumentation: Addressing and solving measurement problems in ice clouds, *Bull. Amer. Meteor. Soc.*, *93*(2), ES29–ES34, doi:10.1175/BAMS-D-11-00123.1.

Bennartz, R., and G. W. Petty (2001), The sensitivity of microwave remote sensing observations of precipitation to ice particle size distributions, *J. Appl. Meteor.*, *40*(3), 345–364, doi:10.1175/1520-0450(2001)040<0345:TSOMRS>2.0.CO;2.

Bentley, W. A. (1901), Twenty years' study of snow crystals, *Mon. Wea. Rev.*, *29*(5), 212–214, doi:10.1175/1520-0493(1901)29[212b:TASOSC]2.0.CO;2.

Bentley, W. A. (1903), Studies among the snow crystals during the winter of 1901–2, with additional data collected during previous winters, *Mon. Wea. Rev.*, *30*(13), 607–616, doi:10.1175/1520-0493-30.13.607.

Bodas-Salcedo, A., M. J. Webb, S. Bony, H. Chepfer, J.-L. Dufresne, S. A. Klein, Y. Zhang, R. Marchand, J. M. Haynes, R. Pincus, and V. O. John (2011), COSP: Satellite simulation software for model assessment, *Bull. Amer. Meteor. Soc.*, *92*(8), 1023–1043, doi:10.1175/2011BAMS2856.1.

Bohren, C. F., and L. J. Battan (1980), Radar backscattering by inhomogeneous precipitation particles, *J. Atmos. Sci.*, *37*(8), 1821–1827, doi:10.1175/1520-0469(1980)037<1821:RBBIPP>2.0.CO;2.

Bohren, C. F., and D. R. Huffman (1983), *Absorption and Scattering of Light by Small Particles*, John Wiley & Sons.

Boudala, F. S., G. A. Isaac, S. G. Cober, and Q. Fu (2004), Liquid fraction in stratiform mixed-phase clouds from in situ observations, *Q.J.R. Meteorol. Soc.*, *130*(603), 2919–2931, doi:10.1256/qj.03.153.

Bouniol, D., A. J. Illingworth, and R. J. Hogan (2003), Deriving turbulent kinetic energy dissipation rate within clouds using ground based 94 GHz radar, in *Proc. of the 31st Conf. on Radar Meteorology*, pp. 193–196, Am. Meteor. Soc., Seattle, WA.

Bringi, V. N., and V. Chandrasekar (2001), *Polarimetric Doppler Weather Radar: Principles and Applications*, Cambridge University Press, Cambrigde.

Bringi, V. N., R. M. Rasmussen, and J. Vivekanandan (1986a), Multiparameter radar measurements in Colorado convective storms. Part I: Graupel melting studies, *J. Atmos. Sci.*, *43*(22), 2545–2563, doi:10.1175/1520-0469(1986)043<2545:MRMICC>2.0.CO;2.

Bringi, V. N., J. Vivekanandan, and J. D. Tuttle (1986b), Multiparameter radar measurements in Colorado convective storms. Part II: Hail detection studies, *J. Atmos. Sci.*, *43*(22), 2564–2577, doi:10.1175/1520-0469(1986)043<2564:MRMICC>2.0.CO;2.

Bringi, V. N., V. Chandrasekar, N. Balakrishnan, and D. S. Zrnić (1990), An examination of propagation effects in rainfall on radar measurements at microwave frequencies, *J. Atmos. Oceanic Technol.*, *7*(6), 829–840, doi:10.1175/1520-0426(1990)007<0829:AEOPEI>2.0.CO;2.

Brown, P. R. A., and P. N. Francis (1995), Improved measurements of the ice water content in cirrus using a total-water probe, *J. Atmos. Oceanic Technol.*, *12*(2), 410–414, doi:10.1175/1520-0426(1995)012<0410:IMOTIW>2.0.CO;2.

Brown, R. A., L. R. Lemon, and D. W. Burgess (1978), Tornado detection by pulsed Doppler radar, *Mon. Wea. Rev.*, *106*(1), 29–38, doi:10.1175/1520-0493(1978)106<0029:TDBPDR>2.0.CO;2.

Cadeddu, M., and D. Turner (2011), Evaluation of water permittivity models from ground-based observations of cold clouds at frequencies between 23 and 170 GHz, *IEEE Trans. Geosci. Remote Sens.*, *49*(8), 2999–3008, doi:10.1109/TGRS.2011.2121074.

Call, D. A. (2011), The effect of snow on traffic counts in western New York State, *Wea. Climate Soc.*, *3*(2), 71–75, doi:10.1175/WCAS-D-10-05008.1.

Capsoni, C., M. D'Amico, and R. Nebuloni (2001), A multiparameter polarimetric radar simulator, *J. Atmos. Oceanic Technol.*, *18*(11), 1799–1809, doi:10.1175/1520-0426(2001).

Caumont, O., V. Ducrocq, G. Delrieu, M. Gosset, J.-P. Pinty, J. Parent du Châtelet, H. Andrieu, Y. Lemaître, and G. Scialom (2006), A radar simulator for high-resolution nonhydrostatic models, *J. Atmos. Oceanic Technol.*, *23*(8), 1049–1067, doi:10.1175/JTECH1905.1.

Chandrasekar, V., M. Schwaller, M. Vega, J. Carswell, K. Mishra, R. Meneghini, and C. Nguyen (2010), Scientific and engineering overview of the NASA dual-frequency dual-polarized Doppler radar (D3R) system for GPM ground validation, in *Geoscience and Remote Sensing Symposium (IGARSS), 2010 IEEE International*, pp. 1308–1311, doi:10.1109/IGARSS.2010.5649440.

Colle, B. A., D. Stark, and S. E. Yuter (2014), Surface microphysical observations within East Coast winter storms on Long Island, New York, *Mon. Wea. Rev.*, *142*(9), 3126–3146, doi:10.1175/MWR-D-14-00035.1.

Czekala, H., and C. Simmer (1998), Microwave radiative transfer with nonspherical precipitating hydrometeors, *J. Quant. Spectrosc. Radiat. Transfer*, *60*(3), 365–374, doi:10.1016/S0022-4073(98)00012-0.

Delanoë, J., and R. J. Hogan (2008), A variational scheme for retrieving ice cloud properties from combined radar, lidar, and infrared radiometer, *J. Geophys. Res.*, *113*, D07,204, doi:10.1029/2007JD009000.

Delanoë, J., A. Protat, J. Testud, D. Bouniol, A. J. Heymsfield, A. Bansemer, P. R. A. Brown, and R. M. Forbes (2005), Statistical properties of the normalized ice particle size distribution, *J. Geophys. Res.*, *110*(D10), D10,201, doi:10.1029/2004JD005405.

Delanoë, J. M. E., A. J. Heymsfield, A. Protat, A. Bansemer, and R. J. Hogan (2014), Normalized particle size distribution for remote sensing application, *J. Geophys. Res. Atmos.*, *119*(7), 4204–4227, doi:10.1002/2013JD020700.

Deng, M., and G. G. Mace (2006), Cirrus microphysical properties and air motion statistics using cloud radar Doppler moments. Part I: Algorithm description, *J. Appl. Meteor. Climatol.*, *45*(12), 1690–1709, doi:10.1175/JAM2433.1.

DeVoe, H. (1964), Optical properties of molecular aggregates. I. Classical model of electronic absorption and refraction, *J. Chem. Phys.*, *41*(2), 393–400, doi:10.1063/1.1725879.

DeVoe, H. (1965), Optical properties of molecular aggregates. II. Classical theory of the refraction, absorption, and optical activity of solutions and crystals, *J. Chem. Phys.*, *43*(9), 3199–3208, doi:10.1063/1.1697294.

Doppler, C. (1842), *Ueber das farbige Licht der Doppelsterne und einiger anderer Gestirne des Himmels Versuch einer das Bradley'sche Aberrations-Theorem als integrirenden Theil in sich schliessenden allgemeineren Theorie*, *Abhandlungen der k. böhm. Gesellschaft der Wissenschaften*, vol. 2, Borrosch & André, Prag.

Doviak, R. J., and D. S. Zrnic (1993), *Doppler Radar & Weather Observations, Second Edition*, 2 ed., Academic Press, San Diego.

Dufournet, Y., and H. W. J. Russchenberg (2011), Towards the improvement of cloud microphysical retrievals using simultaneous doppler and polarimetric radar measurements, *Atmos. Meas. Tech.*, *4*(10), 2163–2178, doi:10.5194/amt-4-2163-2011.

Ebell, K., U. Löhnert, S. Crewell, and D. D. Turner (2010), On characterizing the error in a remotely sensed liquid water content profile, *Atmos. Res.*, *98*(1), 57–68, doi:10.1016/j.atmosres.2010.06.002.

Eliasson, S., S. A. Buehler, M. Milz, P. Eriksson, and V. O. John (2011), Assessing observed and modelled spatial distributions of ice water path using satellite data, *Atmos. Chem. Phys.*, *11*(1), 375–391, doi:10.5194/acp-11-375-2011.

Ellison, W. J. (2007), Permittivity of pure water, at standard atmospheric pressure, over the frequency range 0–25THz and the temperature range 0–100°C, *J. Phys. Chem. Ref. Data*, *36*(1), 1–18, doi:10.1063/1.2360986.

Eriksson, P., S. A. Buehler, C. P. Davis, C. Emde, and O. Lemke (2011), ARTS, the atmospheric radiative transfer simulator, version 2, *J. Quant. Spectrosc. Radiat. Transfer*, *112*(10), 1551–1558, doi:10.1016/j.jqsrt.2011.03.001.

ESA (2004), EGPM – European contribution to global precipitation measurement SP-1279(5), available online: http://www.esa.int/esapub/sp/sp1279/sp1279_5_EGPM.pdf (Accessed 22. Nov 2014).

Evans, K. F., and G. L. Stephens (1995a), Microwave radiative transfer through clouds composed of realistically shaped ice crystals. Part I. Single scattering properties, *J. Atmos. Sci.*, *52*(11), 2041–2057, doi:10.1175/1520-0469(1995)052<2041:MRTTCC>2.0.CO;2.

Evans, K. F., and G. L. Stephens (1995b), Microwave radiative transfer through clouds composed of realistically shaped ice crystals. Part II. Remote sensing of ice clouds, *J. Atmos. Sci.*, *52*(11), 2058–2072, doi:10.1175/1520-0469(1995)052<2058:MRTTCC>2.0.CO;2.

Evans, K. F., S. J. Walter, A. J. Heymsfield, and G. M. McFarquhar (2002), Submillimeter-wave cloud ice radiometer: Simulations of retrieval algorithm performance, *J. Geophys. Res.*, *107*(D3), AAC 2–1, doi:10.1029/2001JD000709.

Fabry, F., and I. Zawadzki (1995), Long-term radar observations of the melting layer of precipitation and their interpretation, *J. Atmos. Sci.*, *52*(7), 838–851, doi:10.1175/1520-0469(1995)052<0838:LTROOT>2.0.CO;2.

Field, P. R., R. J. Hogan, P. R. A. Brown, A. J. Illingworth, T. W. Choularton, and R. J. Cotton (2005), Parametrization of ice-particle size distributions for mid-latitude stratiform cloud, *Q.J.R. Meteorol. Soc.*, *131*(609), 1997–2017, doi:10.1256/qj.04.134.

Field, P. R., A. J. Heymsfield, and A. Bansemer (2006), Shattering and particle interarrival times measured by optical array probes in ice clouds, *J. Atmos. Oceanic Technol.*, *23*(10), 1357–1371, doi:10.1175/JTECH1922.1.

Gans, R. (1912), Über die Form ultramikroskopischer Goldteilchen, *Ann. Phys.*, *342*(5), 881–900, doi:10.1002/andp.19123420503.

Garnett, J. C. M. (1904), Colours in metal glasses and in metallic films, *Phil. Trans. Roy. Soc. London*, *203*, 385–420.

Garrett, T. J., and S. E. Yuter (2014), Observed influence of riming, temperature, and turbulence on the fallspeed of solid precipitation, *Geophys. Res. Lett.*, *41*(18), 6515–6522, doi:10.1002/2014GL061016.

Gorodetskaya, I. V., M. Tsukernik, K. Claes, M. F. Ralph, W. D. Neff, and N. P. M. Van Lipzig (2014), The role of atmospheric rivers in anomalous snow accumulation in East Antarctica, *Geophys. Res. Lett.*, *41*(17), 6199–6206, doi:10.1002/2014GL060881.

Gorodetskaya, I. V., S. Kneifel, M. Maahn, K. Van Tricht, W. Thiery, J. H. Schween, A. Mangold, S. Crewell, and N. P. M. Van Lipzig (2015), Cloud and precipitation properties from ground-based remote-sensing instruments in east antarctica, *The Cryosphere*, *9*(1), 285–304, doi:10.5194/tc-9-285-2015.

Gossard, E. E., and R. G. Strauch (1989), *Further Guide for the Retrieval of Dropsize Distributions in Water Clouds with a Ground-based Clear-air-sensing Doppler Radar*, NASA STI/Recon Technical Report N, U.S. Department of Commerce, National Oceanic and Atmospheric Administration, Environmental Research Laboratories.

Grecu, M., and W. S. Olson (2008), Precipitating snow retrievals from combined airborne cloud radar and millimeter-wave radiometer observations, *J. Appl. Meteor. Climatol.*, *47*(6), 1634–1650, doi:10.1175/2007JAMC1728.1.

Gultepe, I., and D. O. Starr (1995), Dynamical structure and turbulence in cirrus clouds: Aircraft observations during FIRE, *J. Atmos. Sci.*, *52*(23), 4159–4182, doi:10.1175/1520-0469(1995)052<4159:DSATIC>2.0.CO;2.

Gunn, K. L. S., and J. S. Marshall (1958), The distribution with size of aggregate snowflakes, *J. Meteor.*, *15*(5), 452–461, doi:10.1175/1520-0469(1958)015<0452:TDWSOA>2.0.CO;2.

Gunn, R., and G. D. Kinzer (1949), The terminal velocity of fall for water droplets in stagnant air, *J. Meteor.*, *6*(4), 243–248, doi:10.1175/1520-0469(1949)006<0243:TTVOFF>2.0.CO;2.

Hall, A. (2004), The role of surface albedo feedback in climate, *J. Climate*, *17*(7), 1550–1568, doi:10.1175/1520-0442(2004)017<1550:TROSAF>2.0.CO;2.

Hansen, J. E., and L. D. Travis (1974), Light scattering in planetary atmospheres, *Space Sci. Rev.*, *16*(4), 527–610, doi:10.1007/BF00168069.

Hashino, T., M. Satoh, Y. Hagihara, T. Kubota, T. Matsui, T. Nasuno, and H. Okamoto (2013), Evaluating cloud microphysics from NICAM against CloudSat and CALIPSO, *J. Geophys. Res. Atmos.*, *118*(13), 7273–7292, doi:10.1002/jgrd.50564.

Haynes, J. M., Z. Luo, G. L. Stephens, R. T. Marchand, and A. Bodas-Salcedo (2007), A multipurpose radar simulation package: QuickBeam, *Bull. Amer. Meteor. Soc.*, *88*(11), 1723–1727, doi:10.1175/BAMS-88-11-1723.

Henson, W., R. Stewart, and D. Hudak (2011), Vertical reflectivity profiles of precipitation over Iqaluit, Nunavut during autumn 2007, *Atmos. Res.*, *99*, 217–229, doi:10.1016/j.atmosres.2010.10.009.

Herman, B. M., and L. J. Battan (1961), Calculations of Mie back-scattering of microwaves from ice spheres, *Q.J.R. Meteorol. Soc.*, *87*(372), 223–230, doi:10.1002/qj.49708737210.

Heymsfield, A. J., and L. M. Miloshevich (2003), Parameterizations for the cross-sectional area and extinction of cirrus and stratiform ice cloud particles, *J. Atmos. Sci.*, *60*(7), 936–956, doi:10.1175/1520-0469(2003)060<0936:PFTCSA>2.0.CO;2.

Heymsfield, A. J., and C. M. R. Platt (1984), A parameterization of the particle size spectrum of ice clouds in terms of the ambient temperature and the ice water content, *J. Atmos. Sci.*, *41*(5), 846–855, doi:10.1175/1520-0469(1984)041<0846:APOTPS>2.0.CO;2.

Heymsfield, A. J., and C. D. Westbrook (2010), Advances in the estimation of ice particle fall speeds using laboratory and field measurements, *J. Atmos. Sci.*, *67*(8), 2469–2482, doi:10.1175/2010JAS3379.1.

Heymsfield, A. J., A. Bansemer, C. Schmitt, C. Twohy, and M. R. Poellot (2004), Effective ice particle densities derived from aircraft data, *J. Atmos. Sci.*, *61*(9), 982–1003, doi:10.1175/1520-0469(2004)061<0982:EIPDDF>2.0.CO;2.

Heymsfield, A. J., C. Schmitt, and A. Bansemer (2013), Ice cloud particle size distributions and pressure-dependent terminal velocities from in situ observations at temperatures from 0° to −86°C, *J. Atmos. Sci.*, *70*(12), 4123–4154, doi:10.1175/JAS-D-12-0124.1.

Hildebrand, P. H., and R. S. Sekhon (1974), Objective determination of the noise level in Doppler spectra, *J. Appl. Meteor.*, *13*(7), 808–811, doi:10.1175/1520-0450(1974)013<0808:ODOTNL>2.0.CO;2.

Hobbs, P. V., S. Chang, and J. D. Locatelli (1974), The dimensions and aggregation of ice crystals in natural clouds, *J. Geophys. Res.*, *79*(15), 2199–2206, doi:10.1029/JC079i015p02199.

Hogan, A. W. (1975), Summer ice crystal precipitation at the South Pole, *J. Appl. Meteor.*, *14*(2), 246–249, doi:10.1175/1520-0450(1975)014<0246:SICPAT>2.0.CO;2.

Hogan, R. J., and C. D. Westbrook (2014), Equation for the microwave backscatter cross section of aggregate snowflakes using the self-similar Rayleigh-Gans approximation, *J. Atmos. Sci.*, *71*(9), 3292–3301, doi:10.1175/JAS-D-13-0347.1.

Hogan, R. J., A. J. Illingworth, and H. Sauvageot (2000), Measuring crystal size in cirrus using 35- and 94-GHz radars, *J. Atmos. Oceanic Technol.*, *17*(1), 27–37, doi:10.1175/1520-0426(2000)017<0027:MCSICU>2.0.CO;2.

Hogan, R. J., A. J. Illingworth, E. J. O'Connor, and J. P. V. P. Baptista (2003), Characteristics of mixed-phase clouds. II: A climatology from ground-based lidar, *Q.J.R. Meteorol. Soc.*, *129*(592), 2117–2134, doi:10.1256/qj.01.209.

Hogan, R. J., L. Tian, P. R. A. Brown, C. D. Westbrook, A. J. Heymsfield, and J. D. Eastment (2012), Radar scattering from ice aggregates using the horizontally aligned oblate spheroid approximation, *J. Appl. Meteor. Climatol.*, *51*(3), 655–671, doi:10.1175/JAMC-D-11-074.1.

Hou, A. Y., S. Q. Zhang, A. M. da Silva, W. S. Olson, C. D. Kummerow, and J. Simpson (2001), Improving global analysis and short–range forecast using rainfall and moisture observations derived from TRMM and SSM/I passive microwave sensors, *Bull. Amer. Meteor. Soc.*, *82*(4), 659–679, doi:10.1175/1520-0477(2001)082<0659:IGAASF>2.3.CO;2.

Hou, A. Y., R. K. Kakar, S. Neeck, A. A. Azarbarzin, C. D. Kummerow, M. Kojima, R. Oki, K. Nakamura, and T. Iguchi (2014), The global precipitation measurement mission, *Bull. Amer. Meteor. Soc.*, *95*(5), 701–722, doi:10.1175/BAMS-D-13-00164.1.

Houze, R. A., P. V. Hobbs, P. H. Herzegh, and D. B. Parsons (1979), Size distributions of precipitation particles in frontal clouds, *J. Atmos. Sci.*, *36*(1), 156–162, doi:10.1175/1520-0469(1979)036<0156:SDOPPI>2.0.CO;2.

Hu, Y., S. Rodier, K.-m. Xu, W. Sun, J. Huang, B. Lin, P. Zhai, and D. Josset (2010), Occurrence, liquid water content, and fraction of supercooled water clouds from combined CALIOP/IIR/MODIS measurements, *J. Geophys. Res.*, *115*(D4), D00H34, doi:10.1029/2009JD012384.

Hudak, D., W. Petersen, G. Skofronick-Jackson, M. Wolde, M. Schwaller, P. Joe, C. Derksen, K. Strawbridge, P. Kollias, and R. Stewart (2012), GPM cold season precipitation experiment (GCPEx), in *2012 EUMETSAT Meteorological Satellite Conference*.

Intrieri, J. M., G. L. Stephens, W. L. Eberhard, and T. Uttal (1993), A method for determining cirrus cloud particle sizes using lidar and radar backscatter technique, *J. Appl. Meteor.*, *32*(6), 1074–1082, doi:10.1175/1520-0450(1993)032<1074:AMFDCC>2.0.CO;2.

IPCC (2014), *Climate Change 2013 - The Physical Science Basis: Working Group I Contribution to the Fifth Assessment Report of the Intergovernmental Panel on Climate Change*, Cambridge University Press, New York, available online: http://www.climatechange2013.org/ (Accessed 22. Nov 2014).

ITU (2000), Nomenclature of the frequency and wavelength bands used in telecommunications, International Telecommunication Union Recommendation V.431-7. Available online: http://www.itu.int/rec/R-REC-V.431-7-200005-I (Accessed 22. Nov 2014).

Jackson, R. C., G. M. McFarquhar, A. V. Korolev, M. E. Earle, P. S. K. Liu, R. P. Lawson, S. Brooks, M. Wolde, A. Laskin, and M. Freer (2012), The dependence of ice microphysics on aerosol concentration in Arctic mixed-phase stratus clouds during ISDAC and m-PACE, *J. Geophys. Res.*, *117*(D15), D15,207, doi:10.1029/2012JD017668.

Jiang, H., W. R. Cotton, J. O. Pinto, J. A. Curry, and M. J. Weissbluth (2000), Cloud resolving simulations of mixed-phase Arctic stratus observed during BASE: Sensitivity to concentration of ice crystals and large-scale heat and moisture advection, *J. Atmos. Sci.*, *57*(13), 2105–2117, doi:10.1175/1520-0469(2000)057<2105:CRSOMP>2.0.CO;2.

Kajikawa, M. (1992), Observations of the falling motion of plate-like snow crystals Part I: The free-fall patterns and velocity, *J. Meteor. Soc. Japan*, *70*(1), 1–9.

Kennedy, P. C., and S. A. Rutledge (2011), S-band dual-polarization radar observations of winter storms, *J. Appl. Meteor. Climatol.*, *50*(4), 844–858, doi:10.1175/2010JAMC2558.1.

Kepler, J., and C. Hardie (2014), *The Six-Cornered Snowflake*, Oxford University Press, Oxford.

Khvorostyanov, V. I., and J. A. Curry (2002), Terminal velocities of droplets and crystals: Power laws with continuous parameters over the size spectrum, *J. Atmos. Sci.*, *59*(11), 1872–1884, doi:10.1175/1520-0469(2002)059<1872:TVODAC>2.0.CO;2.

Kikuchi, K., T. Kameda, K. Higuchi, and A. Yamashita (2013), A global classification of snow crystals, ice crystals, and solid precipitation based on observations from middle latitudes to polar regions, *Atmos. Res.*, *132–133*, 460–472, doi:10.1016/j.atmosres.2013.06.006.

Klugmann, D., K. Heinsohn, and H.-J. Kirtzel (1996), A low cost 24 GHz FM-CW Doppler radar rain profiler, *Contrib. Atmos. Phys.*, *69*(1), 247–253.

Knapp, K. R., S. Ansari, C. L. Bain, M. A. Bourassa, M. J. Dickinson, C. Funk, C. N. Helms, C. C. Hennon, C. D. Holmes, G. J. Huffman, J. P. Kossin, H.-T. Lee, A. Loew, and G. Magnusdottir (2011), Globally gridded satellite observations for climate studies, *Bull. Amer. Meteor. Soc.*, *92*, 893–907, doi:10.1175/2011BAMS3039.1.

Kneifel, S. (2011), Characterization of snowfall using ground-based passive and active remote sensors., Ph.D. thesis, Universität zu Köln, available online: http://kups.ub.uni-koeln.de/4566/ (Accessed 22. Nov 2014).

Kneifel, S., U. Löhnert, A. Battaglia, S. Crewell, and D. Siebler (2010), Snow scattering signals in ground-based passive microwave radiometer measurements, *J. Geophys. Res.*, *115*(D16), D16,214, doi:10.1029/2010JD013856.

Kneifel, S., M. S. Kulie, and R. Bennartz (2011a), A triple-frequency approach to retrieve microphysical snowfall parameters, *J. Geophys. Res.*, *116*(D11), doi:10.1029/2010JD015430.

Kneifel, S., M. Maahn, G. Peters, and C. Simmer (2011b), Observation of snowfall with a low-power FM-CW K-band radar (Micro Rain Radar), *Meteorol. Atmos. Phys.*, *113*(1-2), 75–87, doi:10.1007/s00703-011-0142-z.

Kneifel, S., S. Redl, E. Orlandi, U. Löhnert, M. P. Cadeddu, D. D. Turner, and M.-T. Chen (2014), Absorption properties of supercooled liquid water between 31 and 225 GHz: Evaluation of absorption models using ground-based observations, *J. Appl. Meteor. Climatol.*, *53*(4), 1028–1045, doi:10.1175/JAMC-D-13-0214.1.

Knuteson, R. O., H. E. Revercomb, F. A. Best, N. C. Ciganovich, R. G. Dedecker, T. P. Dirkx, S. C. Ellington, W. F. Feltz, R. K. Garcia, H. B. Howell, W. L. Smith, J. F. Short, and D. C. Tobin (2004), Atmospheric emitted radiance interferometer. Part I: Instrument design, *J. Atmos. Oceanic Technol.*, *21*(12), 1763–1776, doi:10.1175/JTECH-1662.1.

Knuth, S. L., G. J. Tripoli, J. E. Thom, and G. A. Weidner (2010), The influence of blowing snow and precipitation on snow depth change across the Ross ice shelf and Ross sea regions of Antarctica, *J. Appl. Meteor. Climatol.*, *49*(6), 1306–1321, doi:10.1175/2010JAMC2245.1.

Kollias, P., E. E. Clothiaux, M. A. Miller, E. P. Luke, K. L. Johnson, K. P. Moran, K. B. Widener, and B. A. Albrecht (2007a), The atmospheric radiation measurement program cloud profiling radars: Second-generation sampling strategies, processing, and cloud data products, *J. Atmos. Oceanic Technol.*, *24*(7), doi:10.1175/JTECH2033.1.

Kollias, P., E. E. Clothiaux, M. A. Miller, B. A. Albrecht, G. L. Stephens, and T. P. Ackerman (2007b), Millimeter-wavelength radars: New frontier in atmospheric cloud and precipitation research, *Bull. Amer. Meteor. Soc.*, *88*(10), 1608–1624, doi:10.1175/BAMS-88-10-1608.

Kollias, P., J. Rémillard, E. Luke, and W. Szyrmer (2011), Cloud radar Doppler spectra in drizzling stratiform clouds: 1. forward modeling and remote sensing applications, *J. Geophys. Res.*, *116*(D13), D13,201, doi:10.1029/2010JD015237.

Kollias, P., S. Tanelli, A. Battaglia, and A. Tatarevic (2013), Evaluation of EarthCARE cloud profiling radar Doppler velocity measurements in particle sedimentation regimes, *J. Atmos. Oceanic Technol.*, *31*(2), 366–386, doi:10.1175/JTECH-D-11-00202.1.

Korolev, A. (2007), Limitations of the Wegener–Bergeron–Findeisen mechanism in the evolution of mixed-phase clouds, *J. Atmos. Sci.*, *64*(9), 3372–3375, doi:10.1175/JAS4035.1.

Korolev, A., and G. Isaac (2003), Roundness and aspect ratio of particles in ice clouds, *J. Atmos. Sci.*, *60*(15), 1795–1808, doi:10.1175/1520-0469(2003)060<1795:RAAROP>2.0.CO;2.

Korolev, A., E. Emery, and K. Creelman (2013), Modification and tests of particle probe tips to mitigate effects of ice shattering, *J. Atmos. Oceanic Technol.*, *30*(4), 690–708, doi:10.1175/JTECH-D-12-00142.1.

Korolev, A. V., J. W. Strapp, G. A. Isaac, and A. N. Nevzorov (1998), The Nevzorov airborne hot-wire LWC–TWC probe: Principle of operation and performance characteristics, *J. Atmos. Oceanic Technol.*, *15*(6), 1495–1510, doi:10.1175/1520-0426(1998)015<1495:TNAHWL>2.0.CO;2.

Korolev, A. V., G. A. Isaac, and J. Hallett (1999), Ice particle habits in Arctic clouds, *Geophys. Res. Lett.*, *26*(9), 1299–1302, doi:10.1029/1999GL900232.

Kosarev, A. L., and I. P. Mazin (1991), An empirical model of the physical structure of upper-layer clouds, *Atmos. Res.*, *26*(3), 213–228, doi:10.1016/0169-8095(91)90055-2.

Krüger, M. L., S. Mertes, T. Klimach, Y. F. Cheng, H. Su, J. Schneider, M. O. Andreae, U. Pöschl, and D. Rose (2014), Assessment of cloud supersaturation by size-resolved aerosol particle and cloud condensation nuclei (CCN) measurements, *Atmos. Meas. Tech.*, *7*(8), 2615–2629, doi:10.5194/amt-7-2615-2014.

Kulie, M. S., and R. Bennartz (2009), Utilizing spaceborne radars to retrieve dry snowfall, *J. Appl. Meteor. Climatol.*, *48*(12), 2564–2580, doi:10.1175/2009JAMC2193.1.

Kulie, M. S., M. J. Hiley, R. Bennartz, S. Kneifel, and S. Tanelli (2014), Triple-frequency radar reflectivity signatures of snow: Observations and comparisons with theoretical ice particle scattering models, *J. Appl. Meteor. Climatol.*, *53*(4), 1080–1098, doi:10.1175/JAMC-D-13-066.1.

Kummerow, C., and J. Weinman (1988), Radiative properties of deformed hydrometeors for commonly used passive microwave frequencies, *IEEE Trans. Geosci. Remote Sens.*, *26*(5), 629–638, doi:10.1109/36.7689.

Leinonen, J., S. Kneifel, D. Moisseev, J. Tyynelä, S. Tanelli, and T. Nousiainen (2012), Evidence of nonspheroidal behavior in millimeter-wavelength radar observations of snowfall, *J. Geophys. Res.*, *117*(D18), D18,205, doi:10.1029/2012JD017680.

Lenaerts, J. T. M., M. R. van den Broeke, W. J. van de Berg, E. van Meijgaard, and P. Kuipers Munneke (2012), A new, high-resolution surface mass balance map of Antarctica (1979–2010) based on regional atmospheric climate modeling, *Geophys. Res. Lett.*, *39*(4), L04,501, doi:10.1029/2011GL050713.

Levizzani, V., P. Bauer, and F. J. Turk (Eds.) (2007), *Measuring Precipitation from Space: EURAINSAT and the Future*, 1 ed., Springer, Dordrecht.

Levizzani, V., S. Laviola, and E. Cattani (2011), Detection and measurement of snowfall from space, *Remote Sens.*, *3*(1), 145–166, doi:10.3390/rs3010145.

Lhermitte, R. (1987), A 94-GHz Doppler radar for cloud observations, *J. Atmos. Oceanic Technol.*, *4*(1), 36–48, doi:10.1175/1520-0426(1987)004<0036:AGDRFC>2.0.CO;2.

Li, J.-L., D. E. Waliser, J. H. Jiang, D. L. Wu, W. Read, J. W. Waters, A. M. Tompkins, L. J. Donner, J.-D. Chern, W.-K. Tao, R. Atlas, Y. Gu, K. N. Liou, A. Del Genio, M. Khairoutdinov, and A. Gettelman (2005), Comparisons of EOS MLS cloud ice measurements with ECMWF analyses and GCM simulations: Initial results, *Geophys. Res. Lett.*, *32*(18), L18,710, doi:10.1029/2005GL023788.

Li, J.-L., J. H. Jiang, D. E. Waliser, and A. M. Tompkins (2007), Assessing consistency between EOS MLS and ECMWF analyzed and forecast estimates of cloud ice, *Geophys. Res. Lett.*, *34*(8), L08,701, doi:10.1029/2006GL029022.

Libbrecht, K. G. (2005), The physics of snow crystals, *Rep. Prog. Phys.*, *68*(4), 855, doi:10.1088/0034-4885/68/4/R03.

Liebe, H. J., G. A. Hufford, and T. Manabe (1991), A model for the complex permittivity of water at frequencies below 1 THz, *Int. J. Infrared Millimeter Waves*, *12*(7), 659–675, doi:10.1007/BF01008897.

Liebe, H. J., G. A. Hufford, and M. G. Cotton (1993), Propagation modelling of moist air and suspended water/ice particles at frequencies below 1000 GHz, in *Proceedings AGARD 52nd Specialists Meeting of the Electromagnetic Wave Propagation Panel*, AGARD, Palma de Mallorca, Spain.

Liljegren, J., S.-A. Boukabara, K. Cady-Pereira, and S. Clough (2005), The effect of the half-width of the 22-GHz water vapor line on retrievals of temperature and water vapor profiles with a 12-channel microwave radiometer, *IEEE Trans. Geosci. Remote Sens.*, *43*(5), 1102–1108, doi:10.1109/TGRS.2004.839593.

Liu, C.-L., and A. J. Illingworth (2000), Toward more accurate retrievals of ice water content from radar measurements of clouds, *J. Appl. Meteor.*, *39*(7), 1130–1146, doi:10.1175/1520-0450(2000)039<1130:TMAROI>2.0.CO;2.

Liu, G. (2004), Approximation of single scattering properties of ice and snow particles for high microwave frequencies, *J. Atmos. Sci.*, *61*(20), 2441–2456, doi:10.1175/1520-0469(2004)061<2441:AOSSPO>2.0.CO;2.

Liu, G. (2008a), Deriving snow cloud characteristics from CloudSat observations, *J. Geophys. Res.*, *113*(D8), D00A09, doi:10.1029/2007JD009766.

Liu, G. (2008b), A database of microwave single-scattering properties for nonspherical ice particles, *Bull. Amer. Meteor. Soc.*, *89*(10), 1563–1570, doi:10.1175/2008BAMS2486.1.

Liu, G., and J. A. Curry (1997), Precipitation characteristics in Greenland-Iceland-Norwegian seas determined by using satellite microwave data, *J. Geophys. Res.*, *102*(D12), 13,987–13,997, doi:10.1029/96JD03090.

Liu, G., and J. A. Curry (2000), Determination of ice water path and mass median particle size using multichannel microwave measurements, *J. Appl. Meteor.*, *39*(8), 1318–1329, doi:10.1175/1520-0450(2000)039<1318:DOIWPA>2.0.CO;2.

Liu, Q., F. Weng, and S. English (2011), An improved fast microwave water emissivity model, *IEEE Trans. Geosci. Remote Sens.*, *49*(4), 1238–1250, doi:10.1109/TGRS.2010.2064779.

Locatelli, J. D., and P. V. Hobbs (1974), Fall speeds and masses of solid precipitation particles, *J. Geophys. Res.*, *79*(15), 2185–2197, doi:10.1029/JC079i015p02185.

Lord Rayleigh (1899), On the transmission of light through an atmosphere containing small particles in suspension, and on the origin of the blue of the sky, *Phil. Mag.*, *47*(287), 375–384.

Luke, E. P., P. Kollias, and M. D. Shupe (2010), Detection of supercooled liquid in mixed-phase clouds using radar Doppler spectra, *J. Geophys. Res.*, *115*(D19), D19,201, doi:10.1029/2009JD012884.

Lynn, B. H., A. P. Khain, J. Dudhia, D. Rosenfeld, A. Pokrovsky, and A. Seifert (2005), Spectral (bin) microphysics coupled with a mesoscale model (MM5). Part I: Model description and first results, *Mon. Wea. Rev.*, *133*(1), 44–58, doi:10.1175/MWR-2840.1.

Löhnert, U., S. Crewell, O. Krasnov, E. O'Connor, and H. Russchenberg (2008), Advances in continuously profiling the thermodynamic state of the boundary layer: Integration of measurements and methods, *J. Atmos. Oceanic Technol.*, *25*(8), 1251–1266, doi:10.1175/2007JTECHA961.1.

Löhnert, U., S. Kneifel, A. Battaglia, M. Hagen, L. Hirsch, and S. Crewell (2011), A multisensor approach toward a better understanding of snowfall microphysics: The TOSCA project, *Bull. Amer. Meteor. Soc.*, *92*(5), 613–628, doi:10.1175/2010BAMS2909.1.

Löhnert, U., J. H. Schween, C. Acquistapace, K. Ebell, M. Maahn, M. Barreraverdejo, A. Hirsikko, B. Bohn, A. Knaps, E. O'Connor, C. Simmer, A. Wahner, and S. Crewell (2014), JOYCE: Jülich observatory for cloud evolution, *Bull. Amer. Meteor. Soc.*, doi:10.1175/BAMS-D-14-00105.1.

L'Ecuyer, T. S., and J. H. Jiang (2010), Touring the atmosphere aboard the A-Train, *Phys. Today*, *63*(7), 36–41, doi:10.1063/1.3463626.

Maahn, M. (2010), Measuring precipitation with micro rain radars in Svalbard, Diploma thesis, University of Bonn.

Maahn, M., and P. Kollias (2012), Improved Micro Rain Radar snow measurements using Doppler spectra post-processing, *Atmos. Meas. Tech.*, *5*(11), 2661–2673, doi:10.5194/amt-5-2661-2012.

Maahn, M., C. Burgard, S. Crewell, I. V. Gorodetskaya, S. Kneifel, S. Lhermitte, K. Van Tricht, and N. P. M. van Lipzig (2014), How does the spaceborne radar blind zone affect derived surface snowfall statistics in polar regions?, *J. Geophys. Res. Atmos.*, *119*(24), 13,604–13,620, doi:10.1002/2014JD022079.

Maahn, M., U. Löhnert, P. Kollias, R. C. Jackson, and G. M. McFarquhar (2015), Developing and evaluating ice cloud parameterizations for forward modeling of radar moments using in situ aircraft observations, *J. Atmos. Oceanic Technol.*, *accepted*.

Mace, G. G., A. J. Heymsfield, and M. R. Poellot (2002), On retrieving the microphysical properties of cirrus clouds using the moments of the millimeter-wavelength Doppler spectrum, *J. Geophys. Res.*, *107*(D24), 4815, doi:10.1029/2001JD001308.

Magono, C., and C. W. Lee (1966), Meteorological classification of natural snow crystals, *J. Fac. Sci. Hokkaido Univ. Ser. 7*, *2*(4), 321–335.

Marchand, R., G. G. Mace, T. Ackerman, and G. Stephens (2008), Hydrometeor detection using Cloudsat—an earth-orbiting 94-GHz cloud radar, *J. Atmos. Oceanic Technol.*, *25*(4), 519–533, doi:10.1175/2007JTECHA1006.1.

Marshall, J. S. (1954), Book review: Snow crystals: Natural and artificial by U. Nakaya, *Am. J. Phys.*, *22*(8), 573–573, doi:10.1119/1.1933845.

Marshall, J. S., and K. L. S. Gunn (1952), Measurement of snow parameters by radar, *J. Meteor.*, *9*(5), 322–327, doi:10.1175/1520-0469(1952)009<0322:MOSPBR>2.0.CO;2.

Marshall, J. S., and W. M. K. Palmer (1948), The distribution of raindrops with size, *J. Meteor.*, *5*(4), 165–166, doi:10.1175/1520-0469(1948)005<0165:TDORWS>2.0.CO;2.

Marshall, J. S., R. C. Langille, and W. M. K. Palmer (1947), Measurement of rainfall by radar, *J. Meteor.*, *4*(6), 186–192, doi:10.1175/1520-0469(1947)004<0186:MORBR>2.0.CO;2.

Massey, F. J., Jr. (1951), The Kolmogorov-Smirnov test for goodness of fit, *J. Amer. Statist. Assoc.*, *46*(253), 68–78, doi:10.2307/2280095.

Masunaga, H., T. Matsui, W.-K. Tao, A. Y. Hou, C. D. Kummerow, T. Nakajima, P. Bauer, W. S. Olson, M. Sekiguchi, and T. Y. Nakajima (2010), Satellite data simulator unit: A multisensor, multispectral satellite simulator package, *Bull. Amer. Meteor. Soc.*, *91*(12), 1625–1632, doi:10.1175/2010BAMS2809.1.

Mather, J. H., and J. W. Voyles (2012), The ARM climate research facility: A review of structure and capabilities, *Bull. Amer. Meteor. Soc.*, *94*(3), 377–392, doi:10.1175/BAMS-D-11-00218.1.

Matrosov, S. Y. (1998), A dual-wavelength radar method to measure snowfall rate, *J. Appl. Meteor.*, *37*(11), 1510–1521, doi:10.1175/1520-0450(1998)037<1510:ADWRMT>2.0.CO;2.

Matrosov, S. Y. (2007), Modeling backscatter properties of snowfall at millimeter wavelengths, *J. Atmos. Sci.*, *64*(5), 1727–1736, doi:10.1175/JAS3904.1.

Matrosov, S. Y., and A. Battaglia (2009), Influence of multiple scattering on CloudSat measurements in snow: A model study, *Geophys. Res. Lett.*, *36*(12), L12,806, doi:10.1029/2009GL038704.

Matrosov, S. Y., R. F. Reinking, R. A. Kropfli, B. E. Martner, and B. W. Bartram (2001), On the use of radar depolarization ratios for estimating shapes of ice hydrometeors in winter clouds, *J. Appl. Meteor.*, *40*(3), 479–490, doi:10.1175/1520-0450(2001)040<0479:OTUORD>2.0.CO;2.

Matrosov, S. Y., A. V. Korolev, and A. J. Heymsfield (2002), Profiling cloud ice mass and particle characteristic size from Doppler radar measurements, *J. Atmos. Oceanic Technol.*, *19*(7), 1003–1018, doi:10.1175/1520-0426(2002)019<1003:PCIMAP>2.0.CO;2.

Matrosov, S. Y., R. F. Reinking, and I. V. Djalalova (2005), Inferring fall attitudes of pristine dendritic crystals from polarimetric radar data, *J. Atmos. Sci.*, *62*(1), 241–250, doi:10.1175/JAS-3356.1.

Matsui, T., T. Iguchi, X. Li, M. Han, W.-K. Tao, W. Petersen, T. L'Ecuyer, R. Meneghini, W. Olson, C. D. Kummerow, A. Y. Hou, M. R. Schwaller, E. F. Stocker, and J. Kwiatkowski (2013), GPM satellite simulator over ground validation sites, *Bull. Amer. Meteor. Soc.*, *94*(11), 1653–1660, doi:10.1175/BAMS-D-12-00160.1.

McFarquhar, G., et al. (2011), Indirect and semi-direct aerosol campaign: The impact of Arctic aerosols on clouds, *Bull. Amer. Meteor. Soc.*, *92*(2), doi:10.1175/2010BAMS2935.1.

McFarquhar, G. M., and A. J. Heymsfield (1998), The definition and significance of an effective radius for ice clouds, *J. Atmos. Sci.*, *55*(11), 2039–2052, doi:10.1175/1520-0469(1998)055<2039:TDASOA>2.0.CO;2.

McFarquhar, G. M., T.-L. Hsieh, M. Freer, J. Mascio, and B. F. Jewett (2014), The characterization of ice hydrometeor gamma size distributions as volumes in No/lambda/gamma phase space: Implications for microphysical process modeling, *J. Atmos. Sci.*, doi:10.1175/JAS-D-14-0011.1.

Mech, M., E. Orlandi, S. Crewell, F. Ament, L. Hirsch, M. Hagen, G. Peters, and B. Stevens (2014), HAMP – the microwave package on the High Altitude and LOng range research aircraft (HALO), *Atmos. Meas. Tech.*, *7*(12), 4539–4553, doi:10.5194/amt-7-4539-2014.

Mech, M., M. Maahn, S. Kneifel, P. Kollias, E. Orlandi, and S. Crewell (2015), PAMTRA - passive and active microwave radiative transfer model: Basic concepts and applications for cloud research, *Atmos. Chem. Phys.*, *in preparation*.

Melchionna, S., M. Bauer, and G. Peters (2008), A new algorithm for the extraction of cloud parameters using multipeak analysis of cloud radar data – first application and preliminary results, *Meteorol. Z.*, *17*(5), 613–620, doi:10.1127/0941-2948/2008/0322.

Metropolis, N., A. W. Rosenbluth, M. N. Rosenbluth, A. H. Teller, and E. Teller (1953), Equation of state calculations by fast computing machines, *J. Chem. Phys.*, *21*(6), 1087–1092, doi:10.1063/1.1699114.

Mie, G. (1908), Beiträge zur Optik trüber Medien, speziell kolloidaler Metallösungen, *Ann. Phys.*, *330*(3), 377–445, doi:10.1002/andp.19083300302.

Mishchenko, M. I. (2000), Calculation of the amplitude matrix for a nonspherical particle in a fixed orientation, *Appl. Opt.*, *39*(6), 1026–1031, doi:10.1364/AO.39.001026.

Misumi, R., H. Motoyoshi, S. Yamaguchi, S. Nakai, M. Ishizaka, and Y. Fujiyoshi (2014), Empirical relationships for estimating liquid water fraction of melting snowflakes, *J. Appl. Meteor. Climatol.*, *53*(10), 2232–2245, doi:10.1175/JAMC-D-13-0169.1.

Mitchell, D. L. (1996), Use of mass- and area-dimensional power laws for determining precipitation particle terminal velocities, *J. Atmos. Sci.*, *53*(12), 1710–1723, doi:10.1175/1520-0469(1996)053<1710:UOMAAD>2.0.CO;2.

Mitchell, D. L., and A. J. Heymsfield (2005), Refinements in the treatment of ice particle terminal velocities, highlighting aggregates, *J. Atmos. Sci.*, *62*(5), 1637–1644, doi:10.1175/JAS3413.1.

Mitchell, D. L., R. Zhang, and R. L. Pitter (1990), Mass-dimensional relationships for ice particles and the influence of riming on snowfall rates, *J. Appl. Meteor.*, *29*(2), 153–163, doi:10.1175/1520-0450(1990)029<0153:MDRFIP>2.0.CO;2.

Moran, K. P., B. E. Martner, M. J. Post, R. A. Kropfli, D. C. Welsh, and K. B. Widener (1998), An unattended cloud-profiling radar for use in climate research, *Bull. Amer. Meteor. Soc.*, *79*(3), 443–455, doi:10.1175/1520-0477(1998)079<0443:AUCPRF>2.0.CO;2.

Mätzler, C. (Ed.) (2006), *Thermal Microwave Radiation: Applications for Remote Sensing*, IET, Stevenage.

Nakaya, U. (1954), *Snow crystals, natural and artificial.*, Harvard University Press, Cambridge.

Nastrom, G. D. (1997), Doppler radar spectral width broadening due to beamwidth and wind shear, *Annales Geophysicae*, *15*(6), 786–796, doi:10.1007/s00585-997-0786-7.

Noel, V., and K. Sassen (2005), Study of planar ice crystal orientations in ice clouds from scanning polarization lidar observations, *J. Appl. Meteor.*, *44*(5), 653–664, doi:10.1175/JAM2223.1.

Noone, K. J., J. A. Ogren, J. Heintzenberg, R. J. Charlson, and D. S. Covert (1988), Design and calibration of a counterflow virtual impactor for sampling of atmospheric fog and cloud droplets, *Aerosol Sci. Technol.*, *8*(3), 235–244, doi:10.1080/02786828808959186.

O'Brien, S. G., and G. H. Goedecke (1988), Scattering of millimeter waves by snow crystals and equivalent homogeneous symmetric particles, *Appl. Opt.*, *27*(12), 2439–2444, doi:10.1364/AO.27.002439.

O'Connor, E. J., R. J. Hogan, and A. J. Illingworth (2005), Retrieving stratocumulus drizzle parameters using Doppler radar and lidar, *J. Appl. Meteor.*, *44*(1), 14–27, doi:10.1175/JAM-2181.1.

Palerme, C., J. E. Kay, C. Genthon, T. L'Ecuyer, N. B. Wood, and C. Claud (2014), How much snow falls on the Antarctic ice sheet?, *The Cryosphere*, *8*(4), 1577–1587, doi:10.5194/tc-8-1577-2014.

Pasqualucci, F., B. W. Bartram, R. A. Kropfli, and W. R. Moninger (1983), A millimeter-wavelength dual-polarization Doppler radar for cloud and precipitation studies, *J. Appl. Meteor. Climatol.*, *22*(5), 758–765, doi:10.1175/1520-0450(1983)022<0758:AMWDPD>2.0.CO;2.

Peters, G., B. Fischer, and T. Andersson (2002), Rain observations with a vertically looking micro rain radar (MRR), *Boreal Environ. Res.*, *7*(4), 353–362.

Peters, G., B. Fischer, H. Münster, M. Clemens, and A. Wagner (2005), Profiles of raindrop size distributions as retrieved by microrain radars, *J. Appl. Meteor.*, *44*(12), 1930–1949, doi:10.1175/JAM2316.1.

Petty, G. W. (2001), Physical and microwave radiative properties of precipitating clouds. Part II: A parametric 1D rain-cloud model for use in microwave radiative transfer simulations, *J. Appl. Meteor.*, *40*(12), 2115–2129, doi:10.1175/1520-0450(2001)040<2115:PAMRPO>2.0.CO;2.

Petty, G. W., and W. Huang (2010), Microwave backscatter and extinction by soft ice spheres and complex snow aggregates, *J. Atmos. Sci.*, *67*(3), 769–787, doi:10.1175/2009JAS3146.1.

Petty, G. W., and W. Huang (2011), The modified gamma size distribution applied to inhomogeneous and nonspherical particles: Key relationships and conversions, *J. Atmos. Sci.*, *68*(7), 1460–1473, doi:10.1175/2011JAS3645.1.

Pfeifer, M., G. C. Craig, M. Hagen, and C. Keil (2008), A polarimetric radar forward operator for model evaluation, *J. Appl. Meteor. Climatol.*, *47*(12), 3202–3220, doi:10.1175/2008JAMC1793.1.

Pokharel, B., B. Geerts, X. Jing, K. Friedrich, J. Aikins, D. Breed, R. Rasmussen, and A. Huggins (2014), The impact of ground-based glaciogenic seeding on clouds and precipitation over mountains: A multi-sensor case study of shallow precipitating orographic cumuli, *Atmos. Res.*, *147–148*, 162–182, doi:10.1016/j.atmosres.2014.05.014.

Posselt, D. J., and G. G. Mace (2014), MCMC-based assessment of the error characteristics of a surface-based combined radar-passive microwave cloud property retrieval, *J. Appl. Meteor. Climatol.*, *53*(8), 2034–2057, doi:10.1175/JAMC-D-13-0237.1.

Posselt, D. J., T. S. L'Ecuyer, and G. L. Stephens (2008), Exploring the error characteristics of thin ice cloud property retrievals using a Markov chain Monte Carlo algorithm, *J. Geophys. Res.*, *113*(D24), D24,206, doi:10.1029/2008JD010832.

Prigent, C., W. B. Rossow, and E. Matthews (1997), Microwave land surface emissivities estimated from SSM/I observations, *J. Geophys. Res.*, *102*(D18), 21,867–21,890, doi:10.1029/97JD01360.

Probert-Jones, J. R. (1960), Meteorological use of pulsed Doppler radar, *Nature*, *186*(4721), 271–273, doi:10.1038/186271a0, WOS:A1960ZQ05400003.

Pruppacher, H. R., and J. D. Klett (1997), *Microphysics of Clouds and Precipitation*, 2 ed., Kluwer Academic Publishers, Dordrecht.

Rauber, R. M., and A. Tokay (1991), An explanation for the existence of supercooled water at the top of cold clouds, *J. Atmos. Sci.*, *48*(8), 1005–1023, doi:10.1175/1520-0469(1991)048<1005:AEFTEO>2.0.CO;2.

Reitter, S. (2013), Evaluating ice microphysics in NWP models with satellite observations, Ph.D. thesis, Universität zu Köln, available online: http://kups.ub.uni-koeln.de/5346/ (Accessed 22. Nov 2014).

Rinehart, R. E. (1991), *Radar for Meteorologists*, 2 ed., Rinehart Pub, Grand Forks.

Rodgers, C. D. (2000), *Inverse Methods for Atmospheric Sounding : Theory and Practice*, World Scientific Publishing Company.

Rogers, R. R., and M. K. Yau (1989), *A short course in cloud physics*, 3 ed., Butterworth-Heinemann, Oxford.

Rosenberg, R. (2005), Why is ice slippery?, *Phys. Today*, *58*(12), 50–54, doi:10.1063/1.2169444.

Rosenkranz, P. (2002), Radiative transfer solution using initial values in a scattering and absorbing atmosphere with surface reflection, *IEEE Trans. Geosci. Remote Sens.*, *40*(8), 1889–1892, doi:10.1109/TGRS.2002.802518.

Rosenkranz, P. W. (1998), Water vapor microwave continuum absorption: A comparison of measurements and models, *Radio Sci.*, *33*(4), 919–928, doi:10.1029/98RS01182.

Rutty, M., and J. Andrey (2014), Weather forecast use for winter recreation, *Wea. Climate Soc.*, *6*(3), 293–306, doi:10.1175/WCAS-D-13-00052.1.

Sassen, K. (1991), The polarization lidar technique for cloud research: A review and current assessment, *Bull. Amer. Meteor. Soc.*, *72*(12), 1848–1866, doi:10.1175/1520-0477(1991)072<1848:TPLTFC>2.0.CO;2.

Saunders, R., M. Matricardi, and P. Brunel (1999), *A fast radiative transfer model for assimilation of satellite radiance observations-RTTOV-5*, European Centre for Medium-Range Weather Forecasts, Reading.

Schmid, B., J. M. Tomlinson, J. M. Hubbe, J. M. Comstock, F. Mei, D. Chand, M. S. Pekour, C. D. Kluzek, E. Andrews, S. C. Biraud, and G. M. McFarquhar (2014), The DOE ARM aerial facility, *Bull. Amer. Meteor. Soc.*, *95*(5), 723–742, doi:10.1175/BAMS-D-13-00040.1.

Schmitt, C. G., and A. J. Heymsfield (2010), The dimensional characteristics of ice crystal aggregates from fractal geometry, *J. Atmos. Sci.*, *67*(5), 1605–1616, doi:10.1175/2009JAS3187.1.

Schmitt, C. G., and A. J. Heymsfield (2014), Observational quantification of the separation of simple and complex atmospheric ice particles, *Geophys. Res. Lett.*, *41*(4), 2013GL058,781, doi:10.1002/2013GL058781.

Schneider, T. L., and G. L. Stephens (1995), Theoretical aspects of modeling backscattering by cirrus ice particles at millimeter wavelengths, *J. Atmos. Sci.*, *52*(23), 4367–4385, doi:10.1175/1520-0469(1995)052<4367:TAOMBB>2.0.CO;2.

Schneider, U., A. Becker, P. Finger, A. Meyer-Christoffer, M. Ziese, and B. Rudolf (2014), GPCC's new land surface precipitation climatology based on quality-controlled in situ data and its role in quantifying the global water cycle, *Theor. Appl. Climatol.*, *115*(1-2), 15–40, doi:10.1007/s00704-013-0860-x.

Seifert, A., and K. D. Beheng (2006), A two-moment cloud microphysics parameterization for mixed-phase clouds. Part 1: Model description, *Meteorol. Atmos. Phys.*, *92*(1-2), 45–66, doi:10.1007/s00703-005-0112-4.

Sekelsky, S. M., W. L. Ecklund, J. M. Firda, K. S. Gage, and R. E. McIntosh (1999), Particle size estimation in ice-phase clouds using multifrequency radar reflectivity measurements at 95, 33, and 2.8 GHz, *J. Appl. Meteor.*, *38*(1), 5–28, doi:10.1175/1520-0450(1999)038<0005:PSEIIP>2.0.CO;2.

Seliga, T. A., and V. N. Bringi (1976), Potential use of radar differential reflectivity measurements at orthogonal polarizations for measuring precipitation, *J. Appl. Meteor.*, *15*(1), 69–76, doi:10.1175/1520-0450(1976)015<0069:PUORDR>2.0.CO;2.

Shupe, M. D., and J. M. Intrieri (2004), Cloud radiative forcing of the Arctic surface: The influence of cloud properties, surface albedo, and solar zenith angle, *J. Climate*, *17*(3), 616–628, doi:10.1175/1520-0442(2004)017<0616:CRFOTA>2.0.CO;2.

Shupe, M. D., P. Kollias, S. Y. Matrosov, and T. L. Schneider (2004), Deriving mixed-phase cloud properties from Doppler radar spectra, *J. Atmos. Oceanic Technol.*, *21*(4), 660–670, doi:10.1175/1520-0426(2004)021<0660:DMCPFD>2.0.CO;2.

Shupe, M. D., J. S. Daniel, G. de Boer, E. W. Eloranta, P. Kollias, E. P. Luke, C. N. Long, D. D. Turner, and J. Verlinde (2008a), A focus on mixed-phase clouds, *Bull. Amer. Meteor. Soc.*, *89*(10), 1549–1562, doi:10.1175/2008BAMS2378.1.

Shupe, M. D., P. Kollias, M. Poellot, and E. Eloranta (2008b), On deriving vertical air motions from cloud radar Doppler spectra, *J. Atmos. Oceanic Technol.*, *25*(4), 547–557, doi:10.1175/2007JTECHA1007.1.

Shupe, M. D., I. M. Brooks, and G. Canut (2012), Evaluation of turbulent dissipation rate retrievals from Doppler cloud radar, *Atmos. Meas. Tech.*, *5*(6), 1375–1385, doi:10.5194/amt-5-1375-2012.

Shupe, M. D., D. D. Turner, V. P. Walden, R. Bennartz, M. P. Cadeddu, B. B. Castellani, C. J. Cox, D. R. Hudak, M. S. Kulie, N. B. Miller, R. R. Neely, W. D. Neff, and P. M. Rowe (2013), High and dry: New observations of tropospheric and cloud properties above the Greenland ice sheet, *Bull. Amer. Meteor. Soc.*, *94*(2), 169–186, doi:10.1175/BAMS-D-11-00249.1.

Sloss, P. W., and D. Atlas (1968), Wind shear and reflectivity gradient effects on Doppler radar spectra, *J. Atmos. Sci.*, *25*(6), 1080–1089, doi:10.1175/1520-0469(1968)025<1080:WSARGE>2.0.CO;2.

Smith, P. L. (1984), Equivalent radar reflectivity factors for snow and ice particles, *J. Climate Appl. Meteor.*, *23*(8), 1258–1260.

Smith, P. L. (2010), The unit symbol for the logarithmic scale of radar reflectivity factors, *J. Atmos. Oceanic Technol.*, *27*(3), 615–616, doi:10.1175/2009JTECHA1360.1.

Spek, A. L. J., C. M. H. Unal, D. N. Moisseev, H. W. J. Russchenberg, V. Chandrasekar, and Y. Dufournet (2008), A new technique to categorize and retrieve the microphysical properties of ice particles above the melting layer using radar dual-polarization spectral analysis, *J. Atmos. Oceanic Technol.*, *25*(3), 482–497, doi:10.1175/2007JTECHA944.1.

Sreenivasan, K. R. (1995), On the universality of the Kolmogorov constant, *Phys. Fluids*, *7*(11), 2778–2784, doi:10.1063/1.868656.

Stark, D., B. A. Colle, and S. E. Yuter (2013), Observed microphysical evolution for two East Coast winter storms and the associated snow bands, *Mon. Wea. Rev.*, *141*(6), 2037–2057, doi:10.1175/MWR-D-12-00276.1.

Stengel, M., A. Kniffka, J. F. Meirink, M. Lockhoff, J. Tan, and R. Hollmann (2014), CLAAS: The CM SAF cloud property data set using SEVIRI, *Atmos. Chem. Phys.*, *14*(8), 4297–4311, doi:10.5194/acp-14-4297-2014.

Stephens, G. L., D. G. Vane, R. J. Boain, G. G. Mace, K. Sassen, Z. Wang, A. J. Illingworth, E. J. O'Connor, W. B. Rossow, S. L. Durden, S. D. Miller, R. T. Austin, A. Benedetti, C. Mitrescu, and the CloudSat Science Team (2002), The CloudSat mission and the a-train, *Bull. Amer. Meteor. Soc.*, *83*(12), 1771–1790, doi:10.1175/BAMS-83-12-1771.

Stephens, G. L., D. G. Vane, S. Tanelli, E. Im, S. Durden, M. Rokey, D. Reinke, P. Partain, G. G. Mace, R. Austin, T. L'Ecuyer, J. Haynes, M. Lebsock, K. Suzuki, D. Waliser, D. Wu, J. Kay, A. Gettelman, Z. Wang, and R. Marchand (2008), CloudSat mission: Performance and early science after the first year of operation, *J. Geophys. Res.*, *113*(D8), D00A18, doi:10.1029/2008JD009982.

Stewart, R. E., J. E. Burford, D. R. Hudak, B. Currie, B. Kochtubajda, P. Rodriguez, and J. Liu (2004), Weather systems occurring over Fort Simpson, Northwest Territories, Canada, during three seasons of 1998–1999: 2. Precipitation features, *J. Geophys. Res.*, *109*(D22), D22,109, doi:10.1029/2004JD004929.

Stogryn, A. P., H. T. Bull, K. Rubayi, and S. Iravanchy (1995), The microwave permittivity of sea and fresh water, *Aerojet internal report*, GenCorp Aerojet, Azusa, CA.

Sun, N., and F. Weng (2012), Retrieval of cloud ice water path from special sensor microwave imager/sounder (SSMIS), *J. Appl. Meteor. Climatol.*, *51*(2), 366–379, doi:10.1175/JAMC-D-11-021.1.

Szyrmer, W., and I. Zawadzki (2014a), Snow studies. Part III: Theoretical derivations for the ensemble retrieval of snow microphysics from dual-wavelength vertically pointing radars, *J. Atmos. Sci.*, *71*(3), 1158–1170, doi:10.1175/JAS-D-12-0285.1.

Szyrmer, W., and I. Zawadzki (2014b), Snow studies. Part IV: Ensemble retrieval of snow microphysics from dual-wavelength vertically pointing radars, *J. Atmos. Sci.*, *71*(3), 1171–1186, doi:10.1175/JAS-D-12-0286.1.

Szyrmer, W., A. Tatarevic, and P. Kollias (2012), Ice clouds microphysical retrieval using 94-GHz Doppler radar observations: Basic relations within the retrieval framework, *J. Geophys. Res.*, *117*(D14), D14,203, doi:10.1029/2011JD016675.

Tanelli, S., S. Durden, E. Im, K. Pak, D. Reinke, P. Partain, J. Haynes, and R. Marchand (2008), CloudSat's cloud profiling radar after two years in orbit: Performance, calibration, and processing, *IEEE Trans. Geosci. Remote Sens.*, *46*(11), 3560–3573, doi:10.1109/TGRS.2008.2002030.

Testud, J., S. Oury, R. A. Black, P. Amayenc, and X. Dou (2001), The concept of normalized distribution to describe raindrop spectra: A tool for cloud physics and cloud remote sensing, *J. Appl. Meteor.*, *40*(6), 1118–1140.

Thode, H. C. (2002), *Testing For Normality*, Marcel Dekker, New York.

Thompson, G., R. M. Rasmussen, and K. Manning (2004), Explicit forecasts of winter precipitation using an improved bulk microphysics scheme. Part I: Description and sensitivity analysis, *Mon. Wea. Rev.*, *132*(2), 519–542, doi:10.1175/1520-0493(2004)132<0519:EFOWPU>2.0.CO;2.

Thériault, J. M., R. Rasmussen, K. Ikeda, and S. Landolt (2012), Dependence of snow gauge collection efficiency on snowflake characteristics, *J. Appl. Meteor. Climatol.*, *51*(4), 745–762, doi:10.1175/JAMC-D-11-0116.1.

Tian, L., G. M. Heymsfield, L. Li, A. J. Heymsfield, A. Bansemer, C. H. Twohy, and R. C. Srivastava (2010), A study of cirrus ice particle size distribution using TC4 observations, *J. Atmos. Sci.*, *67*(1), 195–216, doi:10.1175/2009JAS3114.1.

Tremblay, A., A. Glazer, W. Yu, and R. Benoit (1996), A mixed-phase cloud scheme based on a single prognostic equation, *Tellus A*, *48*(4), 483–500, doi:10.1034/j.1600-0870.1996.t01-3-00001.x.

Turner, D., M. Cadeddu, U. Löhnert, S. Crewell, and A. Vogelmann (2009), Modifications to the water vapor continuum in the microwave suggested by ground-based 150-GHz observations, *IEEE Trans. Geosci. Remote Sens.*, *47*(10), 3326–3337, doi:10.1109/TGRS.2009.2022262.

Turner, D. D., and U. Löhnert (2014), Information content and uncertainties in thermodynamic profiles and liquid cloud properties retrieved from the ground-based Atmospheric Emitted Radiance Interferometer (AERI), *J. Appl. Meteor. Climatol.*, *53*(3), 752–771, doi:10.1175/JAMC-D-13-0126.1.

Tyynelä, J., J. Leinonen, D. Moisseev, and T. Nousiainen (2011), Radar backscattering from snowflakes: Comparison of fractal, aggregate, and soft spheroid models, *J. Atmos. Oceanic Technol.*, *28*(11), 1365–1372, doi:10.1175/JTECH-D-11-00004.1.

Tyynelä, J., J. Leinonen, D. Moisseev, T. Nousiainen, and A. von Lerber (2014), Modeling radar backscattering from melting snowflakes using spheroids with nonuniform distribution of water, *J. Quant. Spectrosc. Radiat. Transfer*, *133*, 504–519, doi:10.1016/j.jqsrt.2013.09.013.

Ulaby, F. T., R. K. Moore, and A. K. Fung (1986), *Microwave Remote Sensing: Active and Passive, Volume I: Fundamentals and Radiometry*, Artech House Publishers, Norwood, Mass.

Vavrus, S. (2007), The role of terrestrial snow cover in the climate system, *Clim. Dyn.*, *29*(1), 73–88, doi:10.1007/s00382-007-0226-0.

Verlinde, J., M. P. Rambukkange, E. E. Clothiaux, G. M. McFarquhar, and E. W. Eloranta (2013), Arctic multilayered, mixed-phase cloud processes revealed in millimeter-wave cloud radar Doppler spectra, *J. Geophys. Res. Atmos.*, *118*(23), 2013JD020,183, doi:10.1002/2013JD020183.

Verlinde, J., et al. (2007), The mixed-phase Arctic cloud experiment, *Bull. Amer. Meteor. Soc.*, *88*(2), 205–221, doi:10.1175/BAMS-88-2-205.

Vrugt, J. A., C. J. F. ter Braak, M. P. Clark, J. M. Hyman, and B. A. Robinson (2008), Treatment of input uncertainty in hydrologic modeling: Doing hydrology backward with Markov chain Monte Carlo simulation, *Water Resour. Res.*, *44*(12), W00B09, doi:10.1029/2007WR006720.

Vrugt, J. A., B. C. ter, C. Diks, B. A. Robinson, J. M. Hyman, and D. Higdon (2009), Accelerating Markov chain Monte Carlo simulation by differential evolution with self-adaptive randomized subspace sampling, *Int. J. Nonlinear Sci. Numer. Simul.*, *10*(3), 273–290, doi:10.1515/IJNSNS.2009.10.3.273.

Waliser, D. E., J.-L. F. Li, C. P. Woods, R. T. Austin, J. Bacmeister, J. Chern, A. Del Genio, J. H. Jiang, Z. Kuang, H. Meng, P. Minnis, S. Platnick, W. B. Rossow, G. L. Stephens, S. Sun-Mack, W.-K. Tao, A. M. Tompkins, D. G. Vane, C. Walker, and D. Wu (2009), Cloud ice: A climate model challenge with signs and expectations of progress, *J. Geophys. Res.*, *114*(D8), D00A21, doi:10.1029/2008JD010015.

Waliser, D. E., J.-L. F. Li, T. S. L'Ecuyer, and W.-T. Chen (2011), The impact of precipitating ice and snow on the radiation balance in global climate models, *Geophys. Res. Lett.*, *38*(6), L06,802, doi:10.1029/2010GL046478.

Wang, Z., K. Sassen, D. N. Whiteman, and B. B. Demoz (2004), Studying altocumulus with ice virga using ground-based active and passive remote sensors, *J. Appl. Meteor.*, *43*(3), 449–460, doi:10.1175/1520-0450(2004)043<0449:SAWIVU>2.0.CO;2.

Wang, Z., J. French, G. Vali, P. Wechsler, S. Haimov, A. Rodi, M. Deng, D. Leon, J. Snider, L. Peng, and A. L. Pazmany (2012), Single aircraft integration of remote sensing and in situ sampling for the study of cloud microphysics and dynamics, *Bull. Amer. Meteor. Soc.*, *93*(5), 653–668, doi:10.1175/BAMS-D-11-00044.1.

Warren, S. G., and R. E. Brandt (2008), Optical constants of ice from the ultraviolet to the microwave: A revised compilation, *J. Geophys. Res.*, *113*(D14), D14,220, doi:10.1029/2007JD009744.

Waterman, P. (1965), Matrix formulation of electromagnetic scattering, *Proc. IEEE*, *53*(8), 805–812, doi:10.1109/PROC.1965.4058.

Weng, F., and N. C. Grody (2000), Retrieval of ice cloud parameters using a microwave imaging radiometer, *J. Atmos. Sci.*, *57*(8), 1069–1081, doi:10.1175/1520-0469(2000)057<1069:ROICPU>2.0.CO;2.

Winker, D. M., M. A. Vaughan, A. Omar, Y. Hu, K. A. Powell, Z. Liu, W. H. Hunt, and S. A. Young (2009), Overview of the CALIPSO mission and CALIOP data processing algorithms, *J. Atmos. Oceanic Technol.*, *26*(11), 2310–2323, doi:10.1175/2009JTECHA1281.1.

Wolfe, J. P., and J. R. Snider (2012), A relationship between reflectivity and snow rate for a high-altitude S-Band radar, *J. Appl. Meteor. Climatol.*, *51*(6), 1111–1128, doi:10.1175/JAMC-D-11-0112.1.

Wood, N. B. (2011), Estimation of snow microphysical properties with application to millimeter-wavelength radar retrievals for snowfall rate, Ph.D. thesis, Colorado State University, available online: http://digitool.library.colostate.edu/R/?func=dbin-jump-full&object_id=123397 (Accessed 22. Nov 2014).

Wood, N. B., T. S. L'Ecuyer, D. G. Vane, G. L. Stephens, and P. Partain (2013), CloudSat Level 2C snow profile process description and interface control document, available online: http://www.cloudsat.cira.colostate.edu/ICD/2C-SNOW-PROFILE/2C-SNOW-PROFILE_PDICD_P_R04.pdf (Accessed 22. Nov 2014).

Xie, X. (2012), Polarized signals from oriented frozen hydrometeors using passive microwave radiometry, Ph.D. thesis, Universität zu Köln, available online: http://kups.ub.uni-koeln.de/4775/ (Accessed 22. Nov 2014).

Xie, X., U. Löhnert, S. Kneifel, and S. Crewell (2012), Snow particle orientation observed by ground-based microwave radiometry, *J. Geophys. Res.*, *117*(D2), D02,206, doi:10.1029/2011JD016369.

Yang, D., D. Kane, Z. Zhang, D. Legates, and B. Goodison (2005), Bias corrections of long-term (1973-2004) daily precipitation data over the northern regions, *Geophys. Res. Lett.*, *32*, 19,501, doi:10.1029/2005GL024057.

Yang, P., L. Zhang, G. Hong, S. Nasiri, B. Baum, H.-L. Huang, M. King, and S. Platnick (2007), Differences between collection 4 and 5 MODIS ice cloud optical/microphysical products and their impact on radiative forcing simulations, *IEEE Trans. Geosci. Remote Sens.*, *45*(9), 2886–2899, doi:10.1109/TGRS.2007.898276.

Young, A. T. (1981), Rayleigh scattering, *Appl. Opt.*, *20*(4), 533, doi:10.1364/AO.20.000533.

Zikmunda, J., and G. Vali (1972), Fall patterns and fall velocities of rimed ice crystals, *J. Atmos. Sci.*, *29*(7), 1334–1347, doi:10.1175/1520-0469(1972)029<1334:FPAFVO>2.0.CO;2.

Zrnić, D. S. (1975), Simulation of weatherlike Doppler spectra and signals, *J. Appl. Meteor.*, *14*(4), 619–620, doi:10.1175/1520-0450(1975)014<0619:SOWDSA>2.0.CO;2.

DANKSAGUNG

This study was carried out within the project ADMIRARI II supported by the *German Research Association* (DFG) under research grant number LO901/5-1.

Uli, tausend Dank für Deine phantastische Betreuung, ich war (und bin!) in besten Händen.

Zu den tragenden Händen gehören natürlich auch die von *Susanne*. Danke, nicht nur für die tollen Arbeitsbedingungen.

Thanks a lot to *Roel* and *Herman* for kindly acting as referees.

Dank geht auch an die weiteren Mitglieder meines Doctoral Comitee für ihren Rat, *Harrie-Jan* und *Clemens*.

Pavlos, thanks for clarifying that I was not a radar meteorologist. Thanks a lot for supporting to change that.

Dank an all die anderen Infernos, es ist eine Freude mit Euch zu arbeiten. Dank gilt besonders denen, die mich beim Korrekturlesen unterstützt haben: *Kerstin*, *Emiliano*, *Claudia*, *Sandra*, *Maria* und ganz besonders *Sonja*. Ich hoffe, wir können noch eine Zeit lang weiter streiten! *Stefan*, es ist immer herausfordernd mit Dir zu arbeiten, ich freue mich schon auf unser nächstes Projekt! Wie Du an der Seitenzahl sehen kannst, kann ich mich jetzt auch nicht mehr kurzfassen. Nicht zu vergessen *Rainer*, durch Dich darf man ohne Sorge zwei linke Forscherhände haben.

Also a thank you to the group at *McGill* in Montreal for being so cordial during my visit, I have great memories of my 27.5 birthday.

Dank geht an *Karin* und *Anastasia* von der IRTG für Ihre großzügige Unterstützung.

Thanks to *Irina*, *Nicole*, *Kristof* and *Stef* of KU Leuven for the great collaboration concerning the blind zone paper, I hope we can repeat this. Thanks to *Bobby* and *Greg* for supporting me with the ISDAC in situ data.

Thanks a lot to all the people taking care of the instruments in the field: the staff of the *UFS*, of the *ARM program*, at the *CARE site*, in *Svalbard* and at the *Princess Elisabeth station*.

Angelika und *Wolf*, Danke, dass ihr mir Inspiration, Mut und Vertrauen schenkt.

Fine, ich danke Dir sehr für Deine unendliche Geduld und Liebe. Du gibst mir Kraft.

ERKLÄRUNG

Ich versichere, dass ich die von mir vorgelegte Dissertation selbständig angefertigt, die benutzten Quellen und Hilfsmittel vollständig angegeben und die Stellen der Arbeit – einschließlich Tabellen, Karten und Abbildungen –, die anderen Werken im Wortlaut oder dem Sinn nach entnommen sind, in jedem Einzelfall als Entlehnung kenntlich gemacht habe; dass diese Dissertation noch keiner anderen Fakultät oder Universität zur Prüfung vorgelegen hat; dass sie – abgesehen von unten angegebenen Teilpublikationen – noch nicht veröffentlicht worden ist, sowie, dass ich eine solche Veröffentlichung vor Abschluss des Promotionsverfahrens nicht vornehmen werde. Die Bestimmungen der Promotionsordnung sind mir bekannt. Die von mir vorgelegte Dissertation ist von PD Dr. Ulrich Löhnert betreut worden.

Köln, Februar 2015

Maximilian Maahn

TEILPUBLIKATIONEN

Mech, M., Maahn, M., Orlandi, E., Kneifel, S., Kollias, P., Redl, S., and Crewell, S. (2015). PAMTRA - passive and active microwave radiative transfer model: Basic concepts and applications for cloud research *Atmospheric Chemistry and Physics*, in preparation.

IN DIESE DISSERTATION INTEGRIERTE PUBLIKATIONEN

Maahn, M. and Kollias, P. (2012). Improved Micro Rain Radar snow measurements using Doppler spectra post-processing. *Atmospheric Measurement Techniques*, 5(11):2661–2673, doi:10.5194/amt-5-2661-2012.

Eigene Beteiligung: Die Konzeption, Theorie, Implementierung und Auswertung der Studie wurden von mir unter Beratung von Prof. Dr. P. Kollias im Rahmen meines Gastaufenthalts an der McGill University in Montreal erstellt.

Maahn, M., Burgard, C., Crewell, S., Gorodetskaya, I. V., Kneifel, S., Lhermitte, S., Van Tricht, K., and van Lipzig, N. P. M. (2014).

How does the spaceborne radar blind zone affect derived surface snowfall statistics in polar regions? *Journal of Geophysical Research: Atmospheres*, 119(24):13604–13620 doi:10.1002/2014JD022079.

Eigene Beteiligung: Die Idee für diesen Artikel entstand im Rahmen der Bachelorarbeit von C. Burgard, die ich zusammen mit Prof. Dr. S. Crewell betreut habe. Die Prozessierung der MRR Daten sowie der Großteil der Auswertung wurde von mir durchgeführt. Bis auf Abbildung 4 habe ich alle Abbildungen selbst erstellt. Des weiteren basieren der Großteil der Beschreibung der Instrumente bzw. Prozessierung (Sec. 3), die Auswertung der Daten (Sec. 5) sowie die Zusammenfassung (Sec. 6) auf meinen Textentwürfen. Dr. I. Grorodetskaya hat mit der Stationsbeschreibung für die Antarktis sowie mit der Klassifikation der Wetterlagen beigetragen, C. Burgard hat die Station auf Svalbard beschrieben. Dr. S. Lhermitte und K. Van Tricht haben den Vergleich mit CloudSat beigesteuert, während Dr. S. Kneifel die Einleitung und die Fallstudie verfasst hat. Prof. Dr. N. Van Lipzig und Prof. Dr. C. Crewell haben uns bei der Diskussion und der Überarbeitung der Ergebnisse unterstützt.

Maahn, M., Löhnert, U., Kollias, P., Jackson, R. C., and McFarquhar, G. M. (2015). Developing and evaluating ice cloud parameterizations for forward modeling of radar moments using in situ aircraft observations. *Journal of Atmospheric & Oceanic Technology*, accepted.

Eigene Beteiligung: Für diese Studie wurden von R. Jackson und Prof. Dr. G. McFarquhar Flugzeugmessungen von Eiswolken bereitgestellt. Prof. Dr. P. Kollias hat die Vorlage für den Radarsimulator zur Verfügung gestellt, den ich in das von der AG Crewell entwickelte und von mir erweiterte Pamtra Model eingebaut habe. Sämtliche Berechnungen, Abbildungen sowie der komplette Textentwurf wurden von mir erstellt. Herr PD Dr. U. Löhnert hat mich bei Konzeption der Studie und Interpretation der Ergebnisse unterstützt.